SIMULATIONS OF VITIATED BLUFF BODY STABILIZED FLAMES

A Thesis
Presented to
The Academic Faculty

by

Andrew G. Smith

In Partial Fulfillment
of the Requirements for the Degree
Doctor of Philosophy in the
School of Aerospace Engineering

Georgia Institute of Technology
August 2016

SIMULATIONS OF VITIATED BLUFF BODY STABILIZED FLAMES

Approved by:

Professor Suresh Menon, Advisor
School of Aerospace Engineering
Georgia Institute of Technology

Professor Lakshmi Sankar
School of Aerospace Engineering
Georgia Institute of Technology

Professor Jerry Seitzman
School of Aerospace Engineering
Georgia Institute of Technology

Professor Jechiel Jagoda
School of Aerospace Engineering
Georgia Institute of Technology

Dr. Jeffery Lovett
Exhaust System Technology
Pratt & Whitney Aircraft Engines

Date Approved: 12 May 2016

ACKNOWLEDGEMENTS

I would like to first and foremost thank my advisor, Dr. Suresh Menon, for giving me the opportunity to pursue this research at the Computational Combustion Laboratory here at Georgia Tech. He allowed me the freedom to study many aspects of reacting flow CFD including flow physics, numerical methods and software design. I appreciate his patience through this long process and want to especially thank him for being supportive and flexible as I concluded this thesis. I also want to thank my committee members, Dr. Jerry Seitzman, Dr. Jechiel Jagoda, Dr. Jeffery Lovett and Dr. Lakshmi Sankar for reading this thesis and providing feedback.

Development of a CFD code and its application to interesting problems cannot be done by a single person and thus I want to thank all my colleagues at the CCL. Specifically my work could not have been completed without collaboration and input from Dr. Srikant Srinivasan, Dr. Leandro Gryngarten, Dr. Matthieu Masquelet, Dr. Joey Schulz, Dr. Kalyan Gottiparthi, and Matthew Clay. Last, and certainly not certainly not least, I must thank my lab-mate Timothy Gallagher. Without the countless hours of working on code development together this work would not have been possible.

I also must thank Pratt & Whitney Aircraft Engines for providing the financial support for the majority of my time here.

Finally, I need to thank my family. My brother, Bryan, my mother, Cyrilla, and father, Bill, have supported me throughout this endeavor and never gave up on me. I want to thank my sons, Jenson and Graham, for providing me with additional inspiration and determination to finish this work. Of course I must thank my wife, Jenna, whose understanding, patience and support allowed me to finally finish.

TABLE OF CONTENTS

LIST OF TABLES

LIST OF FIGURES

SUMMARY

Bluff bodies have a wide range of applications where low-cost, light weight methods are needed to stabilize flames in high-speed flow. The principles of bluff body flame stabilization are straightforward, but many details are not understood; this is especially true in vitiated environments where measurements are difficult to obtain. Most work has focused on premixed flames but changing application requirements are now driving studies on non-premixed gaseous and spray flames. This thesis aims to improve the understanding of vitiated, bluff body stabilized flames, specifically on non-premixed, spray flames, through the use of Large Eddy Simulation (LES).

The single flameholder facility at Georgia Tech was chosen as the basis for the simulations in this thesis. The flameholder was a rectangular bluff body with an aerodynamic leading edge with discrete liquid fuel injectors embedded just upstream of the trailing edge in a configuration described as "close-coupled." The liquid phase was modeled using a Lagrangian particle approach where discrete fuel droplets were injected into the domain. Experimental data was used to tune model parameters as well as the stripped droplet velocities and sizes. The discharge coefficient needed to be taken into account to achieve the correct fuel jet penetration.

The experiments were conducted over a range of global equivalence ratios; lean equivalence ratios, $\phi_{\text{global}} \approx 0.5$, exhibited symmetric flame shedding and conversely large scale sinusoidal Bérnard/von-Kármán shedding was observed when the equivalence ratio was near unity. Reacting flow LES were computed at these two fuel flow rates to improve understanding of the different flame dynamics. LES were first completed using a quasi-laminar subgrid turbulence-chemistry interaction model. Spanwise averaging of instantaneous and time-averaged LES results were compared with

experimental high- and low-speed imaging and showed the LES was in qualitative agreement at both fuel flow rates. At $\phi_{\text{global}} \approx 0.5$, the fuel jet did not penetrate as far into the crossflow compared to $\phi_{\text{global}} \approx 0.95$ and thus more fuel was delivered to the shear layers of the bluff body resulting in higher heat release in the shear layers for the low fuel flow rate. The heat release damped the large sinusoidal structures via gas expansion and baroclinic torque generation. Higher fuel jet penetration in the $\phi_{\text{global}} \approx 0.95$ case meant less fuel was delivered to the shear layers and so less heat release occurred directly behind the bluff body so the large scale sinusoidal shedding was not damped. The impact of the subgrid turbulence-chemistry interaction model on the flame dynamics was tested by comparing the quasi-laminar LES with LES using the subgrid linear eddy model (LEMLES). The flame structure predicted with LEMLES matched that of the quasi-laminar LES, at both fuel flow rates in the near-field behind the bluff body but deviated farther downstream. A flame edge analysis showed little sensitivity to the choice of subgrid model in the region $x < 4D$.

A high-order hybrid finite-difference solver with consisting of a WENO upwind method and compact central scheme was implemented to assess the effects of the numerical method. A series of test cases was used to verify, validate and compare several of the available spatial and temporal methods before the high fuel flow rate bluff body case was run. For the simple test cases the higher-order methods were clearly more efficient but for more complex cases the differences between the second-order and high-order methods are smaller.

To test the hypothesis that the fuel jet penetration was the main factor in the flame dynamics another configuration with a modified fuel injector diameter was simulated. The injector size was chosen to match the spray penetration of $\phi_{\text{global}} \approx 0.5$ case while maintaining the fuel flow rate of the $\phi_{\text{global}} \approx 0.95$ case. The results confirmed the hypothesis as the flame dynamics of this configuration match the original low fuel flow rate case.

CHAPTER I

INTRODUCTION AND MOTIVATION

1.1 Motivation

Bluff bodies are used in a variety of applications to stabilize flames in high-speed flow. They are commonly found in aerospace gas turbine applications for stabilization of primary or secondary combustion (thrust augmentation) due to their light weight, low cost and simplicity. Bluff bodies are also important in scramjet, ramjet and ground-based gas turbine flame-holding.

The principles of bluff body flame stabilization are straightforward: the bluff body provides a region of recirculation which allows hot combustion products to interact with incoming reactants and sustain burning. The actual combustion process is complicated by the interaction of the reaction zone with the vortical structures generated by the flow separation from the bluff body. These structures range in size and amplitude from small-scale turbulence to Kelvin-Helmholtz shear-layer instabilities and large coherent Bérnard/von-Kármán vortex streets. These flow structures can directly effect the reaction zone by altering the location of reactants and products and their mixing, as well as create a feedback mechanism for acoustic-vortical interactions.

While most research has focused on premixed applications, changing application requirements are now driving studies on non-premixed gaseous and spray bluff body stabilized flames [118]. The difficult task of observation and measurement of combustion only becomes more complicated at vitiated conditions and with the addition of fuel spray. Computational tools need to be developed and validated with the limited data available in order to help better understand the underlying flow physics and provide insight that cannot be obtained through experiments alone.

1.2 Background

1.2.1 Non-reacting bluff body flow

A simple two-dimensional bluff body is shown in Figure 1 that illustrates the main flow features of typical non-reacting flows. Boundary layers on the bluff body walls grow before flow separation at the trailing edge. At low Reynolds numbers stable, symmetric recirculation zones attach to the trailing edge. Shear layers form aft of the trailing edge and envelop the recirculation zones. As the Reynolds number increases, the shear layers are subject to the inviscid hydrodynamic instability known as the Kelvin-Helmholtz instability, in which small coherent vortices appear downstream of the separation point and shed symmetrically. Once a shape-dependent critical

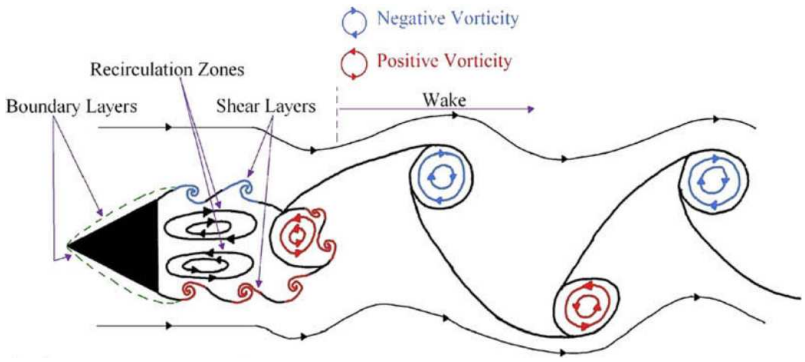

Figure 1 Two-dimensional non-reacting bluff body flow (reprinted from [190] with permission)

Reynolds number is reached, large scale coherent vortices are alternately shed from each side of the bluff body. The rate at which these Bérnard/von-Kármán vortices are shed is often described by the non-dimensional Strouhal number,

$$St = \frac{fD}{U} \tag{1}$$

where U is the incoming flow velocity, D is the characteristic height of the bluff body, and f is the instability frequency. Typical Strouhal numbers range between 0.2–0.29. The large vortical structures occur due to the interaction of the shear layers from both sides of the bluff body.

1.2.2 Heat release effects on bluff body flows

Heat release due to combustion generally has a stabilizing effect on bluff body flows. Large scale asymmetric fluctuations are damped leaving symmetric shear layer rollup. This phenomenon can be explained by examining Eq. (2), the vorticity transport equation.

$$\frac{D\vec{\omega}}{Dt} = \underbrace{(\vec{\omega}\cdot\nabla)\,\vec{V}}_{\text{vortex stretching}} - \underbrace{\vec{\omega}\left(\nabla\cdot\vec{V}\right)}_{\text{gas expansion}} - \underbrace{\frac{\nabla\rho\times\nabla p}{\rho^2}}_{\text{baroclinic torque}} + \underbrace{\nu\nabla^2\vec{\omega}}_{\text{viscous diffusion}} \tag{2}$$

Several factors have stabilizing influences: gas expansion takes place acting as a vorticity sink, baroclinic torque is produced and for gas flows, viscosity increases with temperature increasing vorticity diffusion. Although it may appear the production of baroclinic torque has a destabilizing effect, for confined bluff body flames this vorticity is generated in the opposite direction to that of the vorticity in the shear layers thus decreasing the magnitude [190]. Both gas expansion and baroclinic torque are proportional to the dilation ratio, ρ_u/ρ_b, the ratio of unburned density to burned product density.

Experiments and computational studies have both demonstrated this reduced shear layer vorticity under reacting conditions. Chaudhuri and coworkers examined simultaneous OH PLIF and PIV measurements and found that for stable flames maximum OH concentrations lie in the same region as the high vorticity shear layer [21]. It is interesting to note that high speed images from this study showed the possibility of flame reignition due to downstream wake burning even after reactions cease in the shear layer. Mehta and Soteriou showed the gas expansion effect to be the dominant factor in the near field of the bluff body with the baroclinic vorticity amplifying the effect several diameters downstream [133]. Large eddy simulations of premixed bluff body flames showed strong baroclinic torque and weakening of the Bérnard/von-Kármán structures [156].

Several studies have addressed numerical aspects of simulating bluff body stabilized flames; specifically for LES, the influence of subgrid turbulence-chemistry closure models has been investigated. Fureby tested finite rate chemistry models including quasi-laminar, partially stirred reactor, thickened flame, and presumed PDF models and compared them with flamelet methods [57]. He concluded that for this type of flow the finite rate methods were superior since the the flamelet method assumptions are not valid for all combustion regimes in the flow. The finite rate methods all performed reasonably well. Fureby also compared two chemical mechanisms with the finite rate methods, a one- and a two-step mechanism. As expected, the two-step mechanism showed better agreement with experimental results.

Porumbel and Menon simulated the same case as Fureby and compared the subgrid eddy breakup (SEBU) model with the subgrid linear eddy model, a methodology known as LEMLES [156]. LEMLES more accurately predicted vorticity and temperature fields as well as the velocity fluctuations, though it should be noted the LEMLES approach is more computationally expensive than the subgrid eddy breakup model.

1.2.3 Influence of vitiation

As the incoming reactant temperature is increased, the ρ_u/ρ_b ratio decreases reducing the stabilizing effects of gas expansion and baroclinic torque generation. Erickson et al. completed a computational study demonstrating the reduction in Bérnard/von-Kármán vortices as the T_b/T_u ratio increased [46]. Figure 2 shows the transition from asymmetric to symmetric shedding.

Varying the equivalence ratio also changes the ρ_u/ρ_b ratio and thus the stability of the flame, with vitiation amplifying the effects. This has major implications especially for lean flames near blowout. Figure 3 shows a sequence of snapshots of a vitiated flame as the equivalence ratio is reduced [100].

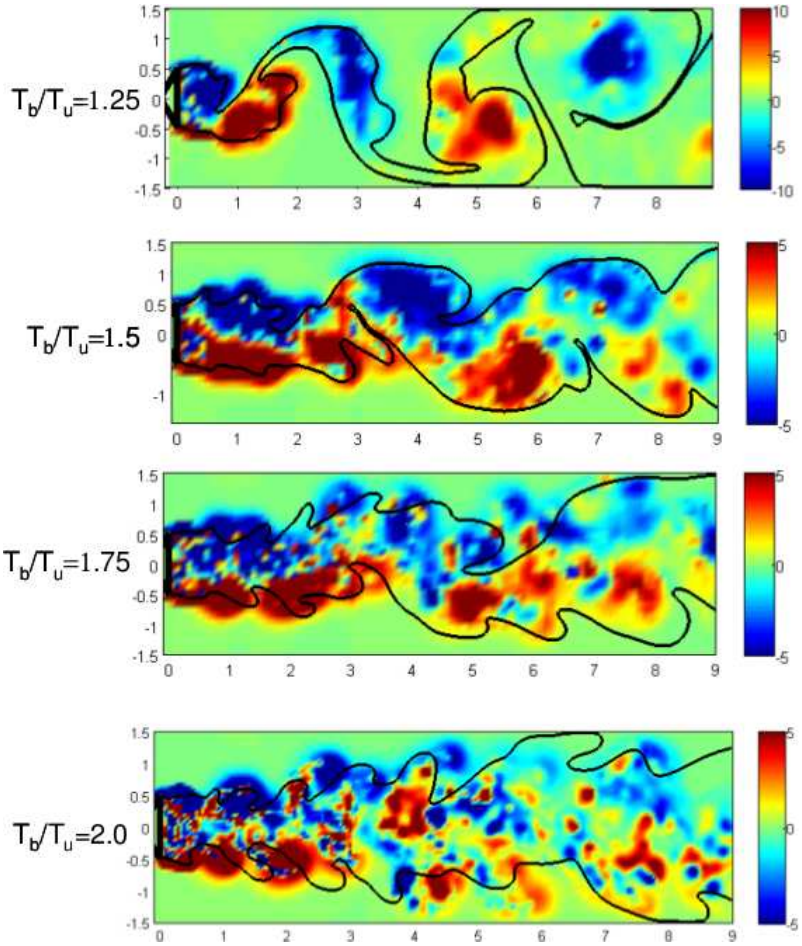

Figure 2 Vorticity and flame location for bluff body flames at different temperature ratios (reprinted from [46] with permission of the American Institute of Aeronautics and Astronautics)

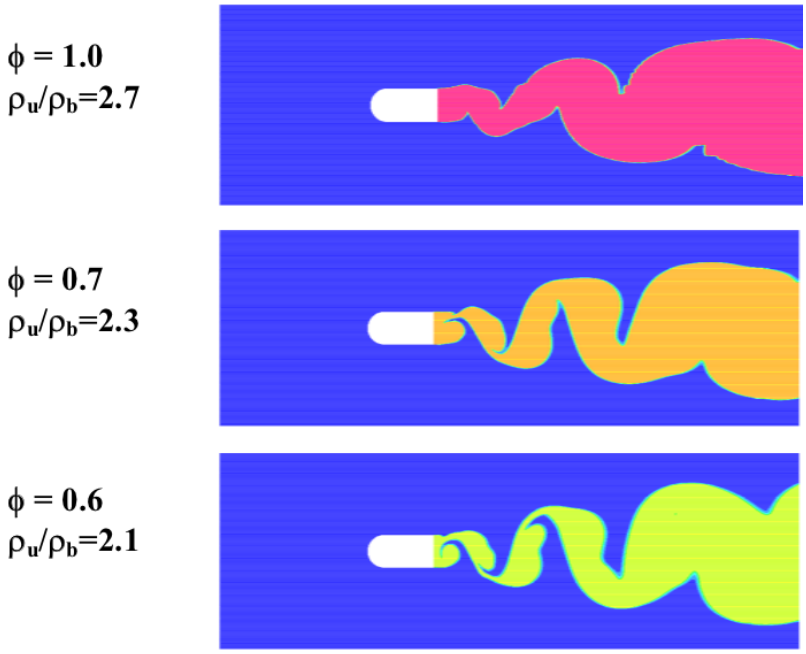

Figure 3 Blowout sequence for low-density ratio/highly vitiated flames (reprinted from [100] with permission of the American Institute of Aeronautics and Astronautics)

Kiel investigated non-reacting and reacting V-gutter bluff body flows under non-vitiated and vitiated conditions using LDV and high speed imaging and used unsteady Reynolds averaged Navier-Stokes (URANS) simulations to study the non-reacting cases [102, 101]. They reported that under non-vitiated conditions the flow was dominated by smaller vortices generated in the boundary layer. High speed images of high Reynolds number flows under vitiated conditions near lean blowout clearly showed the flow was dominated by the large scale Bérnard/von-Kármán vortices.

Tuttle et al. completed experiments using the same geometry as Chaudhuri et al. taking high speed images of vitiated bluff body flames near lean blowout [217, 21]. In contrast to the non-vitiated results, no reignition events were recorded; once reactions were no longer visible in the shear layers the flame would eventually blowout. Another important conclusion from this study is that the ρ_u/ρ_b density ratio at blow-off is significantly less for vitiated flows compared with non-vitiated flows. The authors state that this indicates the Bérnard/von-Kármán instability is more important for

blow-off in vitiated flames than in non-vitiated flames.

In a separate study the same authors looked at fuel distribution effects for vitiated premixed flames [218]. They varied the equivalence ratio of the incoming fuel/air mixture across the height of the bluff body and observed that the lean side exhibited a fragmented flame sheet structure even under stable operating conditions. The global equivalence ratio at blowout increased with increasing equivalence ratio non-uniformity suggesting that fuel distribution effects can significantly influence stability even for premixed flames. Both studies were completed with inflow temperatures between 720–820 K and bluff body Reynolds and Mach numbers around 10000 and 0.1, respectively.

LES has been performed on vitiated premixed bluff body flames as well. Smith et al. simulated a V-gutter type bluff body in 700 K inlet air at $Re = 29000$ with a propane/air mixture [200]. They matched the trends of experimental results showing that lean blowout occured for at higher equivalence ratio for vitiated flames than non-vitiated flames. Although the simulations helped to improve understanding of the blowoff mechanisms, they did not run at the same conditions as their experimental data and thus could not be directly compared. They noted their simulations could be improved by using a two-step chemical mechanism, fuel first going to carbon monoxide and water, then carbon monoxide to carbon dioxide, rather than the single step global mechanism.

Khosla completed LES on two different blunt-nose bluff body geometries, with and without vertical tabs at the trailing edge [100]. The tabs were attached to eliminate the large scale Bérnard/von-Kármán vortices in an effort to determine if these vortices were a significant contributor to blowout. The simulation conditions were 90 m/s, 700 K, using two-step kinetics for Jet-A fuel. They conclude that although the Bérnard/von-Kármán vortices may affect blowout, the most important factor seems to be the ratio of flow speed to flame speed. They also suggest that

future works investigate non-premixed spray configurations and determine the effects of turbulence-chemistry interaction.

Gokulakrishnan et al. attempted to determine the influence of turbulence-chemistry models in their premixed LES study [66]. They simulated two different propane/air reaction mechanisms (a skeletal 30 species and 110 reactions, and a 44 step semi-global mechanism), on two grids (0.65 M and 2.4 M cells), with two subgrid models (Eddy-Dissipation Concept (EDC) and laminar chemistry). The flow conditions were similar to that of Smith et al. [200]. When using the laminar chemistry model, the choice of chemical mechanism did not affect the flame structure; the mechanism did change the flame structure with the EDC model, the skeletal mechanism showing an unstable flame at $\phi = 0.6$ whereas the semi-global mechanism blows out. There were stark differences between the subgrid models in the shear layers. The laminar chemistry model showed symmetric shedding for several bluff body diameters downstream before Bérnard/von-Kármán vortices appear in contrast to the EDC model where the flow wass much more unstable with Bérnard/von-Kármán vortices directly behind the bluff body.

1.2.4 Non-premixed vitiated bluff body stabilized flames

Khosla et al. limited the scope of their study to premixed flames as fuel injection adds additional complexities, however, more research is necessary for non-premixed bluff body stabilized flames as they will continue to play a role in aerospace applications [118]. In such applications, increasing temperatures and demands for simplified combustors has led to integrated fuel injectors/flameholders. Advantages of such a configuration are increased cooling to the flameholder by the liquid fuel and decreased susceptibility to autoignition. The disadvantage is the fuel spray can directly interact with the wake flow and have a much larger influence on flame dynamics.

Kim and Mungal studied the role of bluff body trailing edge geometry in close-coupled gaseous-fueled systems [106]. In this thesis, the term "close-coupled" refers to the proximity of the fuel injectors to the flame stabilization location [118]. They found that bluff bodies with small cavities in the trailing edge can extend the blowout limits for some situations. El-Asrag and coworkers studied non-premixed close-coupled gaseous fueled bluff body flames experimentally and numerically at vitiated conditions but relatively low velocities [45]. They note that most industrial applications actually use liquid fuel and operate at high velocities.

An important part of understanding liquid fueled close-coupled bluff bodies is the characterization of liquid jets in cross flow (LJICF) under the conditions of interest. Brown and coworkers outlined some of the difficulties in obtaining data under vitiated conditions and made observations about available data [15]. They noted that most LJICF data comes from water at "room temperature" and there is a large amount of discrepancy between the data, some of which can be contributed to the discharge coefficient of the injector, a parameter with a large effect on the spray but often not reported. Studies by Lubarsky et al. have shown that spray modeling is also complicated by the fact the spray is affected by the presence of a flame for close-coupled bluff body spray applications [122, 123]. Many spray models only consider a single mode, the most unstable mode, when predicting droplet breakup though other experiments by Lubarsky suggest in certain Weber number regimes there exists multimode breakup [167, 124].

Cross et al, performed experiments at realistic high temperature, high velocity conditions with liquid fuel [33, 32]. Their results suggested that fuel distribution and thus heat release distribution plays an important role in flame stability. Higher fuel flow rates with global equivalence ratios closer to unity exhibited more large scale Bérnard/von-Kármán instabilities than lower global equivalence ratios. The more symmetric flame shedding seen at the low fuel flow rate conditions was similar to

the flame dynamics of the combustor using an upstream-fueled configuration. The differences in the flame dynamics at the two different fuel flow rate operating conditions was attributed to differences in the fuel penetration of the fuel spray and the subsequent spatial distribution of the heat release.

To the author's knowledge no computational studies for this type of problem have been completed, specifically for liquid fueled close-coupled bluff bodies at vitiated conditions. Time accurate simulations are needed to capture combustion dynamics which rules out Reynolds Averaged Navier-Stokes (RANS) simulations leaving Large Eddy Simulation (LES) or Direct Numerical Simulation (DNS) as possible methods, though DNS for practical combustors is computational intractable. This class of problem presents many challenges for any numerical study including but not limited to choice of chemical mechanism, multiphase modeling methodology, boundary condition specification, spatial and temporal integration methods and subgrid models. Once the appropriate parameters and models are selected simulations can be completed to supplement the knowledge gained through experiments.

CHAPTER II

OBJECTIVES

The overall objective of this work is to use LES to improve understanding of vitiated, bluff body stabilized flames, with a specific emphasis on spray flames. This objective is quite broad and as such will be broken down into several objectives each with subtasks necessary for completion. Each objective should address at least one of three areas: physics, numerics and modeling.

1. Assess the effects of fuel distribution and mixing on flame dynamics. For non-premixed problems, spray penetration directly effects where fuel is located in time and space and as such is a controlling factor for the heat release and thus flame dynamics. The spray penetration and fuel distribution predicted by LES is dependent on many factors including spray injection and break-up models, turbulent mixing parameters and physical injection parameters.

   (a) Select a suitable experimental test facility for vitiated bluff body stabilized spray flames and simulate a non-reacting case to validate the flow simulation methodology and establish a baseline for reacting cases.

   (b) Simulate several reacting conditions that show different flame dynamics and compare with experimental results.

   (c) The primary and secondary breakup models currently in use were developed for use with RANS and/or for use at specific operating conditions [128, 167]. Identify the sensitivities of liquid droplet distribution and evaporated fuel vapor distribution to breakup model parameters, e.g. jet regime stripped droplet velocities and sizes, and model tuning parameters, at typical operating conditions for bluff body stabilized spray flames.

2. Investigate the role of the LES subgrid turbulence-chemistry interaction closure model for non-premixed vitiated bluff body stabilized flames. Several studies have shown that simple models such as the quasi-laminar chemistry provide adequate accuracy while others have shown that the subgrid model can have a significant effect on the results [57, 66, 156]. The previous studies focused on premixed applications only; work now needs to be done for non-premixed configurations as well.

   (a) Simulate a reacting case with the baseline grid and simple turbulent closure such as quasi-laminar chemistry and compare with experiments.

   (b) Researchers have previously shown good results for spray combustion with more complex closures, such as LEM, at increased computational cost [135, 148]. Simulations will be conducted with LEMLES and compared with previous results to determine if the added cost is necessary to accurately simulate this configuration.

3. Address the impact of the numerical method on the simulation solution, as some studies have indicated under certain conditions the numerical method is as important as the choice of subgrid models [228, 27]. To achieve this, a high-order numerical method will be implemented and simulations with this method compared with the baseline results.

The goal for industrial application is the use of LES as a predictive tool. The final step in completing the thesis will be to select a different operating condition and run a final reacting simulation with the goal of predicting the flame dynamics based on the simulation conditions.

CHAPTER III

MATHEMATICAL FORMULATION AND MODELING

3.1 The Navier-Stokes equations

The Navier-Stokes equations describe the motion of unsteady, compressible, multi-species, reacting fluids. Neglecting body forces such as gravity and assuming the fluid of interest is a continuum, the equations for the conservation of mass, momentum, total energy and species are as follows:

$$\frac{\partial \rho}{\partial t} + \frac{\partial \rho u_i}{\partial x_i} = \dot{\rho}_s \tag{3}$$

$$\frac{\partial \rho u_i}{\partial t} + \frac{\partial}{\partial x_j}\left[\rho u_i u_j + p\delta_{ij} - \tau_{ij}\right] = \dot{F}_{s,i} \tag{4}$$

$$\frac{\partial \rho E}{\partial t} + \frac{\partial}{\partial x_i}\left[\left(\rho E + p\right) u_i + q_i - u_j \tau_{ij}\right] = \dot{Q}_s \tag{5}$$

$$\frac{\partial \rho Y_k}{\partial t} + \frac{\partial}{\partial x_i}\left[\rho u_i Y_k + J_{i,k}\right] = \dot{\omega}_k + \dot{S}_{s,k}, \quad k = 1, \ldots, N_s. \tag{6}$$

In the above Navier-Stokes equations, ρ is the density, p is the pressure, u_i is the Cartesian velocity vector and Y_k is the mass fraction of species k where there are a total of N_s species in the flow. The total energy, E is a combination of internal energy, e and kinetic energy:

$$E = e + \frac{1}{2} u_k u_k \tag{7}$$

where for the internal energy is the summation of the internal energies for all the species present:

$$e = \sum_{k=1}^{N_s} Y_k e_k \tag{8}$$

where e_k is the sensible energy of the k^{th} species. The viscous stress tensor is denoted as τ_{ij}; the heat flux vector is q_i and the species diffusion flux is $J_{i,k}$. The species chemical reaction rates are $\dot{\omega}$. The formulation here includes source terms from a

dispersed phase, indicated by the the subscript $_s$, that may possibly be present. These quantities will be described in more detail later.

3.1.1 Equation of state

Under the conditions studied in this work, all gases are assumed to obey the perfect gas equation of state.

$$p = \rho RT \tag{9}$$

where R is the gas constant and T is the temperature. The gas constant is determined based on the species mass fractions and their molecular weights,

$$R = R_u \sum_{k=1}^{N_s} \frac{Y_k}{W_k} \tag{10}$$

where R_u is the universal gas constant and W_k is the molecular weight of the k^{th} species.

The internal energy of each species is a function of temperature only:

$$e_k = e_k^0 + \int_{T_0}^{T} C_{v,k}\left(T'\right)\, dT' \tag{11}$$

where $C_{v,k}$ is the constant volume specific heat for the k^{th} species and e_k^0 is the reference sensible energy at the reference temperature T_0.

It is often convenient to use enthalpy,

$$h = e + \frac{p}{\rho} \tag{12}$$

and defining the enthalpy of the k^{th} species as

$$h_k = h_k^0 + \int_{T_0}^{T} C_{p,k}\left(T'\right)\, dT' \tag{13}$$

where $C_{p,k}$ is the specific heat at constant pressure and h_k^0 is the reference enthalpy. The specific heats are related:

$$C_{p,k}\left(T\right) = C_{v,k}\left(T\right) + \frac{R_u}{W_k}. \tag{14}$$

The ratio of the specific heats, γ is defined as:

$$\gamma_k(T) = \frac{C_{p,k}(T)}{C_{v,k}(T)}. \tag{15}$$

3.1.2 Viscous stress tensor

The viscous stress tensor for Newtonian fluids is defined as

$$\tau_{ij} = \mu\left(\frac{\partial u_i}{\partial x_j} + \frac{\partial u_j}{\partial x_i}\right) + \lambda\frac{\partial u_k}{\partial x_k}\delta_{ij} \tag{16}$$

where μ is the dynamic viscosity, λ is the bulk viscosity and δ_{ij} is the Kronecker delta:

$$\delta_{ij} = \begin{cases} 1 & \text{if } i = j \\ 0 & \text{if } i \neq j \end{cases}. \tag{17}$$

All fluids under consideration in this study are assumed Newtonian, i.e., the stresses are linearly proportional to the rate of strain. In addition here we follow Stokes' hypothesis which postulates that the trace of the stress tensor should be zero which implies that the bulk viscosity is $\lambda = -2/3\mu$. With this assumption, the stress tensor can be written as

$$\tau_{ij} = 2\mu\left(S_{ij} - \frac{1}{3}S_{kk}\delta_{ij}\right) \tag{18}$$

where the rate of strain tensor, S_{ij}, is defined as:

$$S_{ij} = \frac{1}{2}\left(\frac{\partial u_i}{\partial x_j} + \frac{\partial u_j}{\partial x_i}\right). \tag{19}$$

The dynamic viscosity can be computed in a variety of ways with varying complexity and accuracy. For all methods used in this study the dynamic viscosity is a function of temperature and composition only.

3.1.3 Heat flux vector

The heat flux vector in the energy equation is

$$q_i = -\kappa\frac{\partial T}{\partial x_i} + \rho\sum_{k=1}^{N_s} h_k Y_k V_{i,k}. \tag{20}$$

The first term is heat conduction due to temperature gradients where κ is the thermal conductivity. This relationship is known as Fourier's law. Like with the dynamic viscosity, in this work κ is a function of temperature and composition only and often computed using the definition of the Prandtl number,

$$Pr = \frac{C_p \mu}{\kappa}. \tag{21}$$

The second term is the energy flux due to species diffusion.

3.1.4 Species diffusion flux

The species diffusion flux term is modeled with a Fickian diffusion approximation and neglects any Soret effects

$$J_{i,k} = \rho Y_k V_{i,k} = -\rho D_k \frac{W_k}{\overline{W}} \frac{\partial X_k}{\partial x_i} \tag{22}$$

where $V_{i,k}$ is the species diffusion velocity in the $i-$th direction for the $k-$th species. The diffusion coefficient, D_k, is generally a function of the temperature, pressure and local species concentrations and can be related to other thermodynamic and transport properties with the Lewis number,

$$Le = \frac{\kappa}{\rho C_p D_k}. \tag{23}$$

Using the expression in Eq. (22) in Eq. (6) can result in mass conservation problems so a correction velocity defined as

$$V^c = \sum_{k=1}^{N_s} D_k \frac{W_k}{\overline{W}} \frac{\partial X_k}{\partial x_i} \tag{24}$$

is added to the species diffusion term [153],

$$J_{i,k} = \rho Y_k \left(V_{i,k} + V^c \right) \tag{25}$$

Direct numerical simulations (DNS) discretize and numerically solve these equations. Doing so requires that all features of the flow are sufficiently resolved. This

becomes computationally intractable for many turbulent combustion applications at high Reynolds numbers where the small scales of turbulence are orders of magnitude smaller than the large mean flow scales governed by the combustor geometry. To mitigate this problem one method where the large flow scales are simulated and the small scales are modeled has been developed which is known as Large Eddy Simulation (LES). LES provides the basis for the work in this thesis and will be described in more detail in the following section.

3.2 Large Eddy Simulation equations

The large and small scales are separated by applying a spatial filter to the governing equations which decomposes flow variables into resolved and unresolved quantities. Thus a generic flow variable, f, can be written as $f = \overline{f} + f''$ where the $(\bar{\cdot})$ denotes resolved scales and the $('')$ indicates the unresolved, subgrid scales. The separation of scales for a variable f is achieved by applying a filter kernel, G, over the domain, Ω,

$$\overline{f}\left(\mathbf{x},t\right) = \int_{\Omega} f\left(\mathbf{x}',t\right) G\left(\mathbf{x}-\mathbf{x}'\right)\, \mathbf{dx}' \tag{26}$$

where $\mathbf{x}$ and $\mathbf{x}'$ are position vectors and t is time. There are a variety of filter kernels that can be use and in practice the three-dimensional filter kernel is often the product of three one-dimensional kernels

$$G\left(\mathbf{x}-\mathbf{x}'\right) = \prod_{i=1}^{3} g_i\left(x_i - x_i'\right). \tag{27}$$

The specific filter kernel is the Box or top-hat filter defined as

$$g_i\left(x_i - x_i'\right) = \begin{cases} \dfrac{1}{\Delta_i} & \left|x_i - x_i'\right| < \dfrac{\Delta_i}{2} \\ 0, & \text{otherwise} \end{cases} \tag{28}$$

where Δ_i is the filter size in the $i-$direction. The three-dimensional filter size can be expressed as

$$\overline{\Delta} = \left(\Delta_1\Delta_2\Delta_3\right)^{1/3}. \tag{29}$$

The spatial filtering operation is sufficient to derive the LES equations but it is convenient to define a mass-weighted filtered variable, also known as a Favré-filtered variable, for LES of compressible flows,

$$\tilde{f} = \frac{\overline{\rho f}}{\overline{\rho}}. \tag{30}$$

This Favré-filtering reduces the number of unclosed terms in the filtered, compressible Navier-Stokes equations. Further information concerning the properties of the filtering operations can be found in works by Sagaut and collaborators [177, 63].

3.3 Filtered Navier-Stokes equations

To obtain the resolved-scale filtered Navier-Stokes equations, the spatial filter is first applied then the commutative property of the filter with both spatial and temporal derivatives is used and finally the resulting expressions are simplified with the Favré-averaging procedure. The filtered equations for mass, momentum, energy and species conservation are

$$\frac{\partial \overline{\rho}}{\partial t} + \frac{\partial \overline{\rho}\tilde{u}_i}{\partial x_i} = \overline{\dot{\rho}_s} \tag{31}$$

$$\frac{\partial \overline{\rho}\tilde{u}_i}{\partial t} + \frac{\partial}{\partial x_j}\left[\overline{\rho}\tilde{u}_i\tilde{u}_j + \overline{p}\delta_{ij} - \overline{\tau}_{ij} + \tau_{ij}^{\text{sgs}}\right] = \overline{\dot{F}_{s,i}} \tag{32}$$

$$\frac{\partial \overline{\rho}\tilde{E}}{\partial t} + \frac{\partial}{\partial x_j}\left[\left(\overline{\rho}\tilde{E} + \overline{p}\right)\tilde{u}_j + \overline{q}_j - \tilde{u}_i\overline{\tau}_{ij} + H_j^{\text{sgs}} + \sigma_j^{\text{sgs}}\right] = \overline{\dot{Q}_s} \tag{33}$$

$$\frac{\partial \overline{\rho}\tilde{Y}_k}{\partial t} + \frac{\partial}{\partial x_i}\left[\overline{\rho}\tilde{u}_i\tilde{Y}_k + J_{i,k} + Y_{i,k}^{\text{sgs}} + \theta_{i,k}^{\text{sgs}}\right] = \overline{\dot{\omega}_k} + \overline{\dot{S}_{s,k}} \tag{34}$$

The filtered viscous stress tensor and heat flux vector are

$$\overline{\tau}_{ij} = 2\mu\left(\tilde{S}_{ij} - \frac{1}{3}\tilde{S}_{kk}\delta_{ij}\right) \tag{35}$$

and

$$\overline{q}_i = -\overline{k}\frac{\partial \tilde{T}}{\partial x_i} + \overline{\rho}\sum_{k=1}^{N_s}\tilde{h}_k\tilde{Y}_k\tilde{V}_{i,k} + \sum_{k=1}^{N_s}q_{i,k}^{\text{sgs}} \tag{36}$$

where the filtered strain rate is

$$\tilde{S}_{ij} = \frac{1}{2}\left(\frac{\partial \tilde{u}_i}{\partial x_j} + \frac{\partial \tilde{u}_j}{\partial x_i}\right). \tag{37}$$

The filtered total energy is the sum of the filtered internal energy, resolved kinetic energy and subgrid kinetic energy,

$$\tilde{E} = \tilde{e} + \frac{1}{2}\tilde{u}_i\tilde{u}_i + k^{\text{sgs}}, \tag{38}$$

and the subgrid kinetic energy is defined as,

$$k^{\text{sgs}} = \frac{1}{2}\left(\widetilde{u_i u_i} - \tilde{u}_i\tilde{u}_i\right). \tag{39}$$

The species diffusion flux is

$$J_{ik} = \overline{\rho}\tilde{Y}_k\left(V_{ik} + V_i^c\right). \tag{40}$$

Assuming Fickian diffusion and a mixture-averaged diffusion coefficient, the diffusion velocity term is

$$\tilde{Y}_k\tilde{V}_{i,k} = -\overline{D}_k\frac{W_k}{\overline{W}}\frac{\partial\tilde{X}_k}{\partial x_i}. \tag{41}$$

To avoid computing mole fractions this term is sometimes approximated using mass fraction gradients rather than mole fraction gradients,

$$\tilde{Y}_k\tilde{V}_{i,k} \approx -\overline{D}_k\frac{\partial\tilde{Y}_k}{\partial x_i}. \tag{42}$$

To maintain mass conservation, the correction velocity is added,

$$V_i^c = \sum_{k=1}^{N_s}\overline{D}_k\frac{\partial\tilde{Y}_k}{\partial x_i}. \tag{43}$$

The filtered perfect gas equation of state is used to relate the conservative and primitive variables,

$$\overline{p} = \overline{\rho}\left(\tilde{R}\tilde{T} + \mathcal{C}^{\text{sgs}}\right), \tag{44}$$

where

$$\tilde{R} = \sum_{k=1}^{N_s}\tilde{Y}_k\frac{R_u}{W_k}. \tag{45}$$

The source terms from the dispersed phase will be discussed further later in Section 3.6.

All subgrid-scale terms, indicated with the $^{\text{sgs}}$ superscript, are "unclosed" and will require modeling,

$$\begin{aligned}
\tau_{ij}^{\text{sgs}} &= \overline{\rho}\left(\widetilde{u_i u_j} - \tilde{u}_i\tilde{u}_j\right) \\
H_i^{\text{sgs}} &= \overline{\rho}\left(\widetilde{Eu_i} - \tilde{E}\tilde{u}_i\right) + \left(\overline{u_i p} - \tilde{u}_i\overline{p}\right) \\
\sigma_i^{\text{sgs}} &= \overline{u_j\tau_{ij}} + \tilde{u}_j\overline{\tau}_{ij} \\
Y_{i,k}^{\text{sgs}} &= \overline{\rho}\left(\widetilde{u_i Y_k} - \tilde{u}_i\tilde{Y}_k\right) \\
\theta_{i,k}^{\text{sgs}} &= \overline{\rho}\left(\widetilde{V_{i,k}Y_k} - \tilde{V}_{i,k}\tilde{Y}_k\right) \\
q_{i,k}^{\text{sgs}} &= \overline{\rho}\left(\overline{h_k D_k \frac{\partial Y_k}{\partial x_i}} - \tilde{h}_k\overline{D}_k\frac{\partial\tilde{Y}_k}{\partial x_i}\right) \\
\mathcal{C}^{\text{sgs}} &= \widetilde{RT} - \tilde{R}\tilde{T}.
\end{aligned}$$

Models for τ_{ij}^{sgs}, H_i^{sgs}, σ_i^{sgs}, $Y_{i,k}^{\text{sgs}}$ and filtered reaction rate, $\overline{\dot{\omega}}_k$, are presented in the following sections. The remaining unclosed terms $\theta_{i,k}^{\text{sgs}}$, $q_{i,k}^{\text{sgs}}$, and $\mathcal{C}^{\text{sgs}}$ are neglected as is done in other LES studies [58].

3.4 Closures for the LES equations

3.4.1 Momentum transport closure

The subgrid terms in the momentum equation are closed using an eddy viscosity and gradient diffusion approach. The filter width is $\overline{\Delta} = (\text{cell volume})^{1/3}$. The eddy viscosity and subgrid stress tensor are,

$$\nu_t = C_\nu\overline{\Delta}\sqrt{k^{\text{sgs}}} \tag{46}$$

$$\tau_{ij}^{\text{sgs}} = -2\overline{\rho}\nu_t\left(\tilde{S}_{ij} - \frac{1}{3}\tilde{S}_{kk}\delta_{ij}\right) + \frac{2}{3}k^{\text{sgs}}\delta_{ij}. \tag{47}$$

3.4.2 Subgrid kinetic energy transport

Subgrid kinetic energy, k^{sgs}, is computed using a transport equation derived by subtracting the resolved kinetic energy equation from the filtered kinetic energy equation,

$$\frac{\partial k^{\text{sgs}}}{\partial t} + \frac{\overline{\rho}\tilde{u}_i k^{sgs}}{\partial x_i} = T_k\text{sgs} + P_k\text{sgs} - D_k\text{sgs} \tag{48}$$

where $T_k\text{sgs}$, $P_k\text{sgs}$, and $D_k\text{sgs}$ are diffusion, production and dissipation terms, respectively. Again using a gradient diffusion approach and an eddy viscosity assumption the diffusion, production and dissipation terms are modeled as

$$T_k\text{sgs} = \frac{\partial}{\partial x_i}\left[\left(\frac{\overline{\rho}\nu_t}{\sigma_k} + \mu\right)\frac{\partial k^{\text{sgs}}}{\partial x_i} + \frac{\overline{\rho}\nu_t\tilde{R}}{Pr_t}\frac{\partial\tilde{T}}{\partial x_i}\right] \tag{49a}$$

$$P_k\text{sgs} = -\tau_{ij}^{\text{sgs}}\frac{\partial\tilde{u}_j}{\partial x_i} \tag{49b}$$

$$D_k\text{sgs} = \frac{\overline{\rho}C_\epsilon\left(k^{\text{sgs}}\right)^{3/2}}{\overline{\Delta}}. \tag{49c}$$

3.4.3 Energy and scalar transport closure

The two unclosed terms from the energy equation are modeled together,

$$H_i^{\text{sgs}} + \sigma_i^{\text{sgs}} = -\left(\overline{\rho}\nu_t + \mu\right)\frac{\partial k^{\text{sgs}}}{\partial x_i} - \frac{\overline{\rho}\nu_t\overline{C}_p}{Pr_t}\frac{\partial\tilde{T}}{\partial x_i} + \tilde{u}_j\tau_{ij}^{\text{sgs}}. \tag{50}$$

Subgrid diffusion of species is modeled as

$$Y_{i,k}^{\text{sgs}} = -\frac{\overline{\rho}\nu_t}{Sc_t}\frac{\partial\tilde{Y}_k}{\partial x_i}. \tag{51}$$

In this work the turbulent Schmidt number is a constant, in many cases $Sc_t = 1.0$. Some cases $Sc_t = 0.4$ as suggested for LES by Pitsch and Steiner [152] and used by other researchers [228, 212], with the exact value detailed on a case by case basis. All other coefficients computed using the dynamic approach outlined below.

3.4.4 Localized Dynamic k^{sgs} Model (LDKM)

The coefficients C_ν, C_ε, and Pr_t used for the mometum, energy and subgrid kinetic energy equations are determined using a dynamic procedure originally developed by Kim and Menon[105] and extended to include compressibility effects by Génin and Menon[65]. The model is based on experimental observations that the subgrid stress tensor, τ_{ij}^{sgs} computed at the grid filter, $\overline{\Delta}$, is self-similar to the Leonard's stress, Eq. (52), computed at a larger test filter, $\hat{\Delta}$. The notation $\langle f\rangle$ indicates a variable

that is explicitly filtered at the test filter which in this work is $\hat{\Delta} = 2\overline{\Delta}$.

$$\mathcal{L}_{ij} = \langle\overline{\rho}\rangle \left(\frac{\langle\overline{\rho}\tilde{u}_i\tilde{u}_j\rangle}{\langle\overline{\rho}\rangle} - \frac{\langle\overline{\rho}\tilde{u}_i\rangle}{\langle\overline{\rho}\rangle}\frac{\langle\overline{\rho}\tilde{u}_j\rangle}{\langle\overline{\rho}\rangle} \right). \tag{52}$$

At the test filter level the resolved kinetic energy is the trace of the Leonard stress tensor

$$k^{\text{test}} = \frac{1}{2}\frac{\mathcal{L}_{kk}}{\langle\overline{\rho}\rangle} = \frac{1}{2}\left(\frac{\langle\overline{\rho}\tilde{u}_k\tilde{u}_k\rangle}{\langle\overline{\rho}\rangle} - \frac{\langle\overline{\rho}\tilde{u}_k\rangle}{\langle\overline{\rho}\rangle}\frac{\langle\overline{\rho}\tilde{u}_k\rangle}{\langle\overline{\rho}\rangle} \right). \tag{53}$$

The similarity between the Leonard stress at the test filter level and the subgrid stress tensor can be used to cast the Leonard stress in terms of the test filter resovled kinetic energy

$$\mathcal{L}_{ij} = -2\,\langle\overline{\rho}\rangle\, C_\nu \sqrt{k^{\text{test}}}\hat{\Delta}\left(\frac{\left\langle\overline{\rho}\tilde{S}_{ij}\right\rangle}{\langle\overline{\rho}\rangle} - \frac{1}{3}\frac{\left\langle\overline{\rho}\tilde{S}_{kk}\right\rangle}{\langle\overline{\rho}\rangle}\delta_{ij} \right) + \frac{2}{3}\,\langle\overline{\rho}\rangle\, k^{\text{test}}\delta_{ij}. \tag{54}$$

The only unknown is the coefficient C_ν which can be estimated using a least squares method

$$C_\nu = -\frac{\mathcal{M}_{ij}\mathcal{L}'_{ij}}{\mathcal{M}_{ij}\mathcal{M}_{ij}}, \tag{55}$$

$$\mathcal{M}_{ij} = \sqrt{k^{\text{test}}}\hat{\Delta}\left(\left\langle\overline{\rho}\tilde{S}_{ij}\right\rangle - \frac{1}{3}\frac{\left\langle\overline{\rho}\tilde{S}_{kk}\right\rangle}{\delta_{ij}} \right), \tag{56}$$

$$\mathcal{L}'_{ij} = \mathcal{L}_{ij} - \frac{2}{3}\,\langle\overline{\rho}\rangle\, k^{\text{test}}\delta_{ij}. \tag{57}$$

The transport equation for kinetic energy at the test filter can be derived in a similar way to that of subgrid kinetic energy with the exception that the terms for diffusion, production and dissipation are defined completely with resolved quantities and subgrid stresses. The dissipation of k^{test} is assumed to be similar to the dissipation of k^{sgs} allowing the definition of the dissipation coefficient as

$$\begin{aligned} C_\varepsilon = & \frac{\hat{\Delta}}{\langle\overline{\rho}\rangle\,(k^{\text{test}})^{\frac{3}{2}}} \\ & \left\{ (\mu+\mu_t)\left[\left\langle\tilde{\Sigma}_{ij}\frac{\partial\tilde{u}_j}{\partial x_i}\right\rangle - \frac{1}{\langle\overline{\rho}\rangle}\left\langle\tilde{\Sigma}_{ij}\right\rangle\left\langle\overline{\rho}\frac{\partial\tilde{u}_j}{\partial x_i}\right\rangle \right] - \right. \\ & \left. \frac{2}{3}\left[\left\langle\overline{\rho}\frac{\partial\tilde{u}_k}{\partial x_k}\right\rangle - \frac{1}{\langle\overline{\rho}\rangle}\langle\overline{\rho}k^{\text{sgs}}\rangle\left\langle\overline{\rho}\frac{\partial\tilde{u}_k}{\partial x_k}\right\rangle \right] \right\}. \end{aligned} \tag{58}$$

where $\tilde{\Sigma}_{ij} = 2\left(\tilde{S}_{ij} - \frac{1}{3}\tilde{S}_{kk}\delta_{ij}\right)$. The similarity approach is also used to dynamically compute the turbulent Prandtl number. The temperature-velocity correlation is computed exactly at the test filter level and the least squares method is used to solve the over-specified system,

$$\frac{1}{Pr_t} = -\frac{d_i n_i}{d_i d_i}, \tag{59}$$

$$d_i = c_\nu \sqrt{k^{\text{test}}}\hat{\Delta}\frac{1}{\langle\overline{\rho}\rangle}\left\langle\overline{\rho}\frac{\partial\tilde{T}}{\partial x_i}\right\rangle, \tag{60}$$

$$n_i = \frac{\left\langle\overline{\rho}\tilde{u}_i\tilde{T}\right\rangle}{\langle\overline{\rho}\rangle} - \frac{\langle\overline{\rho}\tilde{u}_i\rangle}{\langle\overline{\rho}\rangle}\frac{\left\langle\overline{\rho}\tilde{T}\right\rangle}{\langle\overline{\rho}\rangle}. \tag{61}$$

3.4.5 Turbulence-chemistry interaction

The simplest turbulence-chemistry interaction model is the quasi-laminar or "no model" closure,

$$\overline{\dot{\omega}}_k = \dot{\omega}\left(\overline{\rho}, \widetilde{T}, \widetilde{Y}_i\right), \tag{62}$$

i.e., the filtered rates are determined directly from the filtered LES quantities neglecting subgrid species and temperature fluctuations. Several studies have shown that simple models such as the quasi-laminar chemistry provide adequate accuracy [67, 57, 12, 205, 43] while others have shown that the subgrid model can have a significant effect on the results, especially under unstable conditions such as blow-out [66, 156].

3.5 Subgrid Linear Eddy Model

Instead of solving the filtered species equation, Eq.(6), turbulent convection at large and small scales, molecular diffusion and chemical reactions are all modeled separately and solved at their own respective time scales using method originally developed for standalone turbulent scalar mixing and combustion applications [92, 93, 94, 97, 95, 96, 98] and then integrated into LES as a subgrid model and applied for many

premixed and non-premixed turbulent combustion simulations [89]. The method will be outlined here for completeness.

The exact species transport equation is written as,

$$\rho\frac{\partial Y_k}{\partial t} = -\rho\left[\tilde{u}_i + (u_i')^R + (u_i')^S\right]\frac{\partial Y_k}{\partial x_i} - \frac{\partial}{\partial x_i}\left(\rho Y_k V_{i,k}\right) + \dot{\omega} \tag{63}$$

where the exact velocity is split into three components, $u_i = \tilde{u}_i + (u_i')^R + (u_i')^S$: LES resolved velocity, $\tilde{u}_i$, LES resolved subgrid fluctations, $(u_i')^R$, which is obtained via k^{sgs}, and unresolved subgrid velocity fluctuations, $(u_i')^S$. The LEM-LES subgrid model solves this equation is a two steps, one for large scale advection,

$$\frac{Y_k^{n+1} - Y_k^*}{\Delta t_{LES}} = -\left[\tilde{u}_i + (u_i')^R\right]\frac{\partial Y_k^n}{\partial x_i} \tag{64}$$

and one for the subgrid reaction-diffusion process,

$$Y_k^* - Y_k^n = \int_t^{t+\Delta t_{LES}} -\frac{1}{\rho}\left\{\rho\,(u_i')^S\frac{\partial Y_k^n}{\partial x_i} + \frac{\partial}{\partial x_i}\left[\rho Y_k\left(V_{i,k} - V_k^C\right)\right]\dot{\omega}_k^n - \dot{S}_k^n\right\}dt'. \tag{65}$$

3.5.1 Subgrid reaction-diffusion process

One-dimensional lines are embedded in each LES cell on which an unsteady reaction-diffusion equation is solved with turbulent convection modeled through a series of instantaneous stirring events

$$\rho\frac{\partial Y_k}{\partial t} = F_{k,\text{stir}} - \frac{\partial}{\partial s}\left[\rho Y_k\left(V_{k,s} - V_k^C\right)\right] + \dot{\omega}_k \tag{66}$$

The total length of the LEM line equals that of the LES filter width, $\overline{\Delta}$, and the number of LEM cells is chosen such that all turbulent scales scales are revolved. Unlike the species, the energy equation is still solved at LES level. An energy equation is solved in the non-conservative, incompressible form on the LEM lines where viscous

work and viscous dissipation are ignored.

$$\rho C_p \frac{\partial T}{\partial t} = F_{T,\text{stir}} - \rho \frac{\partial T}{\partial s} \left[\sum_{k=1}^{N_s} C_{p,k} Y_k \left(V_{k,s} - V_k^C \right) \right] + \frac{\partial}{\partial s} \left(\kappa \frac{\partial T}{\partial s} \right) - \sum_{k=1}^{N_s} h_k \dot{\omega}_k W_k. \tag{67}$$

It should also be noted that *LES inter-cellular diffusion effects cannot be included* in either the subgrid species or temperature equations because LEM lines are non-contiguous.

3.5.2 Subgrid stirring

Turbulent convection on the subgrid LEM lines, $\rho \left(u_i'\right)^S \frac{\partial Y_k^n}{\partial x_i} = F_{k,\text{stir}}$, is modeled through a series of instantaneous stirring events. The turbulent field is assumed to be isotropic and with no boundaries and/or body forces which allows the use of well-established inertial range and scaling laws. The stirring frequency is computed based on scaling laws

$$\lambda = \frac{54}{5} \frac{\nu Re_{\overline{\Delta}}}{C_\lambda \overline{\Delta}^3} \frac{\left[\left(\overline{\Delta}/\eta \right)^{5/3} - 1 \right]}{\left[1 - \left(\eta/\overline{\Delta} \right)^{4/3} \right]} \tag{68}$$

where the subgrid Reynolds number is $Re_{\overline{\Delta}} = \sqrt{2k^{\text{sgs}}}\,\overline{\Delta}/\nu$ and an estimate of the Kolmogorov length scale is $\eta = N_\eta \overline{\Delta} Re_{\overline{\Delta}}^{-3/4}$. For the current simulations $C_\lambda = 15$ and $N_\eta = 1$. There has been some confusion about the C_λ as it has appeared in both the numerator and denominator of Eq. (68) in previously published works. This is not a problem as long as the reported value is adjusted properly, i.e., if it were in the numerator here, the value would be $C_\lambda^{num} = 1/15 \approx 0.067$. If this is reported improperly the stirring frequency would be 225 times to large. The eddy size, ℓ, is selected randomly from a distribution ranging from η to $\overline{\Delta}$,

$$f(\ell) = \frac{5}{3} \frac{\ell^{-8/3}}{\eta^{5/3} - \overline{\Delta}^{5/3}}. \tag{69}$$

The eddy location randomly selected from a uniform distribution over the LEM domain. The most common stirring algorithm is known as triplet mapping in which a

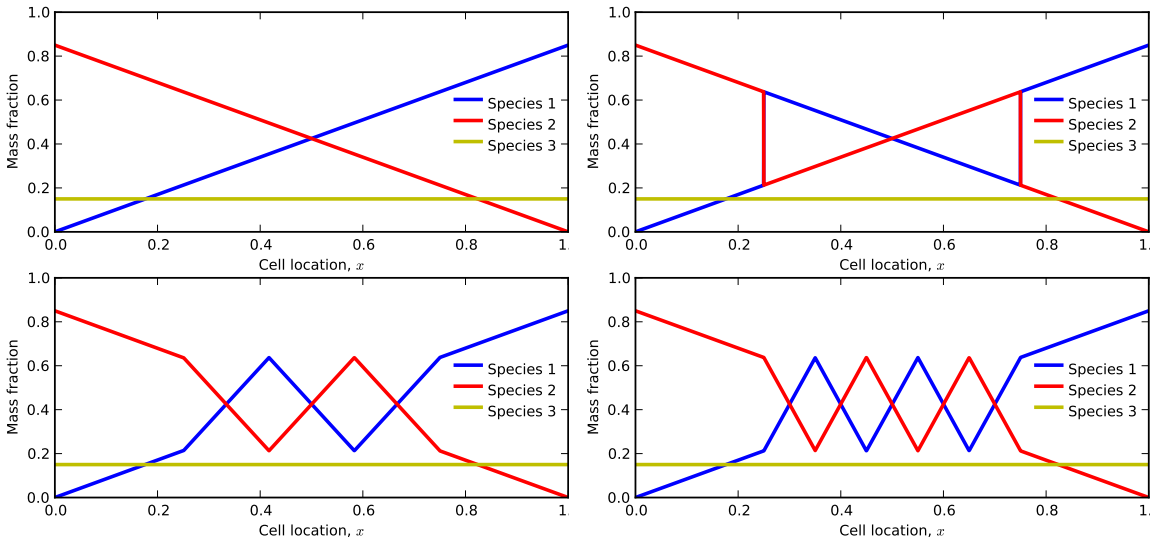

Figure 4 An initial three species LEM line (upper left) is stirred using block inversion (upper right), triplet mapping, $n = 3$ (lower left), and quintuplet mapping, $n = 5$ (lower right).

segment is copied, compressed by a factor of three and reinserted three times, with the middle segment reversed. Triplet mapping is part of a family of n-tuplet maps which can be stated mathematically as

$$\hat{c}(x,t_0) = \begin{cases} c(nx + (1-n)x_0, t_0) & x_0 \le x \le x_0 + \dfrac{1}{n}\ell \\ c(-nx + (n+1)x_0 + j\ell, t_0) & x_0 + \dfrac{j-1}{n}\ell \le x \le x_0 + \dfrac{j}{n}\ell \quad \text{for } j = 2,4,6,\ldots \\ c(nx + (1-n)x_0 + (1-j)\ell, t_0) & x_0 + \dfrac{j-1}{n}\ell \le x \le x_0 + \dfrac{j}{n}\ell \quad \text{for } j = 3,5,7,\ldots \\ c(nx + (1-n)x_0(1-n), t_0) & x_0 \le \dfrac{n-1}{n}x \le x_0 + \ell \end{cases} . \tag{70}$$

It has be argued that the triplet map physically represents a two-dimensional eddy passing through a scalar gradient. This rationale makes sense as each stirring event represents the action of a single turbulent eddy, but since the nature of all small eddies is not known and in most real-life scenarios turbulent eddies are three-dimensional, $n-$tuplet mappings should not be overlooked with careful analysis. It should also be noted that all these maps are measure preserving and all n-tuplet maps maintain continuity of the scalar field, but not with the scalar gradients. Figure 4 shows an example of three different stirring algorithms on a three species LEM line.

The physical processes at the LEM level are each integrated at their own time scales, the LES time step, Δt_{LES}, the diffusion time step, Δt_{diff}, the chemical time step, Δt_{chem}, which for this work is assumed equal to the diffusion time step, $\Delta t_{chem} = \Delta t_{diff}$, and the stirring time step, Δt_{stir}.

3.5.3 Subgrid scalar transport: splicing

Subgrid structures are advected across LES cells via a Lagrangian transport process called splicing. Mass fluxes at each LES cell face are computed based on the LES resolved scale density and momentum equations. The mass flux determines the number of LEM cells to be transferred across each LES cell face noting that partial LEM cells can be spliced. The receiving cells order the fluxes based on their magnitudes, from largest to smallest, and the LEM subgrid cells to be exchanged are then queued based on that flux ordering. The flux ordering ensures subgrid splices travel through the LES cell in a first-in, first-out manner. Once the LEM cells are exchanged across LES cell faces, the LEM lines are regridded back to to uniform lines. The entire process is explained in Figure 5.

3.5.4 LEMLES coupling

The LES resolved fields provide information for subgrid stirring and splicing operations. The subgrid LEM lines provide filtered species mass fractions back to the LES resolved field via an explicit Favré-averaging

$$\tilde{Y}_k = \frac{\sum_{i=1}^{N_{\text{LEM}}} \rho_i Y_{k_i}}{\sum_{i=1}^{N_{\text{LEM}}} \rho_i}. \tag{71}$$

The filtered temperature field

$$\tilde{T}^* = \frac{\sum_{i=1}^{N_{\text{LEM}}} \rho_i T_i}{\sum_{i=1}^{N_{\text{LEM}}} \rho_i} \tag{72}$$

at the LES level from LEM is tracked but not used at the LES level since the energy equation is still solved. In practice the LEM and LES temperature fields usually only

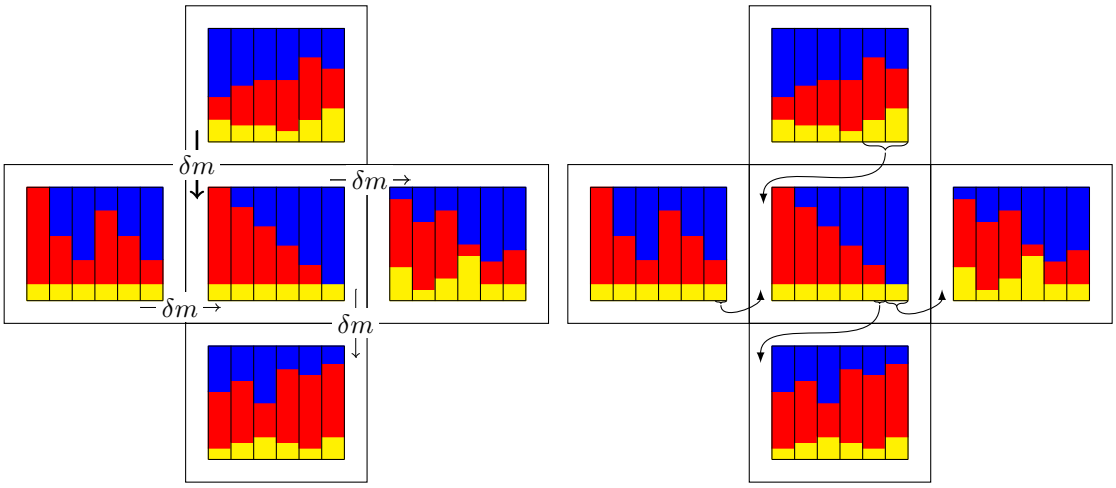

(a) Mass fluxes computed based on the LES resolved scale density and momentum equations

(b) LEM cells queued in the receiving LES cell based on flux magnitude

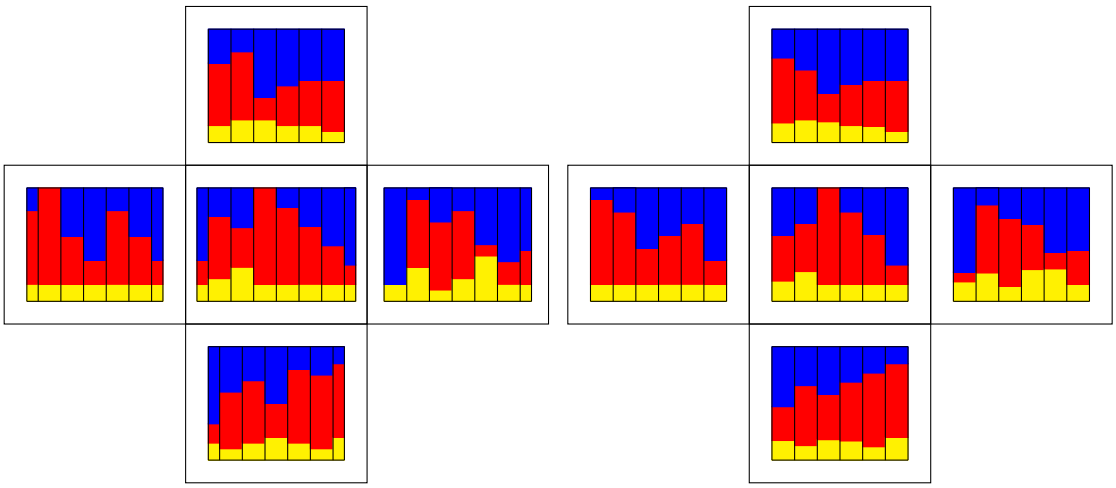

(c) LEM cells move across LES cells resulting in a non-uniform LEM field

(d) LEM fields regridded back to uniform lines

Figure 5 LEMLES transport process of subgrid fields called "splicing"

deviate by a few percent but to ensure zero drift the LEM temperature field is often rescaled based on the LES resolved temperature, $T_i^{\mathrm{LEM}} = T_i^{\mathrm{LEM}} \left(\tilde{T} / \tilde{T}^* \right)$.

3.5.5 LEMLES summary

The LEMLES simulation timeline is as follows:

1. Solve the filtered equations for density, momentum and energy at the LES level. Since the species equations are *not* solved at the LES level the filtered density equation *must* be solved there.

2. Solve the subgrid reaction-diffusion equation with stirring on the LEM line in each LES cell.

3. Compute large scale advection of species based on filtered values (splicing).

4. Filter LEM fields back to the LES level to couple the subgrid and resolved scales.

For simulations that satisfy the underlying assumptions of LEMLES, this simulation strategy is attractive for several reasons: subgrid strain effects are captured via the stirring events, there is no need to solve for filtered reaction rates since the species equation is solved at the DNS level, premixed, non-premixed and partially premixed flames can be simulated with the same framework and there is little to no model tuning. The main disadvantage of LEMLES is the increased computation cost associated with solving the reaction-diffusion equation on each of the subgrid lines. In well-resolved regions of the flow with little turbulence neglecting inter-LES-cell diffusion can also cause errors. The splicing algorithm can cause excessive numerical diffusion, especially the regridding step if only a few small partial LEM cells are transferred at each time step. LEMLES is most successful when there is a large disparity in grid resolution requirements, i.e., a relatively coarse grid can be used to accurately

model the main features of the underlying fluid dynamics but a fine grid is needed to capture the flame.

3.6 Lagrangian phase equations

Simulations involving solids or liquids as well as gases at subcritical conditions are generally split into two main classes depending on how the solid or liquid phase is handled, using an Eulerian or a Lagrangian approach. Eulerian-Eulerian simulations treat both the gas and liquid phases as continuums and are solved in an Eulerian reference frame. In the Eulerian-Lagrangian approach, the liquid is modeled as discrete droplets solved in a Lagrangian reference frame and thus each droplet or group of droplets must be tracked independently.

The main advantage of the Eulerian-Eulerian approach is computational efficiency when a large number of droplets are present in the domain since the droplets do not need to be explicitly tracked in the simulation. This method also allows for the use of the same numerical algorithm for both phases although thermodynamic relations and boundary conditions are often more difficult to apply. Physically it is difficult to account for droplet size effects and droplet-fluid interactions.

The Eulerian-Lagrangian approach, while computationally expensive, easily includes droplet size effects, which are especially important for droplet evaporation. Errors due to numerical diffusion are generally less of a concern for this method compared with the Eulerian-Eulerian approach [48]. Other complex droplet physics are also more easily modeled including droplet-droplet interactions, droplet-wall collisions and, most critically for the current study, droplet breakup effects. For these reasons, all simulations conducted in this work will use the Eulerian-Lagrangian approach.

For the current simulations the dispersed phase is assumed to be dilute [47, 48], i.e., droplet-to-droplet interactions are neglected, which is generally valid except for

near injectors. This assumption significantly reduces the computational effort involved since droplet-to-droplet distances do not need to be tracked and simplifies thermodynamic and transport property calculations [49]. The Lagrangian governing equations for the dispersed phase [34] are:

$$\dot{x}_{i,d} = u_{i,d}, \tag{73}$$

$$\dot{u}_{i,d} = \left(3C_D\mu Re_d\right) / \left(16\rho_d r_d^2\right)\left(u_i - u_{i,d}\right), \tag{74}$$

$$\dot{m}_d = -2\pi\rho_m D_m r_d Sh^* \ln\left(1 + B_M\right), \tag{75}$$

$$m_d C_d \dot{T}_d = h_d \pi d_d^2 (\widetilde{T} - T_d) - \dot{m}_d L_v. \tag{76}$$

The subscripts i, d and m correspond to coordinate index, the dispersed phase and an average gas-fuel mixture, respectively. The drag coefficient, away from injectors, is obtained from empirical correlations:

$$C_D = \begin{cases} \left(1 + \frac{1}{6}Re^{2/3}\right) & \text{if } Re \leq 1000 \\ 0.424Re & \text{if } Re > 1000 \end{cases} \tag{77}$$

where the Reynolds number is calculated as

$$Re = \frac{\rho_g u_{rel} d_d}{\mu_m} \tag{78}$$

where the density is taken as the gas density but the viscosity is computed as some kind of average value [243], and u_{rel} is the relative velocity between the gas and the liquid drop.

The droplet heat and mass transfer correlations are based on assumption of spherically symmetric droplets, each at a uniform temperature using the model by Abramzon and Sirginano [1]. The non-dimensional parameter Sh^*, is defined as

$$Sh^* = 2 + \frac{Sh_0 - 2}{F_M}. \tag{79}$$

The correction function $F_M = F\left(B_M\right)$ where the Spalding mass transfer number is

$$B_M = \frac{Y_{F,s} - Y_{F,\infty}}{1 - Y_{F,s}} \tag{80}$$

and

$$F(B) = (1+B)^{0.7} \frac{\ln(1+B)}{B} \tag{81}$$

which is needed to take into account the film effects around evaporating droplets. If a droplet is boiling, i.e., $Y_{F_s} = 1$, the heat and mass transfer are computed using the energy-balance approach,

$$\dot{m} = 2\pi d_p \frac{k_m}{C_{p,m}} Nu^* \ln(1+B_T) \tag{82}$$

where the Spalding heat transfer number is

$$B_T = \frac{C_{p,m}(T_\infty - T_d)}{\mathcal{L}_v} \tag{83}$$

and

$$Nu^* = 2 + \frac{Nu_0 - 2}{F_T} \tag{84}$$

and similarly $F_T = F(B_T)$ with F from Eq. 81. The Sherwood and Nusselt numbers are corrected based on local Reynolds, Schmidt and Prandtl numbers using expressions from Frössling [56] and Clift et al. [25].

$$\left.\begin{aligned} Sh_0 &= 1 + (1 + ReSc)^{1/3} \\ Nu_0 &= 1 + (1 + RePr)^{1/3} \end{aligned}\right\} \quad Re \le 1,$$

$$\left.\begin{aligned} Sh_0 &= 1 + (1 + ReSc)^{1/3} Re^{0.077} \\ Nu_0 &= 1 + (1 + RePr)^{1/3} Re^{0.077} \end{aligned}\right\} \quad 1 < Re \le 400, \ . \tag{85}$$

$$\left.\begin{aligned} Sh_0 &= 2 + 0.552 + Re^{1/2} Sc^{1/3} \\ Nu_0 &= 2 + 0.552 + Re^{1/2} Pr^{1/3} \end{aligned}\right\} \quad 400 < Re$$

The modified Sherwood and Nusslet numbers are related to their actual values by

$$Sh = Sh^* \frac{\ln(1+B_M)}{B_M}, \ Nu = Nu^* \frac{\ln(1+B_T)}{B_T}. \tag{86}$$

The convective heat transfer coefficient used in the droplet temperature equation is

$$h = Nu \frac{k_m}{2r_p}. \tag{87}$$

Under unsaturated conditions the Spalding heat transfer coefficient is related to the mass transfer coefficient via

$$B_T = (1 + B_m)^{\phi} - 1 \tag{88}$$

where

$$\phi = \left(\frac{C_{p,F}}{C_{p,g}}\right)\left(\frac{Sh^*}{Nu^*}\right). \tag{89}$$

These equations assume that the Kolmogorov length scale is larger than the size of the droplets. The reference mixture properties, denoted with the m subscript, are computed using the M3 method described by Kolatis and Founti [111]. For any property, ϕ, such as viscosity, thermal conductivity or diffusivity,

$$\phi_m = \frac{\chi_{ref}\phi_v}{\chi_{ref} + (1 - \chi_{ref})} + \frac{(1 - \chi_{ref})\,\phi_G}{\chi_{ref}\Omega_{Gv} + (1 - \chi_{ref})} \tag{90}$$

where v and G indicate the fuel vapor and local gas mixture properties, respectively and

$$\Omega_{vG} = \left(\frac{MW_G}{MW_v}\right)^{1/2} = \frac{1}{\Omega_{Gv}}. \tag{91}$$

The surface fuel vapor mole fraction is computed using the temperature-dependent vapor pressure and local pressure

$$\chi_{ref} = \frac{p_{vp}}{p}. \tag{92}$$

This method for computing heat and mass transfer has been validated with a test case involving the evaporation of a single droplet of decane in a quiescent environment based on the experiments of Wong and Lin [236]. Figure 6 shows the droplet diameter and temperature profiles compared with the experiments. The numerical experiments used mixture-averaged transport propertes [233].

The effect of turbulence on the dispersed phase, is included by the Stochastic Separated Flow (SSF) model [48, 135] in which a velocity fluctuation is added to the resolved fluid velocities at the droplet locations according to $u_i = \widetilde{u}_i + X\sqrt{2k^{sgs}/3}$

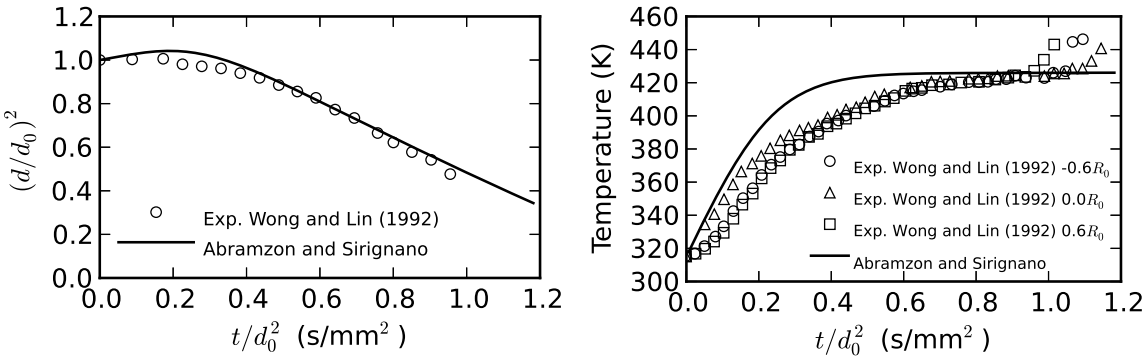

Figure 6 Simulations using the Abramzon and Sirignano [1] model of a single decane droplet evaporating in a quiescent environment compared with experiments [236].

with X, a random number generated from a uniform distribution with zero mean. It can be shown that this approach provides an important correction to the particle path due to the subgrid turbulent fluctuations. Finally, the source terms are obtained by a filtering process using a top hat filter:

$$\begin{pmatrix} \widetilde{\dot{\rho}_s} \\ \widetilde{\dot{F}_{s,i}} \\ \widetilde{\dot{Q}_s} \\ \widetilde{\dot{S}_{i,k}} \\ F_d \end{pmatrix} = \frac{1}{\hat{\Delta}^3} \begin{pmatrix} \sum \dot{m}_d \\ \sum \left[\dot{m}_d u_{i,d} - m_d \dot{u}_{i,d}\right] \\ \sum \left[\dot{m}_d h_{v,s} - h_d \pi d_d^2 \left(\tilde{T} - T\right)\right] \\ \sum \dot{m}_d \\ \sum \left[\widetilde{\dot{F}_{s,i} u_i} - \widetilde{\dot{F}}_{s,i} \widetilde{u}_i\right] \end{pmatrix}. \tag{93}$$

Here, $u_{i,d}$, ρ_d, r_d are the velocity, density and radius of the i^{th} particle, respectively. The summation above is over all parcels within the computational volume defined by $\hat{\Delta}^3$.

3.7 Liquid breakup models

The Lagrangian approach for simulating the liquid phase allows for relatively straightforward inclusion of models for droplet breakup. The breakup model for this study is used for simulating liquid jets in crossflow and can broadly be split into two regimes: the jet regime where the liquid is an intact column prior to fragmentation and the secondary breakup regime after the column breaks up and droplets deform and finally

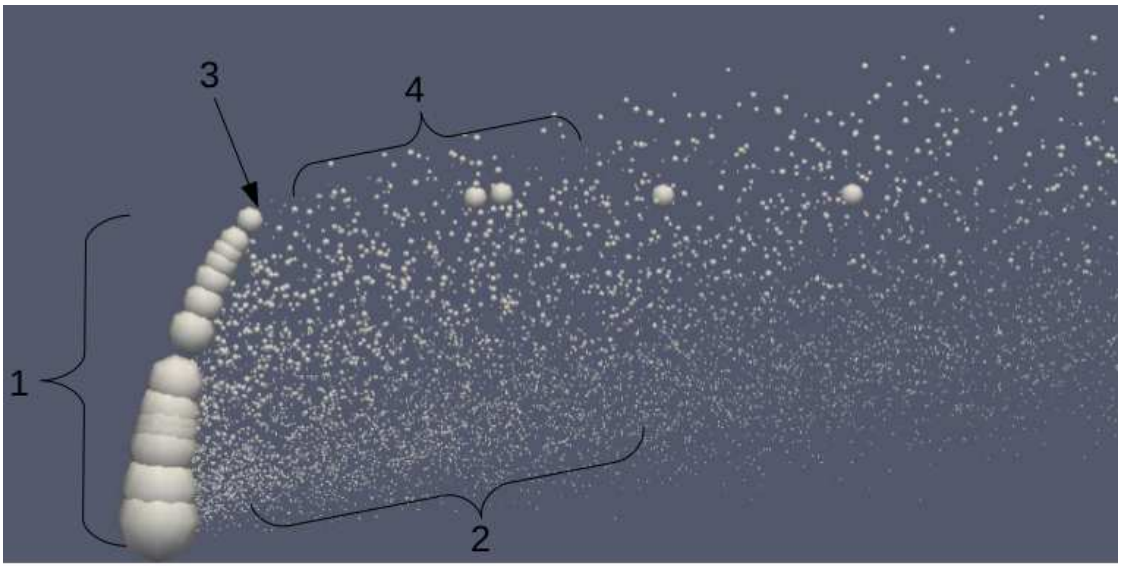

Figure 7 Liquid jet in crossflow as simulated by a Lagrangian breakup model, (1) liquid jet regime, (2) droplets stripped from the liquid column, (3) column breakup point and (4) secondary breakup regime.

break apart [128, 129]. Figure 7 diagrams a Lagrangian simulation of a liquid jet in crossflow.

3.7.1 Jet regime

Liquid spherical droplets are injected into the domain with diameters related to the size of the injector. The droplet velocity is determined based on the mass flow rate, density of the liquid and the size of the droplet. The injector discharge coefficient must be taken into account when setting the actual droplet injection diameter and velocity. This often overlooked parameter is important to capture the correct jet penetration, as detailed by Brown, McDonell and Kiel [15]. Discharge coefficients lower than unity result in droplets that are smaller than the physical dimension of the injector with higher velocities, in order to maintain the same mass flow rate, which yields increased liquid jet penetration.

The drag coefficient of the droplets in the liquid columns is set to a constant value, $C_D = 1.48$, until the time when the liquid column fragments and breaks apart [128].

The column breakup time occurs at:

$$t_{cb} = 3.44 \frac{D_0}{u_g} \sqrt{\frac{\rho_l}{\rho_g}} \tag{94}$$

where D_0 is the original droplet diameter and u_g is the gas phase cross flow velocity.

Small droplets are stripped from the surface of the liquid column and carried downstream. In the original Madabhushi model [128] the size of these stripped droplets was determined by the wave model of Reitz [167]. In the updated Madabhushi model [129], stripped droplet diameters were computed from on correlations based on experimental data.

In the wave model, the stripped droplets have the radius,

$$r_s = B_0 \Lambda \tag{95}$$

where B_0 is a tunable constant which for these simulation is set to the recommended value of $B_0 = 0.61$ [167] and Λ is the most unstable wavelength:

$$\frac{\Lambda}{a} = 9.02 \frac{\left(1 + 0.45 Z^{0.5}\right)\left(1 + 0.4 T^{0.7}\right)}{\left(1 + 0.87 We_g^{1.67}\right)^{0.6}}. \tag{96}$$

$Z = \left(We_l\right)^{0.5} / Re_l$ is the Ohnesorge number and $T = Z\sqrt{We_g}$ is the Taylor number. The liquid and gas Weber numbers are $We_l = \rho_l u_{rel}^2 a / \sigma_l$ and $We_g = \rho_g u_{rel}^2 a / \sigma$, the liquid Reynolds number is $Re_l = \rho_l u_{rel} a / \mu_l$ and a is the jet radius. The rate of change of the parent droplet is:

$$\frac{da}{dt} = -\frac{(a - r_s)}{\tau} \tag{97}$$

with the breakup time constant,

$$\tau = 3.726 \frac{B_1 a}{\Lambda \Omega}. \tag{98}$$

The growth rate of the most unstable wave is:

$$\Omega \left(\frac{\rho_l a^3}{\sigma}\right)^{0.5} = \frac{\left(0.34 + 0.68 We_g^{1.5}\right)}{\left(1 + Z\right)\left(1 + 1.4 T^{0.6}\right)}. \tag{99}$$

The constant B_1 is dependent on the initial disturbance level on the liquid jet and is a tunable parameters. Reitz [167] used $B_1 = 10$ and values ranging from 1.73 to 10 were suggested by Liu, Mather and Reitz [114]. Liu et al note that decreasing B_1 leads to an increased rate drop breakup which decreases the overall fuel jet penetration. Most simulations in this work use $B_1 = 7$ which is tuned for the specific injectors used in this study and lies in the recommended range.

In this work, the two methods for assigning stripped droplet sizes, the method based on the wave model and the method based on correlations, are blended linearly,

$$r_{\text{stripped}} = (RND)\, r_{wave} + (1 - RND)\, r_{corr}, \tag{100}$$

where RND is a random number selected from a uniform distribution between 0 and 1, r_{wave} is stripped droplet size based on the wave model, Eq. 95, and r_{corr} is the stripped droplet size based on the correlations of Madabhushi [129]. The stripped droplet size in that work is calculated as

$$r_{corr} = 1.68 D_0 \sqrt{\frac{\nu_l}{V_j} \frac{y}{D_0^2}}. \tag{101}$$

where D_0 is the injector diameter, ν is the kinematic viscosity of the liquid, V_j is the injection velocity and y is the vertical distance from the injection location and is based on the work of Sallam et al [179]. This is done to match limited experimental droplet data from the current configuration. The experimental data and results from using each of the methods and the combined method are presented in Sec. 6.3.1.1.

The particles stripped from the liquid column are assigned velocities using a method that combines the stripped velocity magnitude specified by Madabhushi[129], which were based on experimental curve fits of Chou [24], and random number feature of Khosla[99]. The random number adds some unsteadiness since the Madabhushi[129] model was originally used in Reynolds-averaged Navier-Stokes (RANS) calculations.

$$u_{shed} = u_{parent} + 7\sqrt{\rho_g/\rho_l}\, RND\ (u_g - u_{parent})\,, \tag{102a}$$

$$v_{shed} = v_{parent} + 0.6\,(RND)\,(v_g - v_{parent})\,, \tag{102b}$$

$$w_{shed} = w_{parent} + 0.175\,(RND - 0.5)\,(u_{rel} - w_{parent})\,. \tag{102c}$$

The stripped droplet radius modifications were guided by experimental data from the specific injector configuration used in this work. It should be reemphasized that since all Lagrangian injection models cannot model the injection process from first principles, some amount of experimental data driven tuning is required.

Droplet are shed when the accumulated mass reaches a user defined percentage of the original mass of the droplet which for these simulations that was 0.5%.

3.7.2 Secondary breakup

Following column breakup the droplets deform into disks and finally breakup [128]. The characteristic breakup time scale is:

$$t^* = \frac{D_0}{u_{rel}}\sqrt{\frac{\rho_l}{\rho_g}}. \tag{103}$$

The deformation time is $t_{def} = 1.6t^*$. The total breakup time, including deformation is:

$$\frac{t_b}{t^*} = \begin{cases} 6\,(We - 12)^{-0.25} & 12 < We < 18 \\ 2.45\,(We - 12)^{0.25} & 18 < We < 45 \\ 14.1\,(We - 12)^{-0.25} & 45 < We < 351 \\ 0.766\,(We - 12)^{0.25} & 351 < We < 2670 \\ 5.5 & 2670 < We \end{cases} \tag{104}$$

where the Weber number is $We = \rho_g u_{rel}^2 D_0/\sigma_l$. Droplet frontal diameter increases as:

$$\frac{D}{D_0} = 1 + 0.19\sqrt{We}\frac{t}{t_{def}} \quad t < t_{def} \tag{105}$$

and the drag coefficient is changed:

$$C_D = (C_D)_{\text{sphere}} \left(1 - \frac{t}{t_{def}}\right) + (C_D)_{\text{disk}} \frac{t}{t_{def}} \quad t < t_{def} \tag{106}$$

where $(C_D)_{\text{disk}} = 1.2$. The C_D is kept at a constant value at the end of the deformation period. After breakup the Sauter Mean Diameter (SMD), D_{32}, is given by:

$$\frac{SMD}{D_0} = 1.5 \frac{Oh^{0.2}}{We_{corr}^{0.25}}. \tag{107}$$

The Ohnesorge number is $Oh = \mu_l / \sqrt{\rho_l D \sigma_l}$ and We_{corr} is the corrected Weber number:

$$We_{corr} = \frac{We}{1 + 1.077 Oh^{1.6}} \quad Oh > 0.1 \tag{108}$$

Volumetric distribution of droplets after breakup follows a root-normal distribution:

$$f(D) = \frac{x}{2\sqrt{2\pi}\sigma D} \exp\left[-\frac{1}{2}\left(\frac{x-\mu}{\sigma}\right)^2\right] \tag{109}$$

with $x = \sqrt{D/D_{0.5}}$, $\mu = 1$, $\sigma = 0.238$ and $D_{0.5}/SMD = 1.2$. Droplets are assigned the same velocity as their parent with an additional component in the normal plane at a random direction with

$$v_t = \frac{5 D_0}{t_b - t_{def}} \tag{110}$$

to take into account rim expansion effects.

Following secondary breakup, the droplets smaller than a user-specified size are no longer allowed to breakup and are tracked as spherical droplets until they evaporate enough to reach a minimum size criteria or leave the domain. The wave model stripping breakup [167] is applied to large droplets until they reach the minimum breakup size criteria.

3.8 Boundary conditions

Numerical simulations must be performed on a finite domain so the accurate specification and treatment of the boundary conditions is essential. Unsteady, turbulent

simulations such as direct numerical simulations and large eddy simulations require schemes with low levels of numerical dissipation making them vulnerable to problems arising with non-physical initial conditions and artificial boundary conditions. This is especially true for turbulent reacting flows where the vorticity, entropy and acoustics are all closely coupled which includes many practical combustion devices such as gas turbines and rocket engines. The coupling between heat release and pressure oscillations in these enclosed chambers has the potential to severely affect performance or cause system failure. In addition, the geometry of many of these systems dictates that the inflow and outflow boundaries must be in close proximity to the heat release zone again emphasizing the need for the proper representation of the boundary conditions.

The accurate description of and control over waves entering and leaving the domain is achieved with non-reflective or partially non-reflective boundary conditions. The seminal work by Thompson [211] used a method that converts a system of hyperbolic conservation laws into a system of nonlinear wave equations each with a characteristic propagation velocity. Based on the propagation velocity of each wave at the boundary, it can be determined if a boundary condition for that wave needs to be supplied, i.e., if a wave is exiting the domain all the information necessary for that wave is known whereas if the wave is entering the domain boundary condition information is needed.

3.8.1 Formulation

The Navier-Stokes equations, Eqs. (3)–(6), can be written in a non-conservative form

$$\frac{\partial \mathbf{U}}{\partial t} + \mathbf{A}_1 \frac{\partial \mathbf{U}}{\partial x_1} + \mathbf{A}_2 \frac{\partial \mathbf{U}}{\partial x_2} + \mathbf{A}_3 \frac{\partial \mathbf{U}}{\partial x_3} - \mathbf{D} \tag{111}$$

where $\mathbf{U}$ is the vector of primitive variables,

$$\mathbf{U} = (u_1, u_2, u_3, \rho, p, Y_i)^T \tag{112}$$

noting that there are several different choices for the primitive variable set with pressure used here [211, 8] instead of temperature [154], $\mathbf{D}$ is a vector containing viscous

and source terms, and $\mathbf{A}_1$, $\mathbf{A}_1$, and $\mathbf{A}_1$ are coefficient matrices. The coefficient matrix $\mathbf{A}_1$ is defined as

$$\mathbf{A}_1 = \begin{pmatrix} u_1 & 0 & 0 & 0 & 1/\rho & 0 \\ 0 & u_1 & 0 & 0 & 0 & 0 \\ 0 & 0 & u_1 & 0 & 0 & 0 \\ \rho & 0 & 0 & u_1 & 0 & 0 \\ \rho c^2 & 0 & 0 & 0 & u_1 & 0 \\ 0 & 0 & 0 & 0 & 0 & u_1 \end{pmatrix} \tag{113}$$

with the other directions computed similarly. The conservative state variables, $\mathbf{Q} = (\rho, \rho u_1, \rho u_2, \rho u_3, \rho E_T, \rho_i)^T$ are computed using the Jacobian

$$\mathbf{P} = \frac{\partial \mathbf{Q}}{\partial \mathbf{U}} = \begin{pmatrix} 0 & 0 & 0 & 1 & 1/\rho & 0 \\ \rho & 0 & 0 & u_1 & 0 & 0 \\ 0 & \rho & 0 & u_2 & 0 & 0 \\ 0 & 0 & \rho & u_3 & 0 & 0 \\ \rho u_1 & \rho u_2 & \rho u_3 & \frac{\partial \rho E_T}{\partial \rho} & \frac{\partial \rho E}{\partial p} & \frac{\partial \rho E}{\partial Y_i} \\ 0 & 0 & 0 & Y_i & 0 & \rho \end{pmatrix} \tag{114}$$

for ideal gases the necessary thermodynamic derivatives are

$$\frac{\partial \rho E_T}{\partial \rho} = \frac{1}{2}\left(u_1^2 + u_2^2 + u_3^2\right), \tag{115}$$

$$\frac{\partial \rho E}{\partial p} = \frac{1}{\gamma - 1}, \tag{116}$$

$$\frac{\partial \rho E}{\partial Y_i} = \rho\left(h_i - \frac{C_p T}{W_i}\right). \tag{117}$$

The coefficient matrices $\mathbf{A}_i$ are not simultaneously diagonalizable so the boundary condition analysis is performed one direction at a time, in the direction normal to the boundary. The matrix $\mathbf{A}_1$ is diagonalized

$$\mathbf{S}^{-1}\mathbf{A}_1\mathbf{S} = \mathbf{\Lambda} \tag{118}$$

where Λ is the diagonal matrix of eigenvalues, λ_i, the columns of $\mathbf{S}$ are the right eigenvectors, r_i of $\mathbf{A}_1$ and $\mathbf{S}^{-1}$ are the left eigenvectors, l_i. The eigenvalues are

$$\lambda_1 = u_1 - c, \quad \lambda_2 = \lambda_3 = \lambda_4 = \lambda_{5+i} = u_1, \quad \lambda_5 = u_1 + c \tag{119}$$

Using Eq. (118) and Eq. (111),

$$\mathbf{S}^{-1}\frac{\partial \mathbf{U}}{\partial t} + \mathbf{L} + \mathbf{S}^{-1}\mathbf{C} = 0 \tag{120}$$

where $\mathbf{L}$ is the wave amplitude vector

$$\mathbf{L} = \begin{bmatrix} L_1 \\ L_2 \\ L_3 \\ L_4 \\ L_5 \\ L_{5+i} \end{bmatrix} = \begin{bmatrix} \frac{\lambda_1}{2}\left(\frac{\partial p}{\partial x_1} - \rho c \frac{\partial u_1}{\partial x_1}\right) \\ \lambda_2\left(\frac{\partial \rho}{\partial x_1} - \frac{1}{c^2}\frac{\partial p}{\partial x_1}\right) \\ \lambda_3 \frac{\partial u_2}{\partial x_1} \\ \lambda_4 \frac{\partial u_3}{\partial x_1} \\ \frac{\lambda_5}{2}\left(\frac{\partial p}{\partial x_1} + \rho c \frac{\partial u_1}{\partial x_1}\right) \\ \lambda_{5+i}\frac{\partial Y_i}{\partial x_1} \end{bmatrix} \tag{121}$$

and

$$\mathbf{C} = \mathbf{A}_2\frac{\partial \mathbf{U}}{\partial x_2} + \mathbf{A}_3\frac{\partial \mathbf{U}}{\partial x_3} - \mathbf{D} \tag{122}$$

Multiplying by $\mathbf{S}$ gives

$$\mathbf{d} = \mathbf{SL} = \begin{pmatrix} d_1 \\ d_2 \\ d_3 \\ d_4 \\ d_5 \\ d_{5+i} \end{pmatrix} = \begin{pmatrix} (L_5 - L_1)/\rho c \\ L_3 \\ L_4 \\ L_2 + (L_5 + L_1)/c^2 \\ L_5 + L_1 \\ L_{5+i} \end{pmatrix} \tag{123}$$

Neglecting the viscous and source terms, $\mathbf{D}$, the conservative variables are updated using,

$$\frac{\partial}{\partial t}\begin{bmatrix}\rho\\ \rho u_1\\ \rho u_2\\ \rho u_3\\ \rho E_T\\ \rho_i\end{bmatrix}+\begin{bmatrix}d_4\\ u_1 d_4+\rho d_4\\ u_2 d_4+\rho d_2\\ u_3 d_4+\rho d_3\\ \dfrac{\partial \rho E_T}{\partial \rho}d_4+\rho\left(u_1 d_1+u_2 d_2+u_3 d_3\right)+\displaystyle\sum_k^{N_s}\rho d_{5+k}\left(\frac{\partial E}{\partial Y_k}\right)_{\rho,p,Y_l}+\frac{\partial \rho E}{\partial p}d_5\\ Y_i d_4+\rho d_{5+i}\end{bmatrix}=0 \tag{124}$$

in what are known as the Local One-Dimensional Inviscid relations [154].

3.8.2 Subsonic reflecting inflow

If the velocity, temperature and species mass fractions are all specified, the inflow boundary is reflecting or "hard". The wave amplitude changes cane be computed with

$$L_3 = L_4 = L_{5+i} = 0, \tag{125}$$

$$L_2 = \frac{\gamma-1}{c^2}\left(L_1+L_5\right), \tag{126}$$

$$L_1 = L_5. \tag{127}$$

In other situations the mass flow rate is fixed rather than the

$$L_1 = L_5\frac{1+\gamma M}{1-\gamma M} = \left(u_1+c\right)\frac{1+\gamma M}{2}\frac{\partial p}{\partial x}, \tag{128}$$

$$L_3 = -\frac{u_2}{\rho}\left(L_2+\frac{L_5+L_1}{c_2}\right), \tag{129}$$

$$L_4 = -\frac{u_3}{\rho}\left(L_2+\frac{L_5+L_1}{c_2}\right). \tag{130}$$

3.8.3 Subsonic non-reflecting inflow

For many problems it is desirable to reduce spurious wave reflections at inflow boundaries while simultaneously maintaining control over the inlet variables. Yoo et al. [241,

242] suggest modified LODI relations

$$\begin{aligned} L_1 &= \beta_1 \left(u_1 - u_{1,0}\right), \\ L_2 &= \beta_2 \left(T - T_0\right), \\ L_3 &= \beta_3 \left(u_2 - u_{2,0}\right), \\ L_4 &= \beta_4 \left(u_3 - u_{3,0}\right), \\ L_{5+i} &= \beta_{5+i} \left(Y_i - Y_{1,0}\right), \end{aligned} \tag{131}$$

where the subscript 0 indicates target values and the β values are relaxation coefficients. Large β values, near $1/\Delta t$, give more control over the inlet variables but oscillations are more likely to occur. Near zero values for β reduce wave reflections but result in poor control over the inlet. For some simplified conditions optimal values for the relaxation coefficients can be estimated [174, 175] as

$$\begin{aligned} \beta_1 &= \eta_1 \rho c^2 \frac{1 - M^2}{2 l_x}, \\ \beta_2 &= \eta_2 \frac{\rho R}{c l_x}, \\ \beta_3 &= \eta_3 \frac{c}{l_x}, \\ \beta_4 &= \eta_4 \frac{c}{l_x}, \\ \beta_5 &= \eta_{5+i} \frac{c}{l_x}, \end{aligned} \tag{132}$$

where M is the Mach number, l_x with $\eta_1 = \eta_2 = \eta_3 = \eta_4 = -\eta_5 = -0.278$. The species relaxation factors are usually set to zero, $\eta_{5+i} = 0$ [209]. These values are used as guides for any pratical problem and in practice must be adjusted for each simulation.

3.8.4 Supersonic inflow

At supersonic inflows no waves leave the domain. All variables, velocity, temperature and species mass fractions are explicitly set.

3.8.5 Subsonic non-reflecting outflow

For this boundary condition, all waves are leaving the domain excluding one acoustic wave that travels upstream. All the wave amplitudes except L_1 are computed using one-sided derivatives. To ensure well-posedness, Poinsot and Lele [154] suggest,

$$L_1 = \alpha \left(p - p_\infty\right) + L_{1,exact} \tag{133}$$

where p_∞ is the target or ambient pressure, and α is a relaxation coefficient, and $L_{1,exact}$ is the desired steady-state value of L_1 which is usually $L_{1,exact} = 0$. The relaxation coefficient is defined as [154]

$$\alpha = \sigma \frac{\left(1 - M^2\right) c}{l_x} \tag{134}$$

where σ is a constant, c is the local speed of sound and M is the maximum Mach number in the flow. Recent test have shown that defining this Mach number locally or with an averaged value on the boundary can reduce pressure oscillations [73]. Higher values of α give greater control over the outlet pressure but cause more pressure reflections. Poinsot and Lele suggest a value of $\sigma = 0.25$ when used in combination with a low dissipation numerical method whereas Rudy and Strikwerda used $\sigma = 0.58$ with the MacCormack scheme which contains inherent numerical dissipation. For viscous flows additional conditions must also be satisfied,

$$q_x = \tau_{x_1 x_2} = \tau_{x_1 x_3} = 0 \tag{135}$$

3.8.6 Supersonic outflow

At supersonic outflow boundaries all the waves propagate from the interior of the domain outward. The waves can be directly computed with Eq. (124) so no modeling is required.

3.8.7 Edges and corners

Several methods for applying characteristic boundary conditions at edges and corners of multidimensional boundaries have been proposed. Lodato, Domingo and

Vervisch [117] recommend solving coupled equations at edges and corners to properly account for the multidimensional effects. Coussement and coworkers [31] propose a simpler approach where if the mean tangential velocities are accounted for, it is unnecessary to solve a coupled system and the boundary conditions can be repeatably applied in all directions independent of one another. This later approach is used in this work.

CHAPTER IV

NUMERICAL METHOD AND IMPLEMENTATION

This chapter presents the numerical methods used to simulate the governing equations of motion. All of the numerical methods presented here and used in this study were implented in the main CFD code in the Computational Combustion Lab at Georgia Tech known as LESLIE (Large Eddy Simulation with the LInear Eddy model). The code uses spatial domain decomposition in combination with the Message Passing Interface (MPI) to run in parallel on distributed memory systems and has been successfully utilzed on a variety of machines ranging from workstations to large scale Department of Defense and NASA supercomputers. During the course of this thesis work the code went through substantial updates and modernization; where it is appropriate, details about these improvements will be given. One example is the conversion of most of the code base from Fortran 77/90 to Fortran 95/2003/2008. Additionally, many pre- and post- processing tasks were shifted to Python which allowed for quicker development and took advantage of tools such as Numpy[220], Scipy [88] and Matplotlib [83] for data analysis and plotting. The configuration and compilation of the code on many different systems is facilitated by the use of the CMake [107] build system. Arguably the most important tool currently in use is the git [215] distributed version control system, which allows for easy tracking of code changes and collaboration amongst lab members.

4.1 Finite volume method

The Navier-Stokes equations, either in their original or filtered form, can be written as,

$$\frac{\partial \mathbf{Q}}{\partial t} + \frac{\partial \mathbf{F}}{\partial x} + \frac{\partial \mathbf{G}}{\partial y} + \frac{\partial \mathbf{H}}{\partial z} = \mathbf{S} \tag{136}$$

where $\mathbf{Q}$ is the vector of conserved state variables, $\mathbf{F}$, $\mathbf{G}$, and $\mathbf{H}$ are the fluxes in each of the coordinate directions, including viscous terms, and $\mathbf{S}$ are the source terms. The equations are integrated over a control volume, V,

$$\iiint_V \frac{\partial \mathbf{Q}}{\partial t}\, dV + \iiint_V \left(\frac{\partial \mathbf{F}}{\partial x} + \frac{\partial \mathbf{G}}{\partial y} + \frac{\partial \mathbf{H}}{\partial z} \right) dV = \iiint_V S\, dV. \tag{137}$$

Using the divergence theorem this set of equations can be rewritten as

$$\iiint_V \frac{\partial \mathbf{Q}}{\partial t}\, dV + \oint_A (\mathbf{F} \cdot dA_x + \mathbf{G} \cdot dA_y + \mathbf{H} \cdot dA_z) = \iiint_V \mathbf{S}\, dV \tag{138}$$

where A_x, A_y, A_z are the normal components in each coordinate direction for the faces of the control volume. The first and third terms can be defined in terms of the volume-averaged state variables and volume-averaged source terms, respectively, denoted with an $\bar{\cdot}$,

$$\frac{\partial \overline{\mathbf{Q}}}{\partial t} + \frac{1}{V} \oint_A (\mathbf{F} \cdot dA_x + \mathbf{G} \cdot dA_y + \mathbf{H} \cdot dA_z) = \overline{\mathbf{S}}. \tag{139}$$

In the finite volume method the physical domain of interest is discretized into small control volumes known as computational cells and Eq. (139) is solved in each one. The values of the volume-averaged state variables can be stored at the nodal grid points, which is called a node-centered finite volume method, or at the centroid of the cell leading to a cell-centered method. In general, there is no restriction on the shape of the computational cell though in practice cells, in three dimensions, are often shaped in hexahedrons, tetrahedrons or prisms. If we limit all the cells to hexahedrons arranged in regular, rectangular shapes in computational space, we arrive at a structured finite volume method.

All finite volume methods in this work fall into the cell-centered structured finite volume category. Cell-averaged values are stored at the cell centers which are labeled with their computational coordinates (i, j, k) and fluxes are computed at the six cell faces, $\left(i \pm \frac{1}{2}, j, k\right)$, $\left(i, j \pm \frac{1}{2}, k\right)$ and $\left(i, j, k \pm \frac{1}{2}\right)$. At each time sub-iteration the state vector is updated with the delta value computed as

$$\Delta \mathbf{Q} = -\frac{\Delta t}{V} \sum_{l=1,6} \mathbf{F}_l \mathbf{A}_l + \mathbf{S} \Delta t \tag{140}$$

where the fluxes computed normal to the six faces are

$$\mathbf{F}_l = \mathbf{F} n_x + \mathbf{G} n_y + \mathbf{H} n_z. \tag{141}$$

Complex geometry is handled by a multiblock approach where a number of non-overlapping structured blocks are used to fill the simulation domain of interest. In most instances each cell at a block interface has a one-to-one correspondence with a neighboring block. To solve the equations of interest on the interior of the block, cell extensions are added in all directions and neighboring cell information is copied into these local "ghost" cells. The ghost cell also allows for parallelization on distributed memory systems and is used in the application of boundary conditions. It should also be noted that the one-to-one cell correspondence criteria can be relaxed using a static mesh refinement method described in Section 4.10.

4.2 MacCormack's predictor-corrector method

This method is a finite volume version of the MacCormack's method [127] that couples the time and spatial integration schemes. Fluxes are computed on the cell faces by a simple first order extrapolation of cell-averaged values that alternates between the upwind and downwind direction at each predictor/corrector step, resulting in a second-order accurate scheme in both time and space. The fluxes at the $i + 1/2$

Table 1 Flux differencing sequence for MacCormack's method to avoid bias.

	i-direction		j-direction		k-direction	
Time step	Predictor	Corrector	Predictor	Corrector	Predictor	Corrector
n	$+$	$-$	$+$	$-$	$+$	$-$
$n+1$	$-$	$+$	$+$	$-$	$-$	$+$
$n+2$	$+$	$-$	$-$	$+$	$+$	$-$
$n+3$	$-$	$+$	$-$	$+$	$+$	$-$
$n+4$	$+$	$-$	$+$	$-$	$-$	$+$
$n+5$	$-$	$+$	$+$	$-$	$+$	$-$
$n+6$	$+$	$-$	$-$	$+$	$-$	$+$
$n+7$	$-$	$+$	$-$	$+$	$-$	$+$
$\vdots$						

interface are computed at the predictor and corrector steps as,

$$F^{s,n}_{i+\frac{1}{2}} = F\left(U^n_i\right) \tag{142a}$$

$$F^{s,*}_{i+\frac{1}{2}} = F\left(U^*_{i+1}\right) \tag{142b}$$

The forward and backward differencing directions are alternated for successive time steps and spatial directions as shown in Table 1. This is done to avoid any solution bias due to the one-sided differencing [210, 131].

4.2.1 Predictor-corrector viscous fluxes

Face-averaged derivatives needed for the viscous fluxes are computed using a "finite difference-like" approach where the metrics, $\partial\xi/\partial x, \partial\eta/\partial x, \partial\zeta/\partial x$, etc, are determined from the grid and calculated and stored during simulation start-up. The derivative for any cell-averaged variable, u, is computed using the chain rule

$$\frac{\partial u}{\partial x} = \frac{\partial u}{\partial \xi}\frac{\partial \xi}{\partial x} + \frac{\partial u}{\partial \eta}\frac{\partial \eta}{\partial x} + \frac{\partial u}{\partial \zeta}\frac{\partial \zeta}{\partial x} \tag{143}$$

and a central explicit method,

$$\left.\frac{\partial u}{\partial \xi}\right|_{i+\frac{1}{2},j,k} = u_{i+1,j,k} - u_{i,j,k}, \tag{144a}$$

$$\left.\frac{\partial u}{\partial \eta}\right|_{i+\frac{1}{2},j,k} = \frac{1}{2}\left(u_{i+\frac{1}{2},j+1,k} - u_{i+\frac{1}{2},j-1,k}\right), \tag{144b}$$

$$\left.\frac{\partial u}{\partial \zeta}\right|_{i+\frac{1}{2},j,k} = \frac{1}{2}\left(u_{i+\frac{1}{2},j,k+1} - u_{i+\frac{1}{2},j,k-1}\right). \tag{144c}$$

The variables at the faces, $u_{i+\frac{1}{2},j\pm1,k\pm1}$ are estimated using the same upwinding / downwinding method of the inviscid flux, Eq. (142). Estimating the cell- or face-centered variables from the cell- or face-averaged values is second order accurate which is consistent with the rest of the scheme. Computing the derivatives in this way allows inviscid and viscous fluxes to be computed one computational direction at a time. This scheme has been successfully applied to a variety of reacting flow LES [148, 199].

4.2.2 Advantages and limitations

The main advantages of the predictor-corrector method over other second-order accurate methods are computational efficiency and simplicity. All quantities needed to compute the fluxes, pressure, velocities, etc, are also needed at the cell centers regardless of flux scheme, so the face flux values are calculated very efficiently.

The combination of upwinding and downwinding provides inherent dissipation that stabilizes numerical oscillations without artificial dissipation or explicit filtering operations. This not only simplifies the code, it reduces the amount of parameters that need to be tuned by the user on a case-by-case basis.

One of the main limitations of the MacCormack method occurs when using this scheme in combination with multiblock grids. Multiblock grids are required when applying a structured finite volume or finite difference method to complex geometry without using embedded boundaries. When the computational coordinates of neighboring grid blocks are not aligned, the flux computed across block faces is not

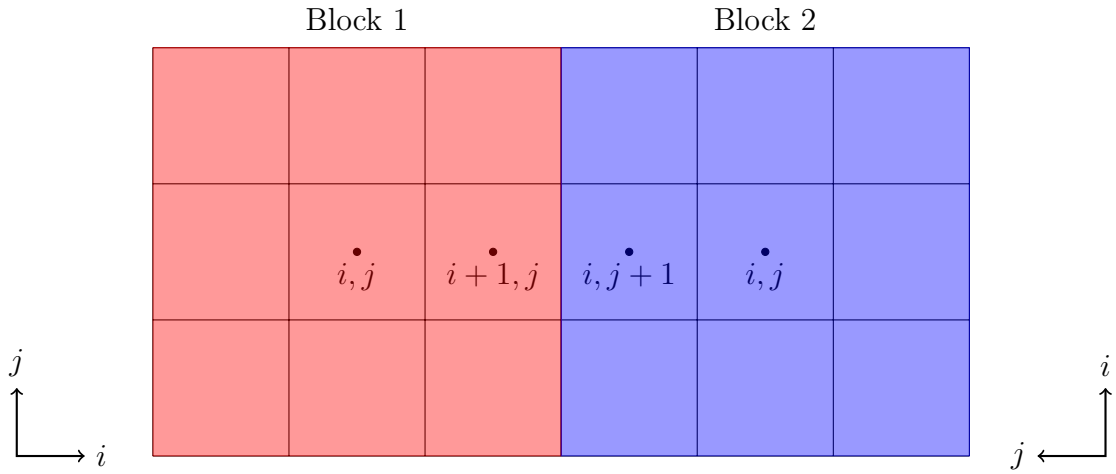

Figure 8 Computationally mis-aligned structured blocks

consistent. These types of grids are common in industrial applications and include any simulation with O-grids.

Figure 8 shows a simple example a simple two-dimensional simulation where the blocks are not aligned; the i-coordinate direction of Block 1 lines up with the j-coordinate direction of Block 2. The block interface is an $i+3/2$ face for Block 1 and a $j+3/2$ for Block 2. At the n time step, as per Table 1, Block 1 computes the fluxes for its local $(i+3/2, j)$ cell face at the predictor step using the values from the $(+)$ cell, $(i+2, j)$. The Block 1 $(i+2, j)$ cell is a ghost cell whose value is taken from the Block 2 $(i, j+1)$ cell. Block 2 computes the fluxes for its local $(i, j+3/2)$ cell face using the $(+)$ cell, $(i, j+2)$, which is a ghost cell whose value is equal to that of Block 1 $(i, j+1)$. This means that Block 1 and Block 2 will compute different values for the flux at the same cell face resulting in a scheme that is no longer strictly conservative this cell face.

The main symptom of the non-conservative cell fluxes is excess numerical dissipation. This can be demonstrated by simulating a simple vortex with periodic boundary conditions similar to the setup used in Section 5.1.3. Figure 9 shows the axial velocity after one, five and ten flow-through periods using MacCormack's method on

a two-dimensional domain split into four different blocks. The left images show the simulation where the blocks are all computationally aligned whereas the right images show the simulation where all four blocks are misaligned.

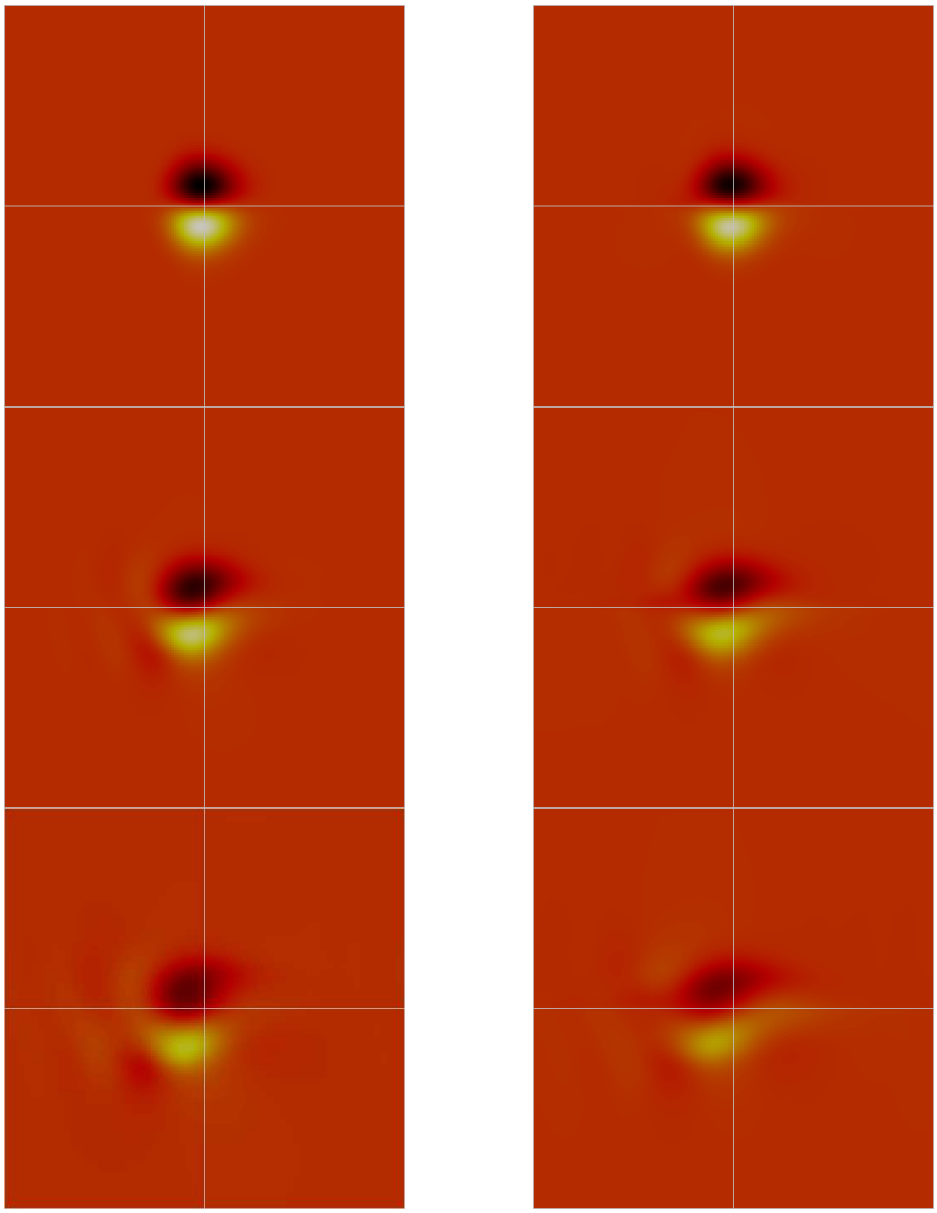

Figure 9 Axial velocity contours of an inviscid convecting vortex with periodic boundary conditions using the MacCormack predictor-corrector method after one (top), five (middle) and ten (bottom) flow-through periods for computationally aligned blocks (left) and misaligned blocks (right).

To solve this problem, mis-aligned blocks could be identified in a preprocessing

step and the fluxes across any such interfaces could be computed using a pure central scheme (with artificial dissipation or numerical filtering if necessary) or with an upwind scheme that does not rely solely on the computational coordinates but takes the physical direction of wave propagation into account. For the simulations in this thesis no explicit steps are taken to avoid this problem noting that the geometries involved in the simulations of this study are relatively simple so this issue is avoided except in a few areas away from the regions of interest.

Higher-order interpolation versions of MacCormack's predictor-corrector method have been used in the context of both finite differences [70, 91] and finite volumes [64] which are implemented into the LESLIE code. They are found to be superior to the second-order method on uniform grids but are quite sensitive to grid stretching and have lower CFL limits for stability. Due to their predictor-corrector nature, they also suffer from the non-aligned multiblock issue addressed above. Further analysis of these schemes will not be performed noting that in general, for uniform grids, their accuracy and efficient lie somewhere between the second-order predictor-corrector method and the finite volume scheme with higher order interpolation that is presented next.

4.3 Finite volume scheme with higher order compact interpolation

A finite volume scheme recently introduced by Fosso P., Deniau, Sicot and Sagaut [146] uses a compact interpolation scheme to estimate face-averaged values from cell-averaged values. Fluxes are then computed based on these interpolated face-averaged values. For linear equations the order of accuracy is the same as that of the interpolation but for non-linear problems the scheme, and others like it, are formally second order accurate since only a single integration point on the cell faces are used[244]. Two versions of the scheme were presented [146], one for "Cartesian-like" grids and the other for general curvilinear grids, both take into account the physical grid coordinates

when determining the coefficients for interpolation. Currently only the "Cartesian-like" version has been implemented which works well for smoothly-varying grids. This scheme is denoted as CompactCART.

The original scheme, which was designed for and applied to computational aeroacoustics [158], used only two ghost layers and an explicit scheme at block boundaries is extended here to use three ghost layers allowing the block boundary cell face-values to be computed with a sixth-order explicit central scheme. At internal faces for any generic variable, u, the interpolation scheme is identical to the original,

$$\begin{aligned} &\alpha\tilde{u}_{i-\frac{1}{2},j,k} + \tilde{u}_{i+\frac{1}{2},j,k} + \beta\tilde{u}_{i+\frac{3}{2},j,k} = \\ &a\overline{u}_{i-1,j,k} + b\overline{u}_{i,j,k} + c\overline{u}_{i+1,j,k} + d\overline{u}_{i+2,j,k}. \end{aligned} \tag{145}$$

Here the tilde indicates variables at the cell faces and the bar denotes cell-averaged values. At block boundaries the sixth-order explicit central scheme is shown below. A centered scheme is used to maintain the conservative property of the finite volume method across block boundaries regardless of the computational block alignment,

$$\begin{aligned} \tilde{u}_{i+\frac{1}{2},j,k} =& e\overline{u}_{i-2,j,k} + a\overline{u}_{i-1,j,k} + b\overline{u}_{i,j,k} + \\ & c\overline{u}_{i+1,j,k} + d\overline{u}_{i+2,j,k} + f\overline{u}_{i+3,j,k}. \end{aligned} \tag{146}$$

At inflow and outflow boundaries a one-sided fourth-order compact scheme utilizing a single boundary ghost layer is used to estimate the face-averaged values at the incoming or outgoing cell face,

$$\begin{aligned} &\tilde{u}_{\frac{1}{2},j,k} + \beta\tilde{u}_{\frac{3}{2},j,k} = \\ &b\overline{u}_{0,j,k} + c\overline{u}_{1,j,k} + d\overline{u}_{2,j,k}. \end{aligned} \tag{147}$$

The coefficients for the interpolation are based on the physical spacing of the grid cells. The complete details of the procedure are given in the appendix of [146]. Table 2 shows the coefficients for grids with uniform spacing.

Table 2 Interpolation coefficients for uniform grids

	Internal	Block Boundaries	Inflow/Outflow Boundaries
α	1/3	–	–
β	1/3	–	1
a	1/36	2/15	–
b	29/36	37/60	1/6
c	29/36	37/60	10/6
d	1/36	2/15	1/6
e	–	1/60	–
f	–	1/60	–

The interpolation is applied to the cell-averaged conservative variables to compute cell face values. Primitive variables at the cell faces necessary for the flux calculations are computed based on these interpolated conservative variables. Since this is a purely central scheme additional numerical stabilization is required. This is achieved using a filtering process detailed in Section 4.8.

4.3.1 Notes on the implementation of the high-order interpolation finite volume scheme

The MacCormack predictor-corrector method was the original scheme implemented in LESLIE and is the default solver. In the original form, the spatial and time integration were closely coupled throughout the code. The addition of this numerical method to the LESLIE code required revision to break this coupling and split the spatial and time integration into discrete program modules. While this took substantial programming effort, it allows for relatively straightforward code modifications to add new spatial or temporal integration schemes. The motivation for the implementation of this scheme was the discovery of the issue of non-conservative fluxes across non-computationally-aligned blocks with the MacCormack method. In addition to the compact interpolation, schemes using explicit interpolation for all faces, interior and at block boundaries, were also implemented for second- through sixth-order.

4.3.2 Viscous fluxes

Derivatives for the viscous fluxes are again computed using a "finite difference-like" approach as with the previous scheme, however, the order of accuracy of the approximation is increased to fourth-order. This is also slightly different than the traditional second-order method employed by the original authors [145]. The higher-order approximation of the derivatives may decrease errors but it should be again emphasized that the formal order of accuracy is still second-order. The grid metrics are also computed to second-order accuracy for this and all finite volume methods implemented in this study [223].

$$\left.\frac{\partial u}{\partial \xi}\right|_{i+\frac{1}{2},j,k} = \frac{1}{24}\left(u_{i-1,j,k} - 27u_{i,j,k} + 27u_{i+1,j,k} - u_{i+2,j,k}\right), \tag{148a}$$

$$\left.\frac{\partial u}{\partial \eta}\right|_{i+\frac{1}{2},j,k} = \frac{1}{12}\left(u_{i+\frac{1}{2},j-2,k} - 8u_{i+\frac{1}{2},j-1,k} + 8u_{i+\frac{1}{2},j+1,k} - u_{i+\frac{1}{2},j+2,k}\right), \tag{148b}$$

$$\left.\frac{\partial u}{\partial \zeta}\right|_{i+\frac{1}{2},j,k} = \frac{1}{12}\left(u_{i+\frac{1}{2},j,k-2} - 8u_{i+\frac{1}{2},j,k-1} + 8u_{i+\frac{1}{2},j,k+1} - u_{i+\frac{1}{2},j,k+2}\right). \tag{148c}$$

4.4 Upwind flux-difference splitting scheme

When simulating flows with discontinuous features the predictor-corrector and compact interpolation finite volume schemes previously presented fail, like all central schemes, near large gradients due to their dispersive nature. Either additional artificial dissipation needs to be added or an alternative numerical method that takes the local flow physics into account is needed. In this study the later method is used; fluxes near discontinuities are computed using an upwind flux-difference splitting scheme. This method reconstructs left and right side interface values at each finite volume cell face and then solves the Riemann problem to compute the flux.

4.4.1 Interface reconstruction

The left and right cell face states are determined using the Monotonic Upstream Centered Schemes for Conservation (MUSCL) method of van Leer [221] noting that the reconstruction is done independently in each computational direction thus the j and k subscripts have been dropped for clarity,

$$\begin{aligned} U^L_{i+1/2} &= U_i + \frac{\epsilon\,(1-\xi_i)}{4}\left[(1-\kappa)\,\Delta^+_{i-1/2}(U) + (1+\kappa)\,\Delta^-_{i+1/2}(U)\right], \\ U^R_{i+1/2} &= U_{i+1} + \frac{\epsilon\,(1-\xi_{i+1})}{4}\left[(1-\kappa)\,\Delta^+_{i+1/2}(U) + (1+\kappa)\,\Delta^-_{i+3/2}(U)\right]. \end{aligned} \tag{149}$$

Setting $\epsilon = 0$ limits the overall extrapolation to first order whereas $\epsilon = 1$ allows for higher order approximations. The parameter κ also plays a role in the order of the extrapolation with $\kappa = -1$ corresponding to a second-order upwind method, $\kappa = 1$ giving a second-order central method and $\kappa = 1/3$ yielding a third-order upwind biased scheme. The variable ξ_i is used for a flattening procedure needed in some situations near strong shocks. Limiting functions are used to enforce monotonicity since the extrapolated face values should not create local extrema. The $\Delta^{\pm}_{i+1/2}(U)$ are defined using

$$\Delta_{i+1/2}(U) = U_{i+1} - U_i \tag{150}$$

$$\begin{aligned} r^+_{i+1/2} &= \frac{\Delta_{i+3/2}(U)}{\Delta_{i+1/2}(U)} = \frac{U_{i+2} - U_{i+1}}{U_{i+1} - U_i}, \\ r^-_{i+1/2} &= \frac{\Delta_{i-1/2}(U)}{\Delta_{i+1/2}(U)} = \frac{U_i - U_{i-1}}{U_{i+1} - U_i} = \frac{1}{r^+_{i-1/2}}, \end{aligned} \tag{151}$$

$$\begin{aligned} \Delta^+_{i+1/2}(U) &= \Delta_{i+1/2}(U)\,\phi\left(r^+_{i+1/2}\right), \\ \Delta^-_{i+1/2}(U) &= \Delta_{i+1/2}(U)\,\phi\left(r^-_{i+1/2}\right), \end{aligned} \tag{152}$$

where the ϕ are the limiter functions. Eq. (149) can be rewritten as

$$\begin{aligned} U^L_{i+1/2} = U_i + \frac{\epsilon\,(1-\xi_i)}{4}\Big[&(1-\kappa)\,\phi\left(r^+_{i-1/2}\right)(U_i - U_{i-1}) + \\ &(1+\kappa)\,\phi\left(r^-_{i+1/2}\right)(U_{i+1} - U_i)\Big], \\ U^R_{i+1/2} = U_{i+1} + \frac{\epsilon\,(1-\xi_{i+1})}{4}\Big[&(1-\kappa)\,\phi\left(r^-_{i+3/2}\right)(U_{i+2} - U_{i+1}) + \\ &(1+\kappa)\,\phi\left(r^+_{i+1/2}\right)(U_{i+1} - U_i)\Big] \end{aligned} \tag{153}$$

and simplified further

$$
\begin{aligned}
U^L_{i+1/2} = U_i + \frac{\epsilon\,(1-\xi_i)}{4}\Big[&(1-\kappa)\,\phi\left(r^+_{i-1/2}\right) + \\
&(1+\kappa)\,\phi\left(\frac{1}{r^+_{i-1/2}}\right) r^+_{i-1/2}\Big]\,(U_i - U_{i-1})\,, \\
U^R_{i+1/2} = U_{i+1} + \frac{\epsilon\,(1-\xi_{i+1})}{4}\Big[&(1-\kappa)\,\phi\left(r^-_{i+3/2}\right) + \\
&(1+\kappa)\,\phi\left(\frac{1}{r^-_{i+3/2}}\right) r^-_{i+3/2}\Big]\,(U_{i+2} - U_{i+1})\,.
\end{aligned}
\tag{154}
$$

Many different limiters have been developed but in this work the only limiter used is the monotonized central limiter [221]

$$
\phi\,(r) = \max\left[0, \min\left(2r, 2, \frac{1+r}{2}\right)\right]. \tag{155}
$$

This limiter is symmetric, i.e., $\phi\,(r)\,/r = \phi\,(1/r)$, and total variation diminishing (TVD) thus making the scheme monotonic [78]. The symmetry property also eliminates the influence of κ on the extrapolation and thus limits the order to second resulting in

$$
\begin{aligned}
U^L_{i+1/2} &= U_i + \frac{\epsilon\,(1-\xi_i)}{4}\phi\left(r^+_{i-1/2}\right)(U_i - U_{i-1})\,, \\
U^R_{i+1/2} &= U_{i+1} + \frac{\epsilon\,(1-\xi_{i+1})}{4}\phi\left(r^-_{i+3/2}\right)(U_{i+2} - U_{i+1})\,.
\end{aligned}
\tag{156}
$$

The primitive variables u_i, p and ρ or ρ_k, or their filtered/Favré-averaged variants in LES, are reconstructed at the cell interfaces and used to compute temperature and other thermodynamic properties needed for the Riemann solver. The limiting procedure described up to this point ensures that the primitive reconstructed variables are TVD but further limiting operations are required to make sure that all other variables needed for the Riemann solver are TVD and that the gradients of each variables do not change sign at the interface. This monotonicity of the gradients is enforced by checking the sign of $(U_{i+1} - U_i)\left(U^R_{i+1/2} - U^L_{i+1/2}\right)$. If this product becomes negative, the interface variables are recomputed as [64]

$$
U^{L,new}_{i+1/2} = \frac{1}{2}\left(U^{L,old}_{i+1/2} + U^{L,odl}_{i+1/2}\right), \quad U^{R,new}_{i+1/2} = U^{L,new}_{i+1/2}\,. \tag{157}
$$

The monotonicity of other variables like temperature are also checked to ensure

$$\max\left(T_i, T_{i+1}\right) \geq T_{i+1/2}^{L,R} \geq \min\left(T_i, T_{i+1}\right). \tag{158}$$

If the temperature does not satisfy this condition a first-order approximation is used for both the left and right side approximations. If the temperature is increasing T_i is used whereas if the temperature is decreasing, the interface value is set to T_{i+1}. If the temperature is modified either the pressure or density needs to be recomputed for thermodynamic consistency [64, 131]; in this work the pressure is recomputed [64].

4.4.2 Riemann Solver

The Riemann problem consists of an initial value problem of a conservation equation with piecewise constant data separated by a central discontinuity,

$$u\left(x, t=0\right) = \begin{cases} u_L & x \leq 0 \\ u_R & x > 0 \end{cases}. \tag{159}$$

The classic physical example of such a system is a shock tube where gases with different thermodynamic states are separated by a very thin wall. Numerical methods used to compute such problems are called Riemann solvers which fall into two general classes: exact or approximate. Exact Riemann solvers are generally only used in combination with simple thermodynamics due their computational expense. A family of approximate Riemann solvers based on the work of Harten, Lax and van Leer [78] (HLL) have been implemented into LESLIE. In this work, most simulations use a version modifed by Toro [214] that takes the contact wave speed into account known as HLLC. Complete details about the Riemann solvers and their implementation can be found elsewhere [64, 189].

4.4.3 Boundary condition implementation

The characteristic boundary conditions for inflow and outflow described in Section 3.8.1 are implemented using a separate library from the main LESLIE code appropriately

referred to as BCLib. The boundary conditions were split from the main code to facilitate unit testing and improved documentation. The BCLib code was written using advanced Fortran 2003 features. Using such features actually caused problems early in the development in 2011 because both the Intel and GNU Fortran compilers at the time did not fully support the Fortran 2003 standard.

The boundary conditions equations themselves are applied in the first ghost layer at inflows and outflows. The equations are actually only coded in a single direction which requires all derivatives to be transformed inside LESLIE before being passed to BCLib for calculation. This method has since been utilized by other researchers [31]. Spatially constant boundary conditions values and relaxation coefficients are set in an XML file; spatially-varying inflow conditions can be prescribed using HDF5 files.

4.5 Central/upwind hybrid flux scheme

As noted in Section 4.4, an upwind numerical method or artificial dissipation is needed near flow discontinuities. Unfortunately these methods are generally much more dissipative and/or computationally expensive in smooth regions of the flow. Hybrid methods seek to combine the low dissipation and lower cost of central methods with the capabilities of upwind schemes to handle flow discontinuities. For a hybrid method the flux at cell face is computed using

$$\mathbf{F}_{i+1/2} = \Lambda_{i+1/2}\mathbf{F}^c_{i+1/2} + \left(1 - \Lambda_{i+1/2}\right)\mathbf{F}^u_{i+1/2} \tag{160}$$

where $\mathbf{F}^c_{i+1/2}$ is the flux obtained using the low-dissipation central scheme, $\mathbf{F}^u_{i+1/2}$ is the flux computed with the upwind scheme, and $\Lambda_{i+1/2}$ is a switching parameter computed based on the local flow field. In theory the switching parameter could be a continuous function between zero and one but often times, this work included, is a Heaviside step function. The hybrid switch is computed using curvature of a variable,

ϕ, where the smoothness parameter is [65]

$$S_{\phi,i} = \begin{cases} \dfrac{|\phi_{i+1} - 2\phi_i + \phi_{i-1}|}{|\phi_{i+1} - \phi_i| + |\phi_i - \phi_{i-1}|} - \phi^{th} & \text{if } |\phi_{i+1} - 2\phi_i + \phi_{i-1}| \geq \epsilon_\phi \phi_i \\ -\phi^{th} & \text{otherwise} \end{cases} \tag{161}$$

where ϕ^{th} and ϵ_ϕ are user-defined inputs and the hybrid switch at the cell interface is calculated as

$$\Lambda_{i+1/2} = \begin{cases} 1 & \text{if } \max\limits_{\phi,n} (S_{\phi,i-n}, S_{\phi,i+1+n}) \leq 0 \\ 0 & \text{otherwise} \end{cases} \tag{162}$$

For flows involving shocks, the hybrid switch is computed using both pressure and density. The pressure switch is not computed for subsonic flows where only large density gradients exist due to flames or evaporating fuel. Previous studies [64] suggest default values for the user-defined inputs are $\epsilon_\rho = \epsilon_p = 0.05$, $\rho^{th} = 0.125$ and $p^{th} = 0.5$. These parameters *must* be tuned on a case-by-case basis to avoid using the upwind scheme is too many places, which would overly dissipate the solution and cause excessive computational runtime, or conversely cause the solution to blow up if the central scheme is applied at a large gradient.

4.6 Conservative finite difference methods

Finite difference methods solve the governing equations in differential form

$$\frac{\partial \mathbf{Q}}{\partial t} + \frac{\partial \mathbf{F}}{\partial x} + \frac{\partial \mathbf{G}}{\partial y} + \frac{\partial \mathbf{H}}{\partial z} = \mathbf{S} \tag{136}$$

as opposed to the finite volume methods which solve the integral form,

$$\iiint\limits_V \frac{\partial \mathbf{Q}}{\partial t}\, dV + \oint\limits_A (\mathbf{F} \cdot dA_x + \mathbf{G} \cdot dA_y + \mathbf{H} \cdot dA_z) = \iiint\limits_V \mathbf{S}\, dV. \tag{138}$$

Solving the differential form simplifies the construction of higher-order methods since only a high-order numerical approximation to the derivative operator is required to achieve a truly high-order solution in contrast to the high-order quadratures for flux integration needed for finite volume schemes. For a conservative finite difference

method the numerical flux function for one direction, $f(u(x))$, can be defined in terms of a function $h(x)$ as

$$f(u(x)) = \frac{1}{\Delta x} \int_{x-\frac{\Delta x}{2}}^{x+\frac{\Delta x}{2}} h(\xi)\, d\xi \tag{163}$$

thus the flux derivatives are

$$\left.\frac{\partial f(u(x_i))}{\partial x}\right|_{x_i} = \frac{1}{\Delta x}\left[h\left(x_{i+1/2}\right) - h\left(x_{i-1/2}\right)\right] \tag{164}$$

The flux vectors in the Navier-Stokes equations, like $\partial \mathbf{F}/\partial x$, are computed as

$$\left.\frac{\partial \mathbf{F}}{\partial x}\right|_i = \frac{\mathbf{F}_{i+1/2} - \mathbf{F}_{i-1/2}}{\Delta x} \tag{165}$$

where the computational indices j and k are not listed because they are constant [86]. To compute the derivatives the numerical fluxes at the "cell" interfaces, $\mathbf{F}_{i+1/2}$, etc, need to be computed. The order of accuracy of the derivative equals that of the reconstruction operation used to compute the interface flux values.

4.6.1 Central conservative finite difference schemes

A family of explicit or tridiagonal compact schemes of up to eighth-order can be described by

$$\alpha F_{i-1/2} + F_{i+1/2} + \alpha F_{i+3/2} = a\left(F_{i-3} + F_{i+4}\right) + b\left(F_{i-2} + F_{i+3}\right) + \tag{166}$$

$$c\left(F_{i-1} + F_{i+2}\right) + d\left(F_i + F_{i+1}\right) \tag{167}$$

where F is any flux component. The coefficients required for these schemes on uniform grids are listed in Table 3. It is interesting to compare the values in Table 3 for the compact sixth-order conservative finite difference coefficients with those in Table 2 for the CompactCART finite volume scheme. The coefficients *are the same* [195]. Note that in the finite volume scheme it is the cell-averaged conservative variables that are being interpolated whereas fluxes are interpolated in the finite difference scheme.

As with the finite volume schemes, a ghost layer approach is used near computational block boundaries and physical boundaries such as inflows and outflows. All

Table 3 Central finite difference flux interpolation coefficients for Eq. 166

Scheme	α	a	b	c	d
Explicit $O(2)$	0	0	0	0	1/2
Explicit $O(4)$	0	0	0	−1/12	7/12
Explicit $O(6)$	0	0	1/60	−2/15	37/60
Explicit $O(8)$	0	−1/280	29/840	−139/840	533/840
Compact $O(4)$	1/4	0	0	0	3/4
Compact $O(6)$	1/3	0	0	1/36	29/36
Compact $O(8)$	3/8	0	−1/480	23/480	199/240

Table 4 One-sided finite difference flux interpolation coefficients for Eq. 168

Scheme	α	a	b	c	d
Explicit $O(2)$	0	1/2	1/2	0	0
Explicit $O(4)$	0	1/4	13/12	−5/12	1/12
Compact $O(4)$	1	1/6	10/6	1/6	0

of the central schemes require $O(-)/2$ ghost layers at computational boundaries and use a single ghost layer at inflows and outflows. The compact schemes use explicit numerical flux reconstruction at the computational block boundaries and high-order schemes drop to lower-order one-sided approximations near inflows and outflows which is consistent with other high order methods [209],

$$F_{i+1/2} + \alpha F_{i+3/2} = aF_i + bF_{i+1} + cF_{i+2} + dF_{i+3} \tag{168}$$

with the coefficients shown in Table 4.

To complete simulations on non-uniform grids the governing equations are transformed into generalized coordinates,

$$\frac{\partial \widehat{\mathbf{Q}}}{\partial t} + \frac{\partial \widehat{\mathbf{F}}}{\partial \xi} + \frac{\partial \widehat{\mathbf{G}}}{\partial \eta} + \frac{\partial \widehat{\mathbf{H}}}{\partial \zeta} = 0 \tag{169}$$

where

$$\widehat{\mathbf{Q}} = J^{-1}\mathbf{Q} \tag{170}$$

$$\widehat{\mathbf{F}} = \widehat{\xi}_x\mathbf{F} + \widehat{\xi}_y\mathbf{G} + \widehat{\xi}_z\mathbf{H} \tag{171}$$

$$\widehat{\mathbf{G}} = \widehat{\eta}_x\mathbf{F} + \widehat{\eta}_y\mathbf{G} + \widehat{\eta}_z\mathbf{H} \tag{172}$$

$$\widehat{\mathbf{H}} = \widehat{\zeta}_x\mathbf{F} + \widehat{\zeta}_y\mathbf{G} + \widehat{\zeta}_z\mathbf{H} \tag{173}$$

with the Jacobian and grid metrics usually described by [40],

$$J^{-1} = \left|\frac{\partial(x,y,z)}{\partial(\xi,\eta,\zeta)}\right| = x_\xi y_\eta z_\zeta - x_\xi y_\zeta z_\eta + x_\eta y_\zeta z_\xi - x_\eta y_\xi z_\eta - x_\zeta y_\eta z_\xi \tag{174}$$

$$\begin{aligned}
\widehat{\xi}_x &= J^{-1}\xi_x = y_\eta z_\zeta - y_\zeta z_\eta, \\
\widehat{\xi}_y &= J^{-1}\xi_y = z_\eta x_\zeta - z_\zeta x_\eta, \\
\widehat{\xi}_z &= J^{-1}\xi_z = x_\eta y_\zeta - x_\zeta y_\eta, \\
\widehat{\eta}_x &= J^{-1}\eta_x = y_\zeta z_\xi - y_\xi z_\zeta, \\
\widehat{\eta}_y &= J^{-1}\eta_y = z_\zeta x_\xi - z_\xi x_\zeta, \\
\widehat{\eta}_z &= J^{-1}\eta_z = x_\zeta y_\xi - x_\xi y_\zeta, \\
\widehat{\zeta}_x &= J^{-1}\zeta_x = y_\xi z_\eta - y_\eta z_\xi, \\
\widehat{\zeta}_y &= J^{-1}\zeta_y = z_\xi x_\eta - z_\eta x_\xi, \\
\widehat{\zeta}_z &= J^{-1}\zeta_z = x_\xi y_\eta - x_\eta y_\xi,
\end{aligned} \tag{175}$$

No metric time derivatives are included here since all simulations in this work involve static grids. In order to maintain the accuracy and stability of the curvilinear finite difference method, the grid metrics need to be computed in a conservative manner using the same method to compute both the grid derivatives and flow derivatives [227, 140, 40]. For this work, the grid metrics were implemented using the Symmetric

Conservative Metric Method S3 of Deng et al [40],

$$
\begin{aligned}
\widehat{\xi}_x &= \frac{1}{2}\left[(zy_\eta)_\zeta + (yz_\zeta)_\eta - (zy_\zeta)_\eta - (yz_\eta)_\zeta\right] \\
\widehat{\xi}_y &= \frac{1}{2}\left[(xz_\eta)_\zeta + (zx_\zeta)_\eta - (xz_\zeta)_\eta - (zx_\eta)_\zeta\right] \\
\widehat{\xi}_z &= \frac{1}{2}\left[(yx_\eta)_\zeta + (xy_\zeta)_\eta - (yx_\zeta)_\eta - (xy_\eta)_\zeta\right] \\
\\
\widehat{\eta}_x &= \frac{1}{2}\left[(zy_\zeta)_\xi + (yz_\xi)_\zeta - (zy_\xi)_\zeta - (yz_\zeta)_\xi\right] \\
\widehat{\eta}_y &= \frac{1}{2}\left[(xz_\zeta)_\xi + (zx_\xi)_\zeta - (xz_\xi)_\zeta - (zx_\zeta)_\xi\right] \\
\widehat{\eta}_z &= \frac{1}{2}\left[(yx_\zeta)_\xi + (xy_\xi)_\zeta - (yx_\xi)_\zeta - (xy_\zeta)_\xi\right] \\
\\
\widehat{\zeta}_x &= \frac{1}{2}\left[(zy_\xi)_\eta + (yz_\eta)_\xi - (zy_\eta)_\xi - (yz_\xi)_\eta\right] \\
\widehat{\zeta}_y &= \frac{1}{2}\left[(xz_\xi)_\eta + (zx_\eta)_\xi - (xz_\eta)_\xi - (zx_\xi)_\eta\right] \\
\widehat{\zeta}_z &= \frac{1}{2}\left[(yx_\xi)_\eta + (xy_\eta)_\xi - (yx_\eta)_\xi - (xy_\xi)_\eta\right]
\end{aligned}
\tag{176}
$$

and the Jacobian calculated as

$$
J^{-1} = \frac{1}{3}\left[(x\xi_x + y\xi_y + z\xi_z)_\xi + (x\eta_x + y\eta_y + z\eta_z)_\eta + (x\zeta_x + y\zeta_y + z\zeta_z)_\zeta\right] \tag{177}
$$

At each time sub-iteration the state vector is updated in a similar manner as Eq. 140

$$
\begin{aligned}
\Delta\mathbf{Q} = -\frac{\Delta t}{J^{-1}}\Bigg(&\frac{\widehat{\mathbf{F}}_{i+1/2,j,k} - \widehat{\mathbf{F}}_{i-1/2,j,k}}{\Delta\xi} + \\
&\frac{\widehat{\mathbf{G}}_{i,j+1/2,k} - \widehat{\mathbf{G}}_{i,j-1/2,k}}{\Delta\eta} + \\
&\frac{\widehat{\mathbf{H}}_{i,j,k+1/2} - \widehat{\mathbf{H}}_{i,j,k-1/2}}{\Delta\zeta}\Bigg)
\end{aligned}
\tag{178}
$$

4.6.2 Viscous fluxes

The simplest method of computing the viscous fluxes in the conservative finite difference framework is to treat them in a similar manner as the inviscid fluxes: compute the derivatives at the cell centers and then reconstruct them to the "cell" faces. First derivatives at the grid points can be computed using second-, fourth-, or sixth-order

accurate approximations which are shown below for a single computational direction, but are equivalent in all three,

$$\left.\frac{\partial u}{\partial \xi}\right|_{i,j,k} = \frac{1}{2\Delta\xi}\left(u_{i+1,j,k} - u_{i-1,j,k}\right) + O\left(\Delta x^2\right) \tag{179a}$$

$$\left.\frac{\partial u}{\partial \xi}\right|_{i,j,k} = \frac{1}{12\Delta\xi}\left(u_{i-2,j,k} - 8u_{i,j,k} + 8u_{i+1,j,k} - u_{i+2,j,k}\right) + O\left(\Delta x^4\right) \tag{179b}$$

$$\left.\frac{\partial u}{\partial \xi}\right|_{i,j,k} = \frac{1}{60\Delta\xi}\left(-u_{i-3,j,k} + 9u_{i-2,j,k} - 45u_{i,j,k} + 45u_{i+1,j,k} - 9u_{i+2,j,k} + u_{i+3,j,k}\right) + O\left(\Delta x^6\right) \tag{179c}$$

Unfortunately, the repeated application of the first derivative operator can cause an odd-even decoupling problem [207, 91]. This issue can be mitigated using a filtering operation, which will be described in Section 4.8, to remove instabilities [226]. The application of such a filter is limited to smooth regions of the flow which excludes discontinuities such as flame fronts. Since the viscous terms are very important in flames, a more general solution for the odd-even decoupling problem is required.

The Navier-Stokes equations without source terms in generalized coordinates, Eq. (169), can be rewritten splitting the flux terms into inviscid and viscous contributions

$$\frac{\partial \widehat{\mathbf{Q}}}{\partial t} + \frac{\partial \widehat{\mathbf{F}}}{\partial \xi} + \frac{\partial \widehat{\mathbf{G}}}{\partial \eta} + \frac{\partial \widehat{\mathbf{H}}}{\partial \zeta} = \frac{\partial \widehat{\mathbf{F}}_{\mathbf{v}}}{\partial \xi} + \frac{\partial \widehat{\mathbf{G}}_{\mathbf{v}}}{\partial \eta} + \frac{\partial \widehat{\mathbf{H}}_{\mathbf{v}}}{\partial \zeta} \tag{180}$$

with detailed definitions of the viscous terms of Eq. (3)-(5) written in generalized coordinates given by Visbal and Gaitande [227]. Following the method of Sun et al [207] the viscous derivative terms like $\dfrac{\partial \widehat{\mathbf{F}}_{\mathbf{v}}}{\partial \xi}$ can be rewritten as

$$\frac{\partial \widehat{\mathbf{F}}_{\mathbf{v}}}{\partial \xi} = \frac{\partial\left(\widehat{\mathbf{F}}_{\mathbf{v}} - \widehat{\mathbf{F}}'_{\mathbf{v}}\right)}{\partial \xi} + \frac{\partial \widehat{\mathbf{F}}'_{\mathbf{v}}}{\partial \xi} \tag{181}$$

where for single species Navier-Stokes equations

$$\widehat{\mathbf{F}}'_{\mathbf{v}} = J^{-1} \begin{bmatrix} 0 \\ \mu\left(\frac{4}{3}\xi_x^2 + \xi_y^2 + \xi_z^2\right)\frac{\partial u}{\partial \xi} \\ \mu\left(\xi_x^2 + \frac{4}{3}\xi_y^2 + \xi_z^2\right)\frac{\partial v}{\partial \xi} \\ \mu\left(\xi_x^2 + \xi_y^2 + \frac{4}{3}\xi_z^2\right)\frac{\partial w}{\partial \xi} \\ u\mu\left(\frac{4}{3}\xi_x^2 + \xi_y^2 + \xi_z^2\right)\frac{\partial u}{\partial \xi} + v\mu\left(\xi_x^2 + \frac{4}{3}\xi_y^2 + \xi_z^2\right)\frac{\partial v}{\partial \xi} \\ +w\mu\left(\xi_x^2 + \xi_y^2 + \frac{4}{3}\xi_z^2\right)\frac{\partial w}{\partial \xi} + k\left(\xi_x^2 + \xi_y^2 + \xi_z^2\right)\frac{\partial T}{\partial \xi} \end{bmatrix} \tag{182}$$

The term $\partial\left(\widehat{\mathbf{F}}_{\mathbf{v}} - \widehat{\mathbf{F}}'_{\mathbf{v}}\right)/\partial\xi$ is computed using the straightforward manner described previously where the first derivatives are calculated with Eq. 179 at the cell-centers and the "cell" face fluxes computed using Eq. 166 and coefficients in Table 3. Since this term does not contain any repeated first derivatives in the same direction the odd-even decoupling problem is eliminated [207]. The $\partial\widehat{\mathbf{F}}'_{\mathbf{v}}/\partial\xi$ terms are computed using a method similar to that presented by Shen and coworkers [191, 193, 192].

The derivative of the $\widehat{\mathbf{F}}'_{\mathbf{v}}$ term is calculated in a conservative manner,

$$\left(\frac{\partial\widehat{\mathbf{F}}'_{\mathbf{v}}}{\partial\xi}\right)_i = \left(\widetilde{\widehat{\mathbf{F}}}'_{\mathbf{v}}\right)_{i+1/2} - \left(\widetilde{\widehat{\mathbf{F}}}'_{\mathbf{v}}\right)_{i-1/2} \tag{183}$$

where the interface values are computed as

$$\left(\widetilde{\widehat{\mathbf{F}}}'_{\mathbf{v}}\right)_{i+1/2} = \sum_{I=i-m}^{i+n} \alpha_I \left(\widetilde{\widehat{\mathbf{F}}}_{\mathbf{v}}\right)_I \tag{184}$$

The values for α_I for second-, fourth- and sixth-order are given in Table 5. All the terms in Eq. 182 at each interface in the local stencil need to be calculated at the desired order of accuracy. Properties such as μ, u, v, w, and the grid metrics needed to compute the flux, $\left(\widetilde{\widehat{\mathbf{F}}}_{\mathbf{v}}\right)_I$, at each interface are determined with the following expression

$$\mu_I = \sum_{l=m}^{n} C_l^I \mu_{i+l} \tag{185}$$

Table 5 Coefficients of α_I [193, 192].

Order $\backslash I$	$i-3/2$	$i-1/2$	$i+1/2$	$i+3/2$	$I+5/2$
2	–	–	1	–	–
4	–	$-1/24$	$26/24$	$-1/24$	–
6	$9/1920$	$-116/1920$	$2134/1920$	$-116/1920$	$9/1920$

Table 6 Fourth-order coefficients of C_l^I [193].

I	C_{-1}^I	C_0^I	C_1^I	C_2^I
$i-1/2$	$5/16$	$15/16$	$-5/16$	$1/16$
$i+1/2$	$-1/16$	$9/16$	$9/16$	$-1/16$
$i+3/2$	$1/16$	$-5/16$	$15/16$	$5/16$

Several options exist for the coefficients C_l^I. Shen et al [193, 192] suggest the values listed in Tables 6 and 7 whereas Zingg and De Rango [165, 247, 248, 166] use "centered" values like those listed in Table 10. The advantage of the former coefficients is that they achieve the same order of accuracy as the latter on a smaller stencil. Unfortunately this is much more computationally expensive as at each interface all the other interface values need to be recomputed since they are not "centered". Derivatives in the computational normal direction at the "cell" interfaces are calculated in a similar manner

$$\left.\frac{\partial u}{\partial \xi}\right|_I = \frac{1}{\Delta\xi}\sum_{l=r}^{s} D_l^I \mu_{i+l} \tag{186}$$

again with non-centered, Tables 8 and 9, and centered, Table 11, coefficients. For the derivatives, the non-centered coefficients use the same stencil as the centered values but are one order higher in accuracy; the computational efficiency disadvantages still exist.

This method is only used for the $\partial \widehat{\mathbf{F}}'_{\mathbf{v}}/\partial\xi$ term, which as noted by Sun et al. [207], is computationally less expensive than using this method exactly as Shen et al. [191, 193, 192] since the cross derivative terms do not need to be computed at the "cell" faces. It should be noted here that, to the author's knowledge, this is the first work

Table 7 Sixth-order coefficients of C_l^I [192].

I	C_{-2}^I	C_{-1}^I	C_0^I	C_1^I	C_2^I	C_3^I
$i-3/2$	$63/256$	$315/256$	$-105/128$	$63/128$	$-45/256$	$7/256$
$i-1/2$	$-7/256$	$105/256$	$105/128$	$-35/128$	$21/256$	$-3/256$
$i+1/2$	$3/256$	$-25/256$	$75/128$	$75/128$	$-25/256$	$3/256$
$i+3/2$	$-3/256$	$21/256$	$-35/128$	$105/128$	$105/256$	$-7/256$
$i+5/2$	$7/256$	$-45/256$	$63/128$	$-105/128$	$315/256$	$63/256$

Table 8 Fifth-order coefficients of D_l^I [193].

I	D_{-2}^I	D_{-1}^I	D_0^I	D_1^I	D_2^I	D_3^I
$i-1/2$	$71/1920$	$-141/128$	$69/64$	$1/192$	$-3/128$	$3/640$
$i+1/2$	$-3/640$	$25/384$	$-75/64$	$75/64$	$-25/384$	$3/640$
$i+3/2$	$-3/640$	$3/128$	$-1/192$	$-69/64$	$141/128$	$-71/1920$

Table 9 Seventh-order coefficients of D_l^I [192].

I	D_{-3}^I	D_{-2}^I	D_{-1}^I	D_0^I	D_1^I	D_2^I	D_3^I	D_4^I
$i-3/2$	$3042/107520$	$-5353/5120$	$4731/5120$	$733/3072$	$-239/1024$	$597/5120$	$-167/5120$	$143/35840$
$i-1/2$	$-143/35840$	$185/1024$	$-1185/1024$	$1175/1024$	$-125/3072$	$-51/5120$	$5/1024$	$-5/7168$
$i+1/2$	$5/7168$	$-49/5120$	$245/3072$	$-1225/1024$	$1225/1024$	$-245/3072$	$49/5120$	$-5/7168$
$i+3/2$	$5/7168$	$-5/1024$	$51/5120$	$125/3072$	$-1175/1024$	$1185/1024$	$-185/1024$	$143/35840$
$i+5/2$	$-143/35840$	$167/5120$	$-597/5120$	$239/1024$	$-733/3072$	$-4731/5120$	$5353/5120$	$-3042/107520$

Table 10 Centered coefficients of C_l^I, $I = i + 1/2$ [165, 247, 248, 166].

Order	C_{-2}^I	C_{-1}^I	C_0^I	C_1^I	C_2^I	C_3^I
2	–	–	$1/2$	$1/2$	–	–
4	–	$-1/16$	$9/16$	$9/16$	$-1/16$	–
6	$3/256$	$-25/256$	$75/128$	$75/128$	$-25/256$	$3/256$

Table 11 Centered coefficients of D_l^I, $I = i + 1/2$ [165, 247, 248, 166].

Order	D_{-2}^I	D_{-1}^I	D_0^I	D_1^I	D_2^I	D_3^I
2	–	–	-1	1	–	–
4	–	$1/24$	$-27/24$	$27/24$	$-1/24$	–
6	$-3/640$	$25/384$	$-75/64$	$75/64$	$-25/384$	$3/640$

to combine the method of Sun et al. [207] with the coefficients of Zingg and De Rango [165, 247, 248, 166]. This further increases the computationally efficiency of the method compared with that of Shen et al. [191, 193, 192]. A laminar flame test case presented in later in Section 5.3 shows the importance of addressing the odd-even decoupling problem near flame fronts when simulating reacting flows with high-order finite difference methods.

4.6.3 Conservative finite difference method implementation notes

The conservative finite difference methods were implemented in the existing finite volume framework. Since the finite volume methods already in place were cell-centered no major changes to the data structures inside the code were necessary; the only distinction is that the stored variable in the finite volume schemes are cell-averages whereas in the finite difference methods they are point values. The capability to run with different methods at different orders allows for error estimation without explicit grid resolution studies [172]. The finite volume grid metrics are computed for both frameworks which allows integration of the Lagrangian phase into the finite difference methods simple. Locating the Lagrangian parcels still occurs using the "finite volume cells" even when the finite difference method. The time update algorithms had to be adjusted slightly to use the grid point Jacobian rather than the cell volume during integration. Because the high-order finite difference methods rely on the metrics also being computed to high-accuracy, grid singularities such as those found in O-grids pose a larger problem for these schemes compared to the formally second-order accurate finite volume methods. Currently the only way to solve this problem is to use the static mesh refinement method, detailed in Section 4.10, for such locations in the domain. Using methods of this type may degrade accuracy slightly but for the problems of interest in this work it is not of a concern since grid singularities are avoided in the region of interest. While this hybrid central/upwind conservative

finite difference solver is similar to others [30, 42, 246], the exact combination of the various methods and strategies is unique. It is also interesting to note that the current high-order conservative finite difference implementation was extended to solve the governing equations for magnetohydrodynamics [189].

4.6.4 Weighted Essentially Non-Oscillatory (WENO) Method

The compact and explicit central conservative finite difference schemes suffer the same problems near discontinuities as their finite volume counterparts, namely dispersive errors, so non-oscillatory finite difference methods are also required for many flows of interest. Several methods have been introduced including the piecewise parabolic method (PPM) [28], the essentially non-oscillatory method (ENO) [77] and weighted essentially non-oscillatory (WENO) scheme [115]. High-order WENO schemes, especially in combination with high-order central schemes, have shown promise in the area of shock-turbulence interaction [150, 116] where highly vortical turbulent structures are in close proximity to large gradients. This situation also occurs in turbulent combustion thus leading to the current investigation and implementation of WENO schemes.

For both ENO and WENO, the fluxes at the $i+1/2$ "cell" interface are computed using n candidate stencils, S_k, $k = 0, 1, \ldots, r-1$ where

$$S_k = (x_{i+k-r+1}, x_{i+k-r+2}, \ldots, x_{i+k}) \tag{187}$$

Each stencil provides an r^{th} order approximation to the flux at the interface. Figure 10 shows the three stencils used in the fifth-order WENO scheme, where each stencil provides a third-order approximation.

In ENO schemes, the single "smoothest" stencil is chosen to calculate the final flux which is advantageous at discontinuities since this avoids using data from discontinuous stencils. Away from discontinuities is smooth flow regions this limits the

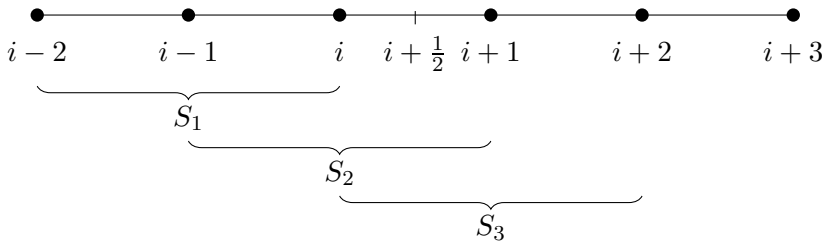

Figure 10 Fifth-order WENO stencils for computing the flux at $i+1/2$

order of accuracy of the overall scheme to that of the flux approximation for each stencil. WENO schemes remedy this situation by instead of selecting a single stencil to compute the flux, all stencils are combined using dynamically and locally computed weights. At flow discontinuities, discontinuous stencils will be assigned near-zero weights while in smooth regions of the flow, information from all stencils will be used to achieve a higher order of accuracy [86]. The flux computed at $i+1/2$ is

$$F_{i+1/2} = \sum_{k=0}^{r} \omega_k F^k \left(x_{i+1/2}\right) \tag{188}$$

The flux at $i+1/2$ computed from each available stencil, k, is

$$F^k \left(x_{i+1/2}\right) = F^k_{i+1/2} = \sum_{j=0}^{r} c_{kj} F_{i-k+j}, \quad i = 0, \ldots, n \tag{189}$$

where c_{kj} are reconstruction coefficients that depend only on k. The weights, ω_k, are caclulated as

$$\omega_k = \frac{\alpha_k}{\sum_{l=0}^{n} \alpha_l}, \quad \alpha_k = \frac{d_k}{(\beta_k + \epsilon)^p} \tag{190}$$

Here the d_k are the ideal weights which are used when all stencils are smooth and β_k are the local smoothness indicators,

$$\beta_k = \sum_{l=1}^{n} \Delta x^{2l-1} \int_{x-1/2}^{x+1/2} \left(\frac{d^l}{dx^l} F^k(x)\right)^2 dx \tag{191}$$

For $r = 3$, the fifth-order WENO scheme the reconstruction coefficients and ideal weights are listed in Table 12 and the smoothness indicators at each of the three

Table 12 Reconstruction coefficients and ideal weights for $r = 3$, the 5th order WENO scheme [86]

Stencil	Reconstruction coefficients			Ideal weights
S_k	c_{k0}	c_{k1}	c_{k2}	d_k
S_0	$1/3$	$-7/6$	$11/6$	$1/10$
S_1	$-1/6$	$5/6$	$1/3$	$3/5$
S_2	$1/3$	$5/6$	$-1/6$	$3/10$

Table 13 Reconstruction coefficients and ideal weights for $r = 2$, the 3rd order WENO scheme [86]

Stencil	Reconstruction coefficients		Ideal weights
S_k	c_{k0}	c_{k1}	d_k
S_0	$-1/2$	$3/2$	$1/3$
S_1	$1/2$	$1/2$	$2/3$

stencils are

$$\begin{aligned}
\beta_0 &= \frac{13}{12}\left(F_{i-2} - 2F_{i-1} + F_i\right)^2 + \frac{1}{4}\left(F_{i-2} - 4F_{i-1} + 3F_i\right)^2 \\
\beta_1 &= \frac{13}{12}\left(F_{i-1} - 2F_i + F_{i+1}\right)^2 + \frac{1}{4}\left(F_{i-1} - F_{i+1}\right)^2 \\
\beta_2 &= \frac{13}{12}\left(F_i - 2F_{i+1} + F_{i+2}\right)^2 + \frac{1}{4}\left(3F_i - 4F_{i+1} + F_{i+2}\right)^2
\end{aligned} \tag{192}$$

Third-, seventh- and ninth-order schemes have also been implemented though most of this work will focus on the fifth-order scheme. This is consistent with many other works [86, 191, 230, 137, 90, 245] as this represents a compromise between accuracy, stencil size and cost. For completeness, Tables 13–15 give the reconstruction coefficients and ideal weights for the other implemented order and the the smoothness indicators are as follows:

- Third-order, $r = 2$ [86]

$$\begin{aligned}
\beta_0 &= \left(F_i - F_{i-1}\right)^2 \\
\beta_1 &= \left(F_{i+1} - F_i\right)^2
\end{aligned} \tag{193}$$

Table 14 Reconstruction coefficients and ideal weights for $r = 4$, the 7th order WENO scheme [6]

Stencil	Reconstruction coefficients				Ideal weights
S_k	c_{k0}	c_{k1}	c_{k2}	c_{k3}	d_k
S_0	$-1/4$	$13/12$	$-23/12$	$25/12$	$1/35$
S_1	$1/12$	$-5/12$	$13/12$	$1/4$	$12/35$
S_2	$-1/12$	$7/12$	$7/12$	$-1/12$	$18/35$
S_3	$1/4$	$13/12$	$-5/12$	$1/12$	$4/35$

- Seventh-order, $r = 4$ [6]

$$
\begin{aligned}
\beta_0 =& F_{i-3}\left(547F_{i-3} - 3882F_{i-2} + 4642F_{i-1} - 1854F_i\right) \\
&+ F_{i-2}\left(7043F_{i-2} - 17246F_{i-1} + 7042F_i\right) \\
&+ F_{i-1}\left(11003F_{i-1} - 9402F_i\right) + 2107F_i^2 \\
\beta_1 =& F_{i-2}\left(267F_{i-2} - 1642F_{i-1} + 1602F_i - 494F_{i+1}\right) \\
&+ F_{i-2}\left(2843F_{i-1} - 5966F_i + 1922F_{i+1}\right) \\
&+ F_{i-1}\left(3443F_i - 2522F_{i+1}\right) + 547F_{i+1}^2 \\
\beta_2 =& F_{i-1}\left(547F_{i-1} - 2522F_i + 1922F_{i+1} - 494F_{i+2}\right) \\
&+ F_i\left(3443F_i - 5966F_{i+1} + 1602F_{i+2}\right) \\
&+ F_{i+1}\left(2843F_{i+1} - 1642F_{i+2}\right) + 267F_{i+2}^2 \\
\beta_3 =& F_i\left(2107F_i - 9402F_{i+1} + 7042F_{i+2} - 1854F_{i+3}\right) \\
&+ F_{i+1}\left(11003F_{i+1} - 17246F_{i+2} + 4642F_{i+3}\right) \\
&+ F_{i+2}\left(7043F_{i+2} - 3882F_{i+3}\right) + 547F_{i+3}^2
\end{aligned}
\tag{194}
$$

- Ninth-order, $r = 4$ [6]

Table 15 Reconstruction coefficients and ideal weights for $r = 5$, the 9$^{\text{th}}$ order WENO scheme [6]

Stencil	Reconstruction coefficients					Ideal weights
S_k	c_{k0}	c_{k1}	c_{k2}	c_{k3}	c_{k4}	d_k
S_0	$1/5$	$-21/20$	$137/60$	$-163/60$	$137/60$	$1/126$
S_1	$-1/20$	$17/60$	$-43/60$	$77/60$	$1/5$	$10/63$
S_2	$1/30$	$-13/60$	$47/60$	$9/20$	$-1/20$	$10/21$
S_3	$-1/20$	$9/20$	$47/60$	$-13/60$	$1/30$	$20/63$
S_4	$1/5$	$77/60$	$-43/60$	$17/60$	$-1/20$	$5/126$

$$
\begin{aligned}
\beta_0 =& F_{i-4}\left(22658F_{i-4} - 208501F_{i-3} + 364863F_{i-2} - 288007F_{i-1} + 86329F_i\right) \\
&+ F_{i-3}\left(7043F_{i-2} - 17246F_{i-1} + 7042F_i\right) \\
&+ F_{i-1}\left(11003F_{i-1} - 9402F_i\right) + 2107F_i^2 \\
\beta_1 =& F_{i-3}\left(6908F_{i-3} - 60871F_{i-2} + 99213F_{i-1} - 70237F_i + 18079F_{i+1}\right) \\
&+ F_{i-2}\left(138563F_{i-2} - 464976F_{i-1} + 337018F_i - 88297F_{i+1}\right) \\
&+ F_{i-1}\left(406293F_{i-1} - 611976F_i + 165153F_{i+1}\right) \\
&+ F_i\left(242723F_i - 140251F_{i+1}\right) + 22658F_{i+1}^2 \\
\beta_2 =& F_{i-2}\left(6908F_{i-2} - 51001F_{i-1} + 67923F_i - 38947F_{i+1} + 8209F_{i+2}\right) \\
&+ F_{i-1}\left(104963F_{i-1} - 299076F_i + 179098F_{i+1} - 38947F_{i+2}\right) \\
&+ F_i\left(231153F_i - 299076F_{i+1} + 67923F_{i+2}\right) \\
&+ F_{i+1}\left(104963F_{i+1} - 51001F_{i+2}\right) + 6908F_{i+2}^2 \\
\beta_3 =& F_{i-1}\left(22658F_{i-1} - 140251F_i + 165153F_{i+1} - 88297F_{i+2} + 18079F_{i+3}\right) \\
&+ F_i\left(242723F_i - 611976F_{i+1} + 337018F_{i+2} - 70237F_{i+3}\right) \\
&+ F_{i+1}\left(406293F_{i+1} - 464976F_{i+2} + 99213F_{i+3}\right) \\
&+ F_{i+2}\left(138563F_{i+2} - 60871F_{i+3}\right) + 6908F_{i+3}^2 \\
\beta_4 =& F_i\left(107918F_i - 649501F_{i+1} + 758823F_{i+2} - 411487F_{i+3} + 86329F_{i+4}\right) \\
&+ F_{i+1}\left(1020563F_{i+1} - 2462076F_{i+2} + 1358458F_{i+3} - 288007F_{i+4}\right) \\
&+ F_{i+2}\left(1521393F_{i+2} - 1704396F_{i+3} + 364863F_{i+4}\right) \\
&+ F_{i+3}\left(482963F_{i+3} - 208501F_{i+4}\right) + 22658F_{i+4}^2
\end{aligned}
\tag{195}
$$

The parameter ϵ is needed to avoid division by zero. The choice of this parameter can affect the solution [80], since depending on the values of the smoothness indicators, ϵ can dominate the α_k terms. As currently implemented, ϵ is computed as

$$\epsilon = \epsilon_{user} \max F^2 + 10^{-99} \tag{196}$$

noting that the fluxes have been pre-multiplied by the metric terms so that $\epsilon = K\Delta x^2$ which is needed to maintain the desired order of accuracy of the scheme near discontinuities [52, 239, 5, 19]. Scaling the user-input value by the local flux values also removes some of the burden of case-by-case user parameter tuning. The power parameter, p, magnifies the relative ratio between the smoothness indicators and for the base WENO scheme is set to 2.

4.6.4.1 WENO-Z scheme

Several methods have been introduced to improve on the classical WENO method presented in the previous section. The revised methods generally involve modifying how the non-linear weights are computed to reduce dissipation at flow discontinuities and/or to obtain optimal convergence at critical points [80, 14, 19, 41, 51, 50]. The WENO-Z scheme [14, 19] was selected due to its ease of implementation and favorable results compared with other methods in terms of both accuracy and computational efficiency for reacting flows [245].

The WENO-Z scheme differs from the original WENO scheme, often denoted as WENO-JS, in the definition of the smoothness indicators. Instead of each sub-stencil having an independent smoothness indicator, a higher-order smoothness indicator is formed based on information at all the stencils which then affects the stencil weights. This global smoothness indicator is defined for WENO schemes with $r \geq 3$ as

$$\tau_{2r-1} = \begin{cases} |\beta_0 - \beta_{r-1}|, & \text{mod } (r,2) = 1, \\ |\beta_0 - \beta_1 - \beta_{r-2} + \beta_{r-1}| & \text{mod } (r,2) = 0 \end{cases} \tag{197}$$

The normalized and un-normalized weights are computed using the global smoothness indicator

$$\omega_k^z = \frac{\alpha_k^z}{\sum_{l=0}^{n} \alpha_l^z}, \quad \alpha_k = \frac{d_k}{\beta_k^z} = d_k \left[1 + \left(\frac{\tau_{2r-1}}{\beta_k + \epsilon} \right)^q \right], \quad k = 0, \ldots, r-1 \tag{198}$$

4.6.4.2 Characteristic decomposition

The WENO method described in the previous sections can be directly applied to the fluxes computed using the conservative variables but studies have shown this can result in spurious oscillations near discontinuities [160]. Instead it is recommended that the fluxes be computed in their local characteristic fields [86, 168, 195, 207] especially when using WENO schemes greater than third order. The solution method when using a characteristic decomposition is described below [207]:

1. At each interface, $i + 1/2$, compute an averaged state of conservative variables, $\mathbf{Q}_{i+1/2}$, using a simple arithmetic mean of the i and $i + 1$ variables. A more complicated Roe average could be computed but testing during scheme implementation showed the Roe averaging made no difference to the solution and was computationally more expensive.

2. Compute the left eigenvectors, $\mathbf{L}_{i+1/2}^{(s)}$, the right eigenvectors, $\mathbf{R}_{i+1/2}^{(s)}$ [38, 173], and eigenvalues, $\lambda_{i+1/2}^{(s)}$ of the flux Jacobian matrix, $\mathbf{A} = \partial \mathbf{F} / \partial \mathbf{Q}$, where $s = 1, 2, 3, 4, 5, \ldots, 5 + N_s$.

3. Use the left eigenvectors to project the conservative variables and inviscid fluxes into characteristic space resulting in characteristic variables, ϕ and fluxes w,

$$\begin{aligned} \phi_m^{(s)} &= \mathbf{L}_{i+1/2}^{(s)} \mathbf{Q}_m, \quad m \in [i - r + 1, i + r] \\ w_m^{(s)} &= \mathbf{L}_{i+1/2}^{(s)} \mathbf{F}_m, \quad m \in [i - r + 1, i + r] \end{aligned} \tag{199}$$

4. The WENO procedure is then applied to split interface fluxes, $w_{i+1/2}^+$ and $w_{i+1/2}^-$ where

$$w_{i+1/2} = w_{i+1/2}^+ + w_{i+1/2}^- \tag{200}$$

This flux splitting can be accomplished in a variety of ways. The simplest is a Roe-type local characteristic decomposition

$$\begin{cases} w_m^+ = w_m \\ w_m^- = 0 \end{cases} \quad \text{if } \lambda_{i+1/2} \geq 0$$
$$\begin{cases} w_m^+ = 0 \\ w_m^- = w_m \end{cases} \quad \text{if } \lambda_{i+1/2} < 0 \tag{201}$$

Another option is the local Lax-Friedrichs (LF) flux splitting

$$\begin{aligned} w_m^{(s),+} &= \frac{w_m^{(s),+}}{2} \max \left| \lambda_l^{(s)} \right| \phi_m^{(s)} \\ w_m^{(s),-} &= \frac{w_m^{(s),-}}{2} \max \left| \lambda_l^{(s)} \right| \phi_m^{(s)} \end{aligned} \tag{202}$$

The $w_{i+1/2}^+$ is computed using a reconstruction with a biased stencil with one more point to the left and $w_{i+1/2}^-$ is calculated symmetrically with a stencil biased with one more point to the right, to allow for the correct upwinding.

The Roe-type flux splitting is less dissipative than the Lax-Friedrichs splitting but admits rarefaction waves which do not satisfy the entropy condition. To avoid this problem, the flux splitting methods are combined into a single Roe-type with entropy fix procedure

$$w_{i+1/2}^{(s)} = \begin{cases} w_{i+1/2}^{(s),\pm Roe} & \text{if } \lambda_i^{(s)} \lambda_{i+1}^{(s)} > 0 \\ w_{i+1/2}^{(s),\pm LF} & \text{otherwise} \end{cases} \tag{203}$$

A slight alternative to this procedure is to use the Roe-type with entropy fix flux splitting for genuinely nonlinear characteristics but always use the local Lax-Friedrichs splitting for the linearly degenerate characteristics [86, 6]. This method is slightly more dissipative but provides extra stability in the solution.

Special care must also be taken for multidimensional simulations with strong shocks to avoid the "Carbuncle" phenomenon. To achieve this, the Roe-type

procedure with the entropy fix is modified slightly [168, 180, 147]

$$w_{i+1/2}^{(s)} = \begin{cases} w_{i+1/2}^{(s),\pm Roe} & \text{if } \min\left(\left|\lambda_i^{(s)}\right|, \left|\lambda_{i+1}^{(s)}\right|\right) > \eta_{i+1/2,j,k} \\ w_{i+1/2}^{(s),\pm LF} & \text{otherwise} \end{cases} \tag{204}$$

where $\eta_{i+1/2,j,k}$ is computed as

$$\begin{aligned} \eta_{i+1/2,j,k} = \max\big(&\eta_{i+1/2,j,k}^{x}, \\ &\eta_{i,j-1/2,k}^{y}, \eta_{i,j+1/2,k}^{y}, \eta_{i+1,j-1/2,k}^{y}, \eta_{i+1,j+1/2,k}^{y}, \\ &\eta_{i,j,k-1/2}^{z}, \eta_{i,j,k+1/2}^{z}, \eta_{i+1,j,k-1/2}^{z}, \eta_{i+1,j,k+1/2}^{z}\big) \end{aligned} \tag{205}$$

and

$$\begin{aligned} \eta_{i+1/2,j,k}^{x} &= |u_{i+1,j,k} - u_{i,j,k}| + |a_{i+1,j,k} - a_{i,j,k}| \\ \eta_{i,j+1/2,k}^{y} &= |v_{i,j+1,k} - v_{i,j,k}| + |a_{i,j+1,k} - a_{i,j,k}| \\ \eta_{i,j,k+1/2}^{z} &= |w_{i,j,k+1} - w_{i,j,k}| + |a_{i,j,k+1} - a_{i,j,k}| \end{aligned} \tag{206}$$

Here $a_{i,j,k}$ is the speed of sound at the point (i, j, k).

5. Finally, the characteristic fluxes are projected back into physical space using the right eigenvectors

$$\mathbf{F}_{i+1/2} = \mathbf{R}_{i+1/2}\left(\mathbf{W}_{i+1/2}^{+} + \mathbf{W}_{i+1/2}^{-}\right) \tag{207}$$

4.7 Time Integration

All the of the time integration schemes used in the current work are explicit which means that updating the solution to the $n+1$ time step only requires information about the solution at the n or previous time levels. This is in contrast to implicit methods where updating the solution to the $n+1$ time step actually involves the solution at the $n+1$. Implicit methods are more computationally expensive per time step but allow for time steps to be as large as the temporal features of interest. Explicit methods are less computationally expensive per time step and generally more accurate and easier to implement, especially for higher-orders, compared to implicit

methods [87]. In addition, in compressible, reacting flow LES the physical time scales of interest, acoustics, turbulence, chemical reactions, etc., dictate that the time step must be reasonably small to maintain accuracy thus explicit integration methods are used more often. The disadvantage of explicit methods is the associated numerical stability requirements which can limit the maximum allowable time step size to below even the time step required for the desired accuracy.

The maximum allowable time step for stability is defined as

$$\Delta t = \mathrm{CFL} \times \frac{V}{v_w} \tag{208}$$

where V is the cell volume, CFL is the Courant-Friedrich-Levy number and v_w is a wave velocity. Inviscid wave propagation due to convection and acoustics are usually grouped together. In computational space this convective wave speed is,

$$v_c = |\mathbf{u} \cdot d\mathbf{A}_i| + |\mathbf{u} \cdot d\mathbf{A}_j| + |\mathbf{u} \cdot d\mathbf{A}_k| + c\,|d\mathbf{A}| \tag{209}$$

where $|\mathbf{u} \cdot d\mathbf{A}_i|$ represents the absolute value of the velocity in the i-direction and $|d\mathbf{A}|$ represents the magnitude of the surface normal vectors and c is the speed of sound. Simulations involving viscosity are further limited by the diffusive wave speed estimated as,

$$v_d = K\lambda \frac{|d\mathbf{A}|^2}{V}. \tag{210}$$

The variable λ can take different forms: for momentum diffusion, $\lambda = \nu$, for species diffusion $\lambda = \max D_k$ and for temperature diffusion $\lambda = \kappa / (\rho C_v)$. For this work the constant $K = 2$ and the diffusion wave speed is computed based on the maximum of momentum, species and temperature,

$$v_d = 2 \max(\lambda) \frac{|d\mathbf{A}|^2}{V}. \tag{211}$$

The time step is determined based on the combination of the convective and diffusive wave speed,

$$\Delta t = \mathrm{CFL} \times \frac{V}{v_c + v_d}. \tag{212}$$

Table 16 Time integration coefficients in $\alpha_{ik} - \beta_{ik}$ format for SSPRK(2,2) [71]

	$i \setminus k$	$k=0$	$k=1$
α_{ik}	1	1	
	2	1/2	1/2
β_{ik}	1	1	
	2	0	1/2

The maximum stable CFL number depends on the time integration scheme being used but for all explicit schemes it is $\mathcal{O}(1)$. To avoid any instabilities when using the second-order scheme, described next, CFL is set to 0.5. For the higher-order time integration methods this value is usually set closer to unity.

The time integration scheme in use with the predictor-corrector finite volume scheme is a second-order predictor-corrector time integration scheme which is equivalent to a strong stability preserving (SSP) second order Runge-Kutta scheme. Runge-Kutta schemes can be written in an $\alpha - \beta$ format,

$$U^{(0)} = U^n \tag{213a}$$

$$U^{(i)} = \sum_{k=0}^{i-1} \left(\alpha_{ik} U^{(k)} + \Delta t \beta_{ik} L\left(U^{(k)}\right) \right), \quad i = 1, 2, \ldots, s \tag{213b}$$

$$U^{n+1} = U^{(s)} \tag{213c}$$

with the second-order coefficients listed in Table 16. Due to the coupling of the spatial integration with the time integration, the predictor-corrector scheme can only be used with Runge-Kutta schemes with an even number of stages such as the classical fourth-order Runge-Kutta method given in Table 17. Numerical experiments have shown that this allows for larger stable time steps and the error is decreased for equivalent time steps, there is no gain in efficiency since the error is dominated by the second-order spatial scheme.

The spatial integration of high-order interpolation finite volume scheme and the

Table 17 Time integration coefficients in $\alpha_{ik} - \beta_{ik}$ format for classical RK4 [196]

	$i \setminus k$	$k=0$	$k=1$	$k=2$	$k=3$
α_{ik}	1	1			
	2	1/2	1/2		
	3	1/9	2/9	2/3	
	4	0	1/3	1/3	1/3
β_{ik}	1	1/2			
	2	−1/4	1/2		
	3	−1/9	−1/3	1	
	4	0	1/6	0	1/6

Table 18 Time integration coefficients in $\alpha_{ik} - \beta_{ik}$ format for SSPRK(3,3) [71]

	$i \setminus k$	$k=0$	$k=1$	$k=2$
α_{ik}	1	1		
	2	3/4	1/4	
	3	1/3	0	2/3
β_{ik}	1	1		
	2	0	1/4	
	3	0	0	2/3

hybrid compact/WENO finite difference scheme are not coupled with the time integration scheme allowing more flexibility in this regard. For the tests conducted here we use either the SSPRK(3,3) or SSPRK(5,4) methods with their $\alpha - \beta$ coefficients listed in Tables 18 and 19 [71, 176]. The high-order interpolation finite volume scheme is formally second-order, as previously discussed, so the SSPRK(3,3) is often sufficient whereas the hybrid compact/WENO finite difference is truly higher order. This necessitates a higher order time integration scheme to avoid having the time integration scheme dominate the overall error and convergence.

Several explicit low-storage Runge-Kutta methods of the 2-N type [234] were also implemented including a five stage, fourth-order method [18] and a six stage, fourth-order method [13]. Brief initial testing showed these methods were not noticeably superior to the SSPRK(5,4) method so they will not be discussed any further.

Table 19 Time integration coefficients in $\alpha_{ik} - \beta_{ik}$ format for SSPRK(5,4) [176]

	$i \setminus k$	$k=0$	$k=1$	$k=2$	$k=3$	$k=4$
	1	1				
	2	0.444370493651235	0.555629506348765			
α_{ik}	3	0.620101851488403	0	0.379898148511597		
	4	0.178079954393132	0	0	0.821920045606868	
	5	0	0	0.517231671970585	0.096059710526147	0.386708617503269
	1	0.391752226571890				
	2	0	0.368410593050371			
β_{ik}	3	0.620101851488403	0	0.251891774271694		
	4	0.178079954393132	0	0	0.544974750228521	
	5	0	0	0	0.063692468666290	0.226007483236906

4.8 Numerical Stabilization

High-order central schemes lack inherent dissipation and as such are subject to numerical instabilities. For the high-order compact interpolation finite volume scheme and the compact finite difference schme, a compact filter introduced by Gaitonde and Visbal [59, 60, 61] is applied to the conservative variables at the end of the Runge-Kutta time integration step as often as every time step if necessary.

$$\alpha_f \hat{u}_{i-1} + \hat{u}_i + \alpha_f \hat{u}_{i+1} = \sum_{n=0}^{N} \frac{a_n}{2} \left(\overline{u}_{i+n} + \overline{u}_{i-n} \right). \tag{214}$$

To maintain the order near boundaries a one-sided scheme is used [60, 62],

$$\alpha_f \hat{u}_{i-1} + \hat{u}_i + \alpha_f \hat{u}_{i+1} = \sum_{n=1}^{N} a_{n,i} \overline{u}_n. \tag{215}$$

The references provide tables for computing the central and boundary filter coefficients for a user-input α_f value for second- through tenth-order filters. One cell remains unfiltered but as Fosso et al. note [146], this is a ghost layer cell. The filtering operation is completed in each computational direction successively though the order in which it occurs changes to avoid bias. It should also be noted that an extra communication step is required after the filtering step to ensure the fluxes across block boundaries are computed correctly at the next time step.

The current implementation allows varying the order of the filter and α_f at block or physical boundaries. Generally the order of the filter is selected to be at least the

same order as the interpolation or derivative scheme [158] usually two to four orders higher [61]. For the current simulations, unless otherwise noted, the eighth-order filter is used for all internal and block boundary cells and a sixth-order filter is used at the inflow and outflow boundaries. The values for α_f vary between 0.45 and 0.499 depending on the grid resolution.

4.8.1 Numerical stabilization near discontinuities

Applying the high-order compact filter across discontinuities results in numerical oscillations. Several methods have been presented to handle flow discontinuities when using compact filtering including dropping the order of the filter and/or turning off the filter completely [224]. Here a method similar to the hybrid compact/Roe scheme [224] and the hybrid compact filter/characteristic filter method [116] is implemented to disable the high-order compact filter at discontinuities. The filter is disabled at grid points wherever the shock capturing scheme is used to compute both the left and right "cell" fluxes. Near these regions the second-order filter is applied and the order of the filter progressively increased further from the discontinuity as seen in Figure 11. To avoid excessive dissipation, the value of α_f is set to match the dissipation characteristics of the highest order scheme at a non-dimensional wavenumber of π. For example, if an eigth-order filter with $\alpha_f = 0.49$ is used in smooth regions, near discontinuities sixth-, fourth- and second-order filters will have $\alpha_f = 0.495$, 0.4975, and 0.49875, respectively.

4.9 Numerical method for the Lagrangian phase

The equations of motion for the Lagrangian phase droplets, Eq. (74)–(76), are integrated in time independently from the Eulerian solver with the coupling between the phases occurring via the interpolation of Eulerian properties to the droplet location and the Eulerian phase source terms from the droplets, Eq. (93). Because the Lagrangian phase and Eulerian phase are integrated separately there is an $\mathcal{O}(\Delta t)$

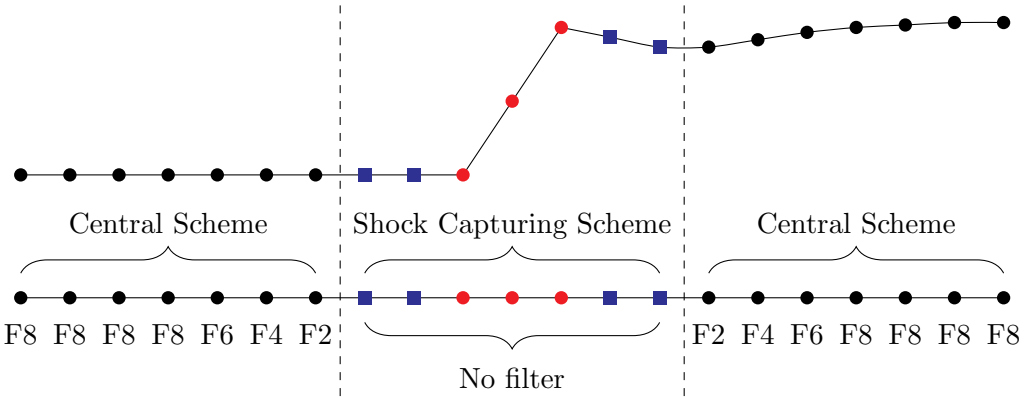

Figure 11 Filtering scheme for numerical stabilization near discontinuities

coupling error, but with the small time steps used in the current LES this error is assumed to be small. This method of time coupling has been used with success in many other simulations [187, 135, 149, 203]. One advantage of this method is that it allows each Lagrangian droplet to be integrated at the smallest relevant physical time scale [23, 48, 186]:

- LES Eulerian time step
- Droplet velocity relaxation time: The time constant for the exact solution of the local linearized equation of motion, Eq. 74, is

$$\tau_{relax} = \frac{16}{3}\frac{\rho_d}{\rho_g}\frac{r_d^2}{\nu_g}\frac{1}{C_D Re_d} \tag{216}$$

- Droplet lifetime: For evaporating droplets the time step should be limited to ensure that the drop size stays positive. The droplet life time is estimated based on the evaporation rate

$$\tau_{life} = \frac{4\pi r_d^3 \rho_d}{3\dot{m}_d} \tag{217}$$

- Droplet heating/evaporation time: If a droplet heats up too quickly in a single time step this could cause large amounts of evaporation and mass loading on the Eulerian phase. To avoid numerical instabilities the droplet time step is

also limited by

$$\tau_{evap} = \frac{\rho_d C_v d_d}{6 h_d} \tag{218}$$

- Droplet-turbulent eddy interaction time: A droplets is assumed to interact with a turbulent eddy over a time that is either the lifetime of the eddy or the time required for the droplet to traverse the eddy, whichever is smaller. The eddy lifetime is estimated using the LES filter width and the subgrid kinetic energy

$$\tau_{eddy} = \frac{\Delta}{\sqrt{2k^{sgs}/3}} \tag{219}$$

and the eddy transit time estimated as

$$\tau_{transit} = \tau_{relax} \ln\left(1 - \frac{\Delta}{\tau_{relax} \left|u_i - u_{i,d}\right|}\right) \tag{220}$$

Using these relations the droplet-turbulent eddy interaction time is computed as

$$\tau_{eddy,int} = \begin{cases} \tau_{eddy} & \Delta > \tau_{relax} \left|u_i - u_{i,d}\right| \\ \min\left(\tau_{eddy}, \tau_{transit}\right) & \Delta \leq \tau_{relax} \left|u_i - u_{i,d}\right| \end{cases} \tag{221}$$

- Local grid cell transit time: Droplets are limited to travel only a single cell in each time step so that local Eulerian properties can be interpolated accurately and droplets can be located easily.

$$\tau_{cell} = \frac{\Delta}{2 \left|u_d\right|} \tag{222}$$

Explicit Runge-Kutta time integration schemes from second- to fourth-order have been implemented for the Lagrangian phase which were previously presented in context of the Eulerian phase in Section 4.7. The finite volume simulations conducted in this study use the classic fourth-order scheme with coefficients of Eq. (213) given in Table 17. In simulations where the SSPRK(5,4) scheme, Table 19, is used for the Eulerian phase, the same scheme is applied for the Lagrangian phase. The ability to choose different time integration schemes for the Lagrangian and Eulerian phases

is another advantage of this Eulerian-Lagrangian approach. Computational memory requirements are also significantly reduced since multiple time sub-stages for droplet variables, positions, velocities, temperatures, etc., do not have to be stored simultaneously for all droplets.

Several methods for interpolating properties from the Eulerian cells to the Lagrangian parcels have been implemented. The most inexpensive method is simply taking the Eulerian value directly from the cell that contains that parcel. A more accurate approach uses a scheme based on Taylor series expansions [130].

$$u_d \approx u_c + \left.\frac{\partial u}{\partial x}\right|_c (x_d - x_c) + \left.\frac{\partial u}{\partial y}\right|_c (y_d - y_c) + \left.\frac{\partial u}{\partial z}\right|_c (z_d - z_c) \tag{223}$$

where u can be any Eulerian property needed at the droplet location. Since only first-order terms are included, this method is formally second order accurate, $O\left(x_{i,d} - x_{i,c}\right)^2$, where $x_{i,c}$ is the location of the nearest Eulerian cell-center, as long as the underlying scheme used for the Eulerian equations and grid metrics computations is as at least second order accurate as well. For the structured, curvilinear finite volume or finite difference schemes used in this study this can be written using a second-order

accurate central difference method for the derivatives as

$$
\begin{aligned}
u_d \approx u_{i,j,k} + \Bigg[& \frac{u_{i+1,j,k} - u_{i-1,j,k}}{2\Delta\xi} \left.\frac{\partial \xi}{\partial x}\right|_{i,j,k} + \\
& \frac{u_{i,j+1,k} - u_{i,j-1,k}}{2\Delta\eta} \left.\frac{\partial \eta}{\partial x}\right|_{i,j,k} + \\
& \frac{u_{i,j,k+1} - u_{i,j,k-1}}{2\Delta\zeta} \left.\frac{\partial \zeta}{\partial x}\right|_{i,j,k} \Bigg] (x_d - x_{i,j,k}) + \\
\Bigg[& \frac{u_{i+1,j,k} - u_{i-1,j,k}}{2\Delta\xi} \left.\frac{\partial \xi}{\partial y}\right|_{i,j,k} + \\
& \frac{u_{i,j+1,k} - u_{i,j-1,k}}{2\Delta\eta} \left.\frac{\partial \eta}{\partial y}\right|_{i,j,k} + \\
& \frac{u_{i,j,k+1} - u_{i,j,k-1}}{2\Delta\zeta} \left.\frac{\partial \zeta}{\partial y}\right|_{i,j,k} \Bigg] (y_d - y_{i,j,k}) + \\
\Bigg[& \frac{u_{i+1,j,k} - u_{i-1,j,k}}{2\Delta\xi} \left.\frac{\partial \xi}{\partial z}\right|_{i,j,k} + \\
& \frac{u_{i,j+1,k} - u_{i,j-1,k}}{2\Delta\eta} \left.\frac{\partial \eta}{\partial z}\right|_{i,j,k} + \\
& \frac{u_{i,j,k+1} - u_{i,j,k-1}}{2\Delta\zeta} \left.\frac{\partial \zeta}{\partial z}\right|_{i,j,k} \Bigg] (z_d - z_{i,j,k})
\end{aligned}
\tag{224}
$$

where i, j, k is the computational index of the nearest Eulerian cell-center and the grid metrics computed as described in previous sections. A moving least squares (MLS) method using polynomials of arbitrary order of accuracy was also implemented. The mathematics of the MLS procedure are described in the context of static mesh refinement in Section 4.10. Figure 12 compares these methods on a steady two-dimensional sinusoidal flow [130]. The Marchioli method is generally a good compromise between accuracy and cost.

To simulate realistic fuel flow rates very large numbers of physical droplets, on the order of 10^6 or more [143], need to be tracked making such simulations computationally demanding. In order to reduce the cost statistically similar groups of droplets are tracked by a single computational "parcel" [135, 148, 4]. The center of mass of

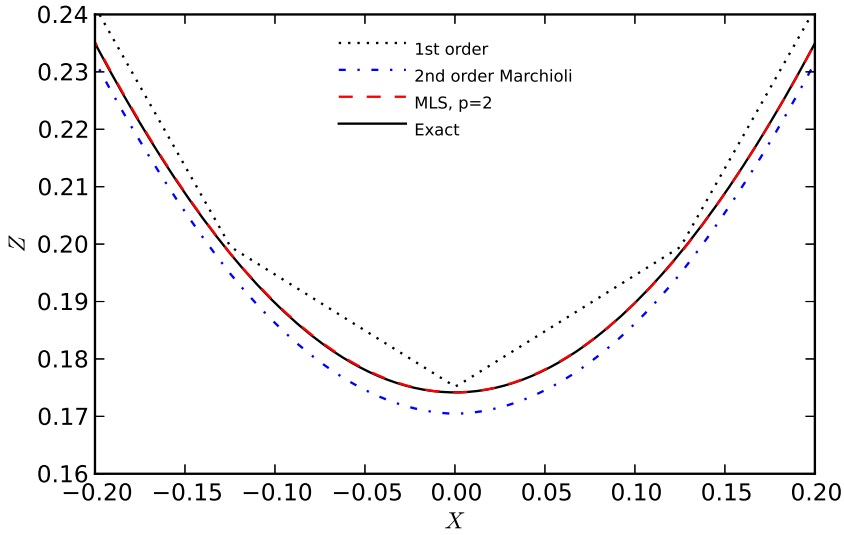

Figure 12 Comparison of Eulerian to Lagrangian interpolation methods on a steady two-dimensional sinusoidal flow.

the parcel is tracked with all constituent droplets assuming the properties of the parcel. The equations of motion for the Lagrangian phase droplets, Eq. (74)–(76), are applied to the parcel instead of an individual droplet. This approach captures the global features of droplet dispersion and combustion while saving substantial computational cost, though errors are incurred. The magnitude of these errors depends largely on the flow conditions and how many physical droplets are grouped into each computational parcel [203]. The source terms of Eq. (93) are modified to include the number of physical particles in the computational parcel.

$$\begin{pmatrix} \widetilde{\dot{\rho}_s} \\ \widetilde{\dot{F}_{s,i}} \\ \widetilde{\dot{Q}_s} \\ \widetilde{\dot{S}_{i,k}} \\ F_d \end{pmatrix} = \frac{1}{\hat{\Delta}^3} \begin{pmatrix} \sum n_d \dot{m}_d \\ \sum n_d \left[\dot{m}_d u_{i,d} - m_d \dot{u}_{i,d}\right] \\ \sum n_d \left[\dot{m}_d h_{v,s} - h_d \pi d_d^2 \left(\tilde{T} - T\right)\right] \\ \sum n_d \dot{m}_d \\ \sum n_d \left[\widetilde{\dot{F}_{s,i} u_i} - \widetilde{\dot{F}}_{s,i} \widetilde{u}_i\right] \end{pmatrix}. \tag{225}$$

Here, n_d is the number of particles per parcel, $u_{i,d}$, ρ_d, r_d are the velocity, density and radius of the i^{th} particle, respectively. The summation above is over all parcels within the computational volume defined by $\hat{\Delta}^3$. Some method of Lagrangian phase source

term distribution or smoothing is necessary to avoid numerical instabilities [136]; here the source terms are distributed to the computational cell containing the parcel and its 26 nearest neighbors using the same method as Patel et al [149].

The parcels are tracked until the representative particle size reaches a predefined cutoff radius at which point the parcel is completely evaporated.

4.9.1 Lagrangian parcel multiblock parallel communication implementation

The original parallel implementation of the Lagrangian phase inside the LESLIE code used the so-called gather-scatter communication approach [203]. This method uses a master-slave paradigm where the processor in the Lagrangian MPI communicator handles most of the bookkeeping operations. All processors involved in the simulation allocate enough memory for a predefined maximum number of computational parcels in the domain. At the beginning of each time step, the root processor scatters the information about all parcels to all processors. Each processor then loops over the entire parcel list to check each parcel to see if it is located within the physical domain of that processor. If the parcel is located within processor the numerical integration for that parcel will occur, if not, all global parcel arrays associated with that parcel are zeroed out within that processor. At the end of the time step, a reduction back to the root processor occurs and the root processor cycles through all the parcels and removes those that have evaporated or left the physical domain and reorganizes the global arrays.

Figure 13 shows a simplified diagram of a parcel crossing a block boundary. Assuming that Block 1 and Block 2 are located in different processors, Processor 1 and 2 respectively, the gather-scatter communication algorithm can be described in the following steps:

1. At $t = t_0$, the root processor sends out all the information, position, velocity, temperature, breakup information, etc, about the parcel to all processors.

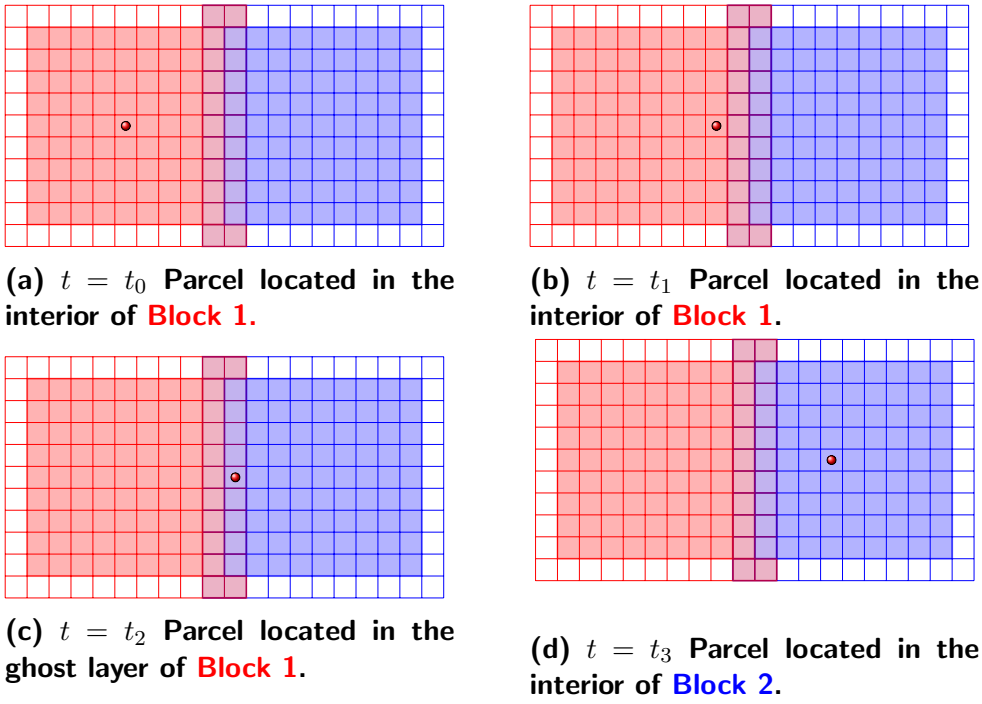

(a) $t = t_0$ **Parcel located in the interior of Block 1.**

(b) $t = t_1$ **Parcel located in the interior of Block 1.**

(c) $t = t_2$ **Parcel located in the ghost layer of Block 1.**

(d) $t = t_3$ **Parcel located in the interior of Block 2.**

Figure 13 Lagrangian parcel traversing a block boundary.

2. All processors check to see if the parcel is in their physical domain.

3. Processor 1 determines the parcel is located within its bounds and numerically integrates the parcel to the next time step, while Processor 2 zeros out all the values in its global array associated with the parcel.

4. Processor 1 and Processor 2 send all array information back to the root processor.

5. The previous steps are repeated at $t = t_1$, $t = t_2$ and $t = t_3$. At the end of $t = t_2$ the parcel moves into the ghost layer of Block 1 so at the beginning of $t = t_3$, Processor 1 will no longer flag the parcel as being located within its domain; instead, Processor 2 will begin to integrate that parcel.

One important thing to note about this communication method is parcel communication occurs at every time step even if parcels have not moved across processor boundaries.

The point-to-point communication method differs significantly in that no global arrays are maintained and communication of parcel array information only occurs if parcels cross processor boundaries. Each block maintains several doubly linked lists of parcels: one main list for parcels within the block, and a buffer list for each block with which communication occurs. The doubly linked list, implemented using modern Fortran capabilities of pointers and derived types, allows for easy insertion and removal of parcels as they evaporate, exit the domain or need to be communicated. When a parcel is in the interior cells of a block it resides in the main linked list, but if the parcel moves into a ghost layer during temporal integration it is moved into a buffer list corresponding to the block to which parcel will be sent. At the end of each time step all processors that could possibly have parcels communicate with each other the amount of data that will be sent to one another. This handshake occurs at every time step regardless of the number of parcels to be sent. If the size of the data to be sent is non-zero, the sending and receiving parcels prepare buffers and use direct communication calls via MPI to transfer the data. If neighboring blocks reside in the same processor, a simple memory copy is used rather than MPI. The communication buffers are then unpacked and the parcels added to the new block's main linked list.

This process can also be described for the simple diagram in Fig. 13, again assuming that Block 1 resides in Processor 1 and Block 2 inside Processor 2.

1. At $t = t_0$ and $t = t_1$, the parcel is in the main list of Block 1. Block 1 integrates the parcel in time. At the end of each step the handshake step occurs with Block 1 and Block 2 telling each other that there is nothing to be exchanged. No further data is communicated and Block 2 has no knowledge of the parcel.

2. At the end of $t = t_3$, the parcel is located in the ghost layer of Block 1 which corresponds to an interior cell of Block 2. Block 1 moves the parcel from the main list to the list that will be sent to Block 2. During the handshake, Block 1 indicates to Block 2 that data will be sent; the size of the data depends on the

type of parcel that is crossing the boundary, i.e., whether it is an evaporating parcel, whether it has breakup information, etc. Since the blocks are on different processors, buffers are prepared and the data is communicated. Block 2 unpacks the data and places the parcel into its main list.

3. At $t = t_4$, the parcel is in the main list of Block 2. Block 2 integrates the parcel in time. The handshake occurs and indicates no data will be communicated between Blocks 1 and 2.

The total amount of data that is communicated at each time step is significantly less with the point-to-point algorithm compared to the gather-scatter approach. This is amplified further for breakup simulations. With liquid jet-in-crossflow simulations only a small number of parcels in the entire domain are in the jet regime at a single time. For the simulations conducted in this study (see Chapter 6 for details), only 1 to 2% of all parcels in the domain are actively undergoing breakup at any give time. With the gather-scatter method, arrays for all the extra jet-in-crossflow information, initial diameter, initial Weber number, breakup times, etc., must be communicated for all parcels even if they are zeroed out. The point-to-point method only communicates this information when needed. Additionally, even within a block once a breakup parcel no longer needs the extra information, since it has undergone breakup or reached a minimum size, the extraneous information is deallocated for that parcel and thus no longer stored.

Even with the point-to-point communication algorithm, load balancing for Eulerian-Lagrangian simulations is made difficult based on the uneven physical spacing of the parcels in the domain. This is especially true for simulations involving injectors since parcels will generally be clustered there. To mitigate this, the user should attempt to create smaller blocks with fewer number of Eulerian cells near the injector to balance the Eulerian vs. Lagrangian load. Also, after the simulation has been run for some time, the spatial distribution of the parcels is incorporated into the load balancing

algorithm to rebalance the simulation across processors. Currently this does not occur during run time thus it requires the user to stop the simulation, rebalance and restart.

Scaling tests using millions of particles uniformly distributed in isotropic turbulence have been carried out and showed essentially linear scaling on thousands of cores [69]. The same test was conducted on various machines, all showing the ideal speedup. It was not possible to run this test case for that number of particles using the gather-scatter approach due to memory limitations.

4.10 Static mesh refinement

All the numerical methods presented is this work are formulated for structured, multiblock grids. Compared to unstructured grids, structured grids allow for simpler code structure and easier implementation of higher-order schemes but creating meshes for complex geometry is significantly more difficult. Clustering grid points in regions of interest without overly refining areas far away is also more challenging with structured, multiblock grids due to one-to-one grid point matching requirements. A technique was developed and implemented to relax the one-to-one grid point matching requirement across structured blocks allowing for static mesh refinement or coarsening.

There is no restriction is placed on the refinement/coarsening ratio or on the placement of nodes on the block interfaces. The number of points may or may not be the same along the interface and the nodes do not have to overlap. In order to make this possible, the procedure in both blocks must be identical and independent of the configuration of the neighboring block. This is distinct from other approaches, which either limit the refinement ratios possible [11, 10] and/or treat the coarse-to-fine procedure different than the fine-to-coarse procedure [222, 161]. The curent approach made it relatively simple to incorporate into existing code with minimal changes to the communication or numerical algorithm routines.

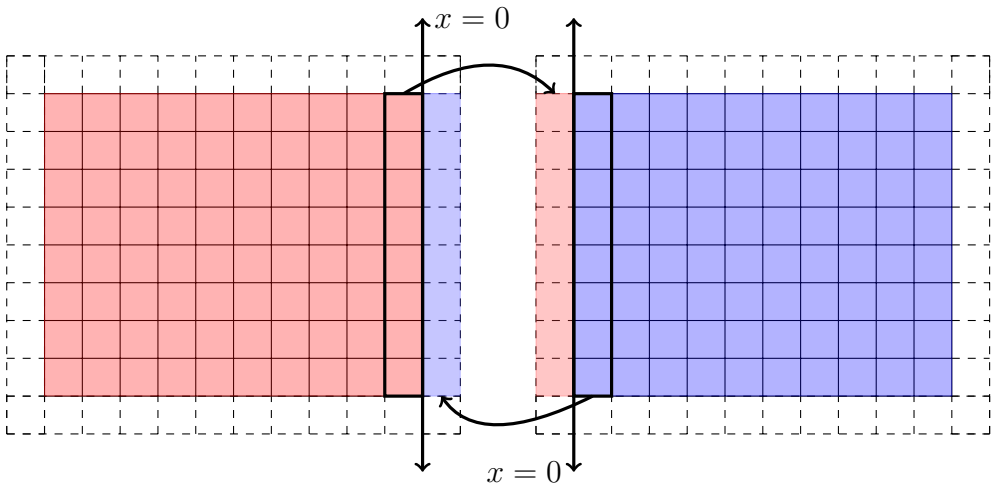

Figure 14 Ghost cell construction/population technique for a standard block-structured interface.

4.10.1 Preprocessing

The unstructured connectivities between the block interfaces is generated as a pre-processing step and stored in files for each block. For the structured block interfaces, a mapping is generated and stored for each neighbor that indicates the alignment of the computational coordinates. This mapping dictates the order of variable packing during message passing and are strictly one-to-one. For any unstructured interfaces in the simulation domain, there may be a one-to-one, one-to-many or many-to-one mapping. Only the blocks flagged during the grid generation process as having an unstructured interface require extra information. All other interfaces and blocks are still treated using the original structured approach.

The implementation of the static algorithm in an existing code needs to be simple and must retain the original performance of the code. As described previously, the original code uses a structured, multi-block framework where each grid block is surrounded by at least one layer of ghost cells that exactly match the cells on the interior of the neighbor block, as shown in Fig. 14. Higher-order scheme requre additional layers of ghost cells which are built in a similar fashion. At the end of each sub-step

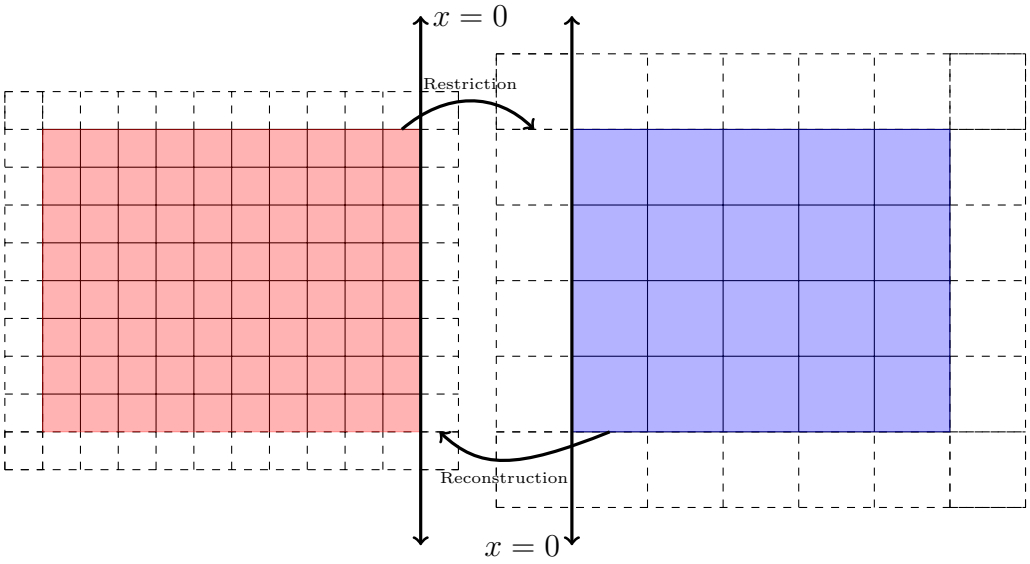

Figure 15 Structure of the block-unstructured grid containing refinement or coarsening. Note, the physical boundaries remain unchanged after coarsening, while the ghost cells are clearly larger and simply extrapolated from the block rather than copied from the neighbor.

in the time integration routine or after any numerical stabilization, the ghost cells are updated by communicating the values from the interior cells marked with a bold outline to the respective ghost layers as indicated by the arrows in Figure 14. These ghost layers provide the boundary conditions for each block and allow the same numerical method to be used at all interior cells. In contrast, the block-unstructured topology shown in Figure 15. For the block-unstructured interface, two procedures are required to populate the ghost cells in Figure 15. *Data restriction* is the process of moving information from the fine grid to the coarse grid ghost cells while the *data reconstruction* procedure is the process of moving information from the coarse grid to the fine grid ghost cells [161]. In the current approach, both procedures are treated the same. The preprocessing procedure uses a spatial tree structure to determine the point cloud of nearest neighbors to each ghost layer cell involved in the data restriction and reconstruction processes. These nearest neighbors are the cell-centers of the neighboring blocks. Within a block some points may require restriction from the

neighboring block while some may require reconstruction depending on the topology. Determining and detecting this is expensive, requiring the intersection of each cell volume with cells across the interface to be determined and the relative ratio of volumes to be computed. The expense can be mitigated if the refinement or coarsening ratios are fixed to known ratios between blocks but this limits the generality and usefulness of the method. The restriction and reconstruction procedures, which are detailed in the following section, are performed by the sending block before the communication phase of each sub-time step, just as the normal ghost cell filling technique. This is the only change required in the core of the underlying code.

4.10.2 Data restriction and reconstruction for large eddy simulations

Data restriction for large eddy simulations can be completed in three ways: interpolation, filtering, and a hybrid method which requires determining the underlying field. The hybrid approach requires the use of an approximate deconvolution method (ADM) [112, 204] to determine the unfiltered field on the fine grid and then filtering the resulting field onto the coarse grid. The filtering approach with and without ADM is attractive but the actual filter size must be known on both the fine and coarse sides. This is difficult to determine for anisotropic, non-uniform refinements and unless the LES is performed with explicit filtering, even if the filter sizes were known, the form of the filter is not [39]. The interpolation approach is selected here due to the difficulty and uncertainty in the other approaches. The data reconstruction process has two primary methods: interpolation and the ADM with filtering approach. Similar to data restriction, filtering is a complicated so interpolation is used for data reconstruction as well.

The approximation of a variable is indicated with $(\hat{\cdot})$ and the superscripts c and f indicate the coarse and fine grid respectively, the interpolation approach for data

restriction and data reconstruction of a Favré-averaged variable, $\widetilde{f}$, yield:

$$\widehat{\widetilde{f}^c} = L(\widetilde{f}^f) + E(\widetilde{f}^c, \widetilde{f}^f) \tag{226a}$$

$$\widehat{\widetilde{f}^f} = L(\widetilde{f}^c) + E(\widetilde{f}^f, \widetilde{f}^c) \tag{226b}$$

where $L()$ is the interpolation operator. The term $E()$ is the error, the form of which is unknown but the order of magnitude may be determined, and includes two components. The first is the error due to the interpolation operator. The second accounts for the difference between filtered values on the different grids. Here the error terms are neglected. The interpolation method is chosen such that the error due to the approximation is of a smaller order than the truncation errors inherent to the numerical scheme. The second component of the error term requires modeling and will be investigated in the future.

Numerous forms of the interpolation operator exist. The two methods implemented in the current code and discussed here, inverse distance weighting and weighted moving least squares, were chosen for their ease of implementation and adaptability to arbitrary orders of accuracy. This should reduce the influence of the neglected error terms.

4.10.2.1 Inverse Distance Weighting

Inverse distance weighting (IDW) is a general class of interpolation methods where points nearest the point of interest contribute more to the interpolation value than points far away. These methods are often also called Shepard's methods are well studied [3, 171, 194]. The method generates a continuous function that is well-bounded by the underlying data used. However, it is not as efficient as other approaches and suffers from isotropy in it's weighting due to dependance only on distance between points and the success of the method depends entirely on careful selection of the parameters [3]. Advantages of this method include the fact that it is non-oscillatory, inexpensive, and simple to implement. The interpolated value is computed at a point

$\mathbf{x_0}$ using N neighboring points [194]:

$$L\left(u\left(\mathbf{x}_0\right)\right) = \sum_{i=0}^{N} \frac{w_i(\mathbf{x}_i)}{\sum_{i=0}^{N} w_i(\mathbf{x}_i)} u_i\left(\mathbf{x}_i\right) \tag{227}$$

where

$$w_i(\mathbf{x}) = \frac{1}{\left(|\mathbf{x}_0 - \mathbf{x}_i| + \epsilon\right)^p} \tag{228}$$

are the weights based on the distance from the point of interest located at $\mathbf{x}_0$ to the point in the support domain located at $\mathbf{x}_i$. The ϵ is a small number added to the distance to ensure there is no singularity. The exponent p is a fall-off parameter used to further localize the weighting. Usually the fall-off parameter is set to two [3], but any value is permitted.

4.10.2.2 Weighted Moving Least Squares

The weighted moving least squares (MLS) interpolation method gives an interpolated value with:

$$L\left(u\left(\mathbf{x}_0\right)\right) = \sum_{i=0}^{N} w_i\left(\mathbf{x}_i\right) u_i\left(\mathbf{x}_i\right) \tag{229}$$

where the weights, w_i, are determined by:

$$w_i\left(\mathbf{x}_i\right) = W_i\left(\mathbf{x}_i\right) p\left(\mathbf{x}_i\right)^T A\left(\mathbf{x}_i\right)^{-1} p\left(\mathbf{x}_i\right) \tag{230a}$$

$$A\left(\mathbf{x}\right) = \sum_{i=0}^{N} W_i\left(\mathbf{x}_i\right) p\left(\mathbf{x}_i\right) p\left(\mathbf{x}_i\right)^T \tag{230b}$$

The basis function $p\left(\mathbf{x}\right)$ can be chosen freely. Here a polynomial basis of a user-specified order is used. For example a second-order polynomial basis is $p\left(\mathbf{x}\right) = [1, x, y, z, x^2, xy, xz, y^2, yz, z^2]$. The weighting functions $W_i(\mathbf{x})$ can likewise be chosen freely, including the use of the IDW weights from the previous section. All results with MLS use a Gaussian weighting function.

Both the inverse distance weighted and weighted least squares interpolation methods require the user to specify the neighborhood size around the nearest neighbor point. For the IDW method, this parameter can range from zero to the number of

points in the neighboring block. If zero is chosen, this puts the nearest neighbor value into the ghost cell and no interpolation is performed. For the MLS, the selection of stencil size has more limitations because the matrix in Eq. (230b) must be invertable and non-singular. Ideally, for points not near the block boundaries, the stencil size can be minimally one more than the order of the basis function. However, near corners, this will be too small and yield a singular matrix. Careful selection of the numerical matrix inversion technique can minimize problems due to near-singular matrices. Although relatively slow, singular value decomposition (SVD)-based matrix solution techniques are the safest way to solve the MLS matrix. The maximum number of points is again the size of the neighboring block. The stencil size should be kept as small as possible to minimize smearing of the fields.

This method has been used with success for several different flow conditions and geometry [72, 199, 104]. Additionally, lagrangian parcels can also be convected across refinement boundaries.

4.11 Conclusions

This work involved the implementation of many numerical methods and it is important to highlight unique contributions. The addition of the conservative finite difference methods inside the existing structured multiblock finite volume framework provides an example for other researchers interested in extending current CFD codes with new spatial integration methods. This allows for the reuse of many important code routines, such as thermodynamics, transport, chemical kinetics, input/output, etc, that are not directly associated with the spatial integration scheme.

While the concept and implementation of a hybrid compact/WENO finite difference scheme is not new, the combination of the necessary components, the compact central scheme in flow regions without discontinuities, the WENO-Z scheme near discontinuities, the high-order compact filter for numerical stabilization and adaptive

filter near discontinuities, the computation of viscous terms specifically to avoid odd-even decoupling and high-order SSPRK(5,4) time integration scheme, is unique. In addition, the application of such a solver to multiphase, reacting flow on non-uniform grids, which will be shown in Chapter 6, to the author's knowledge, has not been previously demonstrated.

CHAPTER V

NUMERICAL SCHEME COMPARISON

The central and upwind finite volume and finite difference schemes implemented in the LESLIE code are tested on a variety of non-reacting and reacting test cases in order to verify their implementation and compare their performance. In cases where analytic solutions are available errors are explicitly computed and performance is based on error versus computational effort. For other cases only qualitative comparisons are possible between the implemented schemes and against other published studies.

5.1 Comparison of numerical schemes on two-dimensional non-reacting test cases

To illustrate the differences between cost and accuracy of the numerical methods presented, three simple test cases are completed. Both use the Euler equations so only highlight differences in the inviscid flux schemes.

5.1.1 Linear Euler system

This test case is a special case where the Euler equations are linear and is useful for testing linear scheme convergence [244]. The initial conditions are

$$\begin{cases} \rho\left(x,y,0\right) = 1 + \frac{1}{2}\sin\left(\pi\left(x+y\right)\right), \\ u\left(x,y,0\right) = 1, \\ v\left(x,y,0\right) = 1, \\ p\left(x,y,0\right) = 1, \end{cases} \tag{231}$$

using periodic boundary conditions. The exact solution is

$$\begin{cases} \rho\left(x,y,t\right) = 1 + \frac{1}{2}\sin\left(\pi\left(x+y-2t\right)\right), \\ u\left(x,y,t\right) = 1, \\ v\left(x,y,t\right) = 1, \\ p\left(x,y,t\right) = 1, \end{cases} \tag{232}$$

Here the test case is run until $t = 0.2$ s. In a finite volume formulation, cell-averaged values are stored rather than point-wise values. If we assume rectangular cells (in 2D) and alignment of the physical x, y with computational coordinates i, j such that $x(i)$ and $y(j)$ the exact solution is

$$\overline{\rho}\left(x_i,y_j,t\right) = \frac{1}{A_{i,j}}\int_{x_{i-\frac{1}{2}}}^{x_{i+\frac{1}{2}}}\int_{y_{j-\frac{1}{2}}}^{y_{j+\frac{1}{2}}} 1 + \frac{1}{2}\sin\left(\pi\left(x+y-2t\right)\right)\,dxdy \tag{233}$$

evaluating the integral

$$\begin{aligned} \overline{\rho}\left(x_i,y_j,t\right) = \frac{1}{A_{i,j}}\Bigg\{ & A_{i,j} + \\ & \frac{1}{2\pi^2}\Big[-\sin\left(\left(x_{i-\frac{1}{2}} + y_{j-\frac{1}{2}} - 2t\right)\pi\right) + \\ & \sin\left(\left(x_{i+\frac{1}{2}} + y_{j-\frac{1}{2}} - 2t\right)\pi\right) + \\ & \sin\left(\left(x_{i-\frac{1}{2}} + y_{j+\frac{1}{2}} - 2t\right)\pi\right) - \\ & \sin\left(\left(x_{i+\frac{1}{2}} + y_{j+\frac{1}{2}} - 2t\right)\pi\right)\Big]\Bigg\} \end{aligned} \tag{234}$$

where the cell area is $A_{i,j} = \left(x_{i+\frac{1}{2}} - x_{i-\frac{1}{2}}\right)\left(y_{j+\frac{1}{2}} - y_{j-\frac{1}{2}}\right)$. A calorically perfect gas with a constant specific heat ratio, $\gamma = 1.4$, is used, i.e., the total energy is $E = p/\left(\gamma-1\right) + \frac{1}{2}\rho\left(u^2+v^2\right)$ and the equation of state, $T = p/\rho$.

Table 20 showing the L^2 errors and orders of accuracy for this test case show each scheme converges at the expected rate. The predictor-corrector FV scheme is run with the SSPRK(2,2) time integration scheme at CFL values of 1.0, 0.5, 0.25, 0.125, and 0.0625 for each of the grids in increasing grid size; the remaining schemes use the SSPRK(5,4). The time steps for this case are all sufficiently small so that overall error

Table 20 L^2 **errors and orders of accuracy for density for the linear Euler test case**

h	Predictor-Corrector FV O(2) Error	Order	MUSCL FV Error	Order	Compact CART66 FV Error	Order	Compact O(6) Error	Order	WENO-Z O(5)	
2/20	7.10×10^{-2}	–	1.58×10^{-2}	–	4.09×10^{-5}	–	4.08×10^{-5}	–	2.39×10^{-4}	–
2/40	1.82×10^{-2}	1.96	3.24×10^{-3}	2.29	1.85×10^{-7}	7.79	1.85×10^{-7}	7.79	7.08×10^{-6}	5.08
2/80	4.57×10^{-3}	2.00	8.22×10^{-4}	1.98	1.20×10^{-9}	7.27	1.19×10^{-9}	7.27	2.21×10^{-7}	5.00
2/160	1.14×10^{-3}	2.00	2.21×10^{-4}	1.90	1.38×10^{-11}	6.43	1.38×10^{-11}	6.44	6.91×10^{-9}	5.00

Table 21 Scaled CPU time for the linear Euler test case

h	Predictor-Corrector FV CPU Time	MUSCL FV CPU Time	Compact CART66 FV CPU Time	Compact FD O(6) CPU Time	WENO-Z FD O(5) CPU Time
2/20	1.00	5.85	3.17	1.99	13.40
2/40	14.55	75.06	37.12	24.22	191.07
2/80	210.43	1064.00	503.13	324.62	2846.05
2/160	3533.40	16928.77	7851.97	4893.78	45649.29

is attributed to the spatial scheme alone. CPU time and error are both important but efficiency is the best way to compare numerical methods. Efficiency in the context of time-dependent flow problems is measured by comparing error against CPU time for simulations run to the same physical time, seen here for the linear Euler test case in Figure 16. The closer each data point is to the origin the more efficient the scheme. For this case the Compact FD O(6) scheme is clearly the most efficient though because the test case is linear, the CompactCART66 FV almost matches the performance of the finite difference scheme. The increased cost is incurred during calculation of primitive variables at the cell faces needed in each computational direction to compute the fluxes. This operation is not necessary in the finite difference framework since fluxes are computed at grid points and reconstructed at the "cell" faces.

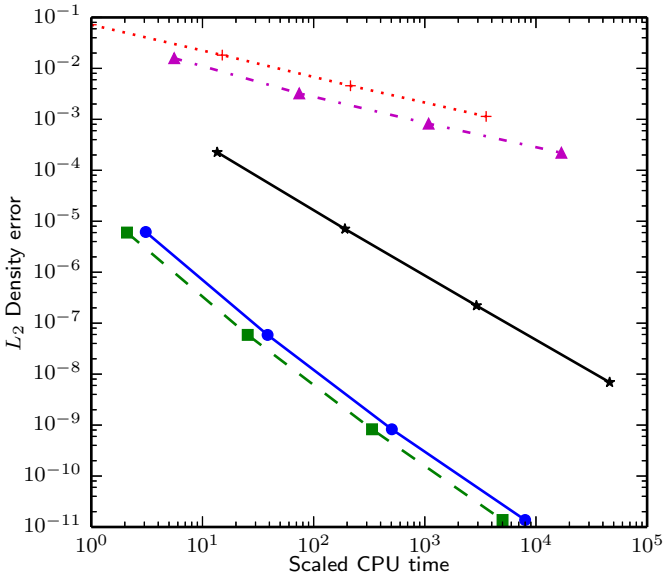

Figure 16 Computational efficiency comparison between schemes for the linear Euler equation test case, (··+··) Predictor-Corrector FV, (- · ▲ · -) MUSCL FV, (—⋆—) WENO-Z FD O(5), (—●—) CompactCART66 FV, (– – ■ – –) Compact FD O(6)

5.1.2 Passive scalar convection

Another linear test of scheme performance is convection of a passive scalar. The initial conditions are

$$\begin{cases} u\left(x,y\right)=1 \\ v\left(x,y\right)=1 \\ T\left(x,y\right)=1 \\ P\left(x,y\right)=1 \\ Y_1\left(x,y\right)=\exp\left[-r^2/\left(2\sigma^2\right)\right] \\ Y_2\left(x,y\right)=1-Y_1 \end{cases} \tag{235}$$

where $r^2=x^2+y^2$ and $\sigma=1$ on the domain $[-5,5]\times[-5,5]$ using periodic boundary conditions. The simulation is run until the vortex convects back to its original location at $t=10$ s.

The errors and convergence rates are shown in Table 22. Again for this test all schemes converge at their maximum rate; the CompactCART66 FV scheme is able to converge at sixth-order.

Table 22 L^2 **errors and orders of accuracy for density for the passive scalar convection test case**

		Predictor-Corrector FV O(2)		MUSCL FV		Compact CART66 FV		Compact FD O(6)		WENO-Z FD O(5)	
h	CFL	Error	Order	Error	Order	Error	Order	Error	Order	Error	Order
10/20	0.8	8.94×10^{-2}	–	3.48×10^{-2}	–	1.38×10^{-3}	–	1.39×10^{-3}	–	9.48×10^{-3}	–
10/40	0.4	3.25×10^{-2}	1.46	7.42×10^{-3}	2.23	2.72×10^{-5}	5.66	2.71×10^{-5}	5.67	4.84×10^{-4}	4.29
10/80	0.2	8.86×10^{-3}	1.88	1.06×10^{-3}	2.81	6.60×10^{-7}	5.36	6.59×10^{-7}	5.36	1.62×10^{-5}	4.90
10/160	0.1	2.23×10^{-3}	1.99	1.36×10^{-4}	2.97	3.57×10^{-8}	4.21	3.56×10^{-8}	4.21	5.15×10^{-7}	4.98

Table 23 Scaled CPU time for the passive scalar convection test case

h	CFL	Predictor-Corrector FV O(2) CPU Time	MUSCL FV CPU Time	Compact CART66 FV CPU Time	Compact FD O(6) CPU Time	WENO-Z FD O(5) CPU Time
10/20	0.8	1.00	2.06	4.84	1.96	12.59
10/40	0.4	15.59	28.11	62.34	23.89	183.72
10/80	0.2	254.15	393.58	890.45	327.54	2824.13
10/160	0.1	4330.47	6271.96	13990.67	5152.11	44906.38

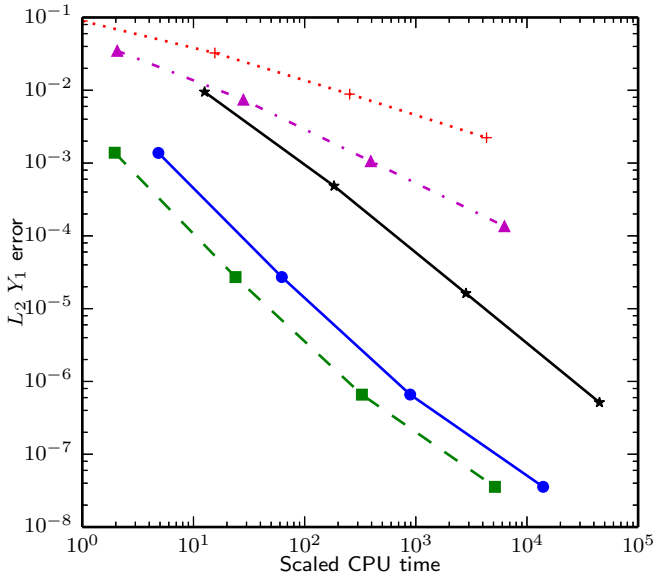

Figure 17 Computational efficiency comparison between schemes for the passive scalar convection test case, (··+··) Predictor-Corrector FV, (- · ▲ · -) MUSCL FV, (—⋆—) WENO-Z FD O(5), (—●—) CompactCART66 FV, (– – ■ – –) Compact FD O(6)

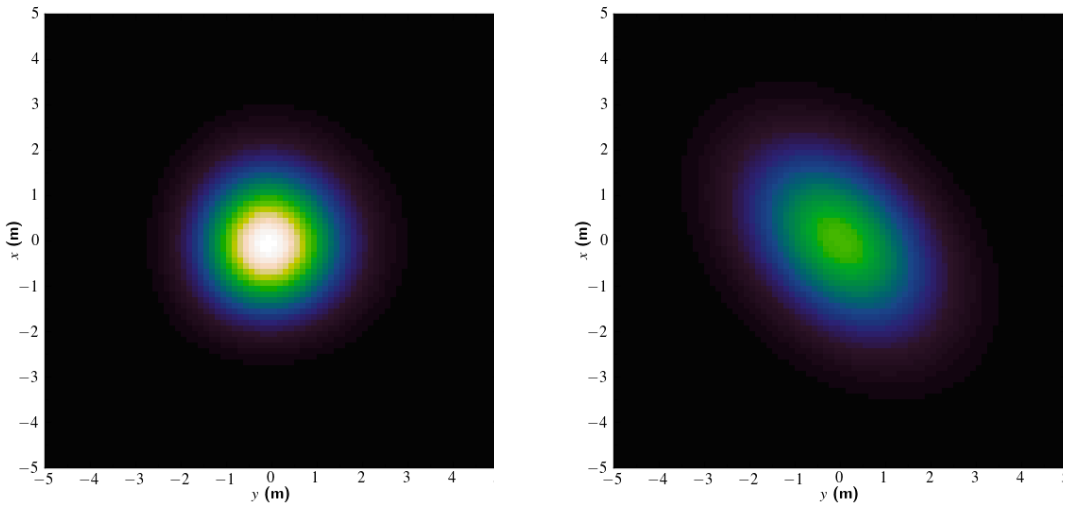

Figure 18 Cell-center contours of Y_1 on the $[80 \times 80]$ grid using the predictor-corrector FV scheme (left) and the predictor-corrector FV scheme with LEMLES (right).

This test can also be used to demonstrate one of the deficiencies of the LEMLES model, namely the numerical diffusion due to the splicing and re-gridding process. Figure 18 compares contours of Y_1 after one convective flow through time using the predictor-corrector FV scheme and the predictor-corrector FV scheme with LEMLES. The LEMLES solution is much more diffuse especially in the direction 90° off the convection direction. This non-grid-aligned convection test case is in fact the worst case scenario for LEMLES due to the nature of the LEMLES splicing flux ordering and first-in, first-out algorithm.

5.1.3 Two-dimensional vortex convection

An isentropic convecting vortex is used to test convergence on a non-linear problem. The initial conditions are [240]

$$\begin{cases} u\left(x,y\right) = 1 - y\dfrac{\varepsilon}{2\pi}e^{\frac{1}{2}\left(1-\left(x^2+y^2\right)\right)}, \\ v\left(x,y\right) = 1 + x\dfrac{\varepsilon}{2\pi}e^{\frac{1}{2}\left(1-\left(x^2+y^2\right)\right)}, \\ T\left(x,y\right) = 1 - \dfrac{\left(\gamma-1\right)\varepsilon^2}{8\gamma\pi^2}e^{1-\left(x^2+y^2\right)}, \end{cases} \tag{236}$$

with $\varepsilon = 5$ and on the domain $[0,20]\times[0,20]$ using periodic boundary conditions. The simulation is run until the vortex convects back to its original location at $t = 20$ s. The size of the domain is chosen to be large enough that boundary effects do not significantly increase the error or reduce the convergence at the highest resolution when using the most accurate scheme.

The errors and convergence rates are shown in Table 24. All of the finite volume schemes converge at second order for this non-linear case, though the difference in the magnitude of the errors is quite substantial. The finite difference schemes converge at orders greater than two demonstrating their efficiency advantages for non-linear problems as compared with this class of finite volume schemes. The WENO-Z scheme is much less efficient than the compact scheme for smooth flows which clearly illustrates the need for the hybrid approach of combining the two schemes for flows with discontinuities. Canonical test cases verifying the operation of the upwind (MUSCL and WENO-Z) schemes for flows with discontinuities are provided in Section 5.2.

5.2 Verification and validation of upwind schemes

Several test cases are provided here for the verification and validation of the upwind solvers for both finite volume and finite difference formulations used in the simulations presented in this paper.

Table 24 L^2 **errors and orders of accuracy for density for the 2D vortex test case**

		Predictor-Corrector FV O(2)		MUSCL FV		Compact CART66 FV		Compact FD O(6)		WENO-Z FD O(5)	
h	CFL	Error	Order	Error	Order	Error	Order	Error	Order	Error	Order
20/20	0.8	7.95×10^{-3}	–	7.81×10^{-3}	–	1.18×10^{-3}	–	9.65×10^{-4}	–	1.54×10^{-3}	–
20/40	0.4	3.55×10^{-3}	1.16	5.16×10^{-3}	0.60	1.77×10^{-4}	2.73	9.91×10^{-6}	6.61	1.72×10^{-4}	3.16
20/80	0.2	9.85×10^{-4}	1.85	9.88×10^{-4}	2.39	4.45×10^{-5}	1.99	1.07×10^{-7}	6.54	8.08×10^{-6}	4.41
20/160	0.1	2.47×10^{-4}	2.00	2.47×10^{-4}	2.00	1.11×10^{-5}	2.00	1.56×10^{-9}	6.10	2.80×10^{-7}	4.85

Table 25 Scaled CPU time for the 2D vortex test case

h	CFL	Predictor-Corrector FV O(2) CPU Time	MUSCL FV CPU Time	Compact CART66 FV CPU Time	Compact FD O(6) CPU Time	WENO-Z FD O(5) CPU Time
20/20	0.8	1.00	4.01	6.38	3.97	34.45
20/40	0.4	21.74	65.99	101.00	62.76	519.98
20/80	0.2	394.83	799.35	1452.85	917.37	7992.04
20/160	0.1	5832.54	11415.35	21229.69	13179.65	174778.50

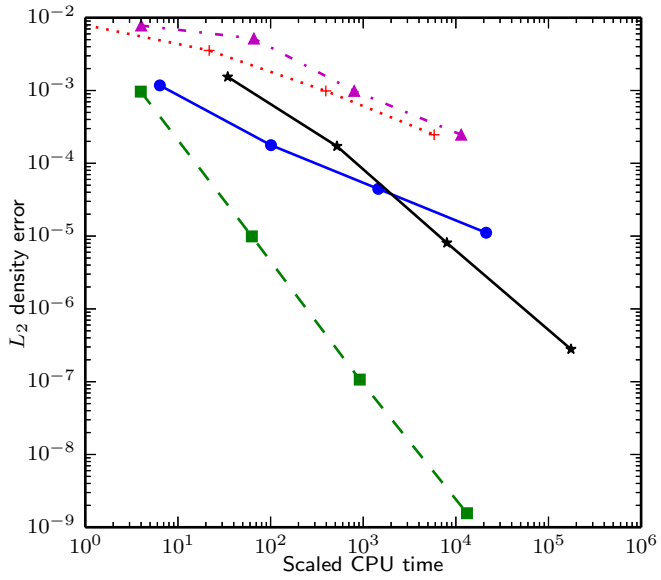

Figure 19 Computational efficiency comparison between schemes for the 2D vortex convection test case, (··+··) Predictor-Corrector FV, (- · ▲ · -) MUSCL FV, (—⋆—) WENO-Z FD O(5), (—●—) CompactCART66 FV, (– – ■ – –) Compact FD O(6)

5.2.1 Shock-entropy wave interaction test case

This test case consists of an one-dimensional shock propagating into a sinusoidal entropy wave [197]. A region of high frequency and amplitude oscillations occur immediately after the shock passes through. The high frequency oscillations decay further downstream of the shock, forming a region of long wavelength oscillations. These eventually steepen into shocks forming an N-wave pattern. To simulate this problem correctly, a method that accurately captures short wavelength smooth flow features as well as computing the shock propagation at the correct speed is needed. This makes this seemingly simple test particularly useful for evaluating the implementation and performance of numerical methods that will be used for simulations of shock/turbulence interaction.

The one dimensional domain, $x \in [0, 10]$ is discretized by 400 computational points with an initial shock positioned at $x = 2$. The initial conditions are given by:

$$\begin{cases} \rho = 3.857143, \\ u = 2.62936, \quad x < 2, \\ p = 10.33333 \end{cases} \qquad \begin{cases} \rho = 1 + 0.2 \sin 5x, \\ u = 0, \qquad\qquad x \geq 2 \\ p = 1 \end{cases} \tag{237}$$

The left boundary condition is set to supersonic inflow with post-shock conditions and the right boundary at $x = 10.0$ is a supersonic outflow.

The density profile at $t = 1.872$ plotted in Fig. 20 shows the hybrid Compact FD O(6) / WENO-Z FD O(5) method most accurately captures the location and amplitude of the oscillations. Note that the reference solution is computed using the WENO FD O(9) scheme with 10000 points.

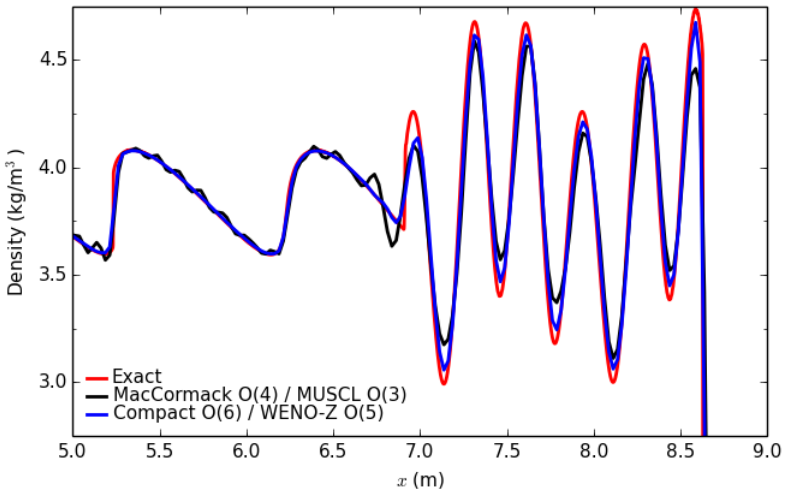

Figure 20 Density profile at $t = 1.872$ for several selected numerical methods.

5.2.2 Shock-vortex interaction

In this two-dimensional test case an isentropic vortex convects through a stationary Mach 1.1 shock [86]. The initial conditions of the vortex are

$$\begin{cases} u' = \varepsilon\tau \exp^{\alpha\left(1-\tau^2\right)} \sin\theta \\ v' = -\varepsilon\tau \exp^{\alpha\left(1-\tau^2\right)} \cos\theta \\ T' = -\frac{(\gamma-1)\varepsilon^2 \exp\left(2\alpha\left(1-\tau^2\right)\right)}{4\alpha\gamma} \\ S' = 0 \end{cases} \tag{238}$$

where entropy is defined as $S = \ln\left(P/\rho^\gamma\right)$, the equation of state is $T = P/\rho$ and the non-dimensional vortex radius is described by $\tau = r/r_c$ and $r = \sqrt{(x-x_c)^2 + (y-y_c)^2}$.

The stationary shock located at $x = 0.5$ has the following conditions,

$$(\rho, u, v, p) = \begin{cases} \left(1, 1.1\sqrt{\gamma}, 0, 1\right) & x < 0.5 \\ (1.169, 1.1134, 0, 1.245) & x \geq 0.5 \end{cases}. \tag{239}$$

The simulation is conducted on a domain of size $[0, 2] \times [0, 1]$. As is done in [86], the vortex strength parameter, ε, is set to $\varepsilon = 0.3$, the vortex radius is taken as $r_c = 0.05$ and the vortex decay parameter, α is set to $\alpha = 0.204$.

The grid used for this test has 251×101 grid points with uniform spacing in the y dimension and clustered around $x = 0.5$ using a Roberts transformation (see

transformation three, Eq. (5.221) in [210]). The top and bottom boundary conditions are periodic and the left boundary is set as a supersonic inflow and the Neumann outflow boundary conditions are imposed on the right side.

A constant time step of 5×10^{-4} is used for the MacCormack/MUSCL FV simulation which uses second-order accurate predictor-corrector time integration. A constant time step of 1×10^{-3} is used in combination with the Compact CART66/MUSCL FV and Compact O(6)/WENO-Z O(5) FD as these spatial schemes are combined with the SSPRK(5,4) time integration scheme [176].

Both of the hybrid finite volume schemes use $\epsilon_\rho = \epsilon_P = 0.001$ and $S_\rho^{th} = S_P^{th} = 0.1$ as sensor parameters, described in Section 4.5, used to switch between the central and upwind scheme. The upwind finite volume scheme uses second-order accurate MUSCL reconstruction, with characteristic wave speeds computed using Roe-averaged variables, and an HLLC approximate Riemann solver. At large discontinuities the reconstruction is forced to first order and the monotonized-central limiter is used to ensure the reconstructed variables are TVD. The compact CART66 FV scheme uses an eighth-order compact filter described in Section 4.8 with $\alpha = 0.49$.

For the finite difference simulations, $\epsilon_\rho = \epsilon_P = 0.01$. The power parameter for the finite difference WENO-Z scheme is set to $p = 1$, $\epsilon = 1 \times 10^{-5}$, Roe flux splitting is used for genuinely nonlinear characteristics and the Local Lax-Friedrichs flux for linearly degenerate characteristics.

Pressure contours at $t = 0.6$ are shown in Fig. 21. The finite difference solution captures the shock and maintains the vortex with the least amount of dissipation. There is less noise in the solution with the hybrid finite difference solution as well.

5.2.3 Double Mach reflection test case

This test case, first introduced by Woodward and Colella [237], features a Mach 10 shock in air initially at a 60° angle with a reflecting wall and passing through the

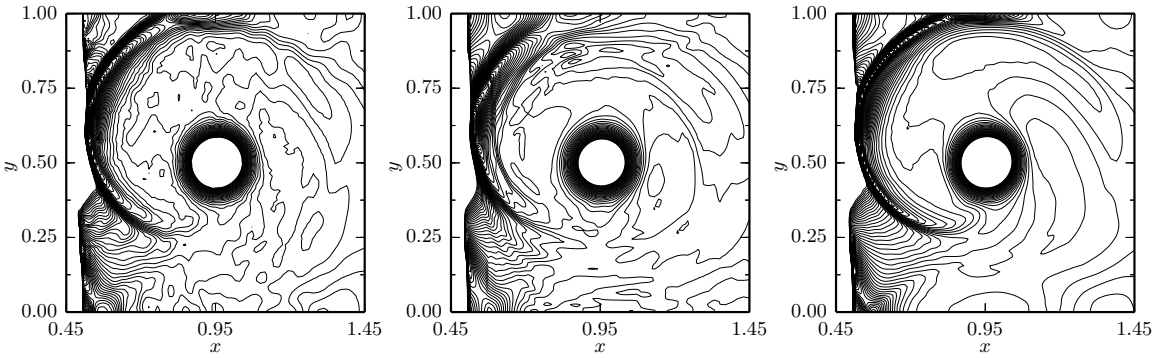

Figure 21 Ninety pressure contours from 1.19 to 1.37 of the 2D shock-vortex interaction problem at $t = 0.6$ using the Predictor-Corrector / MUSCL finite volume scheme (left), the CompactCART66 / MUSCL finite volume scheme (middle) and the Compact O(6) / WENO-Z O(5) finite difference scheme (right)

point $x, y = 1/6, 0$. The specific heat ratio is $\gamma = 1.4$ and the exact initial conditions are:

$$\begin{pmatrix} \rho \\ u \\ v \\ p \end{pmatrix} = \begin{cases} \begin{pmatrix} 8 \\ 8.25\cos\pi/6 \\ -8.25\sin\pi/6 \\ 116.5 \end{pmatrix} & x < 1/6 + y\tan^{-1}\pi/3 \\ \begin{pmatrix} 1.4 \\ 0 \\ 0 \\ 1 \end{pmatrix} & x \geq 1/6 + y\tan^{-1}\pi/3 \end{cases} \tag{240}$$

on a domain of $[0, 4]\times[0, 1]$. The left hand side and bottom region between $x = [0, 1/6)$ boundary conditions are supersonic inflows set to the post-shock conditions. The right hand boundary is a supersonic outflow. The bottom part of the domain, $x \geq 1/6$, is a reflective slip wall. The top boundary is time-dependent and set to the exact motion of initial shock wave.

Three hybrid numerical methods are tested with similar parameters used as with the shock-vortex test case. Each method is tested on three different grids: 100×400, 200×800 and 400×1600 cells with uniform spacing in the x and y directions.

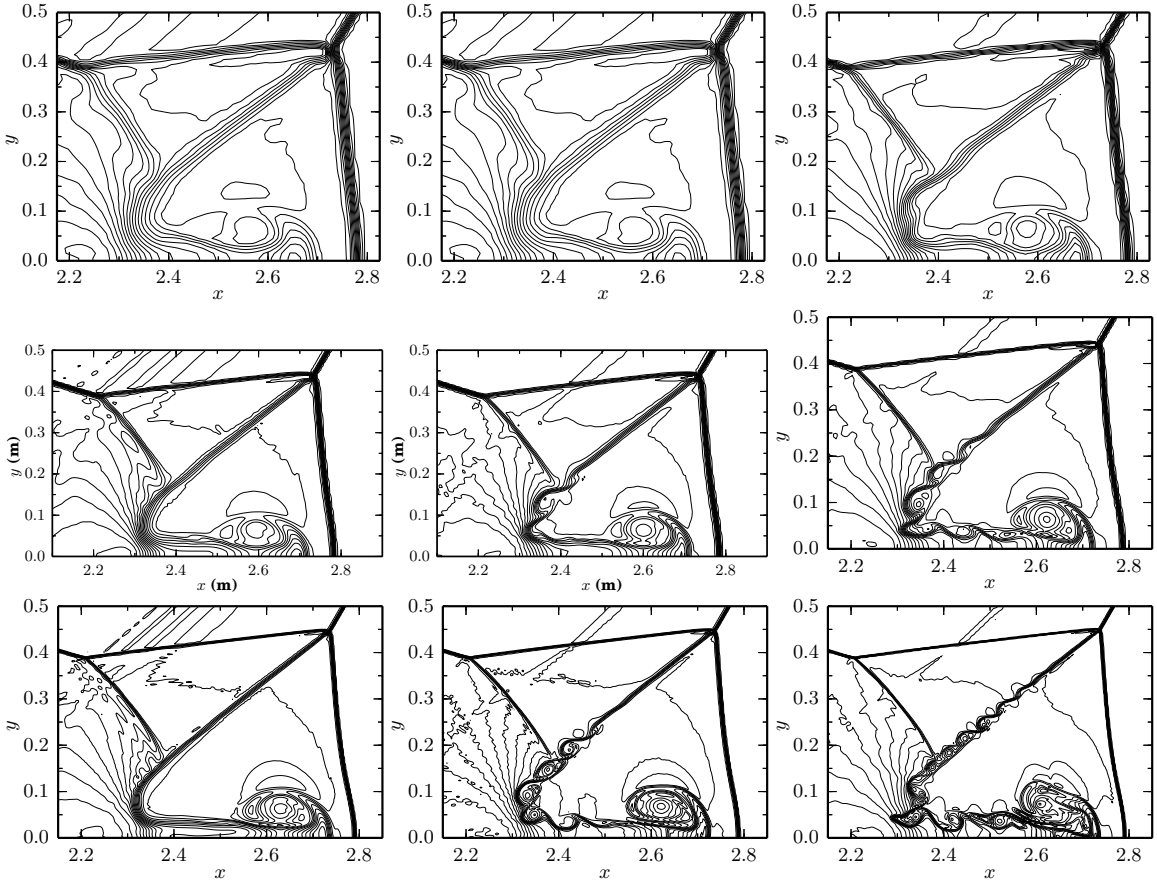

Figure 22 Thirty density contours from 1.731 to 20.92 of the double Mach reflection problem at $t = 0.2$ using three schemes, the Predictor-Corrector / MUSCL finite volume scheme (left column), the CompactCART66 / MUSCL finite volume scheme (middle column) and is the Compact O(6) / WENO-Z O(5) finite difference scheme (right column) on three different grid resolutions $\Delta x = \Delta y = 1/100$ (top row), $\Delta x = \Delta y = 1/400$ (middle row) and $\Delta x = \Delta y = 1/800$ (bottom row).

As the numerical dissipation decreases, either by using a higher-order scheme or increasing the grid resolution, the number of visible features in the region around the double Mach stems increases. These results are similar to those observed by Castro, Costa and Don [19] who tested WENO-Z finite difference schemes at different orders of accuracy and grid resolutions. Comparing the current results in Figure 22 to Figure 10 of Castro et al. [19]), qualitatively the hybrid CompactCART66/MUSCL FV and Compact O(6)/WENO-Z O(5) FD density contours look similar to the pure WENO-Z O(9) and O(11), respectively, which highlights the advantages of using a low dissipation central scheme away from discontinuities.

5.2.4 Shock-mixing layer interaction

The final test case used to evaluate and compare the hybrid central/upwind schemes is the case of an oblique shock interacting with a viscous shear layer [240]. A 12° oblique shock enters the rectangular 200×40 domain from the upper left corner and interacts with the incoming spatial shear layer with a convective Mach number

$$M_c = \frac{u_1 - u_2}{c_1 + c_2} = 0.6. \tag{241}$$

The mean inflow profile at the left boundary is

$$u = 2.5 + 0.5 \tanh(2y) \tag{242}$$

which gives an upper stream velocity $u_1 = 3$ and a lower stream velocity of $u_2 = 2$. Time-dependent velocity fluctuations are added to the v component of the inflow velocity according to

$$v' = \sum_{k=1}^{2} a_k \cos(2\pi k t/T + \phi_k) \exp\left(-y^2/b\right) \tag{243}$$

where the period $T = \lambda/u_c$, the wavelength $\lambda = 30$, $b = 10$ and

$$u_c = \frac{u_1 c_2 + u_2 c_1}{c_1 + c_2} = 2.68 \tag{244}$$

The coefficients for each mode are $a_1 = a_2 = 0.05$, $\phi_1 = 0$ and $\phi_2 = \pi/2$.

The bottom boundary is a reflective slip wall, the right side boundary is a supersonic outflow and the upper boundary is set to the post-oblique shock conditions. These conditions, and conditions for other regions in the domain, are given in the original reference [240] and repeated here in 26 for completeness. The reference density is the average of the upper and lower stream densities and the reference pressure is,

$$p_{ref} = \frac{(\rho_1 + \rho_2)(u_1 - u_2)^2}{2} \tag{245}$$

The Prandtl number is set as 0.72, the specific heat ratio $\gamma = 1.4$ and the Reynolds number is 500. The viscosity is computed using Sutherland's law.

Table 26 Flow properties for the shock-mixing layer test case [240]

Property	(1)	(2)	(3)	(4)	(5)
u-velocity	3.0000	2.0000	2.9709	2.9792	1.9001
v-velcoity	0.0000	0.0000	-0.1367	-0.1996	-0.1273
θ (°)	0.0000	0.0000	2.6343	3.8330	3.8330
Density, ρ	1.6374	0.3626	2.1101	1.8823	0.4173
Pressure, p	0.3327	0.3327	0.4754	0.4051	0.4051
Sound speed, c	0.5333	1.1333	0.5616	0.5489	1.1659
Mach number, M	5.6250	1.7647	5.2956	5.4396	1.6335

Note: (1) upper inflow stream, (2) lower inflow stream, (3) upper stream after oblique shock, (4) upper stream after expansion fan, (5) lower stream after shock wave

The simulations were conducted on a 320×80 cell grid with uniform spacing in the x-direction and stretching in the y-direction using,

$$y = \frac{L_y}{2} \frac{\sinh(b_y \eta)}{\sinh(b_y)} \tag{246}$$

where $L_y = 40$, $b_y = 1$ and η varies uniformly from -1 to 1.

The upwind finite volume scheme settings used in combination with the predictor-corrector finite volume scheme are same as those used with the CompactCART66 finite volume scheme.

For the finite difference calculations the WENO-Z scheme with the power parameter $q = 1$ wherever the upwind scheme is switched on. Fluxes are split using the Roe scheme with the entropy fix and $\varepsilon = 1 \times 10^{-6}$. The hybrid sensor parameters are The central scheme is the compact O(6) method with the eighth-order compact filter, $\alpha = 0.49$

The predictor-corrector finite volume scheme is paired with a second-order explicit time integration method and the time step is set at $\Delta t = 0.05$. The other two hybrid methods again employ the SSPRK(5,4) method [176] with a time step of $\Delta t = 0.1$.

The results for all three simulations are shown in 23 at $t = 120$. The higher-order schemes show less dissipation at the oblique shock and less diffuse vortices

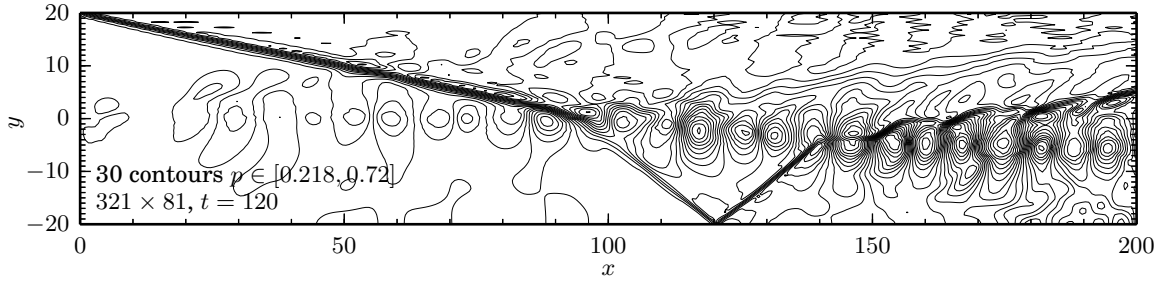

(a) Predictor-Corrector O(2) / MUSCL finite volume

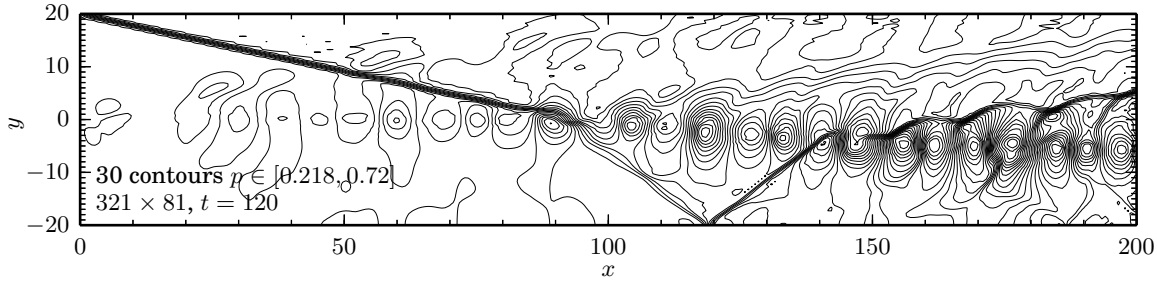

(b) CompactCART66 / MUSCL finite volume

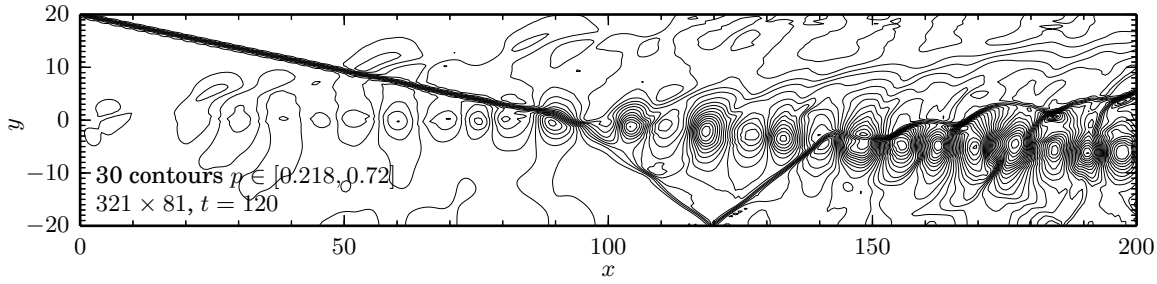

(c) Compact O(6) / WENO-Z O(5) finite difference

Figure 23 Ninety pressure contours from 1.19 to 1.37 of the 2D shock-mixing layer interaction problem at $t = 120$.

downstream. The solutions generated by the CompactCART66/MUSCL FV scheme and the compact O(6)/WENO-Z O(5) FD scheme for this case are more similar to one another than the other test cases previously discussed. As opposed to those cases, this shock-mixing layer case involves physical viscosity at a relatively low Reynolds number which will mask numerical viscosity when the scheme-related dissipation is small.

5.3 One-dimensional laminar flame

To verify that all schemes work properly for reacting flows, a one-dimensional laminar flame was simulated at three different grid resolutions. The inlet conditions were methane-air at $\phi = 0.7$ at an unburned temperature of $T_u = 800$ K. These conditions are the same as the premixed slot burner studied by Sankaran and coworkers [183, 182, 181, 184, 185].

5.3.1 Chemical mechanism

The chemical mechanism used for the current simulations was a reduced mechanism developed from the GRI-1.2 made of 13 species [182]: H_2, H, O, O_2, OH, H_2O, HO_2, CH_3, CH_4, CO, CO_2, CH_2O and N_2.

The mechanism in CHEMKIN-II CKWYP format was obtained from the authors [121] and implemented via the Cantera library. Modifications to the base Cantera library were carried out to allow any CHEMKIN-II CWKYP Fortran files to be used for both standalone Cantera simulations or using LESLIE. In addition, the performance of the methane-air mechanism used here was improved by reordering internal operations to remove costly divisions.

5.3.2 Thermodynamic and transport properties

Thermodynamic properties for individual species were computed using standard seven parameter CHEMKIN/NASA polynomials fits for constant pressure specific heat and enthalpy. Mixture properties were computed based on local mass fractions and molecular weights.

Transport properties were computed using a power law approach for viscosity, thermal conductivity related through the Prandtl number and mass diffusion coefficients are based on constant, but not equal species-specific Lewis numbers

$$\mu = \mu_0 \left(\frac{T}{T_0} \right)^{\beta}, \quad \lambda = \frac{\mu C_p}{Pr}, \quad D_k = \frac{\mu}{\rho Le_k Pr} \tag{247}$$

Table 27 Transport property constants and reference values

Parameter	Current Simulation	Reference [201]
T_0 (K)	298	298
μ_0 (kg/m-s)	1.87384×10^{-5}	1.82664×10^{-5}
Pr	0.703	0.708
β	0.665	0.7

This approach is similar to that used by Smooke and Giovangigli [201] for lean premixed flames with the viscosity computed directly via the power law instead of the thermal conductivity. Constants and reference values μ_0, T_0 and Le_k are tuned for the given system rather than use previously published values. A one-dimensional flame was computed in Cantera [68] using the same chemical mechanism that will be used for the full simulation but with mixture-averaged transport properties. The reference temperature was selected to be 298 K and the reference viscosity and exponent were determined using a non-linear least squares fitting procedure based on all points from the one-dimensional simulation. The Prandtl number was computed in a similar way using the tuned power law viscosity and the simulation data for specific heat and thermal conductivity. Finally the species Lewis numbers were fit using the same least squares method. The constants and reference values used in the current simulations are given in Table 27 as well as values from Smooke and Giovangigli for comparison. Similarly, species Lewis numbers are provided in Table 28.

The effect on flame speed and flame thickness for one-dimensional laminar flame simulations in Cantera are shown in Table 29. It should be noted that the diffusion velocities are estimated based on the simplified assumption of mass fraction gradients rather than compute mole fraction gradients similar to Eq. (42). Although using the tuned parameters provides only a slight improvement over the reference values, the tuning process is quite simple and fast and as such it is recommended for any premixed application where simple transport properties are desired.

Table 28 Species Lewis numbers

Species	Current Simulation	Reference [201]
H_2	0.296	0.30
H	0.177	0.18
O	0.691	0.70
O_2	1.072	1.11
OH	0.704	0.73
H_2O	0.793	0.83
HO_2	1.069	1.10
CH_3	0.969	1.00
CH_4	0.973	0.97
CO	1.077	1.10
CO_2	1.346	1.39
CH_2O	1.233	1.28
N_2	1.031	1.00

Table 29 Effect of transport property values on flame characteristics

	Mixture-Averaged	Current Simulation	Reference[201]
S_L (m/s)	1.815	1.812	1.839
δ_L (mm)	0.304	0.308	0.310

5.3.3 Initialization and boundary conditions

The solution from the steady-state solution obtained using Cantera was interpolated to the finite volume/difference grid cell center locations and used as the initial conditions. The full CFD simulation grid size is set to $L = 0.03$ m, which is approximately 100 times the flame thickness. Since the Cantera simulation provides a constant pressure solution and the full CFD simulations were conducted using a compressible code, there were some initial pressure waves that occur in the solution. Partially non-reflective boundary conditions were imposed at the inlet and outlet. The relaxation factor at the inlet was set at close to $1/\Delta t$ to provide nearly a hard inlet condition in order to have more control over the inlet conditions. The outlet relaxation factor constant of Eq. (134), was set at $\sigma = 0.25$ regardless of the simulation type.

5.3.4 Results

The three simulation methods of predictor-corrector FV, CompactCART66 FV, and Compact O(6) FD were again simulated here on three grid sizes, $\Delta x = 20\,\mu$m, $\Delta x = 60\,\mu$m, and $\Delta x = 100\,\mu$m. The smallest grid size was chosen based on the DNS solutions of the premixed slot burner simulations referenced earlier. At the coarsest resolution the density gradient at the flame front required the use of the hybrid central/upwind scheme to be numerically stable; the upwind scheme was only used at a few locations at the flame front. The central finite volume schemes were paired with the MUSCL upwind scheme whereas the finite difference scheme used the WENO-Z O(5) method. At the $\Delta x = 60\,\mu$m resolution, the flame can be computed using the pure central methods but small pressure oscillations occur with the CompactCART66 FV and Compact O(6) FD methods due to the application of the high-order filter at the flame front. The use of the hybrid methods at this resolution removed those small oscillations. The finite difference simulations used the fourth-order accurate method for computing the viscous terms with modifications to avoid odd-even decoupling with the "centered" coefficients found in Tables 10 and 11.

Each simulation ran for approximately one flow through time defined as $\tau = L/S_L$ and the flame speed and thickness computed using 50 snapshots from the second half of the flow through time. The flame speed was calculated by finding the location the temperature $(T_u + T_b)/2$ at two time instances to determine how far the flame traveled. The flame thickness was computed using the maximum gradient of temperature

$$\delta_L = \frac{T_b - T_u}{dT/dx|_{\max}}. \tag{248}$$

Table 30 shows the results for all the simulations. All schemes on all three grids match relatively well with the Cantera and reference solutions for both flame speed and thickness verifying that the schemes were implemented correctly for reacting flows. The results for the CompactCART66 FV and Compact O(6) FD schemes

Table 30 Flame speed for 1D laminar methane-air, $\phi = 0.7$, $T_u = 800$ K simulations with various numerical methods and grid spacings.

Method	Grid spacing, Δx [μm]	Flame speed, S_L [m/s]	Flame thickness, δ_L [mm]
Reference [182]	20	1.800	0.300
Cantera	–	1.812	0.308
Predictor-Corrector O(2) FV	20	1.819	0.312
CompactCART66 FV	20	1.811	0.308
Compact O(6) FD	20	1.812	0.309
Predictor-Corrector O(2) FV	60	1.839	0.323
CompactCART66 FV	60	1.812	0.328
Compact O(6) FD	60	1.812	0.324
Hybrid CompactCART66 / MUSCL FV	60	1.812	0.315
Hybrid Compact O(6) / WENO-Z O(5) FD	60	1.812	0.318
Hybrid Predictor-Corrector O(2) / MUSCL FV	100	1.812	0.383
Hybrid CompactCART66 / MUSCL FV	100	1.812	0.337
Hybrid Compact O(6) / WENO-Z O(5) FD	100	1.812	0.360

are very close as expected since in one dimension the finite volume scheme is truly high-order.

This test case is also useful to evaluate the various methods for computing the viscous terms for finite difference simulations as described in Section 4.6.2. When using the pure central schemes at the finer resolutions, there are no discernible difference between the repeated application of the first derivative operator and the improved methods. In this situation the high-order numerical filter is applied everywhere thus removing any instabilities [226]. At the coarsest resolution when the hybrid scheme is used, the numerical filter is disabled at the flame front and the effects of the viscous term treatment are evident. Figure 24 shows the velocity near the flame front for all three methods, no odd-even decoupling corrections, odd-even decoupling corrections with "centered" coefficients and odd-even decoupling corrections with "non-centered" coefficients. Without the use of the odd-even decoupling corrections small oscillations appear in the solution. More important than the small oscillations in velocity are the differences in the post-flame velocity and temperature profiles. Without any odd-even

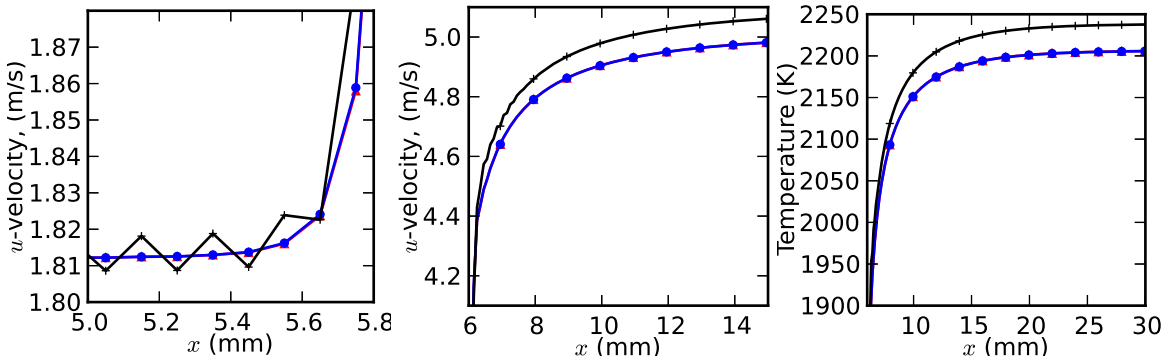

Figure 24 Velocity profile upstream of the flame front (left), downstream of the flame (middle) and post-flame temperature profile for hybrid Compact O(6) / WENO-Z O(5) finite difference simulations using no odd-even decoupling correction for the viscous terms (-+-), "centered" coefficients (–●–) and "non-centered" coefficients (–▲–).

decoupling corrections, the post-flame velocity and temperature are overpredicted. There are no discernible difference between the results using the different odd-even decoupling coefficients. The simulation using the "non-centered" coefficients took 27.5% longer than the simulation using the "centered" coefficients exemplifying the efficiency advantages of the latter coefficients detailed earlier.

5.4 Premixed reacting planar slot burner

The configuration under consideration is a premixed methane-air planar slot burner physically similar to that given in the original DNS paper [182] with the details repeated here for clarity. The preheated methane-air mixture enters the central slot at an equivalence ratio of 0.7 and a temperature of 800 K. The slot is surrounded on both sides by the complete combustion products of the inner methane-air mixture. At this equivalence ratio and temperature the flame thickness based on maximum temperature gradient is $\delta_L = 0.3$ mm. These are the same conditions and same chemical mechanism that were presented in the one-dimensional flame test, Section 5.3. The actual flow conditions tested here correspond with Case C described in [181]. Two of the available numerical methods will be used here: the hybrid predictor-corrector/MUSCL finite volume scheme and the hybrid compact O(6)/WENO-Z O(5)

finite difference scheme.

5.4.1 Computational Grid

The domain size slot width, h, is $L_x \times L_y \times L_z = 13h \times 12h \times 3h$ with $h = 1.8$ mm for this configuration. The structure of the LES grid is similar to the DNS grid; the cell size is uniform in the streamwise, x, and spanwise, z, directions and stretched in the crosswise, y, direction. The grid has uniform spacing from the centerline of the domain to $y \pm 2.5h$ then stretched uniformly to the domain edge. The number of cells in the crosswise direction is selected to limit stretching, $\Delta y_j/\Delta y_{j-1} - 1$, to less than 2.5%. Two different grid resolutions will be used to test the performance of the numerical methods. The finer of the two grids has $\Delta x_{LES} = 3\Delta x_{DNS} = 60\,\mu$m The total number of cells in the y direction based on the aforementioned stretching function is 180 so the resulting grid is $N_x \times N_y \times N_z = 400 \times 180 \times 60 = 4.32$ million cells meaning over a 20 times reduction in total spatial degrees of freedom (DOF) compared with the DNS finite difference calculation. At this resolution a maximum of 9% of the turbulent kinetic energy is unresolved at the grid level. The cell size of the coarser grid is $\Delta x_{LES} = 5\Delta x_{DNS} = 100\,\mu$m which is chosen based on turbulence resolution requirements; here a maximum of 22% of the turbulent kinetic energy is unresolved at the grid level. The grid contains of $N_x \times N_y \times N_z = 144 \times 118 \times 36 = 1.02$ million cells, an 85 times reduction in DOF compared to the DNS.

5.4.2 Boundary Conditions

The boundary conditions are periodic in the spanwise z direction and subsonic, partially-reflective boundary conditions based on the works of Yoo, Wang, Trouvé and Im [241] and Yoo and Im [242] are used at the inflow and outflow in the axial x direction as well as at the outflow boundaries in the cross stream y direction. The outflow relaxation coefficient is $\sigma = 0.58$ which is the value used by Rudy and Strikwerda [174]. They found this relaxation coefficient gave improved results as compared

with "optimal" value of 0.27 when used in combination with the MacCormack spatial integration scheme. The inflow relaxation coefficient for all variables is set to slightly less than $1/\Delta t$ resulting in a nearly reflective boundary condition. Larger relaxation coefficients which give greater control over the prescribed inflow variables are necessary when using time-dependent turbulent inflow.

5.4.2.1 Mean inflow conditions

The mean axial velocity profile was specified analytically as

$$\begin{aligned}\tilde{u}\left(0,y,z\right) =& U_c\left[1-\frac{1}{2}\left(\tanh\left(\frac{y+y_{sl}}{\delta_{sl}}\right)-\tanh\left(\frac{y-y_{sl}}{\delta_{sl}}\right)\right)\right]+\\ & U_j\left[\frac{1}{2}\left(\tanh\left(\frac{y+y_{sl}}{\delta_{sl}}\right)-\tanh\left(\frac{y-y_{sl}}{\delta_{sl}}\right)\right)\right]\end{aligned} \tag{249}$$

where $U_c = 25$ m/s, $U_j = 100$ m/s, $y_{sl} = 0.51$ mm and $\delta_{sl} = 0.03$ mm. The mean fluctuating velocity was specified as

$$\tilde{u}'\left(0,y,z\right) = \frac{U'}{2}\left[\tanh\left(\frac{y+y_{sl}}{\delta_{sl}}\right)-\tanh\left(\frac{y-y_{sl}}{\delta_{sl}}\right)\right] \tag{250}$$

with $U' = 33$ m/s and the other constants the same as the mean velocity. The mean progress variable profile was specified as

$$\begin{aligned}c\left(0,y,z\right) = 1-\frac{1}{4}&\left[1-\tanh\left(\frac{y-y_c}{\sigma_c}\right)\right]\\ &\times\left[1+\tanh\left(\frac{y+y_c}{\sigma_c}\right)\right]\end{aligned} \tag{251}$$

with $y_c = 1.05$ mm and $\sigma_c = 0.15$ mm.

The resulting Reynolds number defined as, $Re_{jet} = U_{jet}h/\nu$, is 1400. The shear layer thickness is the same as the flame thickness so at the two different grid resolutions there are 5 and 3 cells within the flame thickness/shear layer thickness, respectively. Many industrial LES grids are much coarser, relative to the flame thickness, than the grids used for this study. For this configuration if the grid resolution was decreased any further the shear layers would not be resolved which would inhibit the simulation from even properly capturing the fluid mechanics.

5.4.2.2 *Inflow turbulence*

The inflow turbulence for was the same as used in the DNS except it was filtered to the LES grid. The isotropic turbulence field was initialized with the Passout-Pouquet spectrum,

$$E(k) = 16\sqrt{\frac{2}{\pi}}u'^2\frac{k^4}{k_0^5}\exp\left(-2\frac{k^2}{k_0^2}\right) \tag{252}$$

with $u' = 25$ m/s and $l = 1.6$ mm. The turbulence was introduced to the domain with Taylor's hypothesis with $U_{conv} = 100$ m/s.

5.4.3 Initialization

Since both simulations are purely numerical, i.e., there are no representative physical simulations corresponding to these DNS, the reference slot width does not necessarily imply a physical slot of the same size. The DNS inflow conditions were carefully designed to anchor the flame outside the shear layer at the inflow [184]. The flow was initialized with a triangular flame with an estimated turbulent flame speed of 6 m/s and was simulated for a total of six flow through times, where $\tau_U = 0.24$ ms, with statistics taken over the final four flow through times. Both the initialization and physical simulation time are consistent with the DNS [181]. The finite volume method was run using the SSPRK(2,2) time integration scheme with constant $\Delta t = 6\,\mu$s and $\Delta t = 10,\mu$s for the grids with $\Delta x = 60\,\mu$m and $\Delta 100\,\mu$m, respectively. The finite difference scheme was run with the SSPRK(5,4) time integration method with larger time steps of $\Delta t = 15\mu$s and $\Delta t = 25\,\mu$s.

5.4.4 Results

A contour image of the progress variable $c = 0.65$, where c is computed as:

$$c = 1 - \frac{Y_{O_2} - 0.067}{0.224 - 0.067} \tag{253}$$

from both methods was created and compared with the DNS solution in Figure 25. The results from the finite difference method capture the small wrinkling better than

the finite volume solution since there is less numerical diffusion. The slot burner walls are in the images for reference only; in the LES images they are placed at the exact slot burner width but it is not known if the DNS slot walls are to scale. The domain size is known to be identical so the images were scaled based on the domain length. In all simulations, DNS included, there are small contours at $c = 0.65$ that are leaving the domain, thus allowing the length of the domain to be determined from these images. The fact that the flame surface at some time instances leaves the domain exit boundary may adversely affect the statistics, especially the mean length based on the $c = 0.65$ progress variable contour. More accurate statistics would be achieved by a longer domain though here, at least, the results are post-processed in a consistent manner with the DNS so the comparisons are still applicable. The mean flame lengths, shown in Figure 26, for all simulations are shorter than the DNS though the high-order finite difference solution is closer to the DNS value. The reaction rates in the core of the jet are over-predicted leading to the reduced flame length.

Figures 27 and 28 compare the results from the finite difference and finite volume schemes at both grid resolutions for several time and spanwise averaged quantities. At the $x = 0.005$ m location, all the LES results are similar with the fine resolution finite difference solution slightly closer to the DNS data on the centerline. Farther downstream at $x = 0.015$ m, the finite difference results are much closer to the DNS data than the finite volume results on the centerline. The maximum percentage centerline error for the fine grid finite difference results at this location is the error on CH_4 mass fraction of 21% compared with an error of 40% for the finite volume solution of the same grid. The centerline density errors for these two solutions are 0.1% and 9.7% on the $\Delta x = 60\,\mu$m grid for the finite difference and finite volume results, respectively.

Figures 29 and 30 show the flame thickness at $\Delta x = 60\,\mu$m and $\Delta x = 100\,\mu$m conditioned by the progress variable. The finite difference flame thickness results

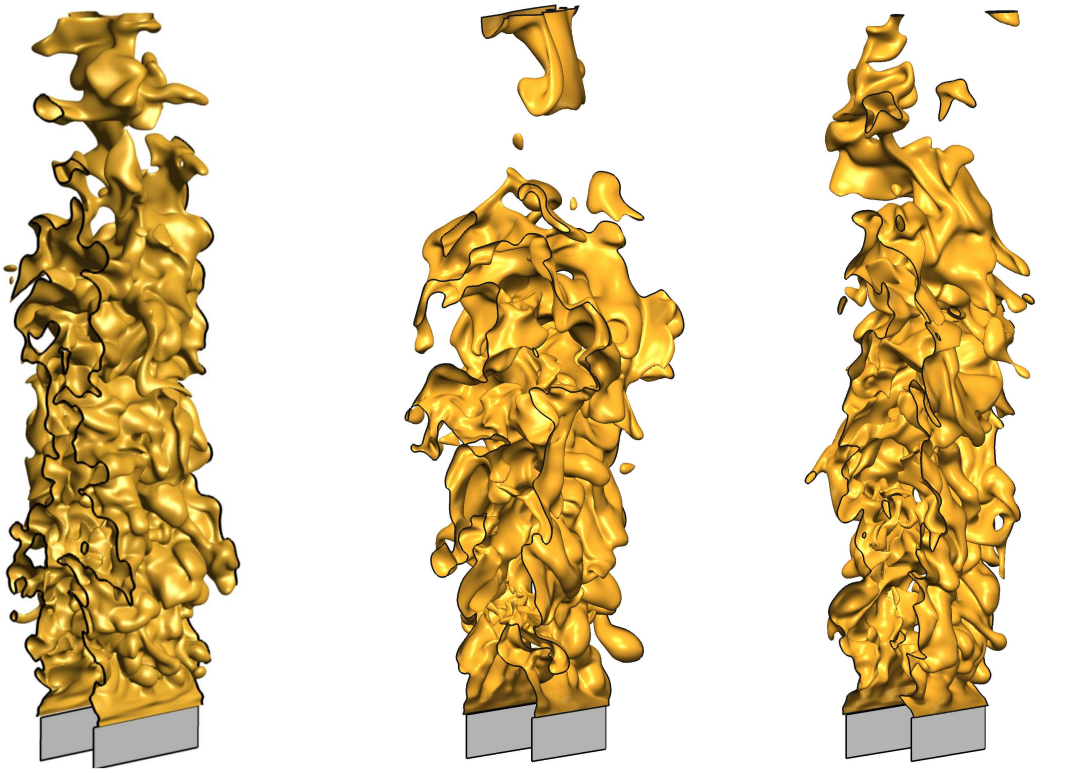

(a) DNS (b) Finite volume $\Delta x = 60\,\mu$m (c) Finite difference $\Delta x = 60\,\mu$m

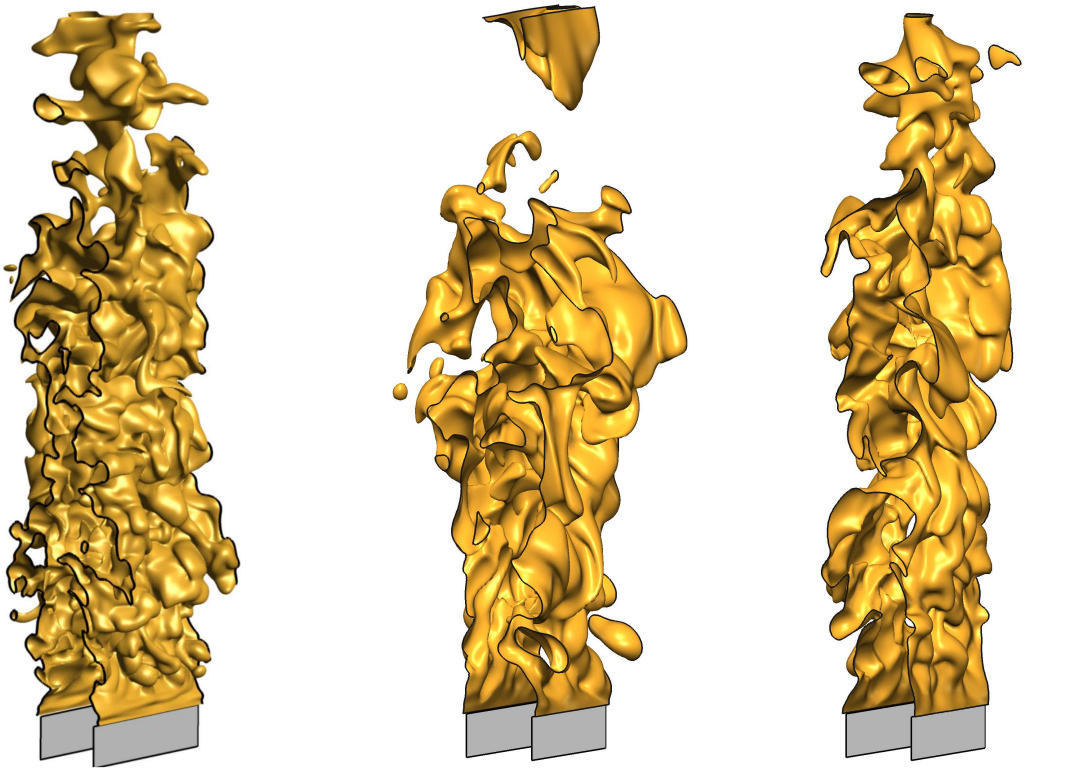

(d) DNS (e) Finite volume $\Delta x = 100\,\mu$m (f) Finite difference $\Delta x = 100\,\mu$m

Figure 25 Instantaneous iso-contours of $c = 0.65$ for Case C. (DNS flame image reprinted from [185] with permission)

compare more favorably to the DNS near the flame front, $c = 0.65$. At low values of the progress variable, $c \approx 0.25$, the finite volume results are closer to the DNS with the finite difference results over-predicting the flame thickness. Both LES under-predict the flame thickness on the coarser of the two tested grids.

These results show that the higher-order method does show some improvements over the lower-order method but the differences for this more complex case are smaller than the simpler test cases presented earlier. The previous test cases involved simple thermodynamics, a single species and no chemical reaction which avoids these possible sources of additional errors. Both methods yield decent results compared with the DNS especially considering that the boundary conditions were very close to the flame itself and the relaxation coefficient were not tuned for either scheme.

5.5 Summary and conclusions

The test cases presented here verify the operation of the numerical methods implemented in LESLIE and show how the scheme choice can affect the results. For simplified geometries the higher-order methods are preferred for accuracy and efficiency. It must also be noted that the higher-order methods generally involve more user input with regards to tunable parameters resulting in schemes that are less robust. Also, while the finite difference methods have been tested on these and numerous other test cases not presented here, further verification and validation on other configurations, especially those with more "industrial" geometry, needs to be completed.

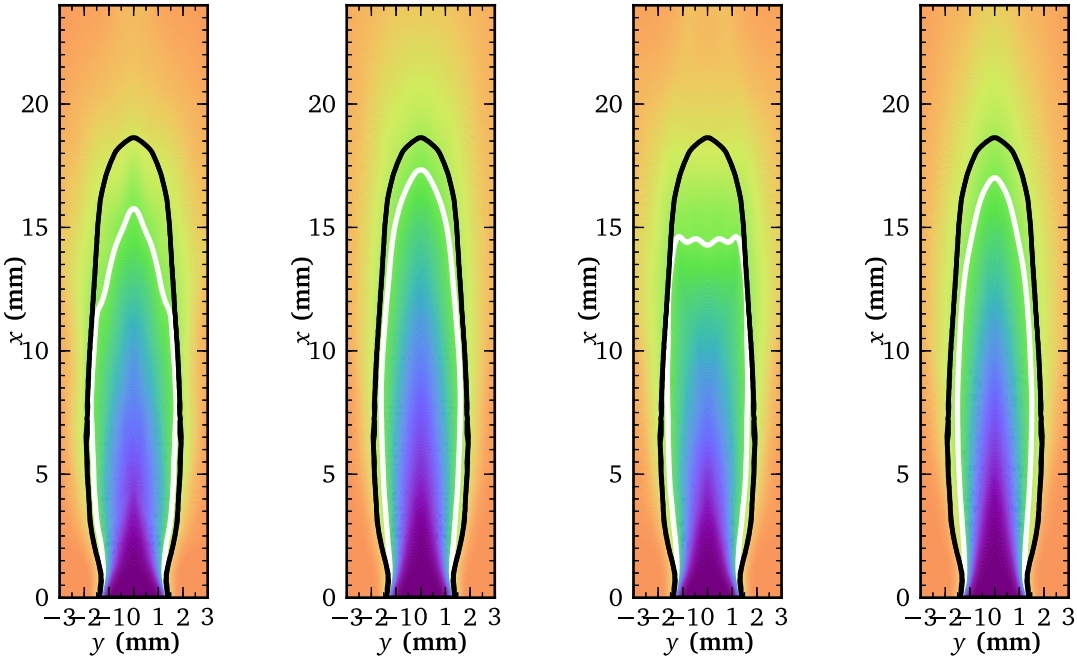

(a) Finite volume $\Delta x = 60\,\mu$**m** **(b) Finite difference** $\Delta x = 60\,\mu$**m** **(c) Finite volume** $\Delta x = 100\,\mu$**m** **(d) Finite difference** $\Delta x = 100\,\mu$**m**

Figure 26 Averaged contour plots of the progress variable for Case C. The solid lines show the progress variable contour $\tilde{c} = 0.65$ with the DNS in black and LES in white.

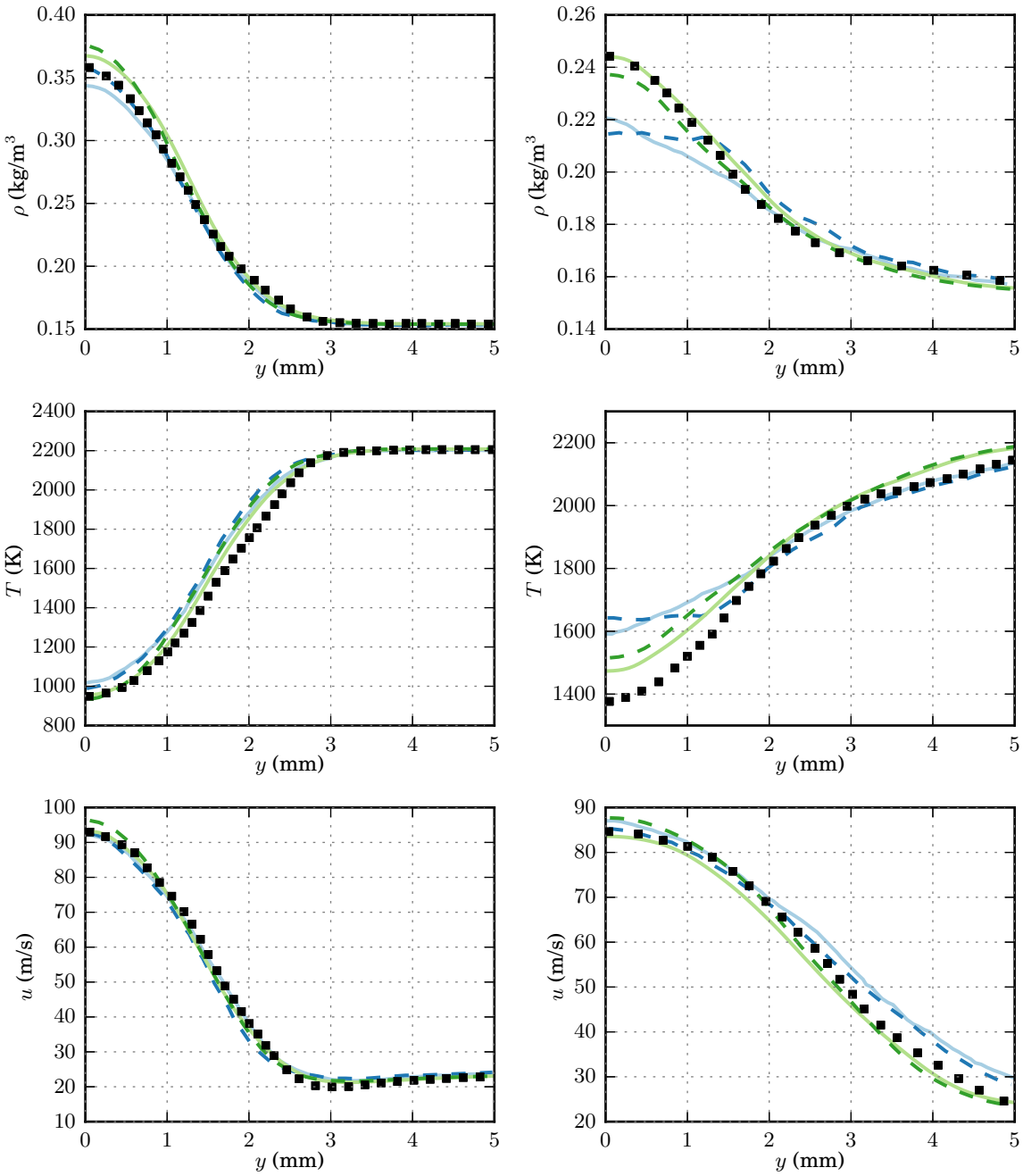

Figure 27 Time and spanwise averaged density, temperature and axial velocity at $x = 0.005$ m (left), and $x = 0.015$ m (right), (—) FD $\Delta x = 60\,\mu$m, (– –) FD $\Delta x = 100\,\mu$m, (—) FV $\Delta x = 60\,\mu$m, (– –) FV $\Delta x = 100\,\mu$m, (■) DNS (results from [213]).

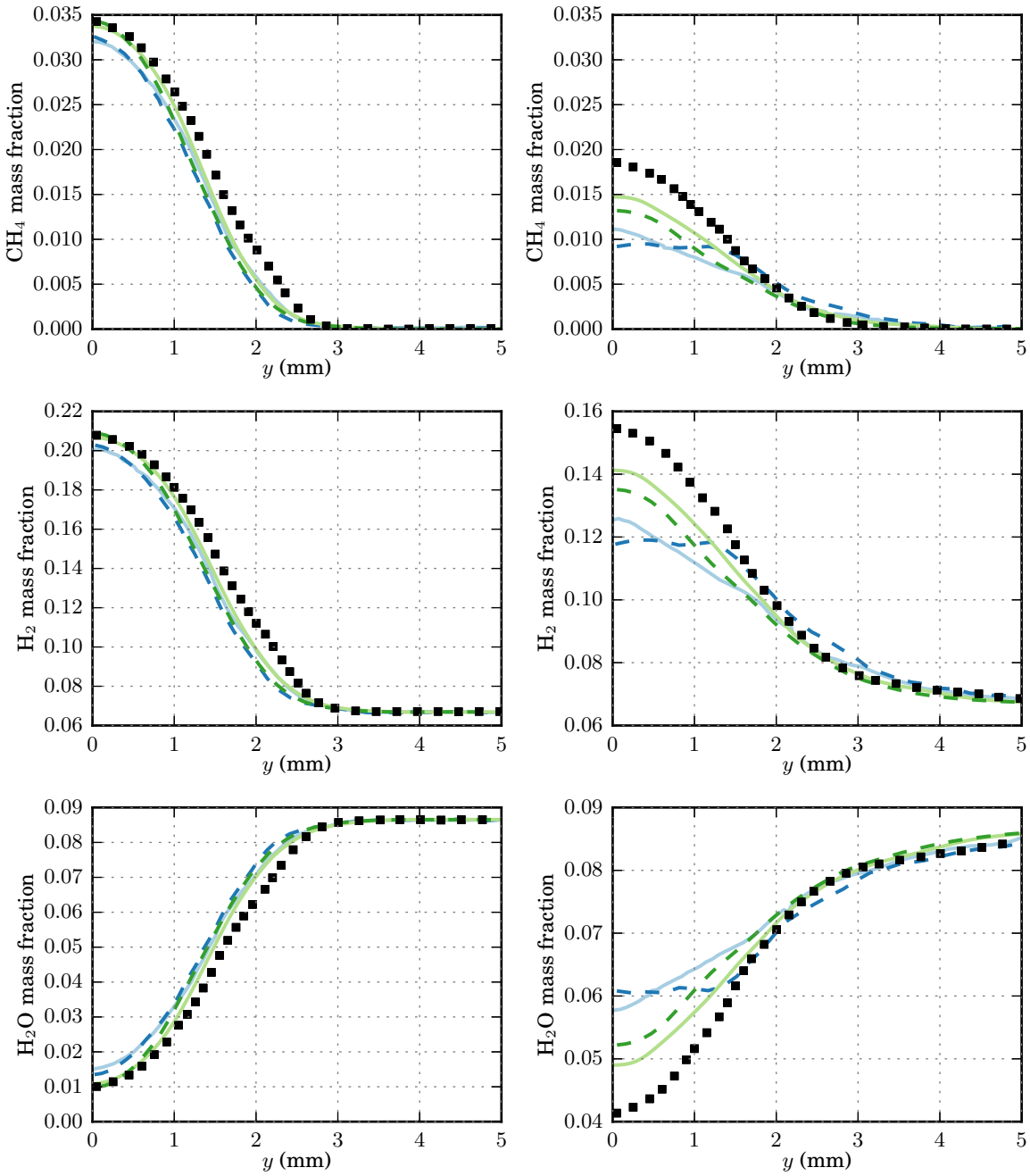

Figure 28 **Time and spanwise averaged CH_4, O_2 and H_2O mass fractions at $x = 0.005$ m (left), and $x = 0.015$ m (right), (—) FD $\Delta x = 60\,\mu$m, (– –) FD $\Delta x = 100\,\mu$m, (—) FV $\Delta x = 60\,\mu$m, (– –) FV $\Delta x = 100\,\mu$m, (■) DNS (results from [213]).**

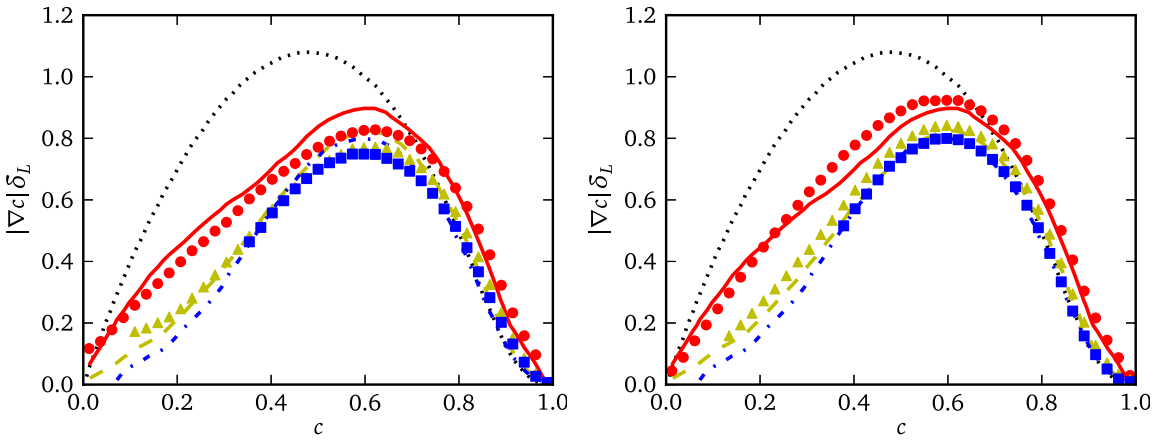

(a) Finite volume **(b) Finite difference**

Figure 29 Conditional means of $|\nabla c|\,\delta_L$ for Case C on the fine grid, $\Delta x = 60\,\mu$m, at three axial locations;
(·····) Laminar, (—) DNS 1/4, (- - -) DNS 1/2, (- · -) DNS 3/4, (●) LES 1/4, (▲) LES 1/2, (■) LES 3/4

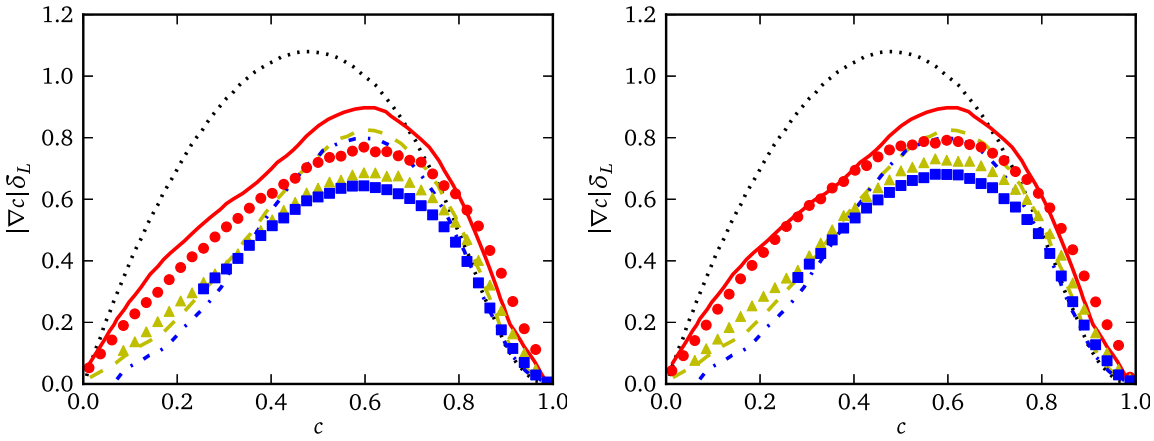

(a) Finite volume **(b) Finite difference**

Figure 30 Conditional means of $|\nabla c|\,\delta_L$ for Case C on the coarse grid, $\Delta x = 100\,\mu$m, at three axial locations;
(·····) Laminar, (—) DNS 1/4, (- - -) DNS 1/2, (- · -) DNS 3/4, (●) LES 1/4, (▲) LES 1/2, (■) LES 3/4

CHAPTER VI

SIMULATIONS OF A CLOSE-COUPLED NON-PREMIXED FLAMEHOLDER

6.1 Computational setup

The simulations are designed to study the single flame holder test facility located at the Georgia Tech combustion lab. The facility consists of a natural gas preburner, a pretest flow conditioning section and the flameholder/test section. The maxmimum test section inlet velocities and temperatures were 250 m/s and 1150 K, respectively. Optical access was available at a few locations upstream of the bluff body inside the test section and all axial locations downstream of the bluff body, but not at the preburner. The top and bottom walls were water cooled and the front and rear quartz windows were air cooled. Complete details of the test rig and instrumentation can be found elsewhere [33].

6.1.1 Combustor Geometry and Grid

The grid used for these studies contains 10.9 million cells split into 2356 structured blocks with refinement near all no-slip walls and the bluff body trailing edge with the block configuration shown in Figure 31. In the boundary/shear layers, $\Delta x_{\min} =$

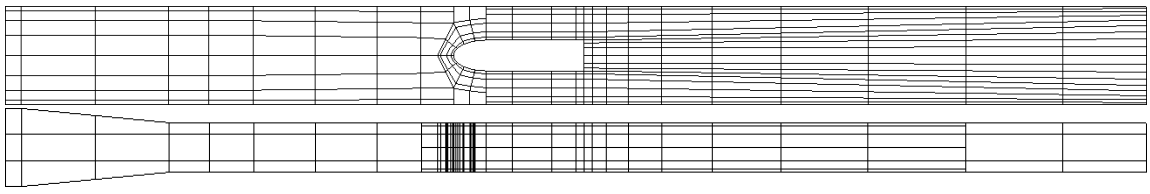

Figure 31 Multiblock structured grid containing 10.9 million cells split over 2356 blocks.

$\Delta y_{\min} = \Delta z_{\min} = 0.254$ mm which is approximately $10 - 20\,\eta$ based on estimates

using k^{sgs}. Figure 32 shows the resolved turbulent kinetic energy spectrum at a point in the shear layer one diameter aft of the bluff body trailing edge, which confirms that the grid resolution is acceptable by reasonably recovering an inertial range [148].

The entire physical domain from the exit of the preburner to the end of the test section, shown in Fig. 33a, is simulated in order to capture longitudinal acoustic modes, although for this particular rig experimental data suggests a lack of coupling between the large scale BVK fluctuations and the combustion chamber acoustics [33, 120]. The bluff body has a length 203.2 mm long, a height $D = 47.625$ mm, a spanwise depth of 76.2 mm, and an elliptical leading edge. The coordinate system is defined such at x is in the axial direction, y in the vertical direction and z in the spanwise direction with the origin in the center on the combustor centerline at the bluff body trailing edge. The test section height is 152.4 mm resulting in a blockage ratio of 31.25%. The only differences in the experimental and computational domains is the shape of the preburner exit. The experimental preburner is circular whereas the computational grid is rectangular in order to simplify the creation and maintain the quality of the structured multiblock grid. The shape difference is not expected to alter boundary conditions significantly especially in light of the uncertainty in the specification of boundary conditions explained later.

6.1.2 Boundary and Flow Conditions

The inflow boundary conditions are approximated from experimental data and set via an iterative process described in the next section. The nominal inflow velocity is $U_{ref} = 230$ m/s which gives $M = 0.347$ and a Reynolds number based on bluff body height of $Re = 7.2 \times 10^4$. The Strouhal number defined by $St = fD/U$ typically ranges from 0.2 to 0.29 for this type of flow configuration. Experimental data reported a value of $St = 0.25$ [33] and non-reacting simulation data here gives $f = 1266$ Hz or $St = 0.26$. The inflow chemical composition consists of products of complete

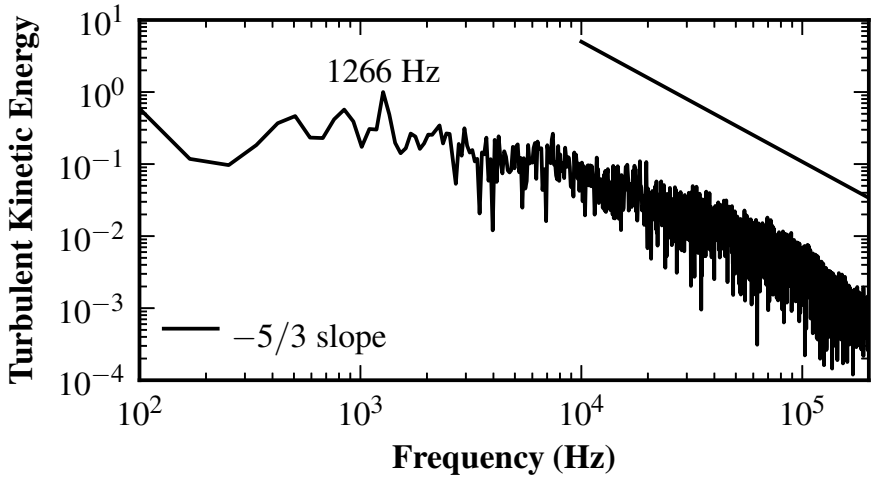

Figure 32 Normalized resolved turbulent kinetic energy in the shear layer at $x = D$ for non-reacting LES

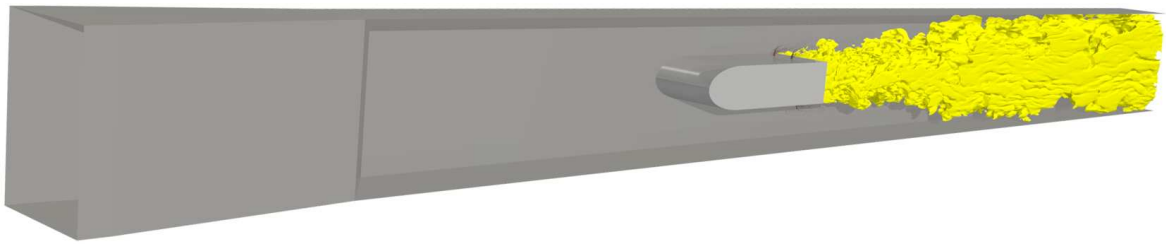

(a)

(b)

Figure 33 Single flameholder test rig, (a) View of entire computational domain with an isosurface of temperature showing flame structure typical of the $\phi_{\text{global}} \approx 0.5$ operating condition; (b) Detail view of bluff body showing the locations of discrete staggerd fuel injectors

lean combustion from the preburner at a temperature of 1150 K and a volumetric oxygen content of 14%. Partially non-reflective inflow and outflow boundary conditions are used [242] with synthetic turbulence injected using the method described by Smirnov, Shi and Celik [198]. The outlet pressure is set to the estimated conditions of slightly over one atmosphere, 107400 Pa. All wall boundary conditions are no-slip, constant temperature boundaries, with estimated temperatures of 850 K for the top and bottom walls and 900 K for the side walls. The bluff body trailing edge is set at 1150 K.

Liquid Jet-A fuel is injected from four 0.635 mm staggered injectors, two on the top of the bluff body at $z = -19.05$ mm and $z = 6.35$ mm and two on the bottom at $z = 19.05$ mm and $z = -6.35$ mm, all located 25.4 mm upstream of the trailing edge, as seen in Fig. 33b. The proximity of the discrete fuel injectors to the flame stabilization location gives rise to the "close-coupled" distinction. The injectors in the actual system are recessed into small cavities approximately 6.35 mm wide and 5 mm deep but these are not modeled in the computational system.

6.2 Chemical kinetics, thermodynamics and transport properties

The choice of a chemical mechanism for Jet-A is difficult since many simple mechanisms exist that can be tuned for a single premixed equivalence ratio or conversely, contain hundreds of species and reaction steps making them computationally intractable for three-dimensional simulations. The mechanism chosen here is seen a good compromise between these two disparate options. The chemical rates are determined from a two-step kerosene mechanism modified by correction functions known

as `2S_KERO_BFER` introduced by Franzelli, Riber, Sanjosé and Poinsot [53]. The mechanism is described by the following reactions:

$$\mathrm{KERO} + 10\,\mathrm{O_2} \Rightarrow 10\,\mathrm{CO} + 10\,\mathrm{H_2O} \tag{254a}$$

$$\mathrm{CO} + \frac{1}{2}\,\mathrm{O_2} \Leftrightarrow \mathrm{CO_2} \tag{254b}$$

with the rate coefficients written as:

$$k_{f,1} = A_1 f_1\left(\phi\right) e^{\left(-E_{a,1}/RT\right)} \left[\mathrm{KERO}\right]^{n_{\mathrm{KERO}}} \left[\mathrm{O_2}\right]^{n_{\mathrm{O_2},1}} \tag{255}$$

$$k_{f,2} = A_2 f_2\left(\phi\right) e^{\left(-E_{a,2}/RT\right)} \left[\mathrm{CO}\right]^{n_{\mathrm{CO}}} \left[\mathrm{O_2}\right]^{n_{\mathrm{O_2},2}} \tag{256}$$

The reaction rate parameters are listed in the table below.

Table 31 Reaction rate parameters [53]. Units in: mol, s, cm^3, J and cal/mol

	KERO oxidation		CO-CO_2 equilibrium	
Activation energy	4.15×10^4		2.0×10^4	
Pre-exponential factor	8.00×10^{11}		4.5×10^{10}	
Reaction	n_{KERO}	0.55	n_{CO}	1.00
exponents	$n_{\mathrm{O_2}}$	0.90	$n_{\mathrm{O_2}}$	0.50

The correction functions based on local equivalence ratio are:

$$f_1(\phi) = 2 \times \left\{ \left[1 + \tanh\left(\frac{\phi_{0,1} - \phi}{\sigma_{0,1}}\right)\right] + B_1 \left[1 + \tanh\left(\frac{\phi - \phi_{1,1}}{\sigma_{1,1}}\right)\right] + C_1 \left[1 + \tanh\left(\frac{\phi - \phi_{2,1}}{\sigma_{2,1}}\right)\right] \right\}^{-1} \tag{257}$$

$$f_2(\phi) = \frac{1}{2}\left[1 + \tanh\left(\frac{\phi_{0,2} - \phi}{\sigma_{0,2}}\right)\right] + \frac{B_2}{2}\left[1 + \tanh\left(\frac{\phi - \phi_{1,2}}{\sigma_{1,2}}\right)\right] + \frac{C_2}{2}\left[1 + \tanh\left(\frac{\phi - \phi_{2,2}}{\sigma_{2,2}}\right)\right] \times \left[1 + \tanh\left(\frac{\phi_{3,2} - \phi}{\sigma_{3,2}}\right)\right] \tag{258}$$

Table 32 Parameters for correction functions [53]

	$\phi_{0,j}$	$\sigma_{0,j}$	B_j	$\phi_{1,j}$	$\sigma_{1,j}$	C_j	$\phi_{2,j}$	$\sigma_{2,j}$	$\phi_{3,j}$	$\sigma_{3,j}$
$j=1$	1.173	0.04	0.29	1.2	0.02	7.1	1.8	0.18	-	-
$j=2$	1.146	0.045	0.00015	1.2	0.04	0.035	1.215	0.03	1.32	0.09

The local equivalence ratio, which is computed using the following method. First, all carbon atoms are summed $Y_C = \sum_{k=1}^{N_s} \left(N_{C,k} W_C / W_k\right) Y_k$, where $N_{C,k}$ is the number of carbon atoms in species k and W_C is the molecular weight of carbon. Next, a progress variable is calculated, $Z = \left(Y_C - Y_{C,Ox}\right) / \left(Y_{C,F} - Y_{C,Ox}\right)$, along with the stoichiometric progress variable, $Z_s = \left(1 + AFR_{\text{stoich}}\right)^{-1}$. The equivalence ratio is computed as $\phi = Z\left(1 - Z\right)^{-1}\left(1 - Z_s\right) Z_s^{-1}$. For this fuel and air, $AFR_{\text{stoich}} = 14.715$. Franzelli et al. validated the reaction mechanism with exhaust gas recirculation and it accurately predicts flame speeds and burnt gas temperatures with no modifications. This mechanism has also been used for non-premixed spray applications [76] so it is

expected to perform well for the current simulations. Past research has shown that two-step mechanisms perform better than single step mechanisms in applications similar to the current setup [57].

Kerosene/Jet-A is modeled as a single fuel represented by $C_{10}H_{20}$. The thermodynamic properties are described using the seven coefficient NASA polynomials of the form:

$$\frac{c_p^\circ}{R}(T) = a_0 + a_1 T + a_2 T^2 + a_3 T^3 + a_4 T^4 \tag{259}$$

$$\frac{h_p^\circ}{R}(T) = a_0 + \frac{a_1}{2} T + \frac{a_2}{3} T^2 + \frac{a_3}{4} T^3 + \frac{a_4}{5} T^4 + \frac{a_5}{T} \tag{260}$$

$$\frac{s_p^\circ}{R}(T) = a_0 \ln(T) + a_1 T + \frac{a_2}{2} T^2 + \frac{a_3}{3} T^3 + \frac{a_4}{4} T^4 + a_6 \tag{261}$$

The coefficents for two temperature ranges are given in Table 33. Note that the a_6 NASA polynomial coefficient for the high temperature range given in the paper is incorrect (Franzelli personal communication, 2011).

Table 33 NASA polynomial coefficient for kerosene for two temperature ranges [53]

Coefficient	$T \in [300; 1000]$ K	$T \in [1000; 5000]$ K
a_0	-4.15	22.0
a_1	1.28×10^{-1}	5.61×10^{-2}
a_1	-1.08×10^{-4}	5.61×10^{-5}
a_1	6.53×10^{-8}	-2.09×10^{-9}
a_1	-2.08×10^{-11}	-2.30×10^{-13}
a_1	$-2.83 \times 10^{+4}$	$-3.61 \times 10^{+4}$
a_6	$5.09 \times 10^{+1}$	$-8.60 \times 10^{+1}$

Since the mechanism is a global mechanism, a simple model for transport is used as well. The dynamic viscosity is computed as $\mu(T) = \mu_0 (T/T_0)^\alpha$. The thermal conductivity is $\lambda = \mu c_p / Pr_0$ and the diffusion coefficients are determined from the Lewis number, $Le_k = \lambda / (\rho c_p D_k)$, which is constant and for this case set to unity for all species. For this mechanism, $Pr_0 = 0.739$, $\mu_0 = 1.8456 \times 10^{-5}$ kg m^{-1} s^{-1}, $T_0 = 300$ K, $\alpha = 0.6695$. All thermodynamic and transport properties are computed using

resolved quantities, i.e., $\overline{c}_p\left(\tilde{T}\right)$, $\overline{\mu}\left(\tilde{T}\right)$, etc. The chemical reaction rates are computed using Cantera [68], which is coupled to the main CFD solver. The mechanism was originally implimented in Cantera and provided by the author (Franzelli personal communication, 2011) which provided the initial motivation to couple LESLIE with Cantera. This functionality has proven quite useful [75, 104, 202, 16]. Initially the thermodynamics and transport properties were also computed using the Cantera library but it was found to be much more computationally efficient to compute them inside LESLIE due to the requirements of passing data between the LESLIE data structures and the Cantera data structures. The performance penalty for computing thermodynamic properties in Cantera is relatively small but is quite significant for transport properties. The flame speed tests completed in the original work at several inlet temperatures and pressures were replicated here to ensure the mechanism was implemented properly and shown in Figure 34.

Liquid properties are computed by fitting experimental data [29] with various functional forms [36] in a manner similar to other CFD codes [232]. The functions and coefficients are listed in Table 34. Figure 35 compares the density and surface tension of Jet-A to other fuels.

Table 34 Jet-A property curve-fit parameters

Property	NSRDS Function [36]	a	b	c	d	e	f	T_c
ρ kg/m^3	5	64.9	0.255	680.0	0.294	-	-	-
p_v Pa	1	84.4	-7000.0	-9.95	1.6×10^{-5}	2.0	-	-
h_v	6	660.0	4.5×10^5	0.4	0.0	0.0	0.0	-
c_p	0	1758.183	-1.391	7.546×10^{-3}	0.0	0.0	0.0	-
h	0	-2699436.152	v1958.182	-0.6954	0.00251	0.0	0.0	-
$c_{p,g}$	7	1175.106	3762.167	1614.1	2658.045	742.0	-	-
μ	1	-18.1	1950.0	0.875	0.0	0.0	-	-
μ_g	2	2.64×10^{-8}	0.9487	71.0	0.	-	-	-
λ	0	0.1665	-1.75×10^{-4}	0.0	0.0	0.0	0.0	-
λ_g	2	-668.4	0.9323	-4.071×10^9	0.0	0.0	0.0	-
σ	6	680.0	0.0486	1.3095	0.0	0.0	0.0	-

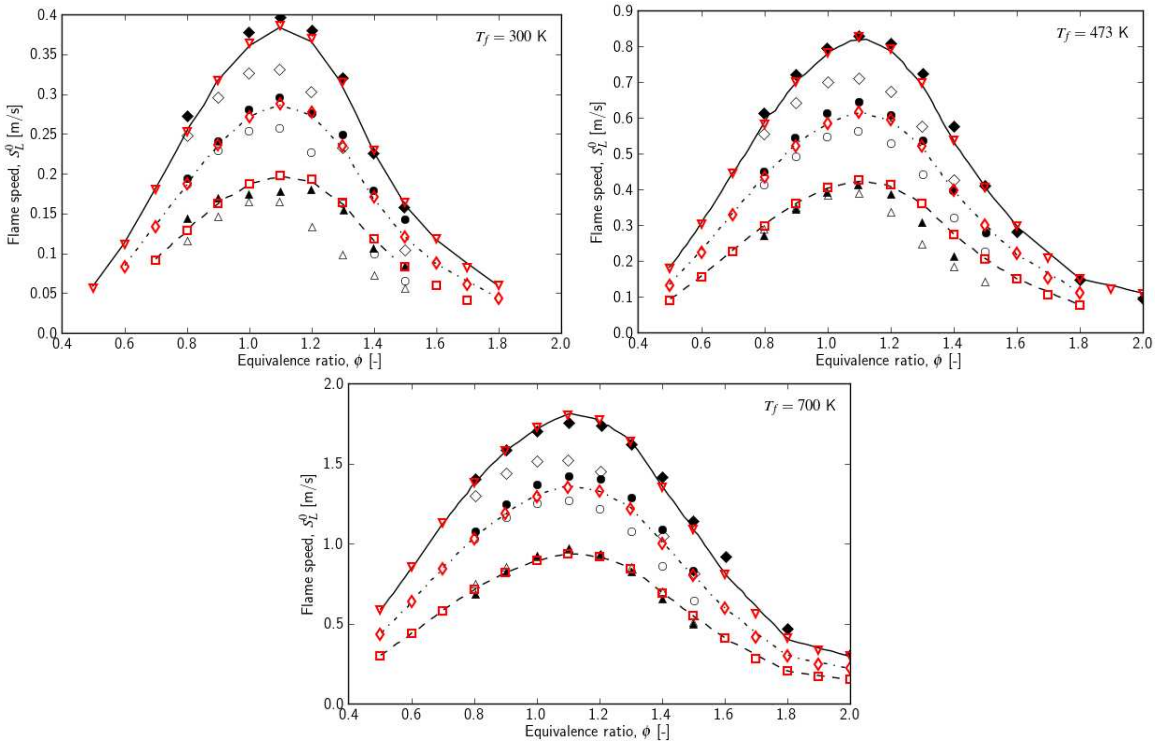

Figure 34 **Laminar flame speed versus equivalence ratio at several fresh gas temperatures, (−, − · −, − −) Franzelli [53], (♦, •, ▲) Luche [125], (◇, ○, △) Dagaut [35], (▽, ◊, □) Current simulations, for pressures of 1, 3, and 12 atm, respectively.**

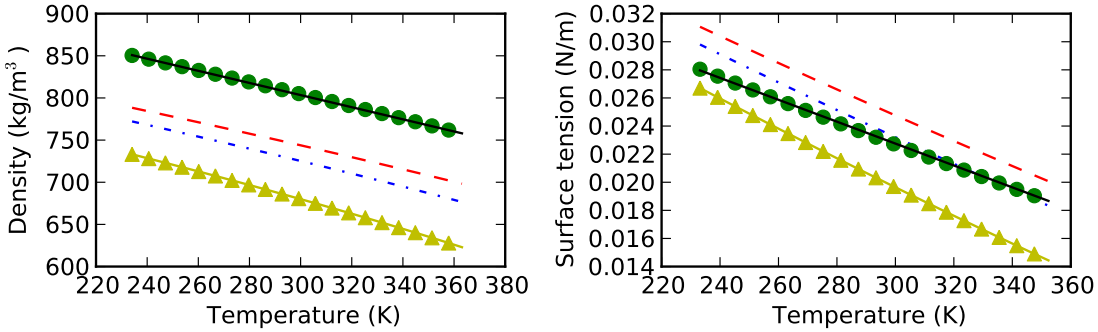

Figure 35 **Liquid density and surface tension for selected fuels including Jet-A. (–) Experimental Data, (– –) $C_{12}H_{26}$, (– ·) $C_{10}H_{22}$, (●) Jet-A, (–▲–) C_7H_{16}**

6.3 Non-reacting results

6.3.1 Non-reacting LES validation

Due the configuration of the test rig, it is very difficult to obtain data at the exit plane of the preburner where the computational domain begins. Optical access was available inside the rectangular section upstream of the bluff body at one flow condition with a centerline Mach number of $M = 0.25$, as measured with a pitot tube several bluff body diameters upstream of the bluff body. Velocity data is available at locations $x = -12.3D$ and $x = -8.5D$ upstream of the bluff body trailing edge. Experimental measurements of velocity near the bluff body trailing edge are also available for several non-reacting conditions ranging from $M = 0.25$ to $M = 0.4$, though no velocity data exists for the exact reacting condition of $M = 0.347$. The experimental data also shows that in this range of centerline Mach numbers the velocity profiles varied linearly. Taking advantage of this linear variation, the non-reacting experimental velocity profiles are all scaled to the reacting flow condition of $M = 0.347$ and used to set the inflow boundary conditions. Conditions are estimated at the computational inlet and modified until non-reacting simulations showed reasonable agreement at these data locations.

Figures 36 and 37 show comparisons between experiments and LES. All velocities are non-dimensionalized by the upstream reference velocity and all length measurements are non-dimensionalized by the bluff body height. It is more important to attempt to match the time-averaged velocity profiles near the bluff body trailing edge, where the flames are anchored, than at the upstream locations hence there are larger differences between experiments and simulations in Figure 36 compared to Figure 37. In Figure 37, the gray shaded regions define the range in the experimental data. Also note that the ordinate axis is the distance from the bluff body non-dimensionalized by the bluff body width so that $\hat{y}/D = 0$ is the shear layer location. This is denoted as $\hat{y}$ to avoid confusion. Experimental data was only taken on the top surface of the

bluff body. Disparities could arise given that not all objects in the physical system were included in the computational domain including the aforementioned pitot tube with an estimated diameter of over $0.125D$ located upstream of the bluff body.

Overall the results of the non-reacting simulations give confidence that the flow conditions for the LES reasonably approximate the experiments and provide a baseline for the reacting simulations.

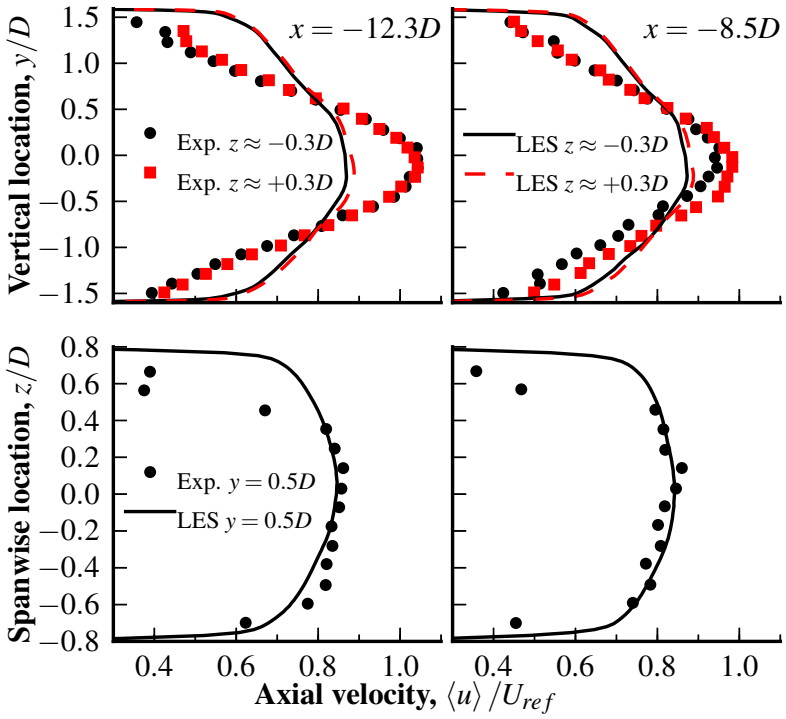

Figure 36 Mean axial velocity in the vertical and spanwise directions at $x = -12.3D$ and $x = -8.5D$

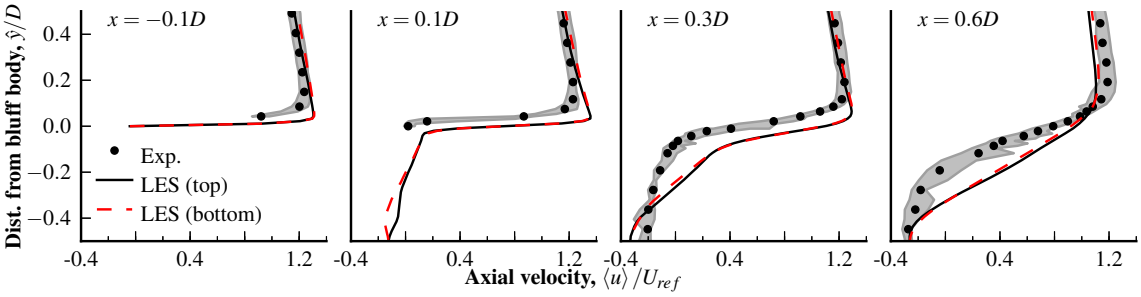

Figure 37 Mean axial velocity on the spanwise centerline at several locations near the bluff body trailing edge

6.3.1.1 Non-reacting spray validation

As was the case for the gas phase, experimental results for the liquid phase were not obtained at the exact conditions of the final reacting simulations. Droplet statistics including velocities and diameters were obtained at an incoming Mach number, temperature and oxygen content of $M = 0.355$, $T_{in} = 850°C$ and $O_2 = 14\%$. The fuel flow rate for all four injectors was $\dot{m} = 21.46$ g/s. This flow rate is inbetween the two fuel flow rates simulated under reacting conditions, as described in Section 6.4.1.

This data was used to tune the parameters for the spray model introduced in Section 3.7 using a single-injector reduced model with inlet velocity profiles scaled to $M = 0.355$. Initial simulations were run setting the stripped droplet diameter based on the correlations used by Madabhushi [129] described by Eq. 101. These simulations were then repeated setting the stripped droplet diameters based only on the wave model of Reitz [167] (see Equations 95 and 96). Figure 38 shows these results along with the results of the new model which blends the correlation and wave model, where the blending is described by Equation 100. Based on the experimental data, the idea for blending the two previous models is apparent. In addition to the stripped droplet

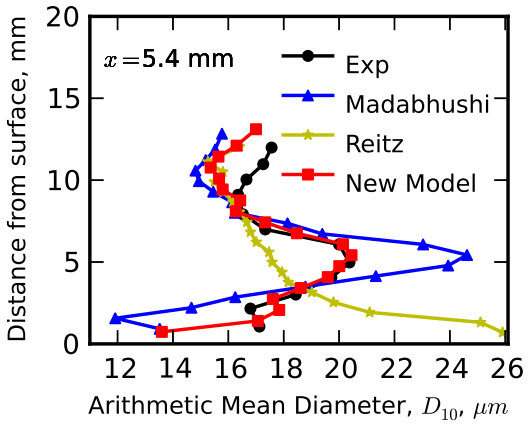

Figure 38 Comparison of several spray models for the recessed injector used in the bluff body simulations

diameter being modified, the stripped droplet velocity was also changed slightly based

on the data from Khosla [99]. The stripped droplet velocites are set as shown in Equation 102. This was a relatively minor change and involved the introduction of a random number that adds some unsteadiness since the Madabhushi[129] model was originally used for steady-state calculations. The final modification was to the B_1 model parameter from the default value of $B_1 = 10$ to $B_1 = 7$. Figure 39 shows the arithmetic mean diameter at several locations downstream of the injector, where for this test case, the injector location is $x = 0$. The updated model matches with the experimental data much more closely than the original model as implemented in the solver. The original model predicted too much spray penetration and not enough droplets near the surface. The axial velocities of the droplets for this case are shown in Figure 40. The original model generally under-predicts the axial velocity compared with the experiments while the updated model has better agreement. Figure 41 compares the droplet diameter profiles for $\dot{m}_f = 16.11$ g/s, $\dot{m}_f = 21.46$ g/s and $\dot{m}_f = 32.23$ g/s with the updated breakup model to show the effect that fuel flow rate has on droplet statistics. Note that the maximum and minimum "distance from the surface" points indicate the fuel jet penetration; no droplets in the simulation were above or below the indicated range. The old model penetrates the crossflow to a much greater extent than the updated model and clearly over-predicts penetration relative to the experimental data.

Experimental spanwise droplet data measuring lateral spreading was not available for this particular injector configuration; some data does exist for the same single flameholder geometry but with larger, flush-mounted injectors [122]. Figure 42a shows the lateral spreading of the current simulations compared with various experimental data presented by Becker [9], which was fit with the following expression: $\hat{z}/d_i = 2.32q^{0.09}\left(\hat{x}/d_i\right)^{0.32}$ where here the $\hat{\cdot}$ indicates coordinates relative to the injector. The experimental data momentum ratio, $q = \rho_l U_l^2/\rho_g U_g^2$, lies in the range of 1–26 whereas the current momentum ratio is approximately 80, based on the actual droplet

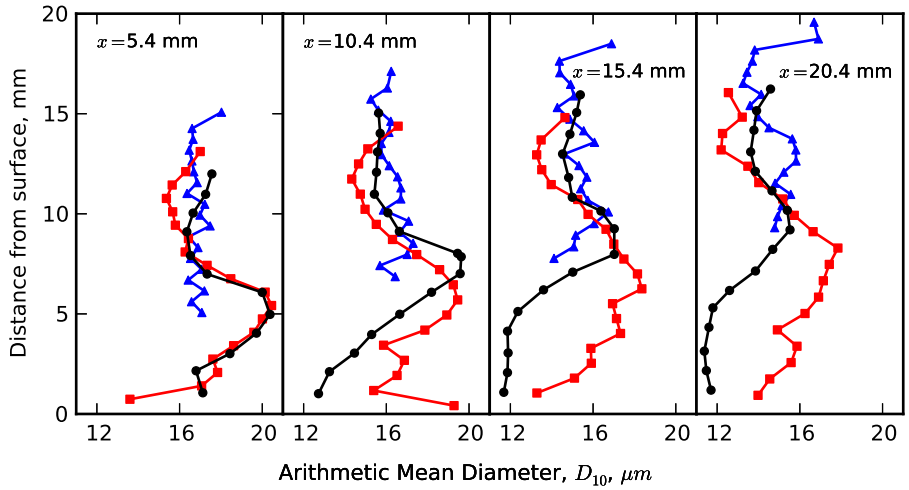

Figure 39 Arithmetic mean diameter of droplets at several axial locations downstream of the liquid injector for the test case with $M = 0.355$ and $\dot{m}_f = 21.46$ g/s. Original breakup model with $B_1 = 10$ (–▲–), Updated breakup model with $B_1 = 7$ (–■–), Exp. (–•–)

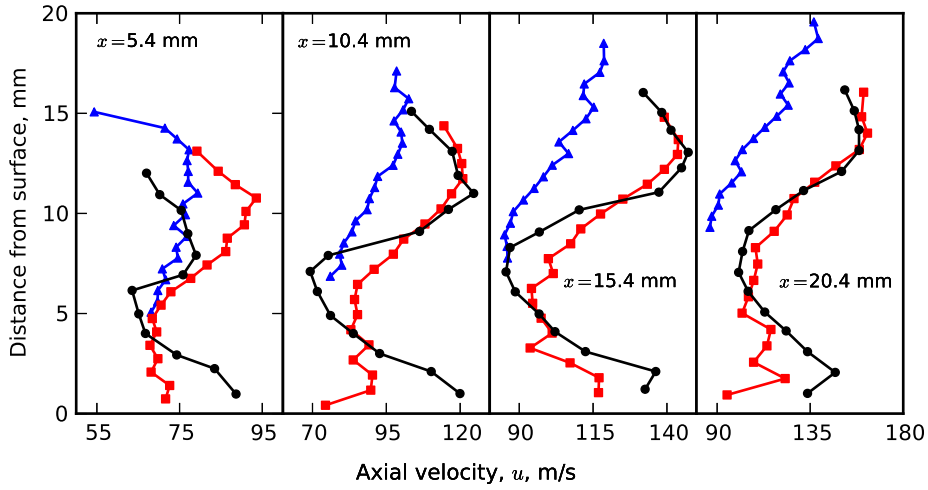

Figure 40 Axial velocity of droplets at several axial locations downstream of the liquid injector for the test case with $M = 0.355$ and $\dot{m}_f = 21.46$ g/s. Original breakup model with $B_1 = 10$ (–▲–), Updated breakup model with $B_1 = 7$ (–■–), Exp. (–•–)

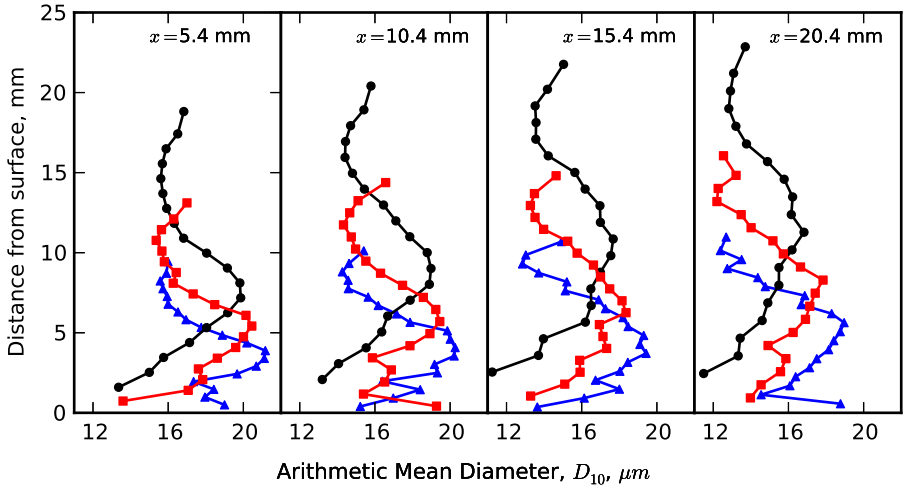

Figure 41 Droplet diameter comparison for three fuel flow rates using the updated breakup model, $\dot{m} = 16.11$ g/s (–▲–), $\dot{m} = 21.46$ (–■–), $\dot{m} = 32.23$ g/s (–●–)

injection velocity. Although the momentum ratio has a small effect on spreading, this partially explains why the simulation data lies on the lower boundary of the other experimental data especially near the injector. For the high fuel flow rate case at the trailing edge of the bluff body, $\hat{x}/d_i \approx 55$, the lateral spreading is approximately ± 7.25 mm which based on actual injected droplet diameter is $15.7\,d$ which compares well to measurements on this geometry, using a slightly different injector, where the spreading at the trailing edge was $\approx 15d$ [120]. Figure 42b compares the simulated transverse droplet sizes to the experimentally obtained data for the aforementioned flush-mounted injector case on the single flameholder rig [122]. The experimental data obtained from a Phase Doppler Particle Analyzer (PDPA) system is shown for a single vertical height away from bluff body surface with the error bars indicating the extent of the droplet sizes at all vertical locations at each particular $\hat{x}/d_i$ location. Near the centerline, the CFD droplet sizes lie within the bounds of the experimental data and the lateral spreading is also similar. The droplets at the periphery of the spray in CFD are larger than those measured in the experiments. This phenomenon has been observed in other numerical studies [163] which postulated this was due to competing effects of turbulent dispersion and droplet inertia. Large droplets stripped

off of the column are carried to the edges of the spray plume based on their assigned velocities and are not as affected by the gas phase as smaller droplets. Model improvements could possibly be made by assigning child droplet velocities based on stripped droplet size but no such effort was attempted in this study.

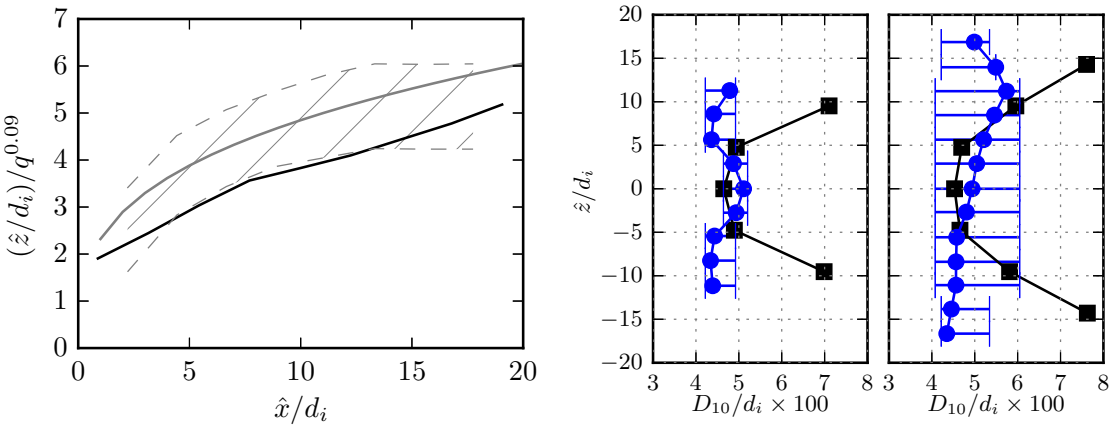

Figure 42 Transverse spray characteristics, (a) Droplet lateral spreading, experimental data range with curve fit [9] (–//–//–), and simulation spray data (—) and (b) spanwise droplet size comparisons between the current simulations (—) and experimental data [122] (—) at $\hat{x}/d_i \approx 30$ and $\hat{x}/d_i \approx 60$.

All of the breakup model tuning was completed after taking the orifice discharge coefficient into account. As previously noted, this subtle but important parameter can have a large impact on the liquid jet penetration. Initial drop sizes in the Lagrangian model are based on the effective area, which differs from the 0.635 mm injector diameter due to orifice effects. Computing v_{inj} based on d_{inj} does not provide the correct spray penetration. The mass flow rate of a single injector is computed as $\dot{m} = C_d \rho V A$, where C_d is the nozzle discharge coefficient. The injection velocity and droplet injection diameter must be computed on the assumption that the effective injection area is $A_{eff} = C_d A_{inj}$. The discharge coefficients for the present simulations lie in the range $0.52 - 0.59$. Figure 43 shows the effect of changing the discharge coefficient from unity to the more appropriate value of 0.527. The spray penetration qualitatively matches with the experimental images much more closely.

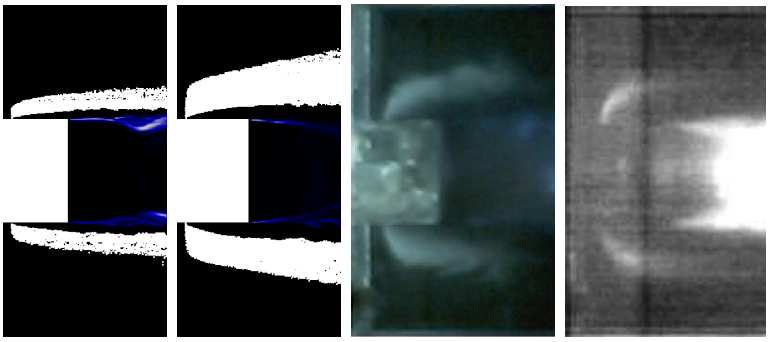

Figure 43 Comparison of modeled spray penetration with different discharge coefficients, (left to right) $C_d = 1.0$, $C_d = 0.527$, instantaneous and time-averaged experimental results

To summarize, tuning of the spray model based on the available experimental data was necessary to get the liquid jet penetration correct. Equally important, if not more important, was taking the injector discharge coefficient into account when computing the Lagrangian spray model injection parameters. Without the correct discharge coefficient the liquid jet did not penetrate into the crossflow far enough. Once this was corrected, the spray model tuning ensured the jet did not penetrate too far and the stripped droplets have the correct sizes and velocities. Appendix A gives implementation details for the final Lagrangian liquid jet in crossflow breakup model.

6.4 Reacting results

6.4.1 Reacting LES comparison with experimental data

Two operating conditions are simulated: $\dot{m} = 16.11$ g/s and $\dot{m} = 31.23$ g/s corresponding to global equivalence ratios of $\phi_{global} \approx 0.5$ and $\phi_{global} \approx 0.95$, both at $M = 0.347$ as measured on the centerline upstream of the bluff body. Experimental observations show marked differences in flame oscillations at these two conditions [33]. Specifically, large scale sinusoidal Bérnard/von-Kármán oscillations are seen at the higher equivalence ratio but are suppressed at $\phi_{\text{global}} \approx 0.5$. At the lower fuel flow rate, the flame exhibited symmetric shedding typical of stable premixed bluff

body flames. This is an critical distinction since the large flame oscillations are often associated with blow out [33, 190].

Most of the available experimental data is CH^* and C_2^* chemiluminescence and images from high- and low-speed cameras. To compare with these data the computational results are averaged in the spanwise direction to create 2D images. A comparison between high-speed experimental flame images and LES results is shown in Figures 44 and 45 for both fuel flow rates over a span of 0.8 ms which is approximately one period of the Bérnard/von-Kármán flame oscillations. The LES images were created by overlaying CO and CO_2 mass fractions on heat release rate. Specifically, an opacity function was applied to the heat release rate field such that in areas where the heat release rate is low, another variable is visible. In this case, that other variable is the sum of CO and CO_2 mass fractions. The effect of overlaying the species mass fractions "fills in" in image especially in the downstream regions. Figure 46 shows one flame image with only the heat release and the same snapshot with the species overlay technique. While this method is not ideal it does provide qualitative comparisons of flame dynamics. Absolute comparisons with chemiluminescence are quite difficult if the chemical mechanism does not include the excited species since the chemiluminescence intensity does not vary linearly with heat release rate and the intensity is a function of equivalence ratio, pressure, temperature and strain [141, 142]. This is complicated in the current combustor due to the non-uniform fueling nature of the close-coupled spray configuration where reactions occur over a wide range of local equivalence ratios and preheat temperatures.

The LES is able to correctly capture the two distinct flame shapes seen at the different fuel flow rates [199].

Time averaged heat release rate from the simulations are also compared with time averaged CH^* chemiluminescence in Figure 47. For the low fuel case, the heat release rate predicted by LES is much more concentrated in the shear layers than in

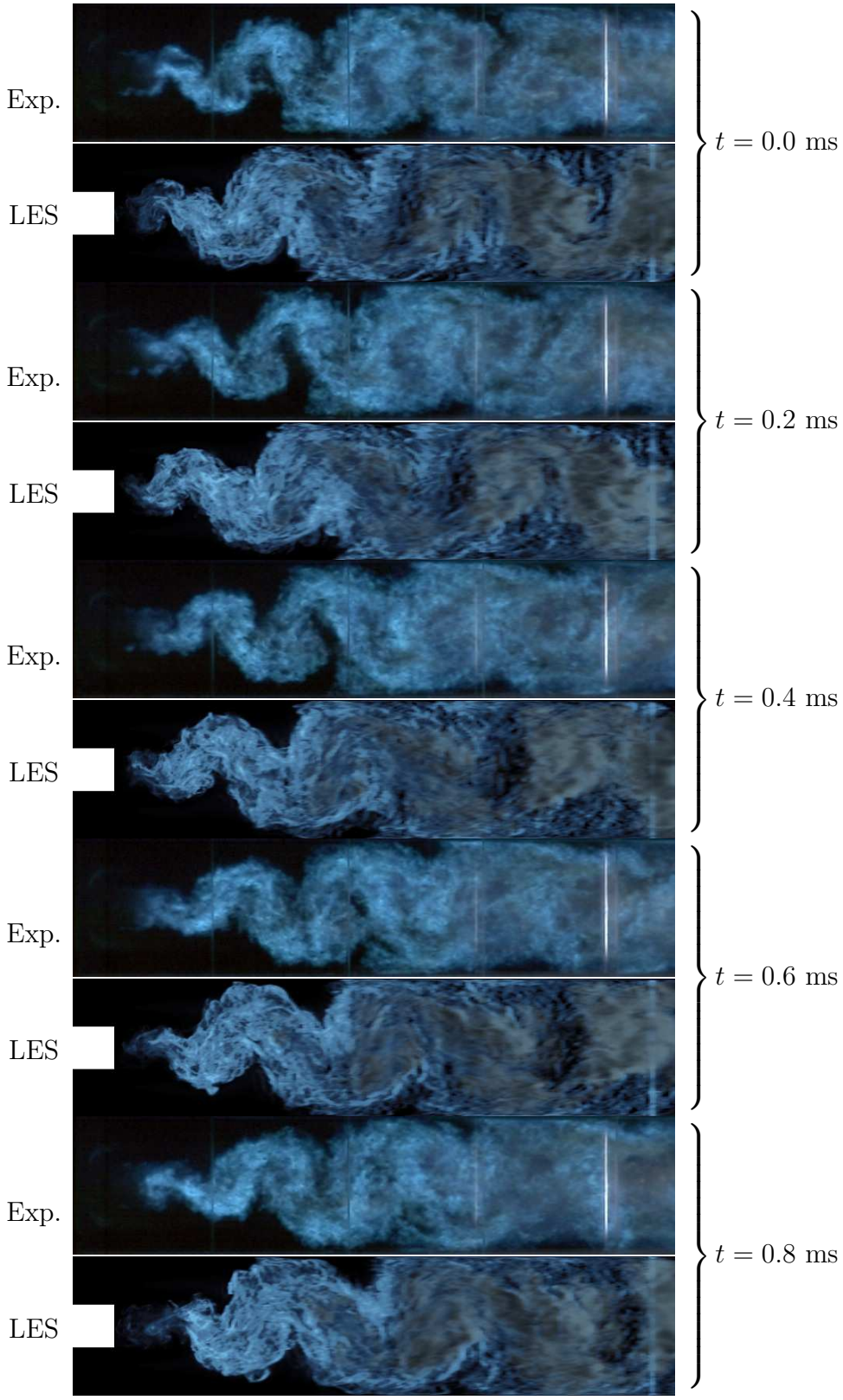

Figure 44 Comparison of experimental flame image sequence [33] with LES (spanwise averaged CO and CO_2 mass fraction overlaid on heat release rate) at $\phi \approx 0.95$

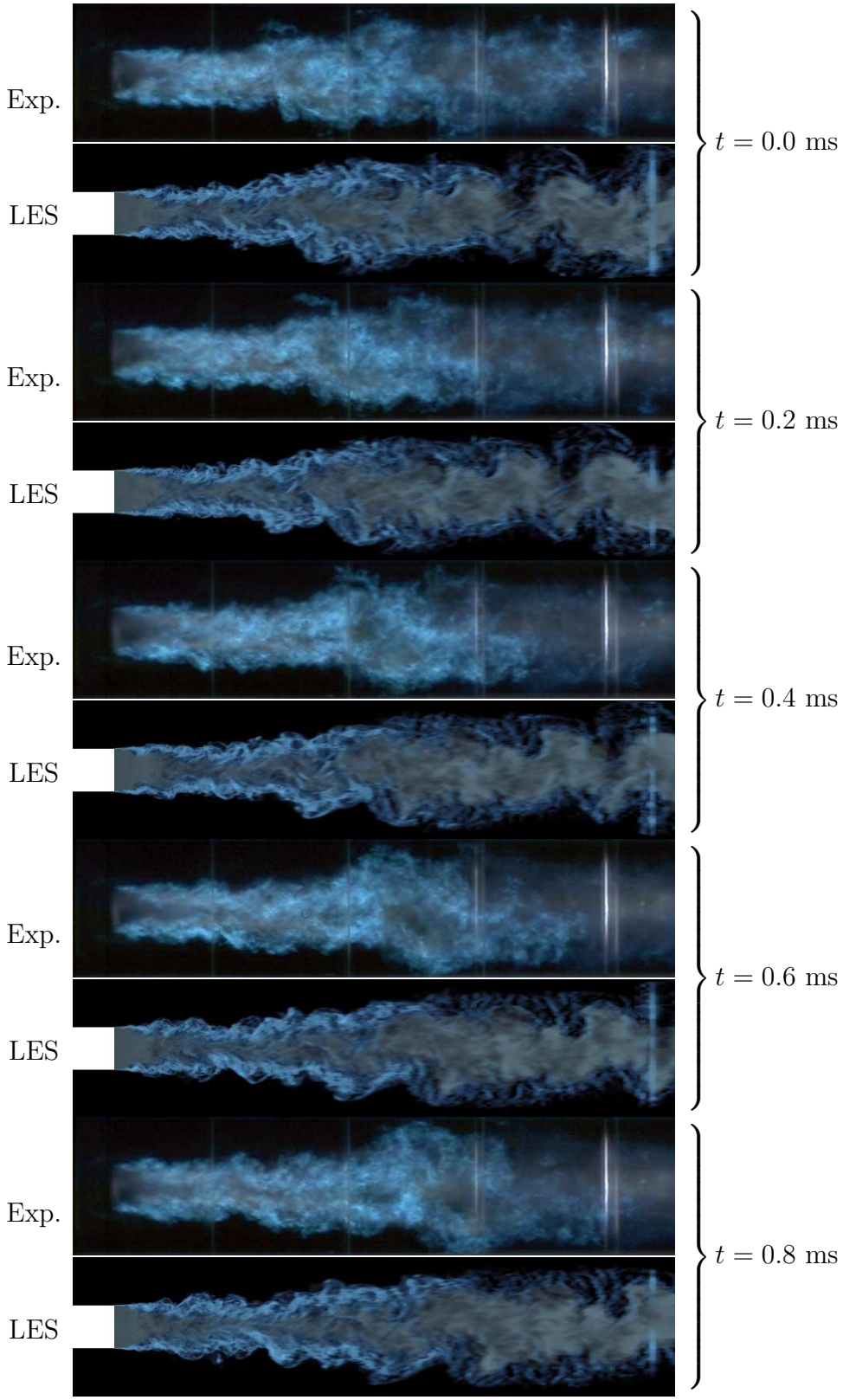

Figure 45 Comparison of experimental flame image sequence [33] with LES (spanwise averaged CO and CO_2 mass fraction overlaid on heat release rate) at $\phi \approx 0.5$

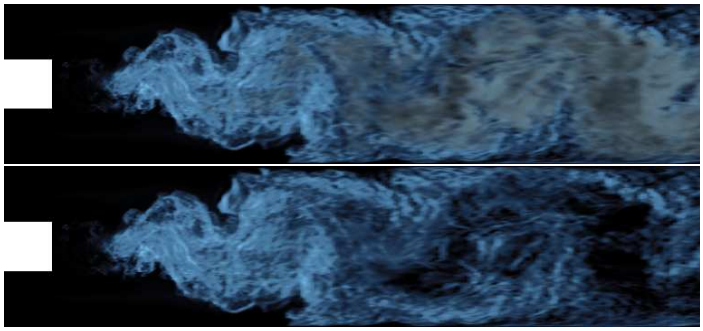

Figure 46 Example of an image with spanwise averaged heat release overlayed with the sum of CO and CO_2 mass fractions (top) and with spanwise averaged heat release alone (bottom).

the experiments. The high fuel flow rate qualitatively matches with the experiments better with most of the heat release occurring in the close-out region [120].

Previous analysis of the experimental results suggests that the flame oscillations are controlled by the heat release in the shear layers just behind the bluff body trailing edge [33]. This heat release is dictated by the spatial location of fuel and thus directly impacted by the liquid spray jet penetration. Since the flame dynamics are correctly predicted with the LES, it is assumed that the jet-in-crossflow breakup model simulates the real spray injection with sufficient accuracy. There is no detailed experimental droplet data at these reacting flow conditions, geometry and injector configuration but comparisons can be made for overall jet penetration using low-speed camera data. Figure 48 shows the low-speed camera images along side LES images of time-averaged CO and CO_2 mass fractions overlaid on heat release rate with a collection of Lagrangian liquid particle snapshots. The outer jet penetration for both fuel flow rates matches quite well.

6.4.2 Analysis of flame dynamics with respect to fuel jet penetration

Heat release due to combustion generally has a stabilizing effect on bluff body flows. Large scale asymmetric fluctuations are damped leaving symmetric shear layer rollup. This phenomenon is explained by examining the vorticity transport equation [120],

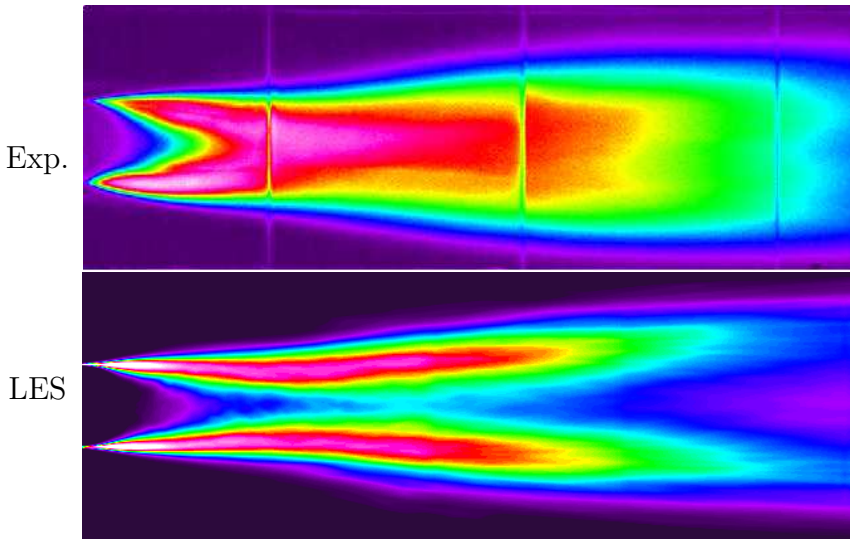

(a) $\phi_{\textbf{global}} \approx 0.5$

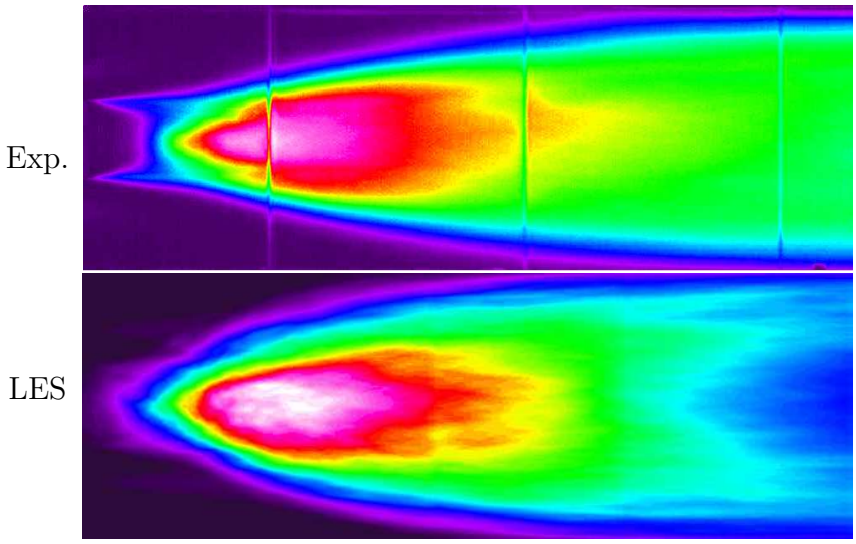

(b) $\phi_{\textbf{global}} \approx 0.95$

Figure 47 Comparison of experimental time averaged CH^* [33] with simulation time averaged heat release rate

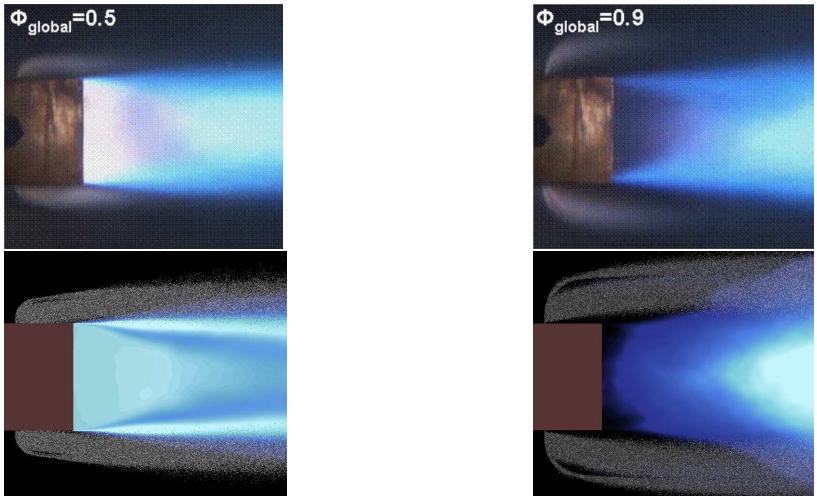

(a) $\phi_{\textbf{global}} \approx 0.5$ **(b)** $\phi_{\textbf{global}} \approx 0.95$

Figure 48 Comparison of experimental spray penetration (top) [33] with simulations (bottom). Note that the high fuel flow rate of the experimental image is slightly different than the simulation.

written for a compressible fluid [55],

$$\frac{D\omega_i}{Dt} = \underbrace{\omega_j S_{ij}}_{\substack{\text{vortex} \\ \text{stretching}}} - \underbrace{\omega_i \frac{\partial u_j}{\partial x_j}}_{\substack{\text{gas} \\ \text{expansion}}} - \varepsilon_{ijk} \left(\underbrace{\frac{1}{\rho^2} \frac{\partial p}{\partial x_j} \frac{\partial \rho}{\partial x_k}}_{\substack{\text{baroclinic} \\ \text{torque}}} - \underbrace{\frac{\partial}{\partial x_j} \left(\frac{1}{\rho} \frac{\partial \tau_{kl}}{\partial x_l} \right)}_{\substack{\text{viscous} \\ \text{diffusion}}} \right). \tag{2}$$

Several factors have stabilizing influences: gas expansion takes place acting as a vorticity sink, baroclinic torque is produced and for gas flows, as temperature rises viscosity increases resulting in increased vorticity diffusion. Although it may appear that the production of baroclinic torque has a destabilizing effect, for confined bluff body flames this vorticity is generated in the opposite direction to that of the vorticity in the shear layers thus decreasing the magnitude [190].

To understand these effects on the close-coupled configuration in this study, the time and spanwise averaged fuel vapor mass fraction is plotted at several locations in the near-field downstream of the bluff body trailing edge in Fig. 49. The results from the shear layers on the top and bottom of bluff body are also averaged and the results normalized by the maximum value at the $x = D/4$ location, $Y_{F,\max} = 0.092$. These

plots highlight what is apparent from the spray penetration images, i.e., the low fuel flow rate, with its lower jet penetration, on average delivers more fuel to the near-field shear layers. The differences between the fuel mass fraction in the shear layers then give rise to large differences in heat release rate also shown in Fig. 49, normalized with $\dot{Q}_{\max} = 6 \times 10^8$ W/m^3. Finally the effect on baroclinic torque generation and gas expansion is seen, with the plots normalized by 9×10^8 s^{-2} and 3×10^8 s^{-2}, respectively. This evidence supports the hypothesis [33, 120] explaining the observed differences between the flame structures at the two operating conditions.

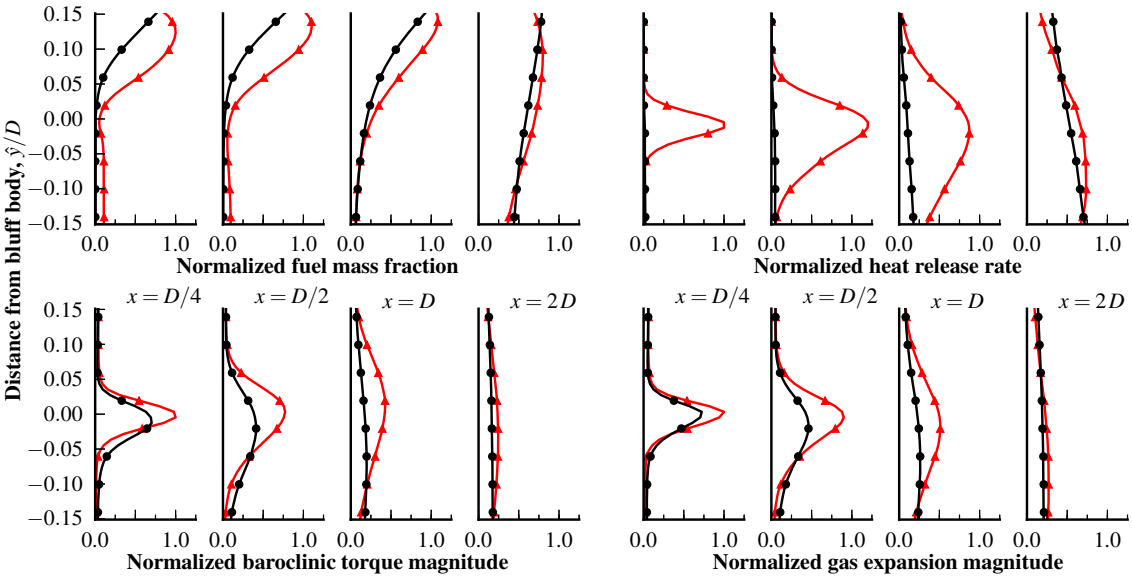

Figure 49 Spanwise and time-averaged quantities in the shear layers at several axial locations, (−●−) $\phi_{\text{global}} \approx 0.95$, (−▲−) $\phi_{\text{global}} \approx 0.5$

6.4.3 Fuel mixing and reaction zone analysis

Although the previous section compared CFD results with the available spanwise-averaged experimental results, the highly three-dimensional nature of this combustor configuration should be emphasized. The close-coupled discrete fuel injectors limit significant premixing prior to the reaction zone making the flame structure fundamentally different from purely premixed systems or upstream-fueled non-premixed

systems. Because of this, flame sheet approximations traditionally used to describe those other configurations cannot be used here [119].

To examine the flame structure, a flame index is calculated [22], which indicates whether combustion is occurring in a diffusion mode ($FI = 0$) or a premixed mode ($FI = 1$). The flame index is related to the alignment of the fuel and oxidizer gradients and is calculated according to the definition,

$$FI = \frac{1}{2}\left(1 + \frac{\nabla Y_F \cdot \nabla Y_{Ox}}{|\nabla Y_F|\,|\nabla Y_{Ox}|}\right) \tag{262}$$

Figure 50 shows a slice of the flame index multiplied by heat release rate on the spanwise centerline plane for the high fuel flow rate case. The results indicate regions of non-premixed and premixed reactions, consistent with experimental images [119], in the inner portion of the near-field region. Local premixed conditions exist in the thin shear layers surrounding recirculation zone. Far downstream local premixed conditions are intermixed with non-premixed conditions.

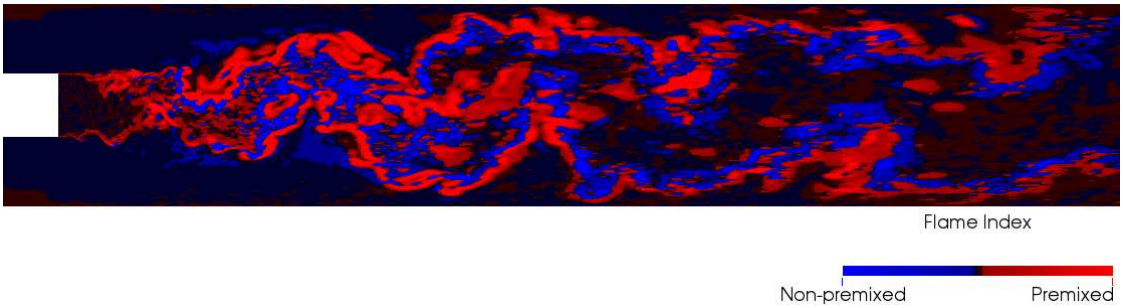

Figure 50 Centerline slice of flame index multiplied by heat release rate for the high fuel flow rate case.

Instantaneous planar cuts of the fuel mass fraction, combustion heat release and flame index conditioned on heat release rate are shown in Figure 51. These axial flame index slices again indicates mixed non-premixed/premixed conditions within the reaction zone, and with non-premixed combustion surrounding the fuel jets, and partially premixed conditions locally within the thin surrounding shear layers. At $x = 5D$, the partially premixed region has widened and distorted in correlation to the

location of the fuel jets. Far downstream, the flow structure becomes more uniformly distributed across the wake flow but there remains some degree of correlation to the remnants of the fuel jets suggesting that combustion field is still closely related to the instantaneous fuel jet distribution.

The strongest heat release occurs in the shear layers between and below the fuel jets at around $x = 2D$. Enough mixing has occurred at this point for reactions to be taking place at near stoichiometric mixture conditions.

Slices at the same axial locations for the low fuel flow rate case are shown in Figure 52. More intense heat release is observed at the $x = D$ compared with the high fuel flow rate case. Although most heat release occurs in premixed zones, more reactions in the non-premixed regime occur at $x = D$ and $x = 2D$ at the low fuel flow rate versus the high fuel flow rate. The fuel jets are in closer proximity to the hot recirculating products and reactions in the shear layer promoting the non-premixed combustion. More fuel is seen farther downstream in the high fuel flow rate case since less evaporation and burning happens near the bluff body and simply due to the larger mass flow rate.

CFD simulations can provide the detailed information about the flame regimes not available with experiments; the premixed flame regimes within the flow field can be computed. Figure 53 shows a flame regime map calculated across the combusting flow field for reaction zones that satisfy a flame index greater than 0.5, plotted in terms of the computational subgrid scale Δ and the local equivalence ratio entering the reaction zone. The results show reactions occurring in a range of flame regimes spanning corrugated flamelets to broken reaction zones. The results indicate that the reactions associated with high local equivalence ratio (indicated in yellow), such as those near and surrounding the fuel jets, occur primarily in the thin reaction zone and broken reaction zone regimes. The reactions that occur near stoichiometric conditions (orange) extend into the corrugated flamelet regime as the reaction zone thickness is

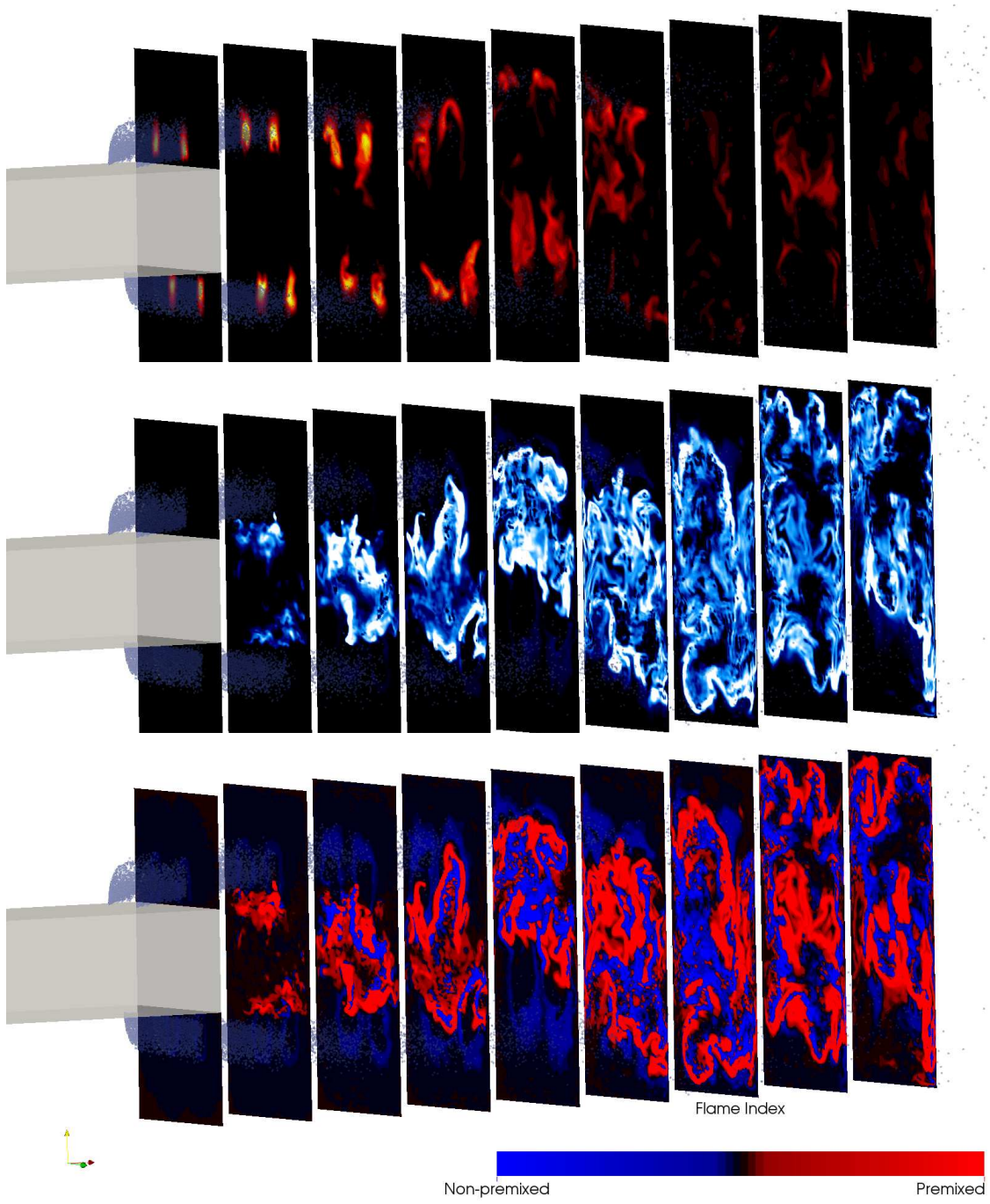

Figure 51 Axial slices at $x = 0, D, 2D, \ldots, 8D$ showing fuel mass fraction (top), heat release rate (middle), and flame index (bottom) along with fuel droplets for the high fuel flow rate case.

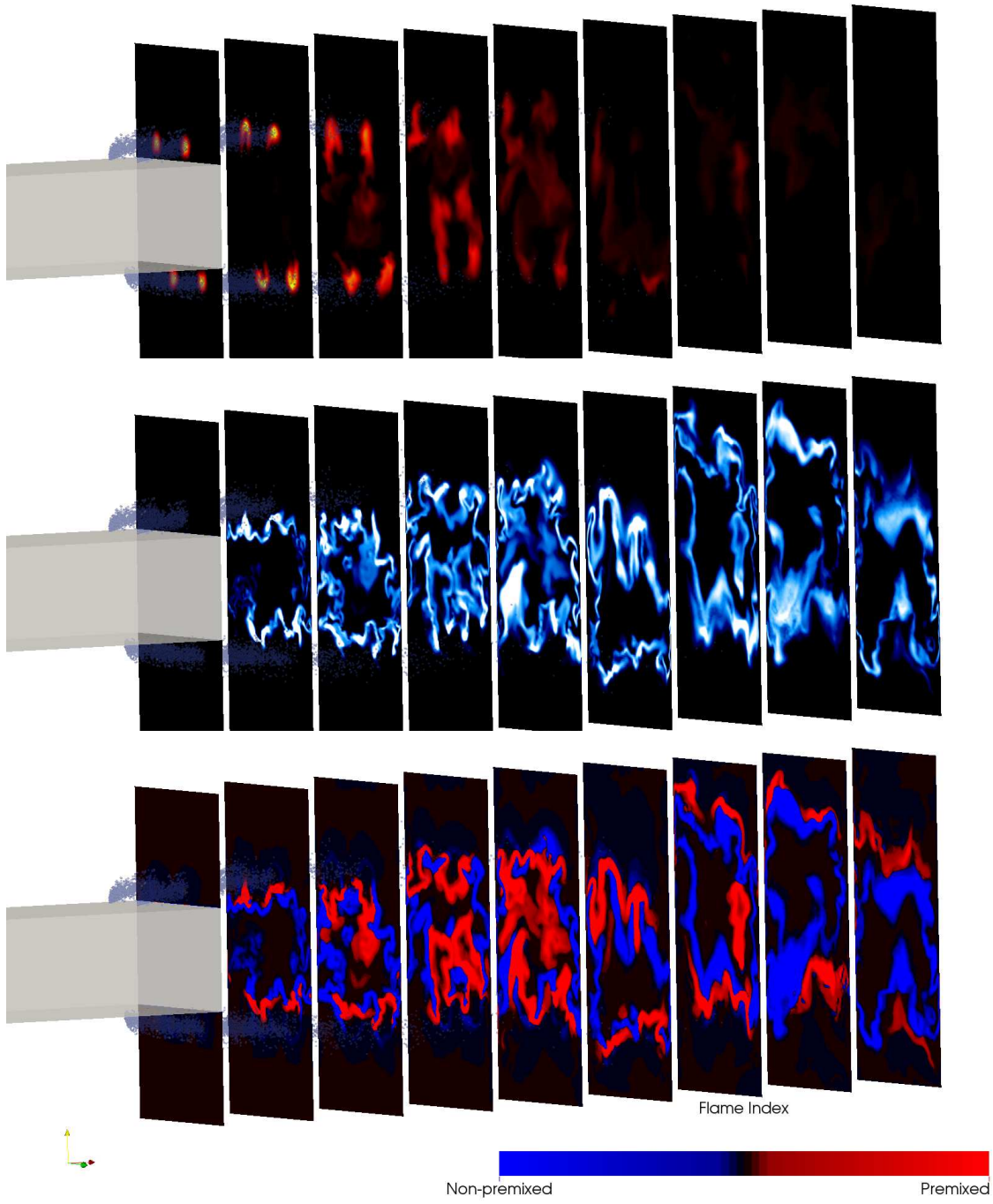

Figure 52 Axial slices at $x = 0, D, 2D, \ldots, 8D$ showing fuel mass fraction (top), heat release rate (middle), and flame index (bottom) along with fuel droplets for the low fuel flow rate case.

expected to be very thin.

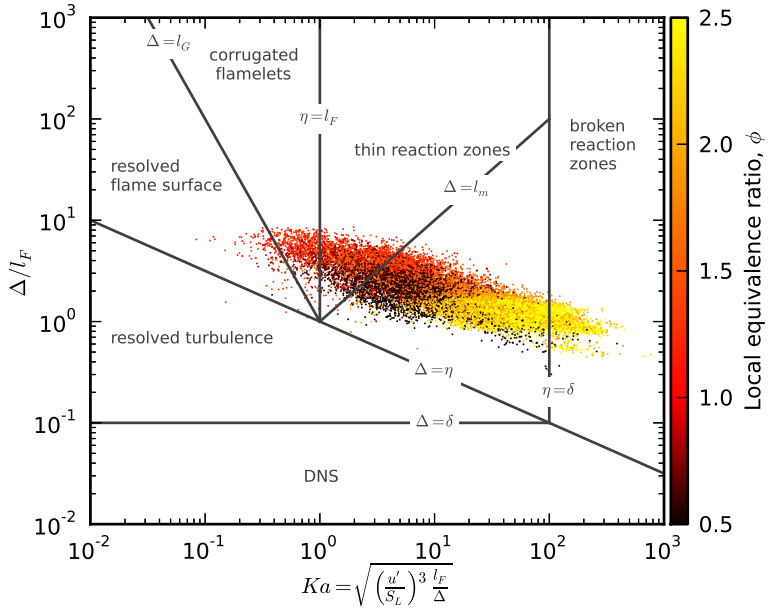

Figure 53 Premixed flame regime map colored by local equivalence ratio.

Figure 54 instead plots the premixed flame regime colored by axial location downstream of the bluff body. The reactions occurring in the near-field shear layers and reaction zone, for $x/D < 2$, are colored black. These data indicate the partially premixed reactions span the thin reaction and broken reaction zone regimes. The reactions existing farther downstream, $2 < x/D < 4$, which are colored blue, similarly span only the thin reaction and broken reaction zone regimes. Only the reactions that are shown in red, which occur in the region far downstream of the bluff body, i.e., $x/D > 4$, are calculated to be in the corrugated flame regime.

These include reactions far downstream in the CFD domain where the length scale becomes very large, greater than the flameholder characteristic length D. In addition, the simulations show that far downstream of the bluff body, the subgrid kinetic energy has been damped significantly by the heat release, which lowers the Karlovitz number associated with those reactions. The premixed flame regimes calculated from these simulations support the hypothesis that reactions occur over a

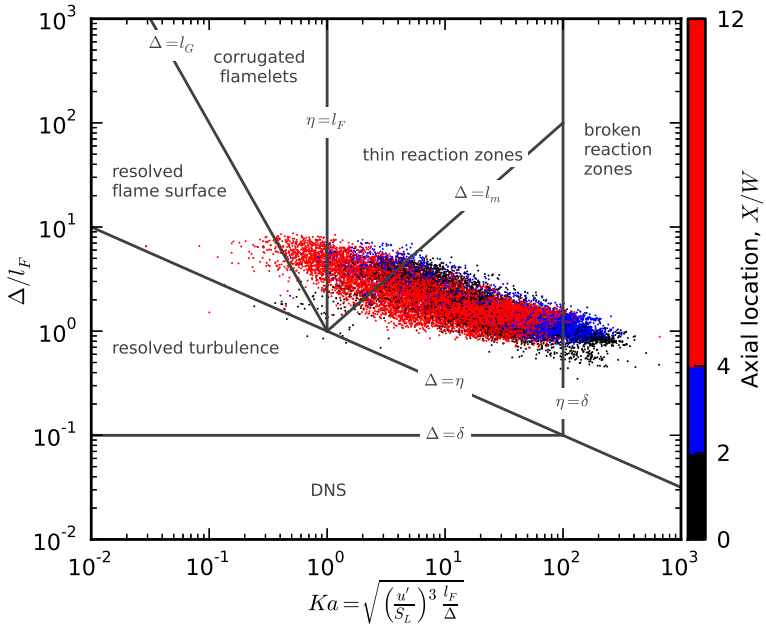

Figure 54 Premixed flame regime map colored by axial location.

wide range of flame regimes and that in the near-field regions they are dominated by thin reaction and broken reaction zones at these conditions. The simulation results indicate the combustion process spans non-premixed and premixed flame types and that the reaction zones are correlated with the spatial and temporal position of the fuel jets consistent with the experimental data.

6.4.4 Effect of Lagrangian injection model on flame dynamics

As was discussed in Section 6.4.2, the flame dynamics in this configuration are largely influenced by the liquid fuel jet penetration. Section 6.3.1.1 discussed the sensitivity of the fuel penetration to the Lagrangian model so it is clear that in turn the flame dynamics are sensitive the Lagrangian injection model as well. The initial simulations in this study did not correctly account for the injector discharge coefficient and no tuning was completed. The net result was fuel jets with penetration that was much lower than experimentally observed.

Figure 55 shows the results of both the low and high fuel rate cases compared with

experimental results. The simulations actually show the opposite flame dynamics as the experiments; the low fuel flow rate case has large scale sinusoidal shedding whereas the flame is damped in the near-field of high fuel flow rate simulation. For the high fuel flow rate case, the simulated fuel jet penetration is similar to the experimentally observed fuel jet penetration for the low fuel flow rate. Under these conditions fuel penetrates far enough for adequate premixing but low enough to deliver the fuel and partially premixed fuel-air mixture to the shear layers. For the low fuel flow rate case the jet penetration is extremely low and does not allow for substantial mixing prior to reaching the bluff body trailing edge. The mixture in the shear layers just behind the trailing edge of the bluff body is much greater than stoichiometric so the heat release is reduced and the large scale shedding is not suppressed. This phenomenon is similar to the flame dynamics observed for a different, but related, close-coupled liquid fueled bluff body configuration [119].

6.5 Effect of subgrid turbulence-chemistry interaction model

Past research has shown that in some instances the subgrid turbulence-chemistry interaction model used in LES has a large influence on the results of bluff body stabilized reacting flows [66, 156]. Conversely, others have demonstrated that simple models provide satisfactory accuracy [57]. To determine the effect of the subgrid turbulence-chemistry interaction on this configuration, both high and low fuel flow rate conditions simulated with the simple quasi-laminar approach were also computed using the subgrid Linear Eddy Model.

The grid resolution in the shear layers behind the bluff body were estimated to be $10 - 20\,\eta$ based on resolved subgrid kinetic energy, k^{sgs}. In order to resolve subgrid fluctuations to approximately η, 18 subgrid LEM cells were used in each LES cell. The LEM stirring constants were set as $N_\eta = 1$ and $C_\lambda = 15$ with the LEMLES standard triplet mapping algorithm used. The LES time step for this simulation was

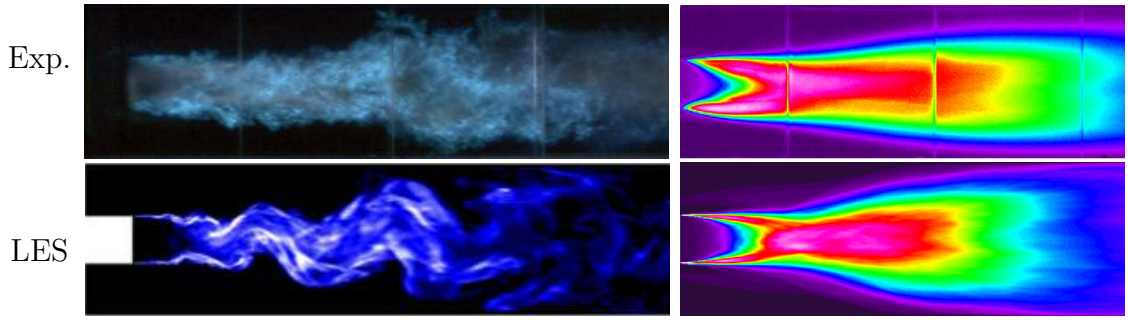

(a) $\phi_{\textbf{global}} \approx 0.5$

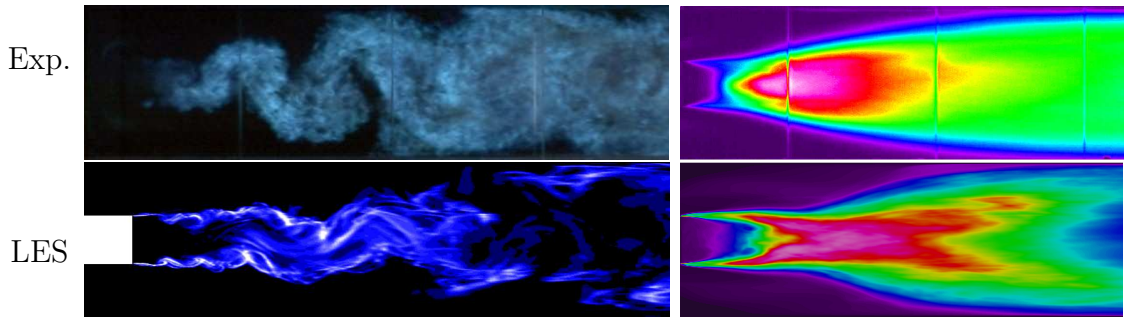

(b) $\phi_{\textbf{global}} \approx 0.95$

Figure 55 Instantaneous and time-averaged comparisons of experimental data with LES using an injector discharge coefficient of $C_d = 1$ and no Lagrangian injection model tuning

approximately 1×10^{-7} s while the LEM subgrid stirring time step was as small as 1×10^{-8} s. Most cells in the domain had $\Delta t_{stir} \approx 5 \times 10^{-8}$ s, thus for every LES time step two subgrid LEM stirring events took place, though in a small number of cells within the shear layer 8–10 stirrings per LES time step occurred. The subgrid LEM reaction-diffusion equation and stirring were computed once at the beginning of each time step; the splicing, coupling and temperature rescaling operations were completed at both the predictor and corrector steps. The use of the LEMLES incurs a significant computational cost; the simulations take approximately one and a half times as long as the quasi-laminar chemistry model.

Figures 56 and 57 show instantaneous comparisons between the LEMLES and quasi-laminar (QL) LES results at the two fuel flow rates. Qualitatively the LEMLES results match those of the QL LES results and are consistent with the high speed images from the experimental data. The LEMLES flame images are most consistent with the QL LES and experimental data in the region just downstream of the bluff body, $\approx x \leq 3D$. Farther downstream the instantaneous snapshots appear smoother with fewer small scale structures. Time-averaged and spanwise averaged results for LEMLES are compared with those from QL LES in Figure 58. The LEMLES results show a slightly shorter reaction zone but more intense reactions in the shear layers. This will be discussed further in Section 6.6 where these results are compared with simulations using a high-order finite difference method.

In order to elucidate what is occurring in the subgrid LEMLES model, Figure 59 shows five instantenous snapshots of temperature and CO mass fraction on the embedded LEM lines at three different spanwise locations in the shear layer at $x \approx D$ for the high fuel flow rate case. The dashed lines are the averaged values over the entire simulation and the symbols are the instantenous values. The shifts of the entire line from one time instance to the next demonstrates the large scale convection at the LES resolved level and occurs on the subgrid level via splicing. Subgrid reaction, diffusion

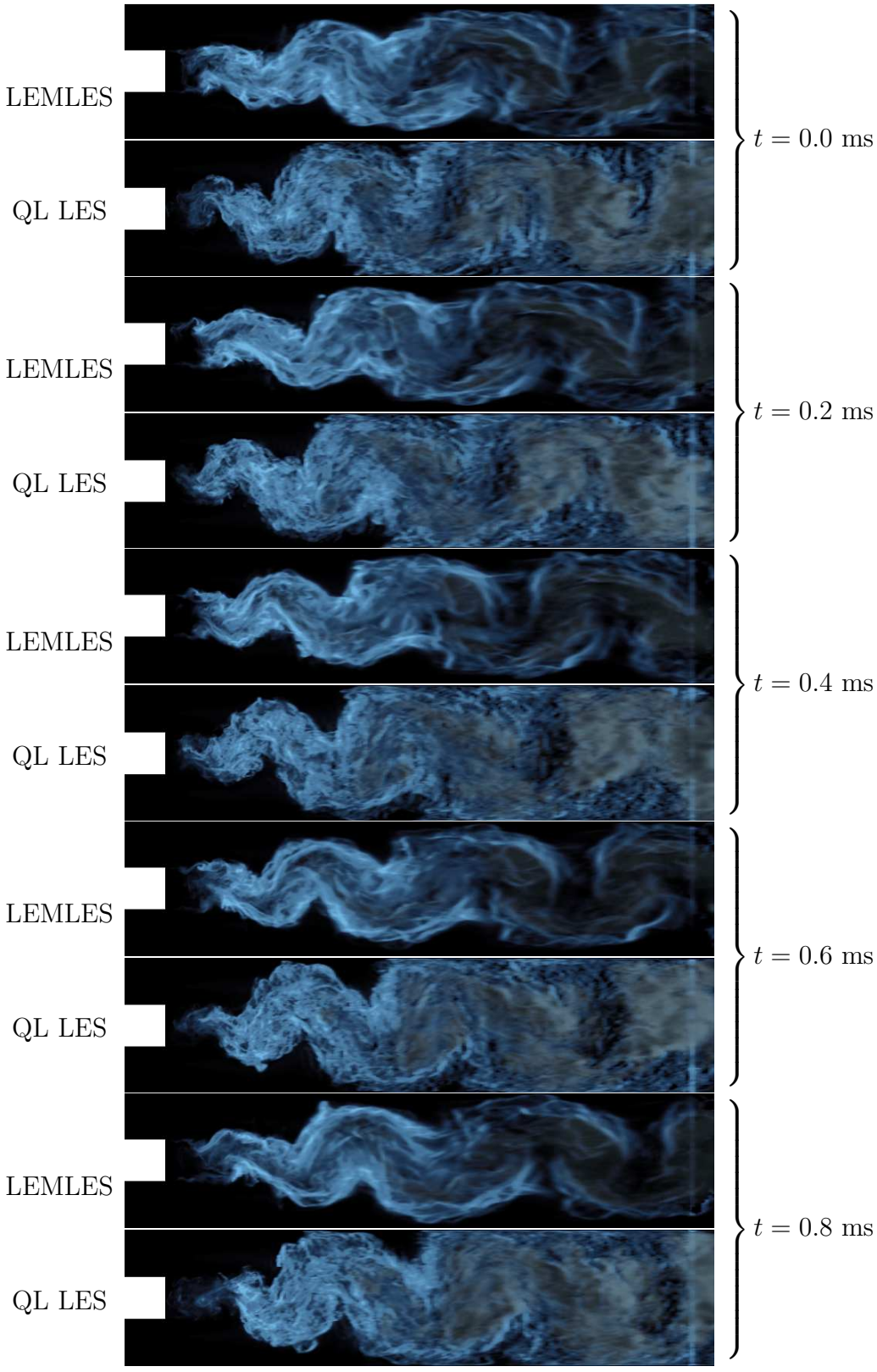

Figure 56 Comparison of LEMLES flame image sequence with QL LES (spanwise averaged CO and CO_2 mass fraction overlaid on heat release rate) at $\phi \approx 0.95$

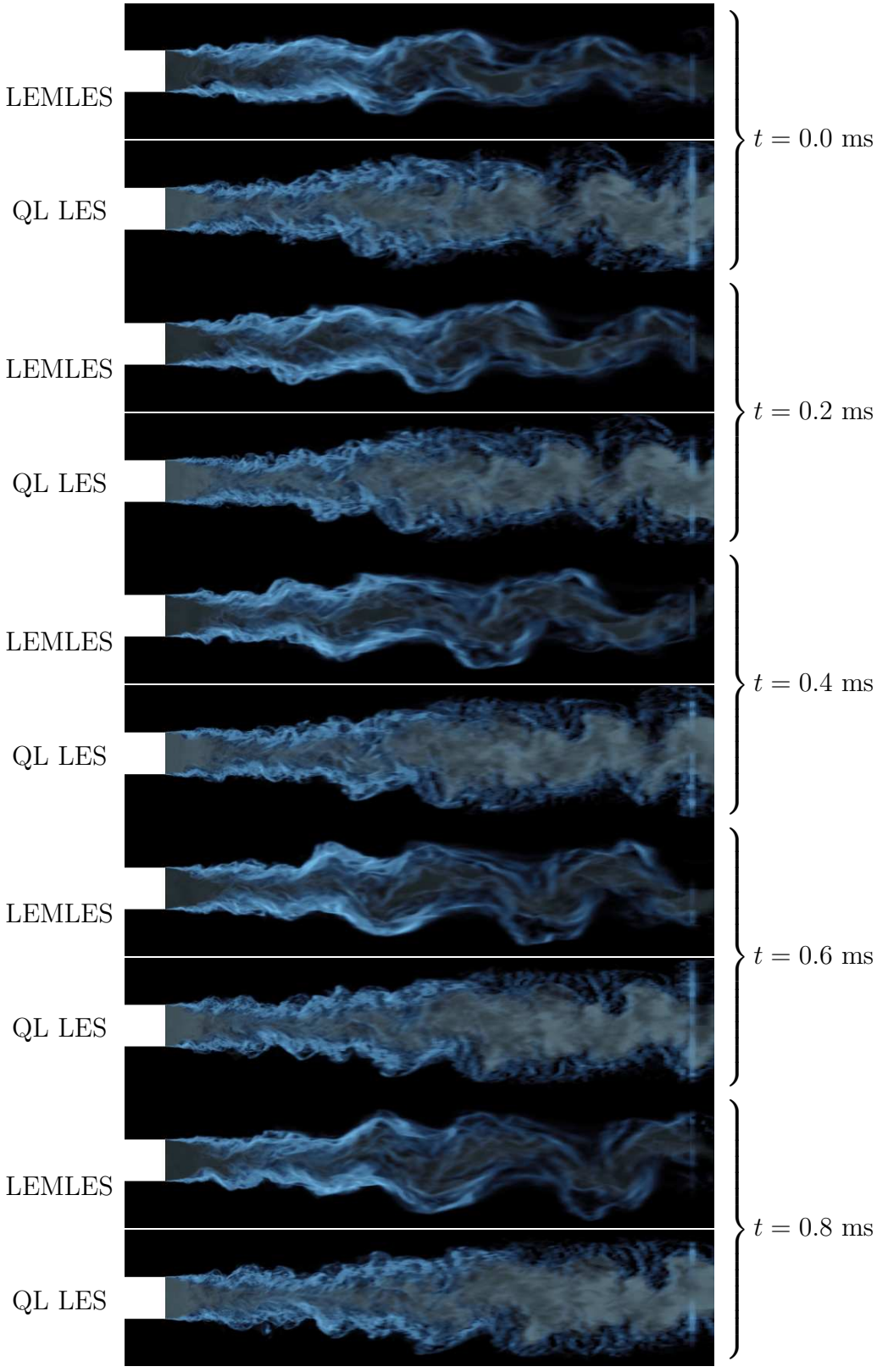

Figure 57 Comparison of LEMLES flame image sequence with QL LES (spanwise averaged CO and CO_2 mass fraction overlaid on heat release rate) at $\phi \approx 0.5$

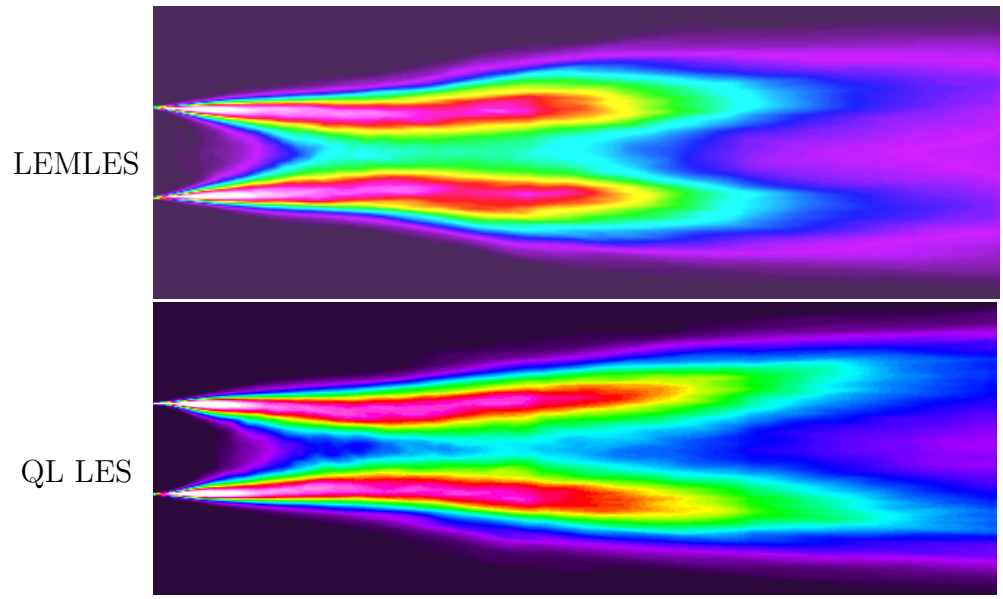

(a) $\phi_{\textbf{global}} \approx 0.5$

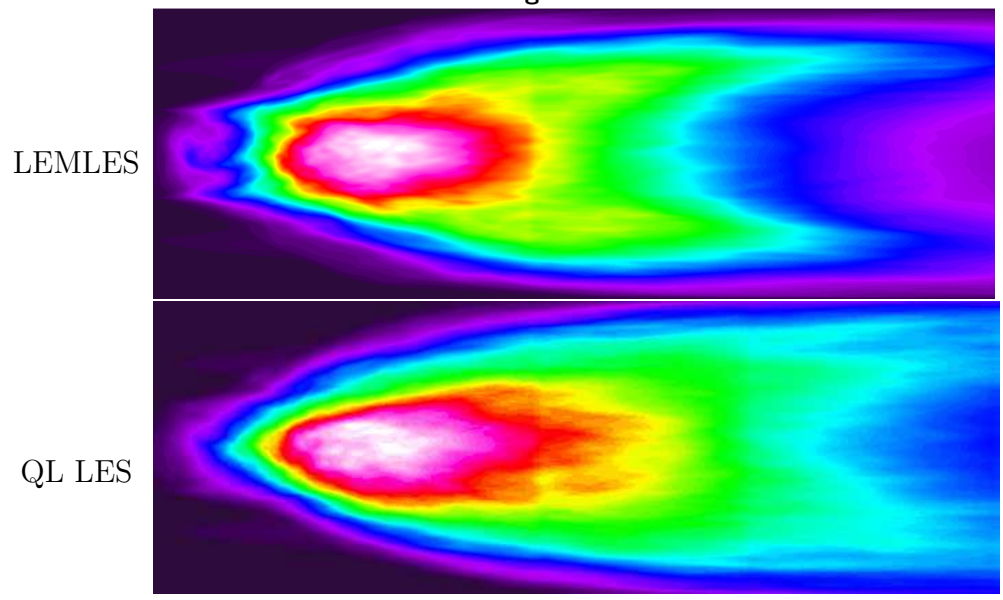

(b) $\phi_{\textbf{global}} \approx 0.95$

Figure 58 Comparison of time averaged heat release rate obtained with LEMLES and QL LES.

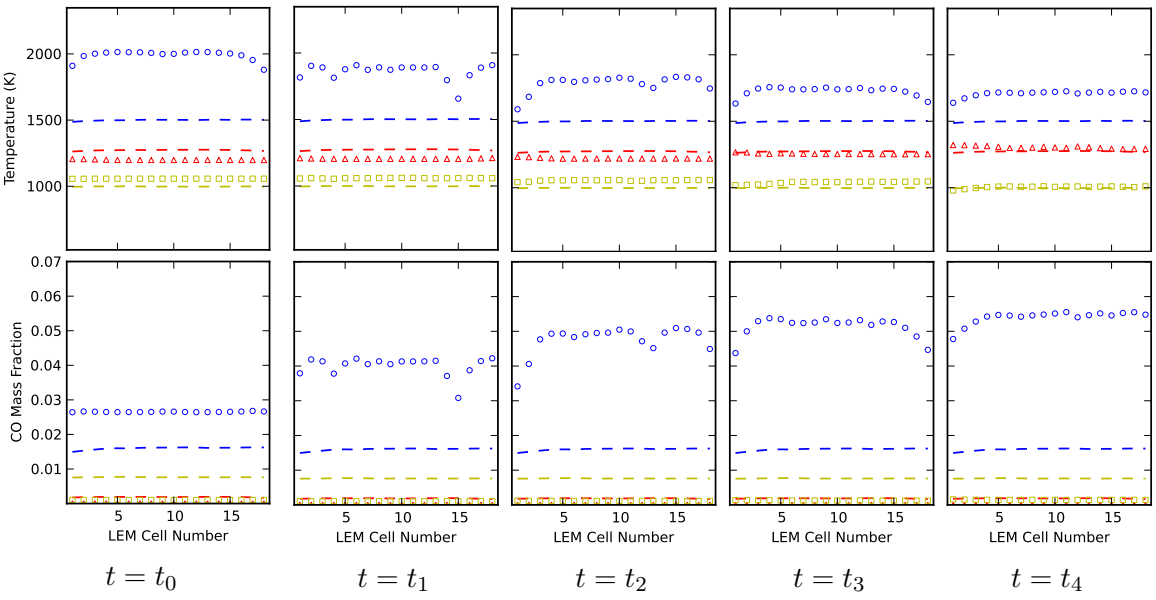

Figure 59 Instantaneous snapshots of temperature and CO mass fraction on subgrid LEM lines within LES cells at three spanwise locations in the shear layer of the high fuel flow rate case. The dashed lines represent the mean values over the entire simulation.

and, most notably, stirring events are seen as the non-uniformities across the LEM lines. The subgrid LEM line do show signs of stirring events but are qualitatively not very "mixed up". This is a consequence of the relatively few number of subgrid LEM stirring events per LES time step as previously described. Outside of the shear layers, subgrid turbulent kinetic energy is even lower meaning even less subgrid stirring. This helps explain why the flame dynamics, i.e. symmetric vs. asymmetric shedding, in the near field are insensitive to the choice of the quasi-laminar or LEMLES approach.

The centerline time-averaged axial velocity for the QL and LEMLES simulations at the high fuel flow rate are similar as shown in Figure 60. The low fuel flow rate simulations show larger differences especially at locations far downstream of the bluff body. Investigating the species mass fractions closer reveals some differences in the simulations. Time-averaged line plots of species along the spanwise centerline are shown in Figure 61–63. As with the axial velocity, there are generally more differences between the LEMLES and QL LES for the low fuel flow rate case. The high fuel flow

rate case has more large scale structures that result in more convective mixing while in the low fuel flow rate case diffusion may be more important. Thus neglecting the inter-LES-cell diffusion in LEMLES may cause more differences for the low fuel flow rate configuration.

The time-average temperatures at the centerline, show in Figure 65, show that this quantity is also insensitive to the choice of the subgrid turbulence-chemistry interaction model. No experimental product species data, temperature or velocity data exists for this configuration so comparisons against the experiments in this regard is not possible. The spray penetration is not directly affected by the choice of subgrid turbulence-chemistry interaction model as seen in Figure 64.

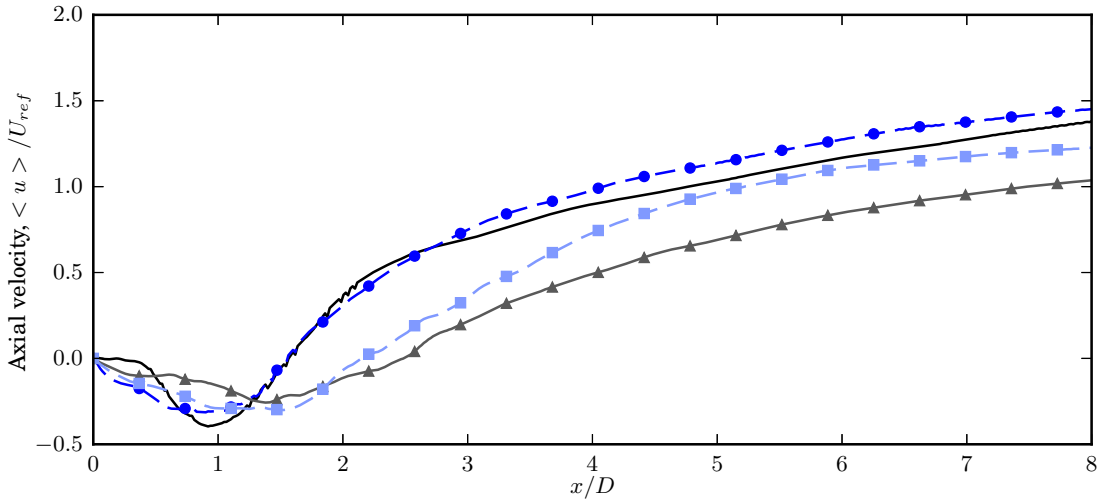

Figure 60 Centerline time-averaged axial velocity, (—) QL LES $\phi \approx 0.95$, (– • –) LEMLES $\phi \approx 0.95$, (–▲–) QL LES $\phi \approx 0.5$, (–■–) LEMLES $\phi \approx 0.5$

Although there are differences in the solution, results show that for this configuration and flow conditions, the flame dynamics are relatively insensitive to the subgrid turbulence-chemistry interaction model. Specifically, switching subgrid turbulence model does not dramatically alter the flame shedding in the bluff body near field. Similar conclusions concerning the sensitivity of combustion dynamics to subgrid models have been made for other simulations with various models [67, 57, 7, 12, 205, 43] and specifically with LEMLES [131, 216, 79].

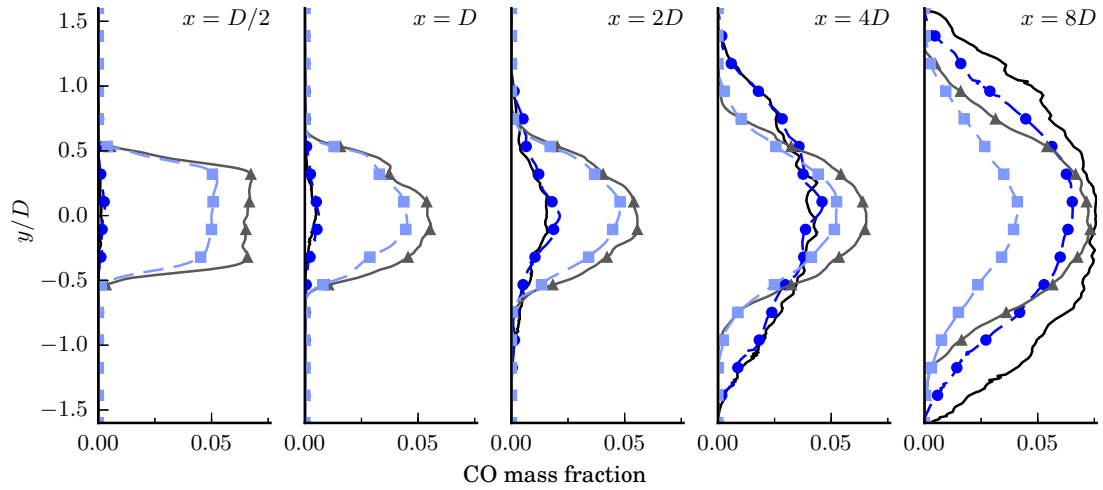

Figure 61 **Time-averaged CO mass fraction along centerline at several axial locations, (—) QL LES** $\phi \approx 0.95$**, (– • –) LEMLES** $\phi \approx 0.95$**, (–▲–) QL LES** $\phi \approx 0.5$**, (–■–) LEMLES** $\phi \approx 0.5$

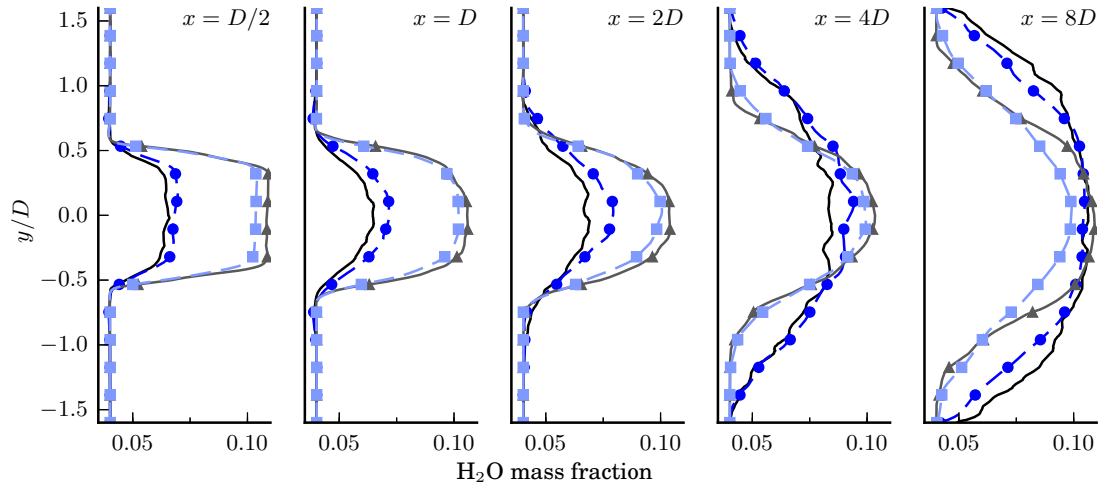

Figure 62 **Time-averaged H_2O mass fraction along centerline at several axial locations, (—) QL LES** $\phi \approx 0.95$**, (– • –) LEMLES** $\phi \approx 0.95$**, (–▲–) QL LES** $\phi \approx 0.5$**, (–■–) LEMLES** $\phi \approx 0.5$

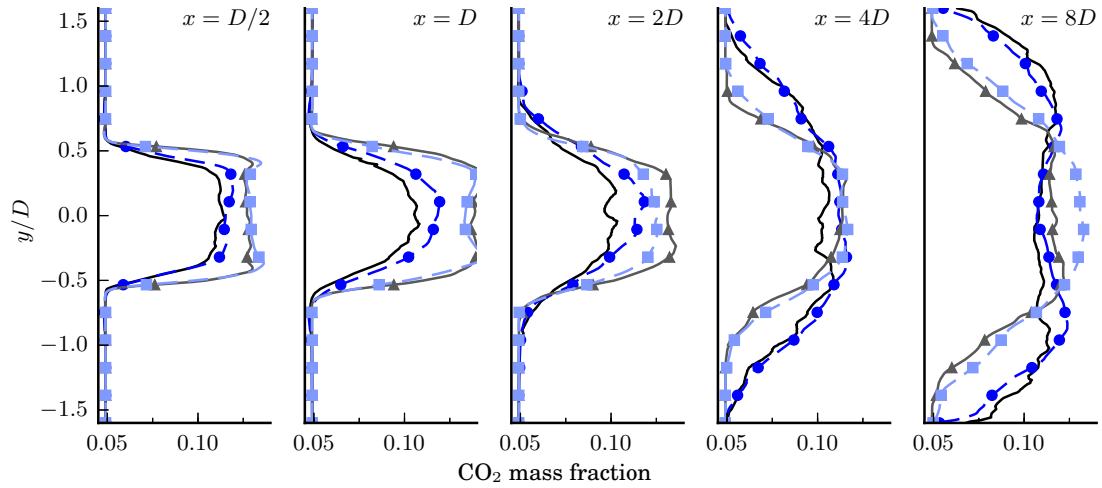

Figure 63 **Time-averaged CO_2 mass fraction along centerline at several axial locations, (—) QL LES $\phi \approx 0.95$, (– • –) LEMLES $\phi \approx 0.95$, (–▲–) QL LES $\phi \approx 0.5$, (–■–) LEMLES $\phi \approx 0.5$**

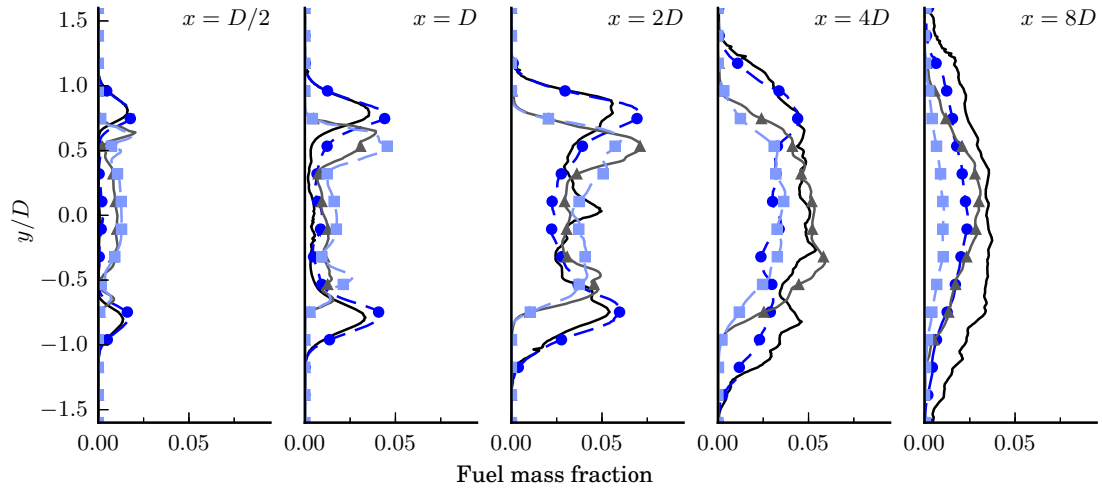

Figure 64 **Time-averaged fuel mass fraction along centerline at several axial locations, (—) QL LES $\phi \approx 0.95$, (– • –) LEMLES $\phi \approx 0.95$, (–▲–) QL LES $\phi \approx 0.5$, (–■–) LEMLES $\phi \approx 0.5$**

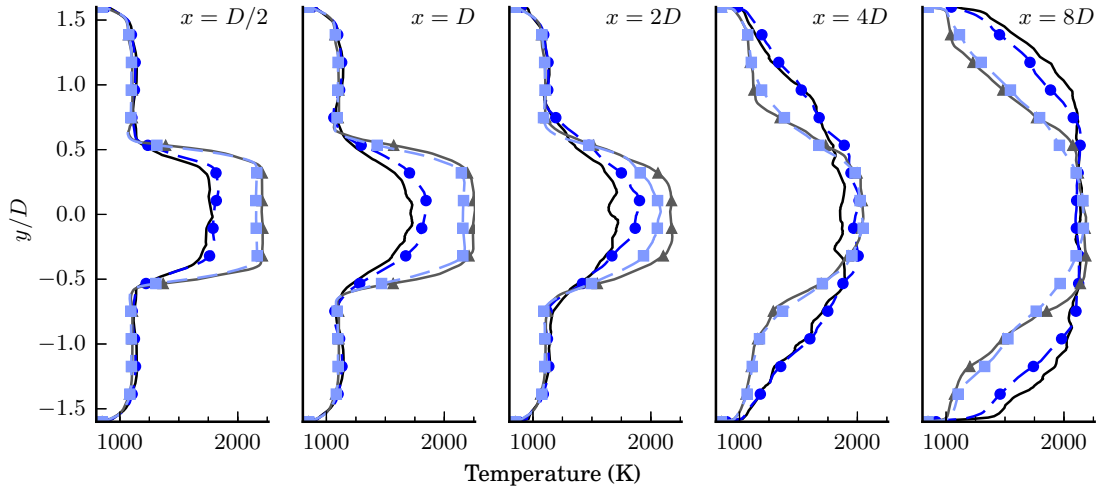

Figure 65 Time-averaged temperature along centerline at several axial locations, (—) QL LES $\phi \approx 0.95$, (– • –) LEMLES $\phi \approx 0.95$, (–▲–) QL LES $\phi \approx 0.5$, (–■–) LEMLES $\phi \approx 0.5$

Subgrid kinetic energy is often used as an input to subgrid turbulence-chemistry interaction models, as is the case for LEMLES, and can be used to estimate the influence of the model. In regions where k^{sgs} is high compared to the total turbulent kinetic energy, the subgrid turbulence-chemistry interaction model is expected to have more of an impact. Figure 66 shows the time-averaged ratio of subgrid kinetic energy to the total turbulent kinetic energy along the centerline. In the near-field behind the bluff body, the peak k^{sgs} is about 10% of the total turbulent kinetic energy, well below the threshold of 20% for a "good" LES [155]. Here the model is expected to have some impact especially considering the ratio of total turbulent kinetic energy, subgrid and resolved, to the total kinetic energy shown in Figure 67. For this bluff body configuration, most reactions occur past one bluff body diameter downstream of the trailing edge as seen in the instantaneous experimental images and LES snapshots. By this location the peak k^{sgs} is less than 10% of the total turbulent kinetic energy indicating the diminshing importance of the subgrid turbulence-chemistry interaction model. In addition the total amount of turbulent kinetic energy decreases away from the bluff body. This simplified *a posteriori* analysis does not imply that the impact of subgrid turbulence-chemistry interaction models is always limited, only that for this

geometry, flow conditions, grid, numerical method, etc. the main flow features are relatively insensitive to the model selection. The interactions of numerical method, grid resolution and subgrid model are all interconnected increasing the difficulty of assessing LES [108, 26].

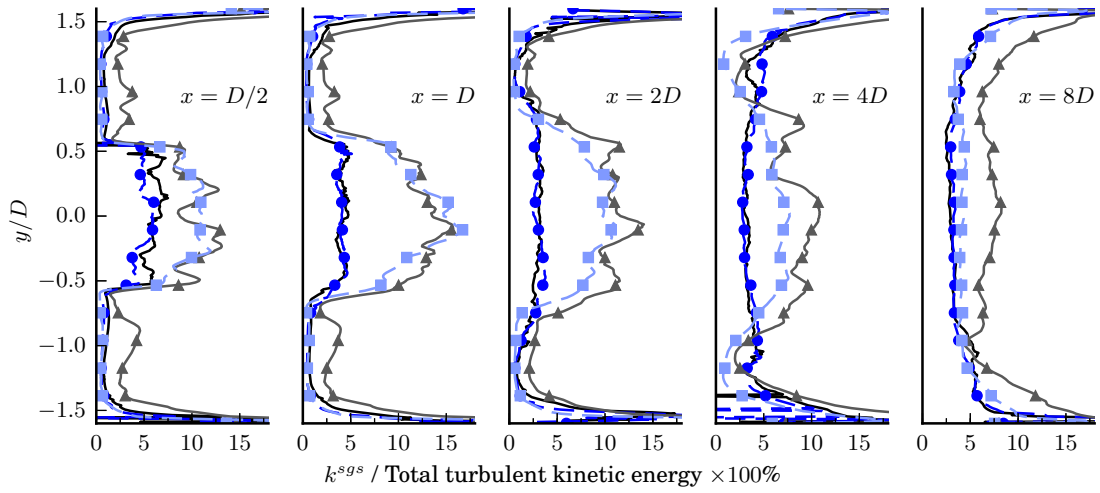

Figure 66 Time-averaged ratio of subgrid kinetic energy to the total turbulent kinetic energy along centerline at several axial locations, (—) QL LES $\phi \approx 0.95$, (– • –) LEMLES $\phi \approx 0.95$, (–▲–) QL LES $\phi \approx 0.5$, (–■–) LEMLES $\phi \approx 0.5$

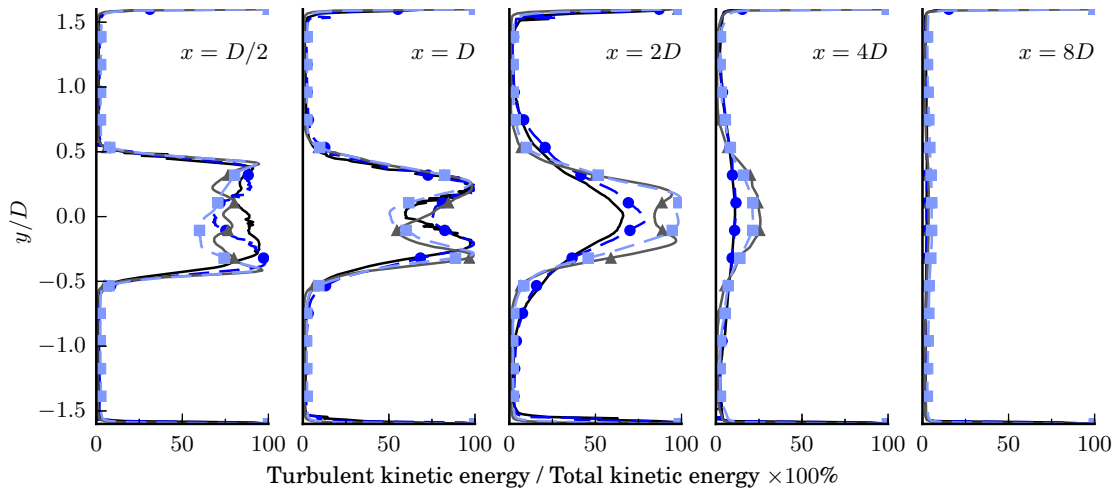

Figure 67 Time-averaged ratio of turbulent kinetic energy to the total kinetic energy along centerline at several axial locations, (—) QL LES $\phi \approx 0.95$, (– • –) LEMLES $\phi \approx 0.95$, (–▲–) QL LES $\phi \approx 0.5$, (–■–) LEMLES $\phi \approx 0.5$

The spanwise-averaged shear layer vorticity analysis was repeated for the LEMLES results and compared with the QL LES results in Figure 68. Again, there are few

obvious differences between the LEMLES and QL LES. To understand the differences in the shear layers at the two different flow rates, and how this possibly affects the overall flame dynamics, deltas were computed, i.e., $\Delta = u_{\phi\approx0.5} - u_{\phi\approx0.95}$, where u refers to any quantity of interest; here those quantities include fuel mass fraction, heat release rate, baroclinic torque and gas expansion. The deltas were normalized by the same values discussed in Section 6.4.1 and plotted in Figure 69. The LEMLES and QL both show the same trends for all four values. Comparing the deltas of the baroclinic torque term and gas expansion term shows that both the normalized and, based on the normalization factor, absolute difference in the baroclinic torque term between the low fuel flow rate case and the high fuel flow rate case is greater than the delta in the gas expansion term. The comparatively larger delta is most apparent in the near-field just behind the bluff body. This relative importance of the increased baroclinic torque generation over the gas expansion for the suppression of large scale vortical structures has also been observed in other bluff body flame studies [156, 157, 138, 139].

Figure 70 shows axial slices of the time averaged baroclinic torque term and the

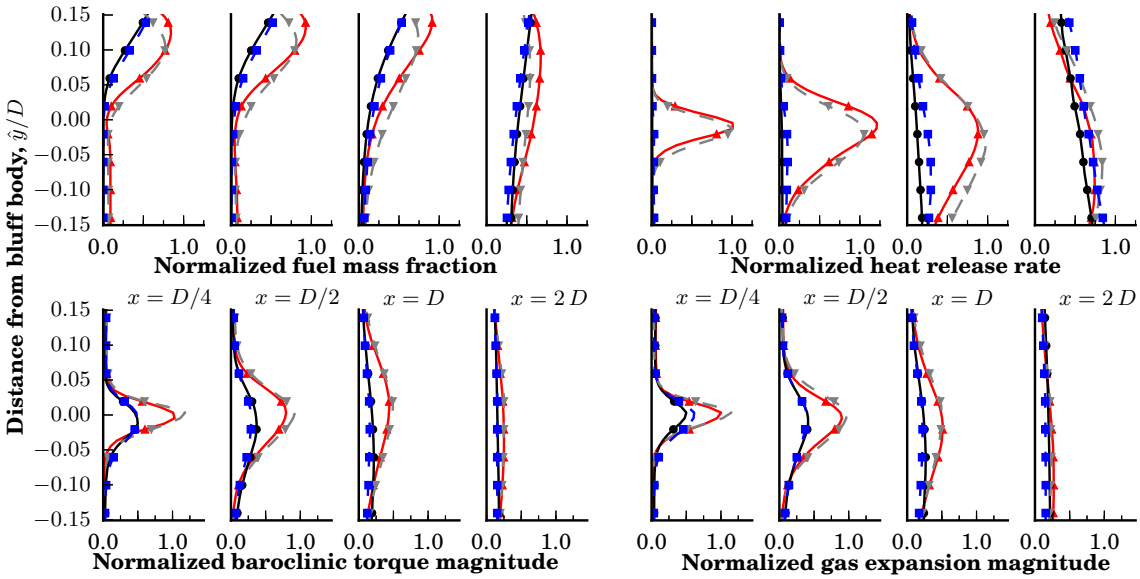

Figure 68 Spanwise and time-averaged quantities in the shear layers at several axial locations, (–●–) $\phi_{\text{global}} \approx 0.95$ QL LES, (–▲–) $\phi_{\text{global}} \approx 0.5$ QL LES, (- - ■ - -) $\phi_{\text{global}} \approx 0.95$ LEMLES, (- - ▲ - -) $\phi_{\text{global}} \approx 0.5$ LEMLES

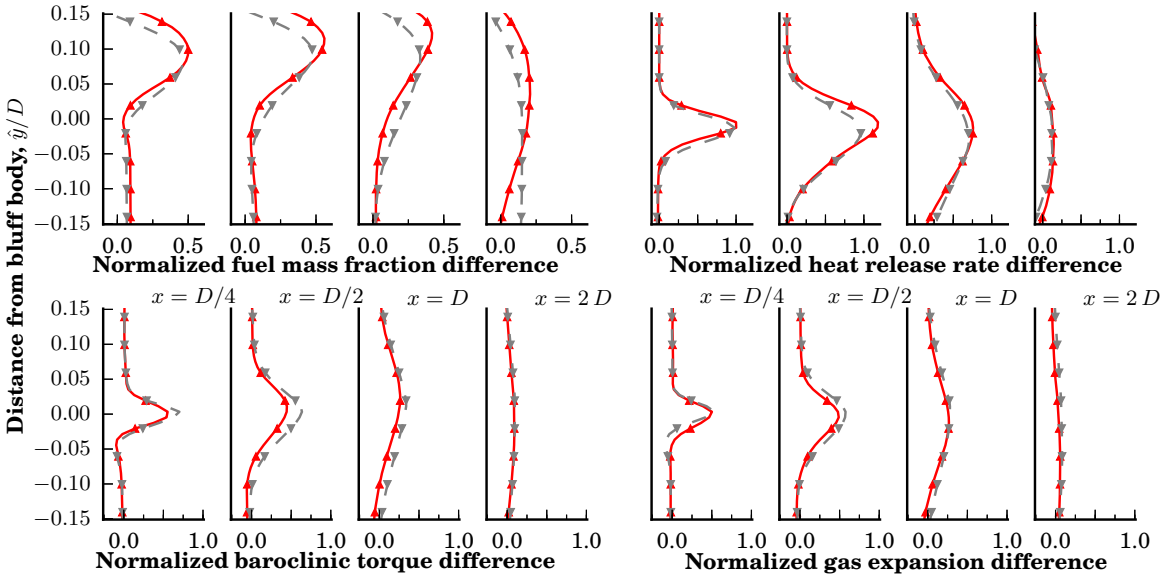

Figure 69 Normalized differences between low fuel flow rate and high fuel flow rate spanwise and time-averaged quantities in the shear layers at several axial locations, (−▲−) QL LES, (- - ▲ - -) LEMLES

slices of gas expansion the high and low fuel LEMLES; all are plotted using the same scale. Baroclinic torque and gas expansion have peak values in the shear layers due to the wall generated vorticity present and the large density ratio between the hot recirculating products and the colder incoming reactants. At these near-field locations the density and temperature gradients are much steeper for the low fuel flow rate case compared with the high fuel flow rate case, as also seen in Figure 65, which contributes to the larger baroclinic torque generation. Both baroclinic torque and gas expansion also appear in the regions surrounding the fuel jets where some non-premixed combustion occurs. On average, baroclinic torque and gas expansion are seen in the same physical locations though the gas expansion is less intense. The baroclinic torque is also greater than the gas expansion father downstream since density and pressure gradients along the flame front still exist but the wall generated vorticity is reduced noting that the gas expansion term is related to the magnitude of the vorticity itself. At the $x = D$ and $x = 2D$ locations the high fuel flow rate case starts to show higher values of baroclinic torque and gas expansion in the center

region directly behind the bluff body. At this downstream position the large scale shedding is entraining the evaporated fuel from the liquid jets and high heat release takes place.

Instantaneous snapshots of the same quantities are shown in Figure 71. As expected, the low fuel flow rate images look very similar to their time averaged counterparts since the lack of large scale shedding results in a stable flame. The instantaneous pictures of the high fuel flow rate are much less diffuse than the time averaged images and at this relatively close downstream location the baroclinic torque and gas expansion show strong correlation with the fuel jet locations.

In an effort to quantify the fluctuations of the flame and compare with experimental results, image processing was used to measure the locations of the flame edges. This is still a somewhat qualitative measure, however, since the experimental and computational images are not showing the exact same value and some user input is required to select the inputs for image processing. A series of images from the LES and high-speed movies were processed with the following method. Each spanwise-averaged image was modified to increase the contrast which was followed by the application of a canny filter [17] to detect the flame edges. Figure 72 shows an example of the original image, the modified image and the flame edges as detected by the Canny filter. The maximum and minimum edge locations in the y-direction as identified by the filter were computed at each axial location. The mean and rms values of the flame location were then plotted and compared for both the low fuel flow rate and the high fuel flow rate and shown in Figures 73. These data reinforce the earlier observation that in the near-field behind the bluff body the LEMLES and QL LES simulations give similar results. Both the mean and rms flame edge values begin to deviate from each other around $x = 4D$. For both fuel flow rates, the LEMLES predicts a narrower flame in the vertical direction with more fluctuations. In the first two to three bluff body diameters both the LEMLES and QL results match well with

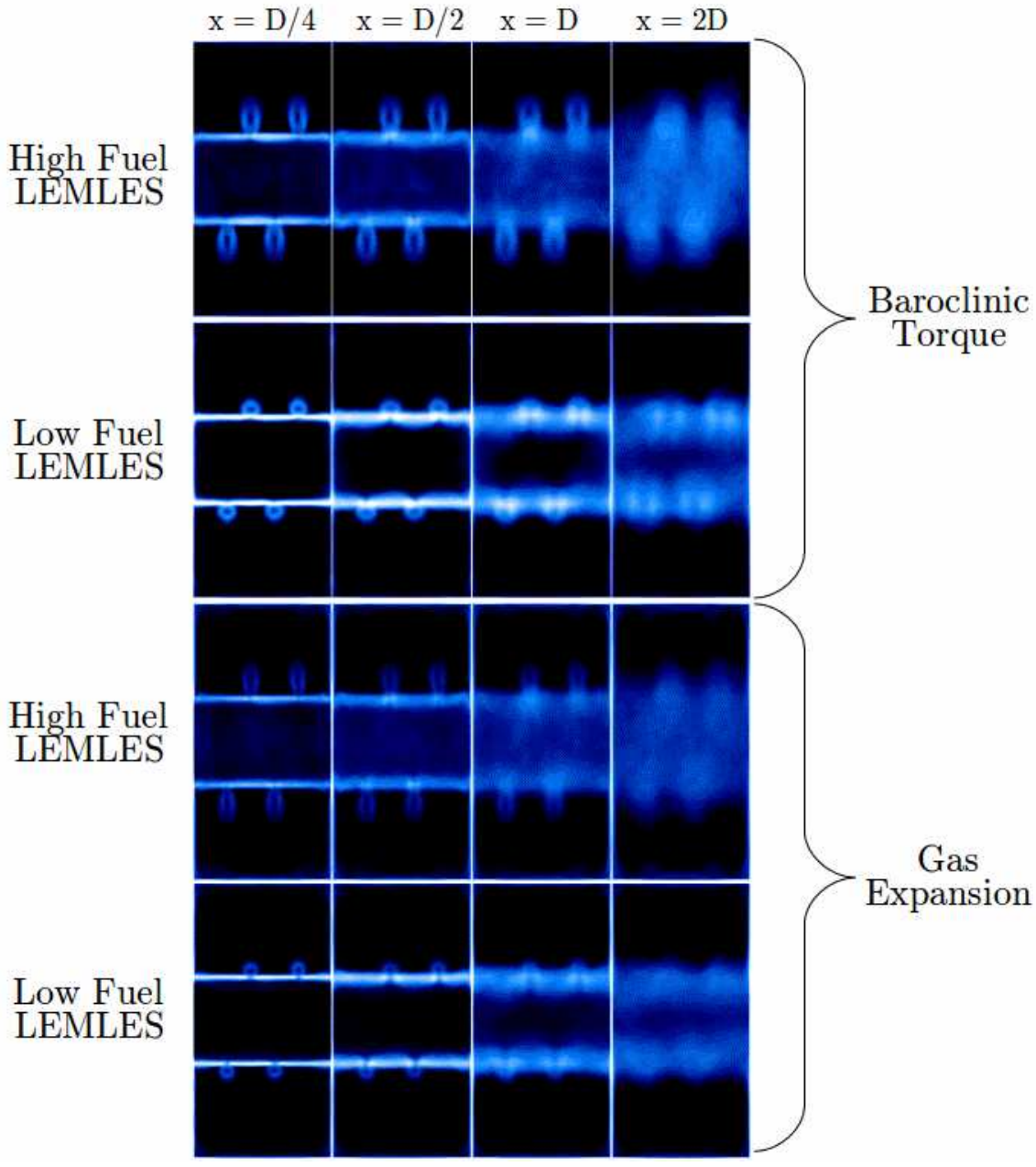

Figure 70 Time averaged baroclinic torque and gas expansion at several axial locations for the high and low fuel LEMLES.

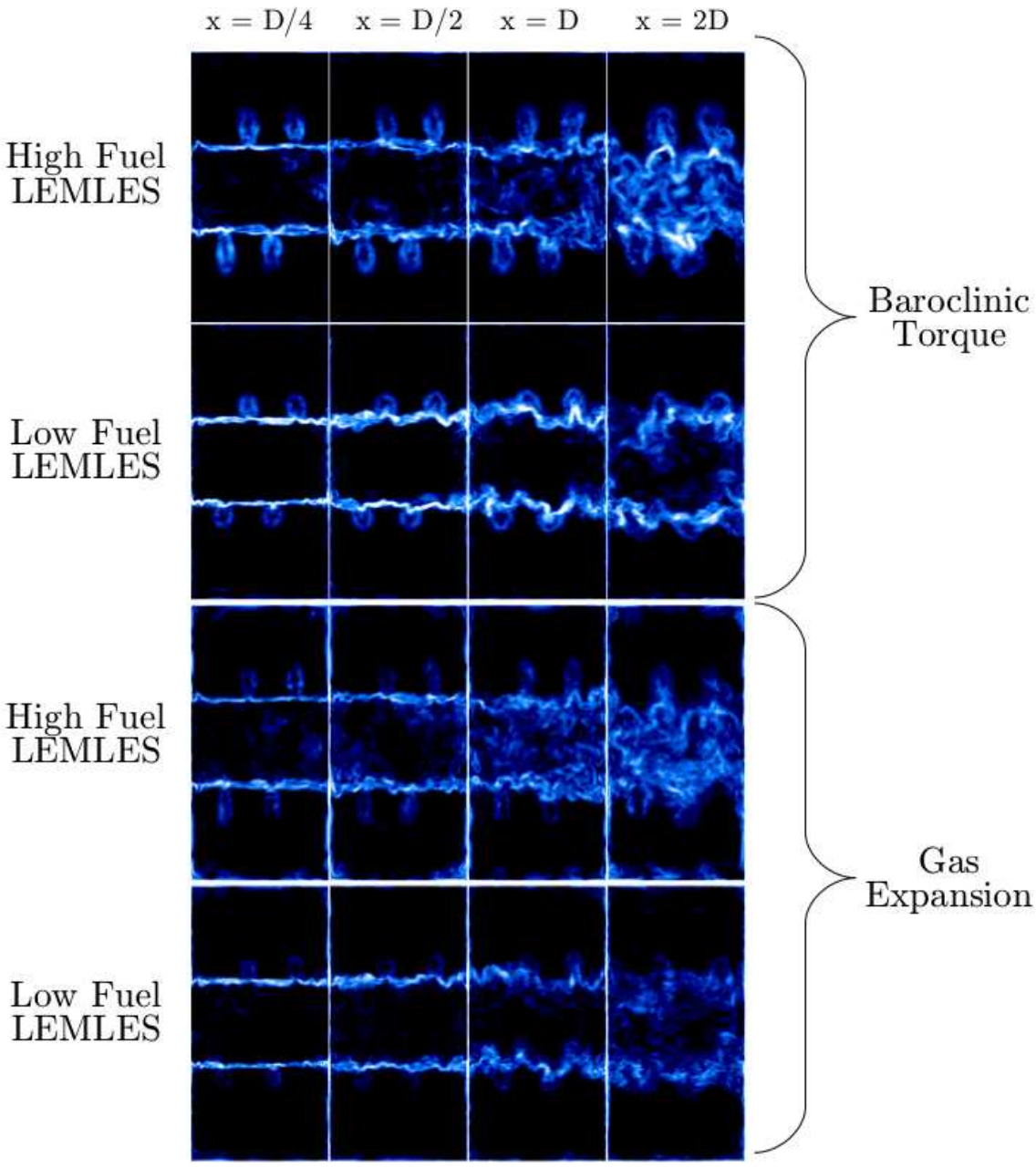

Figure 71 Instantaneous snapshots of baroclinic torque and gas expansion at several axial locations for the high and low fuel LEMLES.

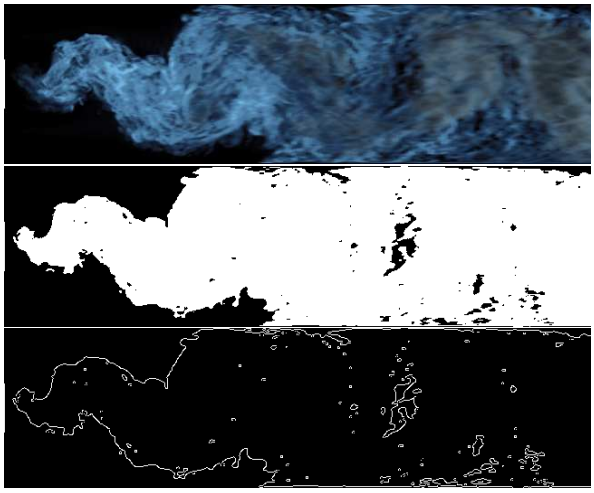

Figure 72 Sequence of image processing used for the flame edge analysis, original image (top), enhanced contrast (middle) and flame edges after applying a Canny filter (bottom).

the experimental data. The LEMLES results from the high fuel flow rate case do not deviate with the QL and experiments significantly until $x/D > 6$ whereas the low fuel flow rate rms results from LEMLES show much larger fluctuations after $x/D > 4$.

The fluctuations in the flame width were computed based on the upper and lower flame edges and shown in Figure 74. The upper and lower flame edges were averaged to compute the mean flame location in the previous figure hence the mean flame width is simply twice that value so here the only quantity of interest is the rms of the flame width. The comparative trends for the flame width fluctuations are nearly identical to those for the edge rms, though in this case the low fuel LEMLES results match more closely with experiments farther downstream. It is also interesting to note that at the high fuel flow rate both the QL LES and LEMLES show the small peak in flame width oscillations around $x/D = 0.75$ and the trough near $x/D = 1.25 - 1.45$ that is seen in the experiments.

The Strouhal number for the high fuel flow rate cases was calculated by computing a fast Fourier transform (FFT) of the flame edge location, $\hat{y}$, at the downstream location of peak fluctuations, $x/D \approx 4$. Analysis from the experiments, QL LES and LEM LES yield Strouhal numbers of $St = 0.21$, $St = 0.22$ and $St = 0.22$,

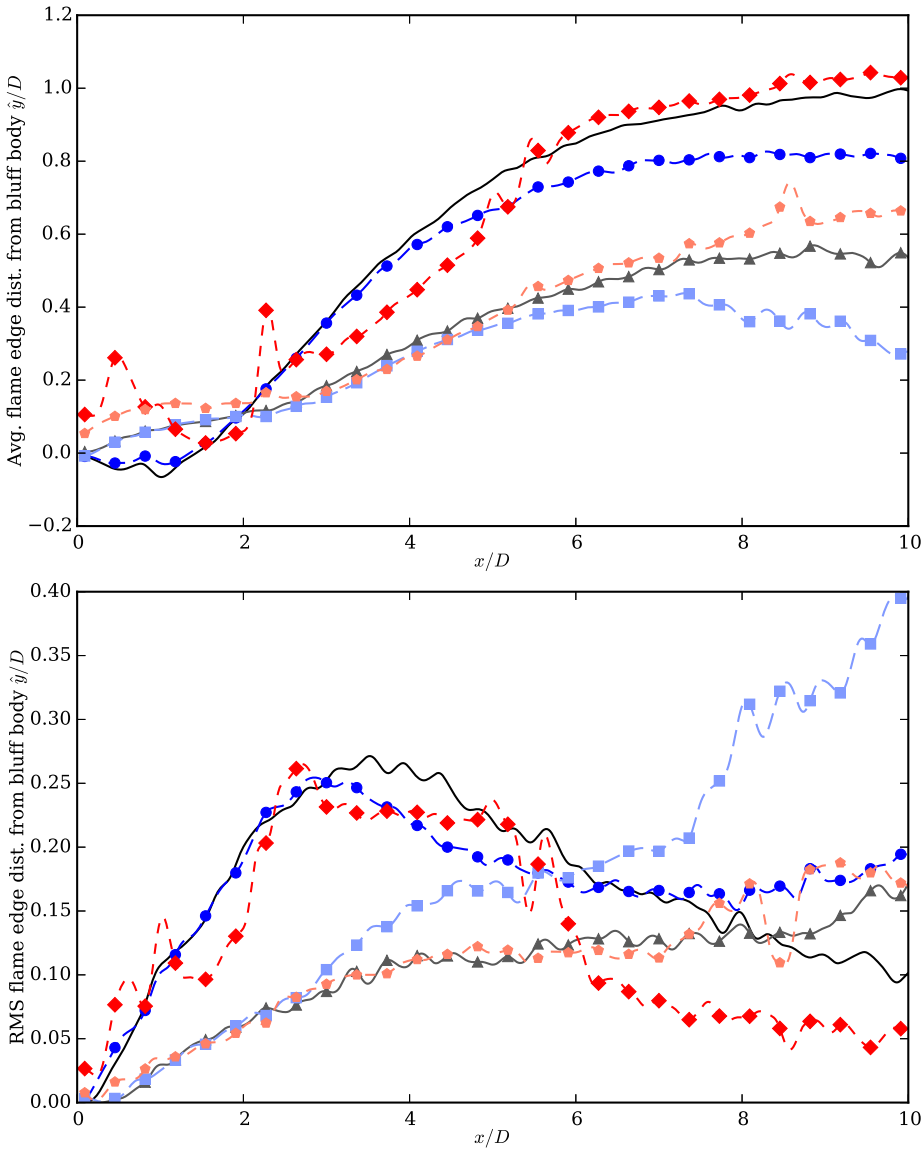

Figure 73 **Time-averaged flame edge vertical distance away from the bluff body (top) and root mean squared value of the same quantity (bottom), (- - ◆ –) Exp** $\phi \approx 0.95$**, (- - ⬟ - -) Exp.** $\phi \approx 0.5$**, (—) QL LES** $\phi \approx 0.95$**, (– ● –) LEMLES** $\phi \approx 0.95$**, (–▲–) QL LES** $\phi \approx 0.5$**, (–■–) LEMLES** $\phi \approx 0.5$

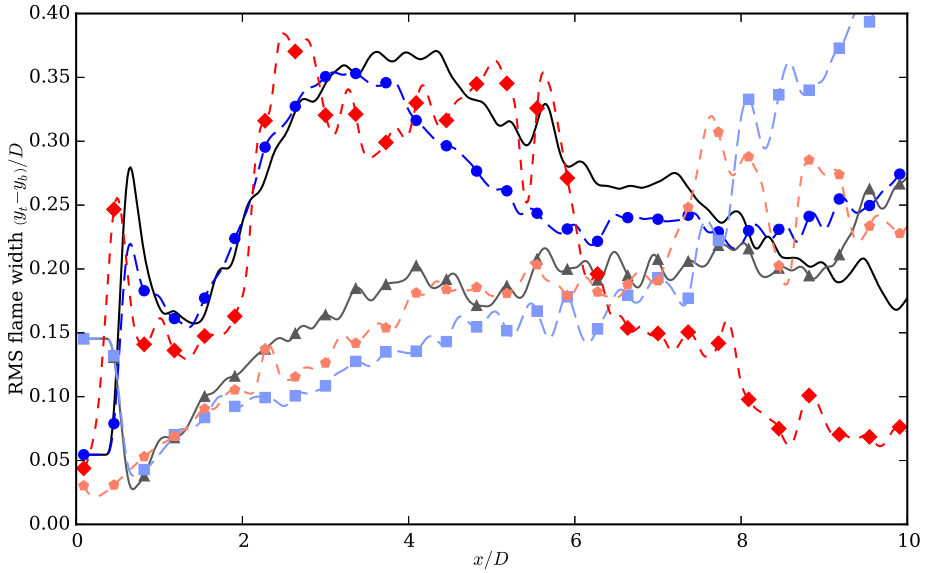

Figure 74 Root mean squared flame width, (- - ◆ –) Exp $\phi \approx 0.95$, (- - ⬟ - -) Exp. $\phi \approx 0.5$, (—) QL LES $\phi \approx 0.95$, (– ● –) LEMLES $\phi \approx 0.95$, (–▲–) QL LES $\phi \approx 0.5$, (–■–) LEMLES $\phi \approx 0.5$

respectively, based on the bluff body lip velocity. This successful prediction of the shedding frequency gives additional confidence in the simulations.

6.6 Influence of numerical method on reacting high fuel flow simulation

To understand the effect of numerical method on this class of problems, the high fuel flow rate simulation was repeated using the conservative finite difference method detailed in Section 4.6. [151, 44, 231] This study is conducted since previous research has emphasized the importance of the numerical method for reacting flow simulations [151, 228, 27]. The quasi-laminar subgrid turbulence-chemistry interaction model was used to understand the direct impact of the numerical method alone. As with the finite volume simulations, a hybrid methodology was used because of the large density gradients due to the evaporating fuel and the density discontinuity at the flame front. The central scheme selected was the sixth-order compact scheme which was paired with the fifth-order WENO-Z method with complete details of the numerical methods given in Chapter 4.

Compact central finite difference methods are often used for simulating turbulent flows because of their low numerical dissipation [113, 227, 225], but because of this, cannot be used in flows where large gradients are present. WENO schemes, which are more dissipative but are applicable in flows with large gradients, have been applied by themselves to LES of non-reacting and reacting flows, [43, 192, 90, 245]. WENO methods have also been used to solve the Euler equations in combination with Lagrangian particle tracking methods [85, 134, 37, 42] and reacting flows with Lagrangian particles [178]. Hybrid explicit central, compact central or compact upwind / WENO finite difference methods have also been used for a variety of DNS and LES on Cartesian and curvilinear grids [150, 168, 103, 30, 191, 208, 20, 229, 246, 42, 169, 206, 159, 162] None of these hybrid methods use the same combination of central, WENO, viscous and time integration schemes as the method developed in this thesis, and only a few have been used for reacting flows [246, 159] or Eulerian-Lagrangian simulations [170]. This brief review of the use of similar numerical methods in various applications again highlights the uniqueness of the current approach in terms of the numerical method, specifically the combination of methods required for the hybrid central/upwind scheme, as well as the problem on which it is being applied. To the author's knowledge, this is the first application of a hybrid compact/WENO-Z finite difference solver for LES of multiphase, reacting flows on curvilinear grids.

The specific details of the flow solver are provided here for reference. The fluxes for the WENO procedure were split using the Roe flux with entropy fix for all genuinely non-linear characteristics and the local Lax-Friedrichs flux for the linearly degenerate characteristics. The WENO-Z power parameter was set as $p = 2$ and the epsilon value was $\epsilon = 1 \times 10^{-40}$. The compact eigth-order filter was used away from discontinuities with $\alpha_f = 0.49$. The viscous terms were computed using the fourth-order accurate method with odd-even decoupling correction "centered" coefficients. These solver settings were selected to minimize numerical dissipation yet still provide a stable

solution.

Time was advanced using the SSPRK(5,4) method for both Eulerian and Lagrangian phases. The use of the high-order time integration scheme allows for larger time steps; here the time step was increased by approximately 30% compared with the baseline simulation. Overall the high-order finite difference simulations took around 35% more total CPU time than the second-order finite volume simulations.

Instantaneous spanwise averaged images are shown; in this instance the finite difference simulation results are compared with the finite volume results in Figure 75. These spanwise-averaged results show little differences between the two simulations, with the flame dynamics of the experiments being correctly captured by both methods.

The spanwise and time averaged heat release rate of the FD simulations is compared with the FV results in Figure 76. Here some differences can be seen, particularly in the shear layers just behind the bluff body. Figure 77 focuses on this region and compares the experiments with the results from all three simulations, QL LES FV, LEMLES (FV) and QL LES FD. The highlighted shear layer zone in the experimental image clearly shows some heat release anchored to the bluff body in the shear layer and a region of little heat release just behind the bluff body in the recirculation zone. The QL LES FV does have some heat release in the shear layers but it is less intense than the experiments and the "dead" zone behind the bluff body is smaller than in the experiments. The LEMLES results show much more pronounced shear layer heat release that matches more closely with the experiments. The QL LES FD results, in this particular region, appear to match with the experimental data the best though the heat release layers in the upper and lower bluff body shear layers are slightly less diffuse than the experiments. The "dead" zone behind the bluff body is larger than in the other two simulations but still slightly smaller than the experiments. These

results are not too surprising in the sense that the LEMLES acts more like the high-order scheme in the shear layer region. The subgrid lines provide additional resolution in the flame/shear layer-normal direction. As discussed in Section 6.5, the subgrid linear eddy model has the most impact in the regions where subgrid turbulent kinetic energy is highest, which is in the shear layers just behind the bluff body.

The flame edge analysis was repeated for this dataset and compared to the experimental data in Figure 78. The mean and rms flame edge positions for the finite difference and finite volume solution are nearly identical with the high-order method rms value slightly closer to the experimental data. Due to the still somewhat qualitative nature of this image analysis, this particular evidence is not enough to say the FD method is conclusively better than the FV method. The similarity of the two simulations does give more confidence to the baseline simulations. The FFT analysis was also repeated for the FD simulation of the high fuel flow rate case and gave $St = 0.22$. All simulated values, regardless of numerical method or subgrid turbulence-chemistry interaction model, were close to the experimental value of $St = 0.21$.

The flame width rms shows the FD results under-predicting the flame width oscillations around $x/D = 3$ as shown in Figure 79. The FD also under-predicts the first peak at $x/D = 0.75$ but matches better with the experiments for the FV solution at the local rms minimum at $x/D = 1.24 - 1.45$.

Time-averaged centerline line plots also reveal subtle differences. The finite difference solution has slightly higher temperatures in the recirculation zone and higher temperature fluctation values in the shear layers as seen in Figure 80 and Figure 81, respectively. This could indicate the ability of the higher-order method to resolve smaller fluctuations in the shear layer because of lower numerical diffusion. This difference in shear layer feature resolution is shown in Figure 82 which shows a slice in the spanwise direction taken at a fuel injector location of temperature for both the simulations. The finite difference solution shows much more defined small-scale

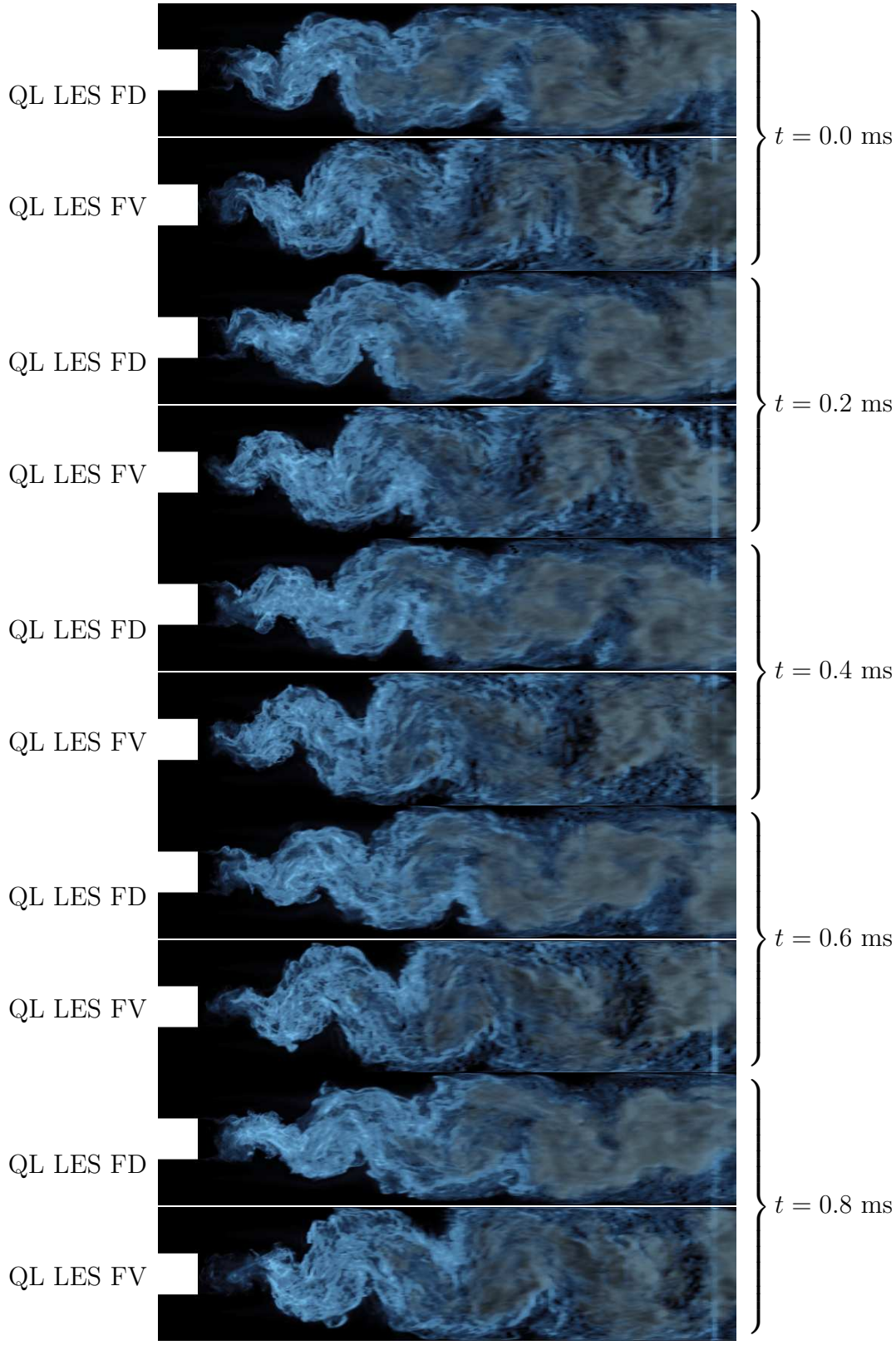

Figure 75 Comparison of finite difference LES with the finite volume LES flame image sequence (spanwise averaged CO and CO_2 mass fraction overlaid on heat release rate) at $\phi \approx 0.95$

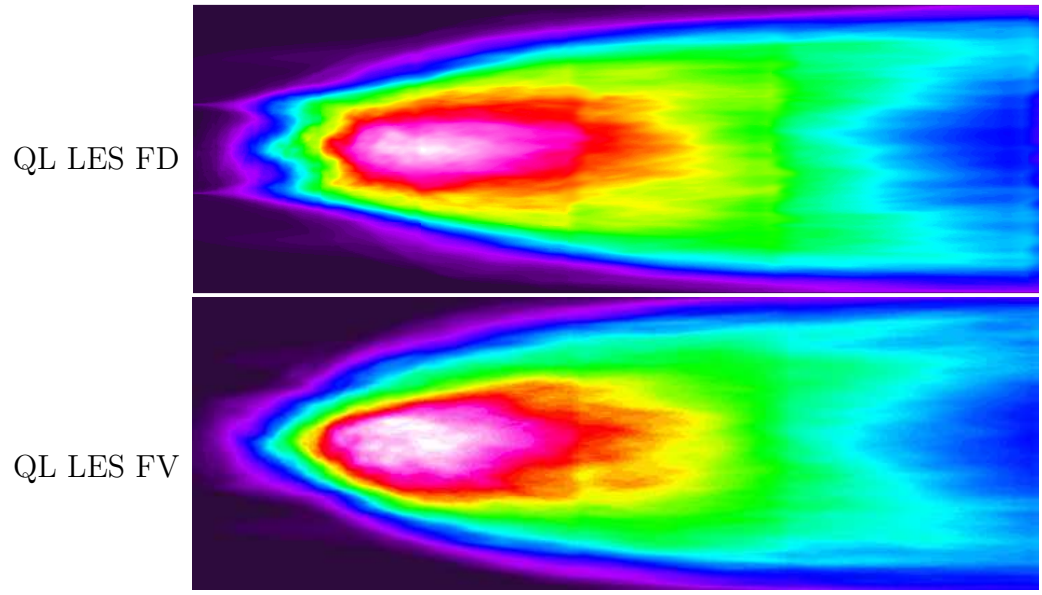

(a) $\phi_{\textbf{global}} \approx 0.95$

Figure 76 Comparison of time averaged heat release rate obtained with finite difference and finite volume LES for the high fuel flow rate case.

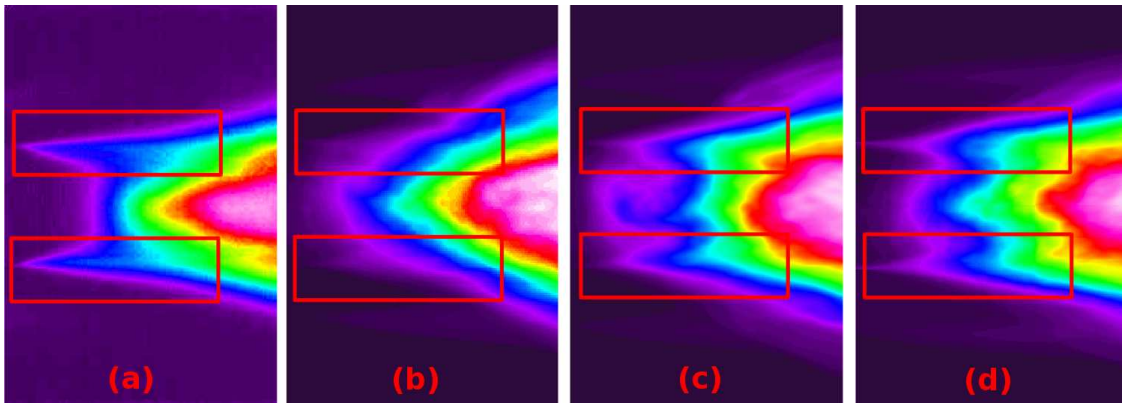

Figure 77 Comparison of time averaged heat release rate in the bluff body near field for the high fuel flow rate case for (a) experiments, (b) QL LES FV, (c) LEMLES, and (d) QL LES FD.

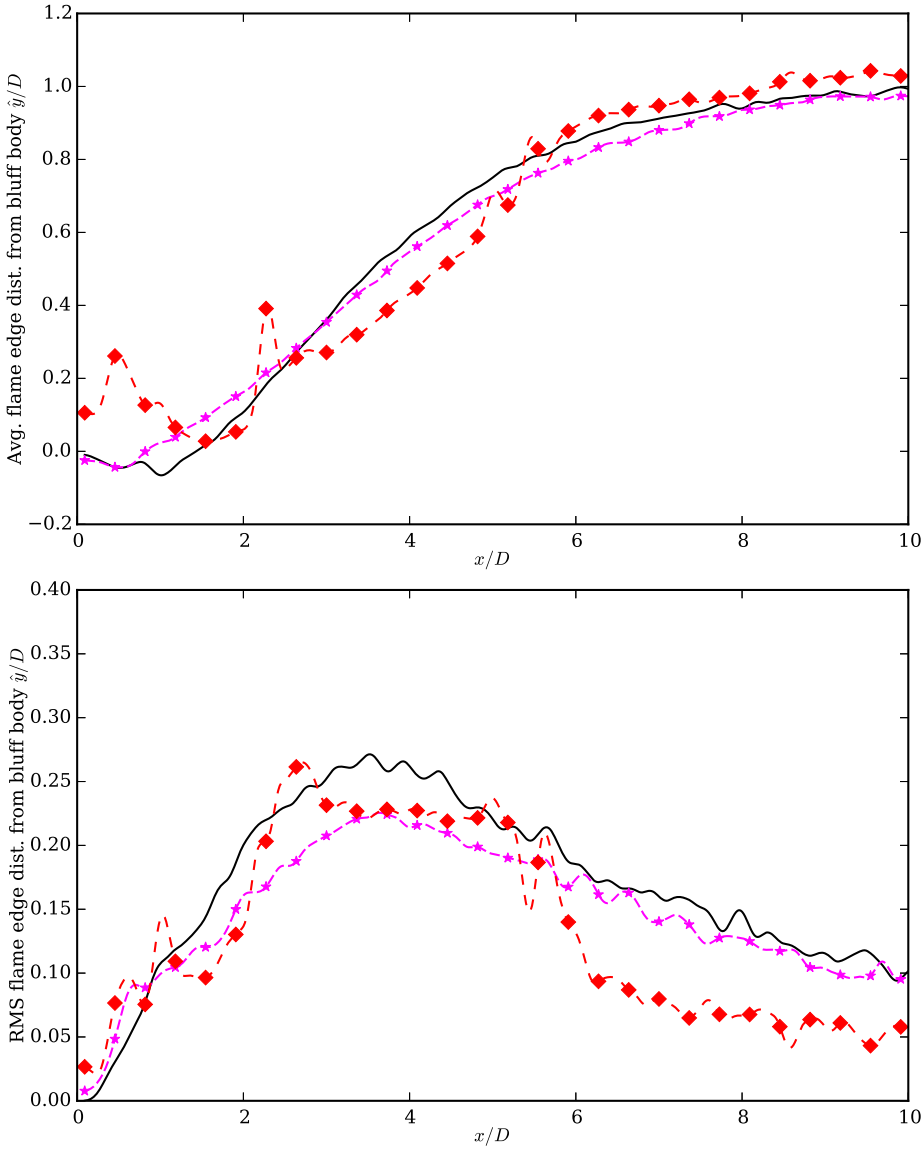

Figure 78 Time-averaged flame edge vertical distance away from the bluff body (top) and root mean squared value of the same quantity (bottom), (- - ◆ –) Exp $\phi \approx 0.95$, (—) QL LES FV $\phi \approx 0.95$, (- - ● - -) QL LES FD $\phi \approx 0.95$

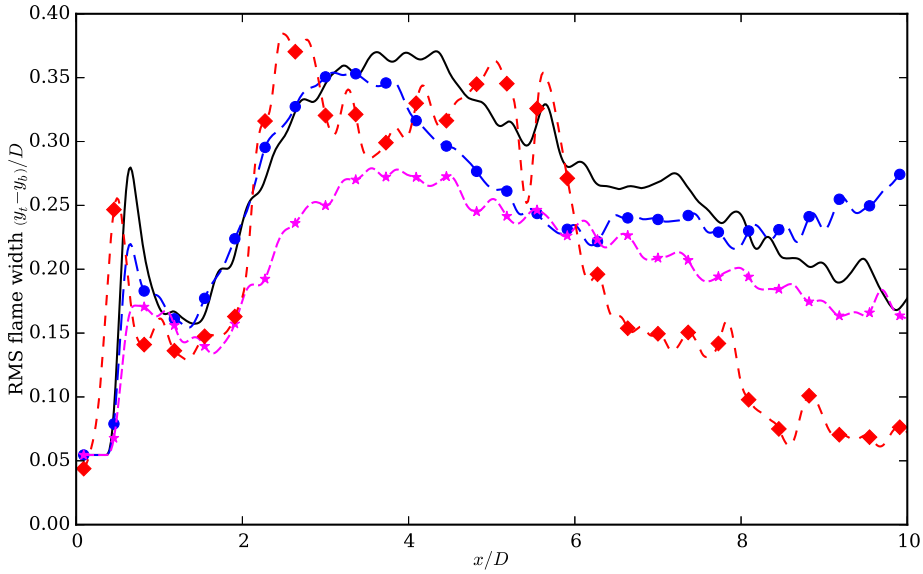

Figure 79 Root mean squared flame width, (- - ◆ –) Exp $\phi \approx 0.95$, (- - ⬟ - -) Exp. $\phi \approx 0.5$, (—) QL LES FV $\phi \approx 0.95$, (- - ● - -) QL LES FD $\phi \approx 0.95$

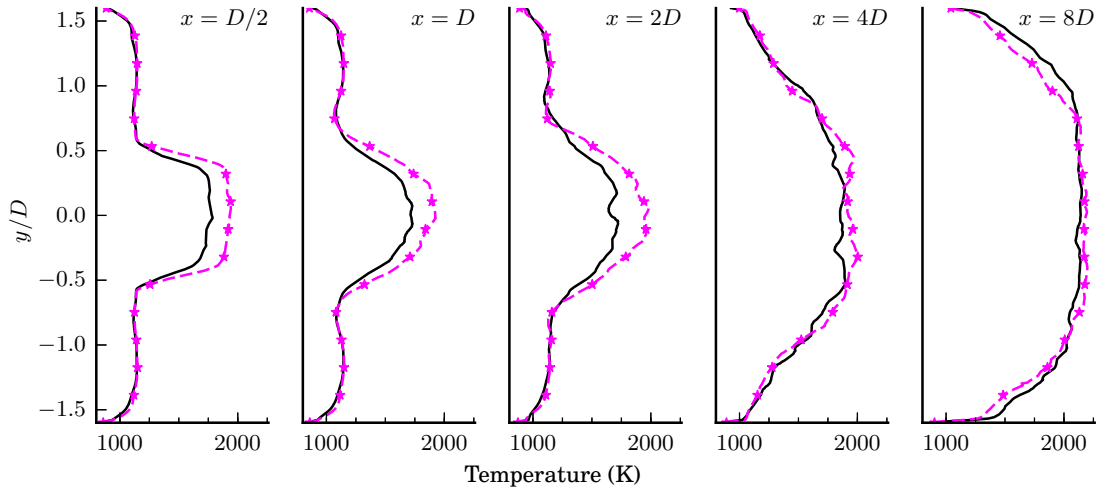

Figure 80 Time-averaged temperature along centerline at several axial locations, (—) QL LES FV $\phi \approx 0.95$, (- - ● - -) QL LES FD $\phi \approx 0.95$

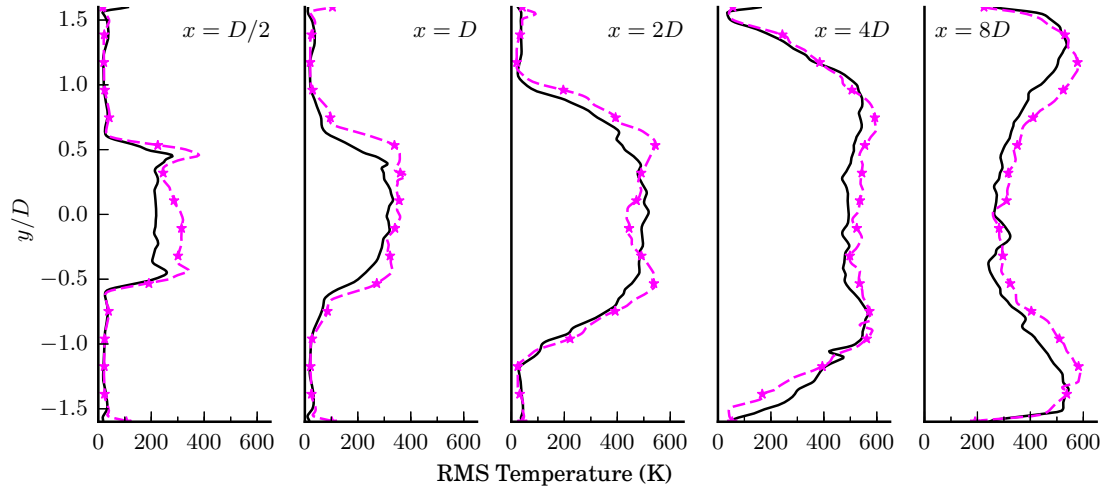

Figure 81 Time-averaged root mean squared temperature along centerline at several axial locations, (—) QL LES FV $\phi \approx 0.95$, (- - • - -) QL LES FD $\phi \approx 0.95$

structures in the shear layers behind the bluff body.

The time- and spanwise-averaged heat release rate comparisons suggest the high-order FD results are more accurate than the second-order FV solutions, as expected. With the limited experimental data available for comparison, it is difficult to explicitly quantify the improvements. These simulations do demonstrate that high-order FD methods can be successfully applied to multiphase, reacting LES.

Based on the coldflow analysis presented in Section 6.3.1, the resolved turbulent kinetic energy spectrum shown in Figure 32 and the fact that the reacting LES captured the two distinct flame dynamics using the baseline grid, we assume the grid has adequate resolution and thus no explicit grid independence study was completed for the reacting flow simulations, which is similar to previous research [104, 54, 219, 149, 135]. Repeating simulations on the same grid with higher-order methods, as done for this study, is another method to prove grid insensitivity [172, 108]. The overall results were shown to be similar between the second-order FV and high-order FD, though some differences do exist in the near-field shear layers, indicating the adequate mesh resolution.

In this study coarser grids or lower-order methods were not examined, though

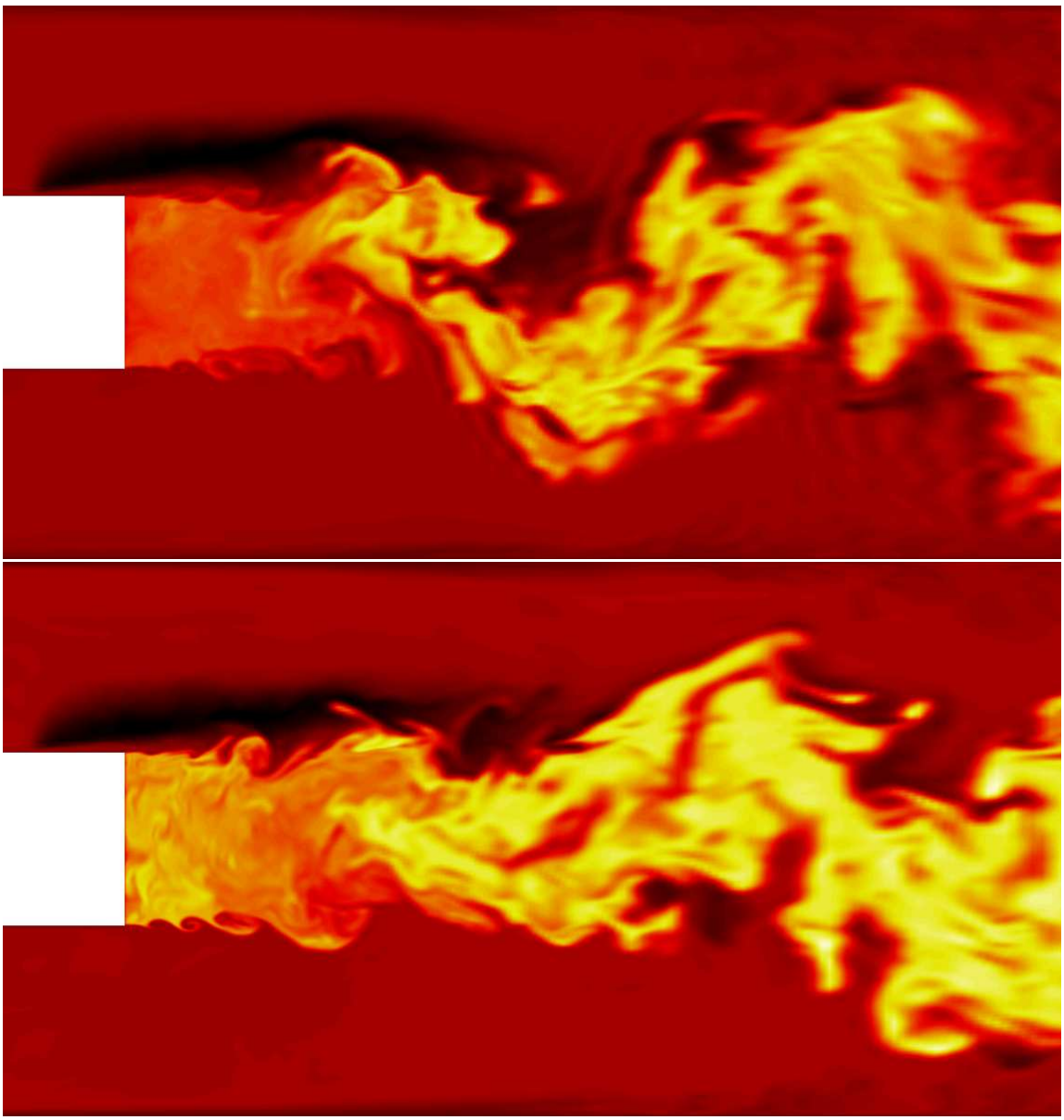

Figure 82 Temperature contours comparing shear layer structures between the finite volume (top) and finite difference (bottom) solutions.

grids are often coarser in industry compared with academic settings. Thus it would be useful to estimate the impact of the subgrid model or numerical method for coarser grids in the current application. Many industrial CFD codes allow for user-defined functions to implement subgrid models but the main flux schemes usually cannot be modified. As such, here the focus is only on the impact of the subgrid model, specifically LEMLES, on coarser grids. Limiting the discussion to "good" LES, where the subgrid kinetic energy only accounts for 20% of the total kinetic energy [155], the results from the low fuel flow rate cases in Figure 66 show that such a simulation would have approximately twice as much subgrid kinetic energy as the current LES. Based inertial range scaling estimates, the mesh size in the shear layer layer would be between $1.5 - 2$ times the current grid. In order to maintain the correct subgrid LEM resolution the amount of LEM cells per LES cell would also increase by a factor of 1.5 to 2. The explicit time step for the coarser grid could be as much as four times larger since the near-wall viscous stability limits scale as Δx^2. With the combination of more subgrid kinetic energy, more LEM cells per LES cell and larger time step, implying a larger number of subgrid turbulent stirrings per LES time step, the impact of LEMLES is expected to be greater, and thus the differences between LEMLES and the QL model larger, in the near-field and persist farther downstream. The greater number of stirring events and larger physical time step would also mitigate scalar dissipation errors related to the splicing events [132]. Larger grid sizes would also reduce the error associated with the lack of inter-cell molecular diffusion [188, 79] in the LEMLES model.

The simulations in this work indicate relative insensitivity of the overall flame dynamics to numerical method, Figure 75, or subgrid model, Figures 56 and 57, but Figure 77 shows that the near-field in the shear layers and reaction zone are sensitive. At coarser mesh resolutions, the dominant flame dynamics, i.e. symmetric vs sinusoidal shedding, would most likely be observed with a less sophisticated subgrid

model as long as the liquid jet-in-crossflow was correct, but the details of the near-field reaction zone, including the reaction rate and temperature profiles, may be predicted incorrectly. The near-field reaction and recirculation zone is particularly important for the estimation of temperatures near the bluff body which have an impact on heat transfer and cooling requirements for the system [118].

6.7 Simulations with modified fuel injectors

Based on the previous analysis, the main driver of the flame dynamics of this liquid-fueled, close-coupled injector configuration is the fuel spray penetration. In order to further test this hypothesis, a third configuration was simulated by modifying the fuel injector diameter to match the spray penetration of the low fuel flow rate case while maintaining the fuel flow rate of the high flow rate case. This required a fuel injector diameter of 0.9525 mm compared to 0.635 mm used for the baseline cases. With the total mass flow rate of 31.23 g/s and a discharge coefficient set to 0.5555, the spray jet inlet velocity was set to 25.082 m/s. Different injector diameters have been tested experimentally on a similar rig [110], but not on this particular configuration.

Figure 83 shows an image of the spray penetration of the original injector at the low and high fuel flow rates and the new injector at the high fuel flow rate. Qualitatively, the liquid jet penetration of the new injector closely matches that of the low fuel flow rate with the baseline injector. It must be emphasized that apart from the injector

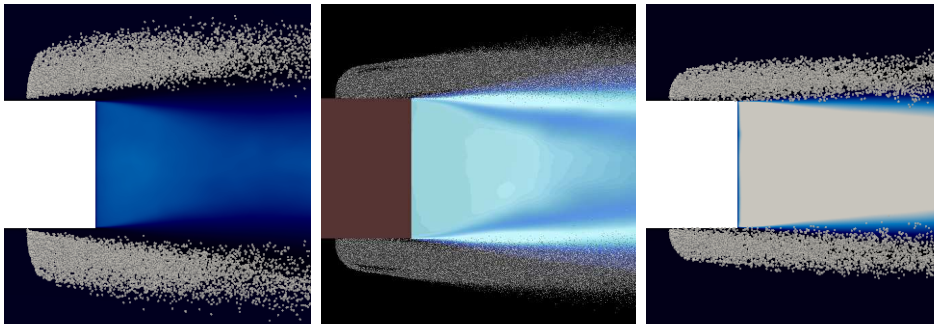

Figure 83 Comparison of spray penetration for $\phi_{\text{global}} \approx 0.95$ with the original injectors (left), $\phi_{\text{global}} \approx 0.5$ with the original injectors (middle), and $\phi_{\text{global}} \approx 0.95$ with the modified, larger injectors (right)

size, the injector spray breakup model and all parameters associated with that model are identical across all simulations. The spanwise-averaged, time-averaged fuel mass fraction is shown in Figure 84.

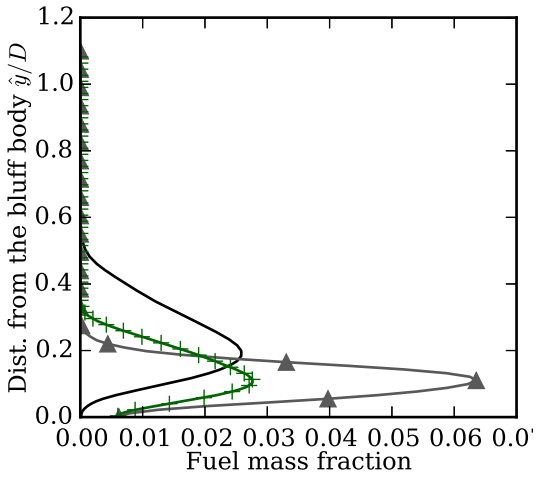

Figure 84 Spanwise-averaged, time-averaged fuel mass fraction at the bluff body trailing edge for (—) $\phi_{\text{global}} \approx 0.95$ with the original injectors, (–▲–) $\phi \approx 0.5$ with the original injectors and (–+–) QL LES $\phi \approx 0.95$ with the modifed larger injectors.

Based on the fuel penetration, the resulting flame dynamics of the larger injector at the high fuel flow rate should be similar to the baseline injector at the low fuel flow rate: relatively symmetric shedding without large scale sinusoidal Bérnard/von-Kármán vortices. Figure 85 shows several instantaneous spanwise images of the simulations with the modified fuel injectors. As expected, these images, as well as the time- and spanwise-average images in Figure 86 look very similar to the low fuel flow rate simulations using the original injector. The fuel jet penetration was high enough to allow for some premixing so the fuel-air mixture delivered to the shear layers was not too rich, but low enough such that the mixture ignited in the shear layer and damped out the large scale sinusoidal structures. Figure 87 shows the spanwise-averaged fuel mass fraction, heat release rate, baroclinic torque and gas expansion for all three simulations, high fuel with the original injector, low fuel with the original injector and the high fuel case with the modified larger injector. The fuel delivered to the shear

layer and subsequent heat release and vorticity quantities of the modified injector case are nearly the same as those quantities computed from the low fuel flow rate case with the original injectors. This test case confirmed the hypothesis regarding the relationship between the flame dynamics and the fuel jet penetration.

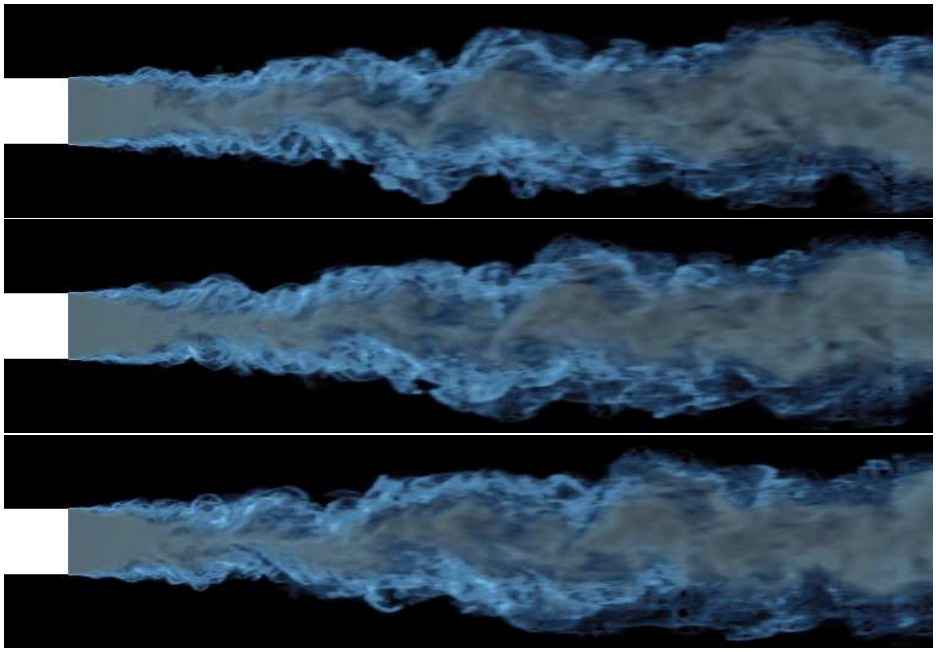

Figure 85 Spanwise averaged snapshots of the simulation with modified (larger) fuel injectors (spanwise averaged CO and CO_2 mass fraction overlaid on heat release rate) at $\phi \approx 0.95$

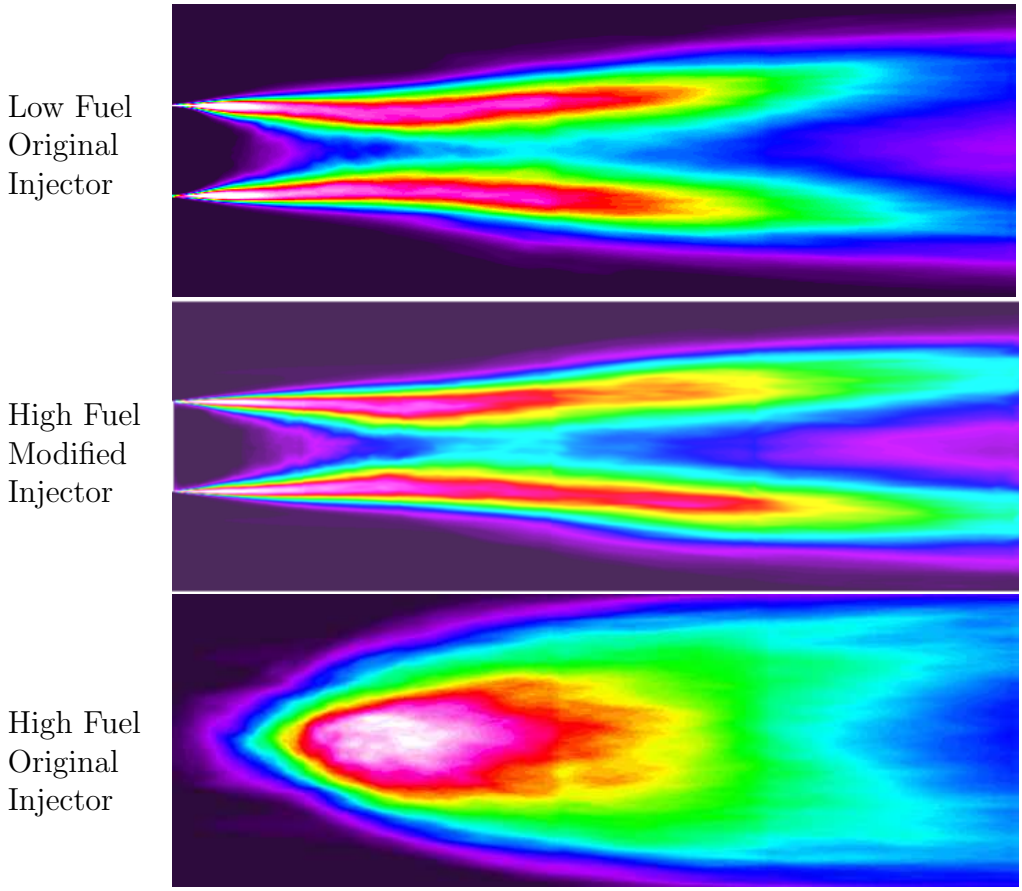

(a) $\phi_{\textbf{global}} \approx 0.95$

Figure 86 Comparison of time averaged heat release rate obtained for the low fuel flow rate case (top), high fuel flow rate case with modified (larger) injectors (middle), and high flow rate case with the original injectors.

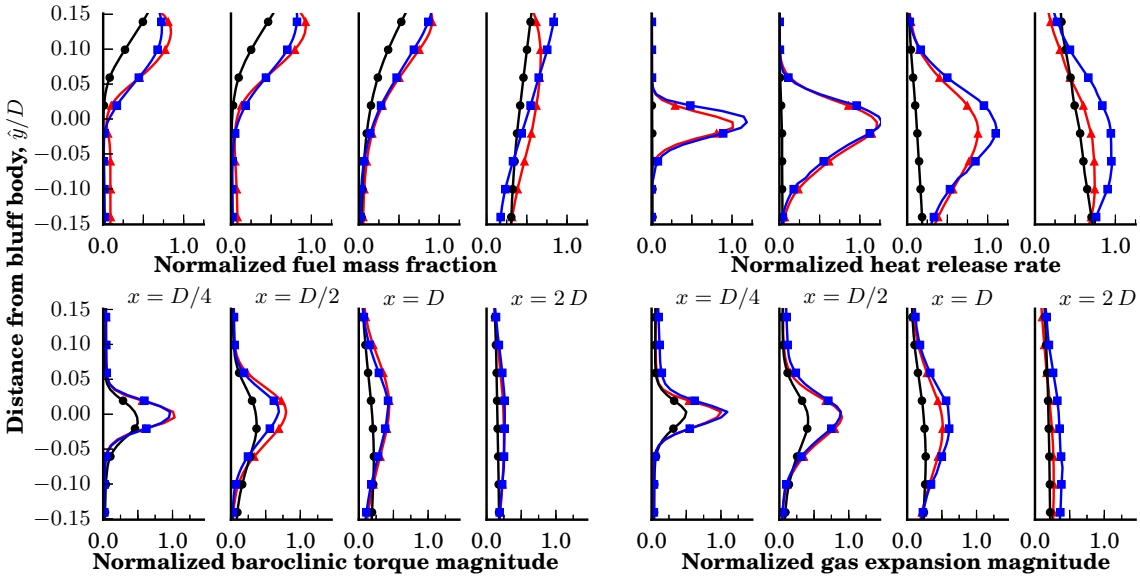

Figure 87 Spanwise and time-averaged quantities in the shear layers at several axial locations, (−●−) $\phi_{\text{global}} \approx 0.95$ original injector, (−▲−) $\phi_{\text{global}} \approx 0.5$ original injector, (−■−) $\phi_{\text{global}} \approx 0.95$ modified (larger) injector

CHAPTER VII

CONCLUSIONS AND FUTURE WORK

7.1 Conclusions

The main goal of this thesis was to use simulations to improve understanding of vitiated, non-premixed bluff body stabilized flames with liquid fueling using computational fluid dynamics. This final chapter summarizes the efforts to achieve the proposed objectives along with key findings from the results.

Large eddy simulations were conducted for non-reacting and reacting flow at two different fuel flow rate conditions on a vitiated, liquid fueled bluff body combustor. The fuel injectors were located just upstream of the bluff body trailing edge in a "close-coupled" configuration. The LES used a second-order finite volume method combined with a second-order predictor-corrector time integration scheme and a simple quasi-laminar subgrid turbulence-chemistry interaction model. The liquid phase was simulated using a Lagrangian parcel approach. Experiments at two fuel flow rates, $\dot{m} = 16.11$ g/s and $\dot{m} = 31.23$ g/s, which correspond to global equivalence ratios of $\phi_{global} \approx 0.5$ and $\phi_{global} \approx 0.95$ based on the incoming air mass flow rate, showed markedly different flame dynamics; at $\phi_{global} \approx 0.5$, the flame exhibited symmetric flame shedding, whereas the $\phi_{global} \approx 0.95$ flame was characterized by large scale sinusoidal Bérnard/von-Kármán shedding. Comparisons to experimental data were limited to high- and low-speed imaging so the LES data required averaging in the spanwise direction. CFD images combining heat release and combustion products qualitatively agree with the flame shedding behavior observed in the experimental images, i.e., the LES images show symmetric flame shedding at a fuel flow rate of $\dot{m} = 16.11$ g/s and sinusoidal shedding at $\dot{m} = 31.23$ g/s. The time-averaged,

spanwise-averaged heat release CFD images were similar to the experimental data though for the low fuel flow rate the CFD predicted more concentrated heat release in the shear layers. At the high fuel flow rate, the flame shedding Strouhal number of $St = 0.22$ computed via a flame edge analysis based on the LES spanwise images was very close to the experimental value of $St = 0.21$ which was calculated using the same method. The mean flame edge location, flame edge fluctuations and flame width fluctuations were also calculated from the flame edge analysis for both the LES and experiments. At the high fuel flow rate, the LES slightly under-predicted the flame edge location near the bluff body, $x/D < 2$, but downstream was close to the experimental values. The LES mean flame spreading rate, as determined by the slope of the flame edge position versus downstream location, was nearly identical to the experiments except for two small inflection points at $x/D \approx 2.5$ and $x/D \approx 5$ present in the experimental data but absent from the LES. For the low fuel flow rate case, the LES flame edge location was consistent with the experiments in the range $2 \leq x/D \leq 8$ but showed a narrower flame in the very near-field and far downstream of the bluff body. The experimental flame edge fluctuations showed different trends at the two different fuel flow rates, at the low fuel flow rate flame edge rms values steadily increased downstream of the bluff body whereas at the high fuel flow rate a peak in flame edge rms was observed around $3 \leq x/D \leq 4$ with a much larger magnitude than that of the low fuel flow rate case. The LES predicted these trends correctly. At the low fuel flow rate the LES matched the experimental flame edge rms magnitudes throughout the domain. For the high fuel flow rate case the LES gave the same peak rms value but showed a more steady decrease of fluctuations $x/D > 6$ than the experiments. The LES also correctly captured the trends in flame width fluctuations where at the high fuel flow rate experiments showed a sharp peak at $x/D \approx 0.75$, a trough at $x/D \approx 1.25 - 1.45$ and another wider peak farther downstream. Both the magnitude and location of these local maxima and minima computed from the

LES were quite close to the experimental values. In the absence of more complete experimental data the flame edge analysis provides limited validation of the reacting flow LES.

These simulations required accurate thermophysical properties for both the Eulerian and Lagrangian phases along with a computationally tractable reaction mechanism that worked over a wide range of equivalence ratios. The simulations not only provided a baseline for subsequent analysis in this thesis, but a starting point for future researchers conducting LES for similar configurations.

Analysis of the simulation setup and results yielded several key findings. The first is that the injector breakup model and subsequent spray penetration are key to successful simulations of this configuration. Initial simulations did not take the injector discharge coefficient into account, which for these injectors ranged from 0.52 to 0.59, and the spray model itself was not properly tuned for the injectors in this study. These deficiencies caused fuel spray that did not penetrate the free-stream far enough compared to experiments and resulted in flame dynamics that were opposite of those observed in the experimental study. Once the discharge coefficient was set properly the spray model was tuned based on experimental data at conditions similar but not identical to the reacting flow cases. The tuning was limited to the jet regime model where the stripped droplet velocities and sizes along with the Reitz B_1 parameter were determined based on the experimental data. The flame dynamics in the reacting simulations completed after correcting these issues matched those from the experiments. Since the injectors used in this study were not "standard" flush-mounted orifice style injectors, the actual tuned model parameters developed in this work may not be applicable to other injector configurations.

Previous work hypothesized that fuel spray penetration was the controlling factor for the flame dynamics for this "close-coupled" configuration. The LES of this work support this hypothesis. At the low fuel flow rate, the shear layer analsysis showed

that the fuel jet did not penetrate very far into the crossflow thus delivering fuel to the shear layers of the bluff body. Some premixing did occur prior to reaching the trailing edge resulting in a complex partially premixed flow field. The recirculation bubble behind the bluff body helped ignite the fuel in the shear layers and the subsequent heat release damped the large scale sinusoidal structures via gas expansion and baroclinic torque generation where the baroclinic torque generation was a slightly more dominant factor. In the high fuel flow rate case, the fuel penetrated farther into the free stream so less fuel was delivered to the shear layers, and thus fewer reactions occurred directly behind the bluff body. The large scale sinusoidal shedding characteristic of bluff body flows was not damped. The maximum time and spanwise-averaged heat release rate in the shear layers just behind the bluff body, $x \leq 2D$, was over 100 times larger for the low fuel flow rate case than the high fuel flow rate case resulting in baroclinic torque and gas expansion values one and a half times larger. More supporting evidence for the hypothesis was supplied by running an additional simulation with no experimental analogue. This third configuration was simulated by modifying the fuel injector diameter to match the spray penetration of the low fuel flow rate case while maintaining the fuel flow rate of the high flow rate case. As expected, the shear layer analysis and flame dynamics of this configuration matched the original low fuel flow rate case since the fuel jet penetration was similar.

The low and high fuel flow rate reacting cases were repeated using the subgrid linear eddy model and the results compared to the baseline LES simulations. The results of this investigation on the impact of the subgrid turbulence-chemistry interaction model showed the model had little effect for this configuration on the overall flame dynamics as both models qualitatively matched the experiments. Time- and spanwise-averaged heat release rate images of the high fuel flow rate case did show that the LEMLES results were closer to the experiments in the near-field region behind the bluff body than those using the quasi-laminar chemistry model. The similarity

of the flame dynamics between the two models was attributed to the time step of the simulation. The time step dictated by the CFL condition for the simulation was small enough that in the majority of the flow field only 1–2 LEM stirrings occurred during each LES time step. Without significant subgrid stirring the LEMLES results do not significantly differ from the quasi-laminar simulations. Subgrid kinetic energy was only significant in the near-field region in the shear layers behind the bluff body and consequently 8–10 subgrid stirring events took place per LES time step in some cells in this region. Here the additional resolution provided by LEMLES enhanced the solution.

A high-order hybrid compact central / WENO-Z finite difference method was implemented in the existing finite volume framework which allowed for easy comparisons between the two methods. The numerical scheme was a unique combination of a compact central scheme in smooth regions of the flow, the WENO-Z scheme near discontinuities, and special treatment of the viscous terms to avoid odd-even decoupling instabilities along with an explicit five-step, fourth order SSPRK time integration method. The lack of inherent dissipation in the compact central scheme required the use of a filtering operation to avoid instabilities in the smooth regions and a method to smoothly transition to turn off the filtering where the WENO-Z scheme was used. A series of linear, non-linear, non-reacting and reacting test cases were used to validate the method and demonstrate that the high-order methods are more efficient and the odd-even decoupling viscous terms are important to avoid oscillations where in regions where the filtering is inactive.

The high-order hybrid finite difference scheme was applied to the high fuel flow rate bluff body case and compared with the second-order finite volume results. The application of high-order hybrid finite difference methods to multiphase, reacting LES is not widespread and this is the first known usage of a hybrid compact/WENO-Z

scheme for multiphase, reacting LES on curvilinear grids. As with the subgrid turbulence model comparisons, the flame dynamics were relatively insensitive to the numerical method. The similarities were attributed to the fact that complex thermodynamics, multiple species, chemical reactions and multiphase models are all additional sources of error not directly controlled by the temporal or spatial integration method and are more difficult to quantify. The time- and spanwise-averaged heat release rate images from the high-order FD simulations matched more closely to the experiments in the shear layers just behind the bluff body than the second order FV simulations. The LEMLES FV and high-order QL LES FD showed similar features in this region demonstrating the capability of LEMLES to achieve high-resolution-like results in regions of high subgrid kinetic energy. Overall, the baseline and high-order simulations were actually quite similar giving more confidence in the baseline solution.

7.2 Recommendations for future work

As computing power in industry increases the use of LES as a design tool will also become more widespread complimenting existing RANS and URANS methods. For an engineering design tool for flows with liquid injectors Eulerian-Lagrangian methods will most likely remain the tool of choice. The accuracy of the liquid injector model is critical to the success of the types of simulations presented in this work and often times experimental data for model tuning is limited or completely unavailable. Further research into first-principles modeling of the liquid injectors into a gaseous environment is needed [81, 82, 164]. Vitiated environments, like the one studied here, emphasize the need to advance these techniques to be able to simulate density ratios of over 2000, which is much greater than currently published results [238]. Many of these schemes include front tracking methods that could be improved with the use of the WENO-Z scheme employed in this thesis [144]. An Eulerian-Eulerian method that includes surface tension effects coupled to an Eulerian-Lagrangian solver may not

currently be computationally tractable for full reacting flow LES. Instead simulations on simplified but representative geometry using such a methodology could be used instead of experiments to tune the more efficient but simpler Eulerian-Lagrangian injector models.

The flame dynamics of the LES presented here did not show extreme sensitivity to the subgrid combustion model but time- and spanwise-averaged image comparisons did show the model had some effect. LEMLES has proven to be an effective model in other simulations and some improvements could be made to increase performance. To improve the overall efficiency, modifying the model to only be applied in certain physical regions of the domain would be the first step; in fact some efforts have already begun in this respect. Eliminating the numerical diffusion associated with splicing is important as is the inclusion of molecular diffusion across LES cell faces [188, 216, 79]. Extending LEMLES to work in the finite difference framework developed in this work could be especially advantageous; the high-order temporal and spatial schemes would allow for larger cell and time-step sizes increasing the advantages of the subgrid linear eddy model. This would most likely be straightforward if the Lagrangian splicing step was eliminated [216].

The expanded use of high-order numerical methods to improve computational efficiency is another area of future work. High-order finite difference methods are quite attractive for simple geometries though usage can be limited in complex industrial geometries unless additional tools such as overset grids or static grid refinement methods, like the one presented in Section 4.10, are employed. The currently implemented numerical methods could be improved based on recent advances for both the central and upwind schemes [206, 2]. Other high-order methods like discontinuous Galerkin methods [74, 126] and flux reconstruction methods [84] seem promising since they can be used with unstructured grids and are particularly efficient on multicore hardware such as graphical processing units (GPUs) [109, 235]. These high-order methods,

which are generally first developed for single phase, non-reacting flows, need to be extended to include multi-species, reactions and two-phase flow capabilities.

APPENDIX A

IMPLEMENTATION OF THE LAGRANGIAN LIQUID JET-IN-CROSSFLOW MODEL

The Lagrangian liquid jet in crossflow spray model used in this study is based on existing models, namely those by Reitz [167] and Madabhushi [128, 129], but tuned to match experimental data for the specific injectors of interest. The model was described in detail in Section 3.7 with details of the tuning given in Section 6.3.1.1.

Explicit steps on the implementation of the model are given below:

1. Compute the Lagrangian injection diameter, d_i, based on the actual injector diameter, d_0, and the injector discharge coefficient, C_d, which ranged for this experiment from 0.52 to 0.59:

$$d_i = \sqrt{d_0^2 C_d}. \tag{263}$$

2. Compute the fuel density using the NSRDS functions [36] and values listed in Table 34 based on the estimated fuel injection temperature which for this simulation was estimated as 325 K.

$$\rho_l = \frac{64.0}{0.25511^{\left(1+(1-T/680.0)^{0.29368}\right)}} \tag{264}$$

3. Compute the Lagrangian injection velocity, V_j, based on the Lagrangian injection diameter, fuel density and fuel mass flow rate:

$$V_j = \frac{4\dot{m}}{\rho_l \pi d_i^2} \tag{265}$$

4. Integrate the parcel in time using the Madabhushi [128] breakup model with the following modifications: In the jet regime (see Figure 7), when the parcel

time is less than the column breakup time defined by

$$t_{cb} = 3.44 \frac{D_0}{u_g} \sqrt{\frac{\rho_l}{\rho_g}}, \tag{94}$$

instead of using the wave model [167], as in the 2003 Madabhushi model [128], or correlations of Sallam et al. [179] as in the 2004 Madabhushi model [129], compute the stripped droplet size based on a linear combination of the two methods

$$r_{\text{stripped}} = (RND)\, r_{wave} + (1 - RND)\, r_{corr}, \tag{100}$$

with complete details of the two sizes r_{wave} and r_{corr} given in Section 3.7.1. Note that the wave model constant was set to $B_1 = 7$, as described in the breakup model formulation section.

The stripped droplet velocities are set using

$$u_{shed} = u_{parent} + 7\sqrt{\rho_g/\rho_l}\, RND\ (u_g - u_{parent})\,, \tag{102a}$$

$$v_{shed} = v_{parent} + 0.6\,(RND)\,(v_g - v_{parent})\,, \tag{102b}$$

$$w_{shed} = w_{parent} + 0.175\,(RND - 0.5)\,(u_{rel} - w_{parent})\,. \tag{102c}$$

which are based on the works of Chou [24] and Khosla [99]. In the simulations in this work, droplets were shed once the stripped mass reached 0.5% of the initial injected droplet mass.

Stripped computational parcels have a maximum of 36 particles per parcel but often have less due to the mass cutoff value.

5. After column breakup, continue integrating the parcels using the secondary breakup model of Madabhushi.

6. If any large parcels are still left in the domain, continue using the Reitz model after secondary breakup while the parcels have diameters larger than $20\,\mu$m.

7. Integrate the parcels until they reach a user-defined cutoff radius which for these simulations was $4\,\mu$m.

REFERENCES

[1] Abramzon, B. and Sirignano, W. A., "Droplet vaporization model for spray combustion calculations," *International Journal of Heat and Mass Transfer*, vol. 32, no. 9, pp. 1605–1618, 1989.

[2] Acker, F., de R. Borges, R. B., and Costa, B., "An improved WENO-Z scheme," *Journal of Computational Physics*, vol. 313, pp. 726–753, 2016.

[3] Amidror, I., "Scattered data interpolation methods for electronic imaging systems: a survey," *Journal of Electronic Imaging*, vol. 11, no. 2, pp. 157–176, 2002.

[4] Apte, S. V., Mahesh, K., Gorokhovski, M., and Moin, P., "Stochastic modeling of atomizing spray in a complex swirl injector using large: eddy simulation," *Proceedings of the Combustion Institute*, vol. 32, no. 2, pp. 2257–2266, 2009.

[5] Aràndiga, F., Baeza, A., Belda, A. M., and Mulet, P., "Analysis of WENO schemes for full and global accuracy," *SIAM Journal on Numerical Analysis*, vol. 49, no. 2, pp. 893–915, 2011.

[6] Balsara, D. S. and Shu, C.-W., "Monotonicity preserving weighted essentially non-oscillatory schemes with increasingly high order of accuracy," *Journal of Computational Physics*, vol. 160, pp. 405–452, May 2000.

[7] Baudoin, E., Yu, R., Nogenmyr, K., Bai, X., and Fureby, C., "Comparison of LES models applied to a bluff body stabilized flame," in *47th AIAA Aerospace Sciences Meeting*, (Orlando, Florida), January 2009. AIAA 2009-1178.

[8] Baum, M., Poinsot, T., and Thévenin, D., "Accurate boundary conditions for multicomponent reactive flows," *Journal of Computational Physics*, vol. 116, pp. 247–261, 1994.

[9] Becker, J. and Hassa, C., "Breakup and atomization of a kerosene jet in crossflow at elevated pressure," *Atomization and Sprays*, vol. 11, pp. 49–67, 2002.

[10] Berger, M. J. and Colella, P., "Local adaptive mesh refinement for shock hydrodynamics," *Journal of Computational Physics*, vol. 82, no. 1, pp. 64–84, 1989.

[11] Berger, M. J. and Oliger, J., "Adaptive mesh refinement for hyperbolic partial differential equations," *Journal of Computational Physics*, vol. 53, no. 3, pp. 484–512, 1984.

[12] Berglund, M., Fedina, E., Fureby, C., Tegnér, J., and Sabelnikov, V., "Finite rate chemistry large-eddy simulation of self-ignition in a supersonic combustion ramjet," *AIAA Journal*, vol. 48, no. 3, pp. 540–550, 2010.

[13] Berland, J., Bogey, C., and Bailly, C., "Low-dissipation and low-dispersion fourth-order Runge–Kutta algorithm," *Computers & Fluids*, vol. 35, no. 10, pp. 1459–1463, 2006.

[14] Borges, R., Carmona, M., Costa, B., and Don, W. S., "An improved weighted essentially non-oscillatory scheme for hyperbolic conservation laws," *Journal of Computational Physics*, vol. 227, pp. 3191–3211, 2008.

[15] Brown, C. T., McDonell, V. G., and Kiel, B. V., "Test bed for characterization of liquid jet injection phenomenon at augmentor conditions," in *42nd AIAA/ASME/SAE/ASEE Joint Propulsion Conference*, (Sacramento, California), July 2006. AIAA Paper 2006-4569.

[16] Bruno, C., Sankaran, V., Kolla, H., and Chen, J. H., "Impact of multi-component diffusion in turbulent combustion using direct numerical simulations," *Combustion and Flame*, vol. 162, no. 11, pp. 4313–4330, 2015.

[17] Canny, J., "A computational approach to edge detection," *IEEE Transactions on Pattern Analysis and Machine Intelligence*, vol. PAMI-8, pp. 679–698, Nov 1986.

[18] Carpenter, M. H. and Kennedy, C. A., "Fourth-Order 2N-Storage Runge-Kutta schemes," Technical Memorandum NASA TM 109112, NASA, June 1994.

[19] Castro, M., Costa, B., and Don, W. S., "High order weighted essentially non-oscillatory WENO-Z schemes for hyperbolic conservation laws," *Journal of Computational Physics*, vol. 230, pp. 1766–1792, 2011.

[20] Chao, J., Haselbacher, A., and Balachandar, S., "A massively parallel multi-block hybrid compact–WENO scheme for compressible flows," *Journal of Computational Physics*, vol. 228, pp. 7473–7491, 2009.

[21] Chaudhuri, S., Kostka, S., Tuttle, S. G., Renfro, M. W., and Cetegen, B. M., "Blowoff mechanism of two dimensional bluff-body stabilized turbulent premixed flames in a prototypical combustor," *Combustion and Flame*, vol. 158, pp. 1358–1371, 2011.

[22] Chen, J. H., "Petascale direct numerical simulation of turbulent combustion - fundamental insights towards predictive models," *Proceedings of the Combustion Institute*, vol. 33, pp. 99–123, 2011.

[23] Chen, K.-H. and Shuen, J.-S., "A coupled multi-block solution procedure for spray combustion in complex geometries," in *31st Aerospace Sciences Meeting & Exhibit*, (Reno, NV), January 1993. AIAA 93-0108.

[24] Chou, W.-H., Hsiang, L.-P., and Faeth, G. M., "Temporal properties of drop breakup in the shear breakup regime," *International Journal of Multiphase Flow*, vol. 23, no. 4, pp. 651–669, 1997.

[25] Clift, R., Grace, J. R., and Weber, M. E., *Bubbles Drops and Particles*. New York: Academic press, 1978.

[26] Cocks, P. A. T., Sankaran, V., and Soteriou, M. C., "Is les of reacting flows predictive? part 1: Impact of numerics," in *51st AIAA Aerospace Sciences Meeting*, (Grapevine, Texas), January 2013. AIAA Paper 2013-170.

[27] Cocks, P. A. T., Soteriou, M. C., and Sankaran, V., "Impact of numerics on the predictive capabilities of reacting flow les," *Combustion and Flame*, vol. 162, 2015.

[28] Colella, P. and Woodward, P., "The Piecewise Parabolic Method (PPM) for gas-dynamical simulations," *Journal of Computational Physics*, vol. 54, no. 1, pp. 174–201, 1984.

[29] Coordinating Reseach Council, "Handbook of aviation fuel properties," Tech. Rep. CRC Report No. 530, Coordinating Reseach Council, 1983.

[30] Costa, B. and Don, W. S., "High order hybrid central–WENO finite difference scheme for conservation laws," *Journal of Computational and Applied Mathematics*, vol. 204, pp. 209–218, 2007.

[31] Coussement, A., Gicquel, O., Caudal, J., Fiorina, B., and Degrez, G., "Three-dimensional boundary conditions for numerical simulations of reactive compressible flows with complex thermochemistry," *Journal of Computational Physics*, vol. 231, no. 17, pp. 5571–5611, 2012.

[32] Cross, C., *Combustion heat release effects on asymmetric vortex shedding from bluff bodies*. PhD thesis, Georgia Institute of Technology, 2011.

[33] Cross, C., Fricker, A., Shcherbik, D., Lubarsky, E., Zinn, B. T., and Lovett, J. A., "Dynamics of non-premixed bluff body-stabilized flames in heated air flow," in *Proceedings of ASME Turbo Expo*, (Glasgow, UK), June 2010. GT2010-23059.

[34] Crowe, C., Sommerfeld, M., and Tsuji, Y., *Multiphase flows with droplets and particles*. Boca Raton: CRC Press, 1997.

[35] Dagaut, P. and Cathonnet, M., "The ignition, oxidation, and combustion of kerosene: A review of experimental and kinetic modeling," *Progress in Energy and Combustion Science*, vol. 32, no. 1, pp. 48–92, 2006.

[36] Dauber, T. E. and Danner, R. P., *Data compilation tables of properties of pure compunds*. New York, NY: American Institute of Chemical Engineers, 1985.

[37] Davis, S., Dittmann, T., Jacobs, G. B., and Don, W. S., "High-fidelity eulerian-lagrangian methods for simulation of three dimensional, unsteady, high-speed, two-phase flows in high-speed combustors," in *9th Annual International Energy Conversion Engineering Conference*, 2011. AIAA 2011-5744.

[38] Deiterding, R., *Parallel Adaptive Simulation of Multi-dimensional Detonation Structures*. PhD thesis, Brandenburgischen Technischen Universit ät Cottbus, Brandenburg, Germany, 2003.

[39] Denaro, F. M., "What does finite volume-based implicit filtering really resolve in Large-Eddy Simulations?," *Journal of Computational Physics*, vol. 230, no. 10, pp. 3849–3883, 2011.

[40] Deng, X., Min, Y., Mao, M., Liu, H., Tu, G., and Zhang, H., "Further studies on Geometric Conservation Law and applications to high-order finite difference schemes with stationary grids," *Journal of Computational Physics*, vol. 239, pp. 90–111, 2013.

[41] Don, W.-S. and Borges, R., "Accuracy of the weighted essentially non-oscillatory conservative finite difference schemes," *Journal of Computational Physics*, vol. 250, pp. 347–372, 2013.

[42] Don, W.-S., de Gregorio, A., Suarez, J.-P., and Jacobs, G. B., "Assessing the performance of a three dimensional hybrid central-WENO finite difference scheme with computation of a sonic injector in supersonic cross flow," *Advances in Applied Mathematics and Mechanics*, vol. 4, pp. 719–736, 12 2012.

[43] Duwig, C., Nogenmy, K.-J., ki Chan, C., and Dunn, M. J., "Large eddy simulations of a piloted lean premix jet flame using finite-rate chemistry," *Combustion Theory and Modelling*, vol. 15, no. 4, pp. 537–568, 2011.

[44] Ekaterinaris, J. A., "High-order accurate, low numerical diffusion methods for aerodynamics," *Progress in Aerospace Sciences*, vol. 41, pp. 192–300, 2005.

[45] El-Asrag, H. A., Pitsch, H., Kim, W., Do, H., and Mungal, M. G., "Damköhler number similarity for static flame stability in gaseous-fueled augmentor flows," *Combustion Science and Technology*, vol. 183, pp. 718–737, 2011.

[46] Erickson, R., Soteriou, M., and Mehta, P., "The influence of temperature ratio on the dynamics of bluff body stabilized flames," in *44th AIAA Aerospace Sciences Meeting and Exhibit*, (Reno, Nevada), 2006. AIAA Paper 2006-753.

[47] Faeth, G., "Current status of droplet and liquid combustion," *Progress in Energy and Combustion Science*, vol. 3, no. 4, pp. 191–224, 1977.

[48] Faeth, G., "Mixing, transport, combustion in sprays," *Progress in Energy and Combustion Science*, vol. 13, no. 4, pp. 293–345, 1987.

[49] Faeth, G., "Spray combustion phenomena," *Proceedings of the Combustion Institute*, vol. 26, no. 1, pp. 1593–1612, 1996.

[50] Fan, P., "High order weighted essentially nonoscillatory weno- schemes for hyperbolic conservation laws," *Journal of Computational Physics*, vol. 269, pp. 355–385, 2014.

[51] Fan, P., Shen, Y., Tian, B., and Yang, C., "A new smoothness indicator for improving the weighted essentially non-oscillatory scheme," *Journal of Computational Physics*, vol. 269, pp. 329–354, 2014.

[52] Fedkiw, R. P., Merriman, B., and Osher, S., "Simplified discretization of systems of hyperbolic conservation laws containing advection equations," *Journal of Computational Physics*, vol. 157, no. 1, pp. 302–326, 2000.

[53] Franzelli, B., Riber, E., Sanjosé, M., and Poinsot, T., "A two-step chemical scheme for kerosene-air premixed flames," *Combustion and Flame*, vol. 157, no. 7, pp. 1364–1373, 2010.

[54] Franzelli, B., Riber, E., Gicquel, L. Y., and Poinsot, T., "Large Eddy Simulation of combustion instabilities in a lean partially premixed swirled flame," *Combustion and Flame*, vol. 159, pp. 621–637, 2012.

[55] Friedrich, R., "Modelling of turbulence in compressible flows," in *Transition, Turbulence and Combustion Modelling*, vol. 6, pp. 243–348, Springer Netherlands, 1999.

[56] Frössling, N., "Über die verdunstung fallender tropfen (on the evaporation of falling drops)," *Gerlands Beirtäge zur Geophysik*, vol. 51, pp. 170–216, 1938.

[57] Fureby, C., "Comparison of flamelet and finite rate chemistry LES for premixed turbulent combustion," in *45th AIAA Aerospace Sciences Meeting*, (Reno, Nevada), 2007. AIAA Paper 2007-1413.

[58] Fureby, C. and Möller, S.-I., "Large eddy simulation of reacting flows applied to bluff body stabilized flames," *AIAA Journal*, vol. 33, no. 12, pp. 2339–2347, 1995.

[59] Gaitonde, D. V., Shang., J. S., and Young, J. L., "Practical aspects of high-order accurate finite-volume schemes for electromagnetics," in *35th AIAA AIAA Aerospace Sciences Meeting*, (Reno, Nevada), January 1997. AIAA Paper 97-0363.

[60] Gaitonde, D. V. and Visbal, M. R., "High-order schemes for Navier-Stokes equations: algorithm and implementation into FDL3DI," Tech. Rep. AFRL-VA-WP-TR-1998-3060, Air Force Research Laboratory, Wright-Patterson Air Force Base, Ohio, August 1998.

[61] Gaitonde, D. V. and Visbal, M. R., "Further development of a Navier-Stokes solution procedure based on higher-order formulas," in *37th AIAA AIAA Aerospace Sciences Meeting*, (Reno, Nevada), January 1999. AIAA Paper 99-0557.

[62] Gaitonde, D. V. and Visbal, M. R., "Padé-type higher-order boundary filters for the Navier–Stokes equations," *AIAA Journal*, vol. 38, pp. 2103–2112, November 2000.

[63] Garnier, E., Adams, N., and Sagaut, P., *Large eddy simulation for compressible flows*. Springer Science+Business Media B.V. 2009, first ed., 2009.

[64] Génin, F., *Study of Compressible Turbulent Flows in Supersonic Environment by Large-Eddy Simulation*. PhD thesis, Georgia Institute of Technology, 2009.

[65] Génin, F. and Menon, S., "Studies of shock/turbulent shear layer interaction using large-eddy simulation," *Computers & Fluids*, vol. 39, pp. 800–819, 2010.

[66] Gokulakrishnan, P., Bikkani, R., Klassen, M. S., Roby, R. J., and Kiel, B., "Influence of turbulence-chemistry interaction in blow-out predictions of bluff-body stabilized flames," in *47th AIAA Aerospace Sciences Meeting*, (Orlando, Florida), 2009. AIAA Paper 2009-1179.

[67] Goldin, G., "Evaluation of LES subgrid reaction models in a lifted flame," in *43rd AIAA Aerospace Sciences Meeting*, (Reno, Nevada), January 2005. AIAA Paper 2005-555.

[68] Goodwin, D., Malaya, N., Moffat, H., and Speth, R., "Cantera: An object-oriented software toolkit for chemical kinetics, thermodynamics, and transport processes." https://code.google.com/p/cantera/, 2011. Version 1.8.

[69] Gottiparthi, K. C., *A study of dispersion and combustion of particle clouds in post-detonation flows*. PhD thesis, Georgia Institute of Technology, 2015.

[70] Gottlieb, D. and Turkel, E., "Dissipative two-four methods for time-dependent problems," *Mathematics of Computation*, vol. 30, no. 136, pp. 703–723, 1976.

[71] Gottlieb, S. and Shu, C.-W., "Total variation diminishing Runge-Kutta schemes," *Mathematics of Computation*, vol. 67, no. 221, pp. 73–85, 1998.

[72] Granet, V., Menon, S., and Roux, A., "arge eddy simulation of the mercato liquid fueled combustor with the linear eddy model," in *6th European Combustion Meeting*, (Lund, Sweden), June 2013.

[73] Granet, V., Vermorel, O., Léonard, T., Gicquel, L., and Poinsot, T., "Comparison of nonreflecting outlet boundary conditions for compressible solvers on unstructured grids," *AIAA Journal*, vol. 48, pp. 2348–2364, October 2010.

[74] Gryngarten, L. D., *Multi-phase flows using discontinuous Galerkin methods*. PhD thesis, Georgia Institute of Technology, 2012.

[75] Guézennec, N., Daweson, T., Sierra, P., and Menon, S., "Flame holding dynamics during combustion instability in a shear coaxial injector," in *8th International Symposium On Turbulence and Shear Flow Phenomena*, (Poitiers, France), August 2013.

[76] Hannebique, G., Sierra, P., Riber, E., and Cuenot, B., "Large eddy simulation of reactive two-phase flow in an aeronautical multipoint burner," *Flow Turbulence and Combustion*, vol. 90, pp. 449–469, 2012.

[77] Harten, A., Engquist, B., Osher, S., and Chakravarthy, S. R., "Uniformly high order accurate essentially non-oscillatory schemes, {III}," *Journal of Computational Physics*, vol. 71, no. 2, pp. 231–303, 1987.

[78] Harten, A., Lax, P. D., and van Leer, B., "On upstream differencing and godunov-type schemes for hyperbolic conservation laws," *SIAM Review*, vol. 25, no. 1, pp. 35–61, 1983.

[79] Harvazinski, M. E., Talley, D. G., and Sankaran, V., "Comparison of laminar and linear eddy model closures for combustion instability simulations," in *51st AIAA/SAE/ASEE Joint Propulsion Conference*, 2015. AIAA 2015-3842.

[80] Henrick, A. K., Aslam, T. D., and Powers, J. M., "Mapped weighted essentially non-osciallatory schemes: Achieving optimal order near critical points," *Journal of Computational Physics*, vol. 207, pp. 542–567, 2005.

[81] Herrmann, M., "A parallel Eulerian interface tracking/Lagrangian point particle multi-scale coupling procedure," *Journal of Computational Physics*, vol. 229, pp. 745–759, 2010.

[82] Herrmann, M., Arienti, M., and Soteriou, M., "The impact of density ratio on the liquid core dynamics of a turbulent liquid jet injected into a crossflow," *Journal of Engineering for Gas Turbines and Power*, vol. 133, June 2011. 061501.

[83] Hunter, J. D., "Matplotlib: A 2D graphics environment," *Computing in Science and Engineering*, vol. 9, no. 3, pp. 90–95, 2007.

[84] Huynh, H. T., "A flux reconstruction approach to high-order schemes including discontinuous galerkin methods," in *18th AIAA Computational Fluid Dynamics Conference*, (Miama, FL), June 2007. AIAA 2007-4079.

[85] Jacobs, G. B. and Don, W.-S., "A high-order WENO-Z finite difference based particle-source-in-cell method for computation of particle-laden flows with shocks," *Journal of Computational Physics*, vol. 228, pp. 1365–1379, 2009.

[86] Jiang, G.-S. and Shu, C.-W., "Efficient implementation of Weighted ENO schemes," *Journal of Computational Physics*, vol. 126, pp. 202–228, 1996.

[87] Jiang, X. and Lai, C.-H., *Numerical techniques for Direct and Large-Eddy Simulations*. CRC Press, 2009.

[88] Jones, E., Oliphant, T., Peterson, P., and others, "SciPy: Open source scientific tools for Python," 2001–.

[89] Jr., W. H. C. and Menon, S., "Subgrid modeling for reacting large eddy simulations," in *34th Aerospace Sciences Meeting and Exhibit*, (Reno, NV), January 1996. AIAA 96-516.

[90] Karaca, M., Lardjane, N., and Fedioun, I., "Implicit large eddy simulation of high-speed non-reacting and reacting air/h_s with a 5th order WENO scheme," *Computers & Fluids*, vol. 62, pp. 25–44, 2012.

[91] Kennedy, C. A. and Carpenter, M. H., "Comparison of several numerical methods for simulation of compressible shear layers," Technical Paper NASA Technical Paper 3484, NASA, December 1997.

[92] Kerstein, A. R., "A linear-eddy model of turbulent scalar transport and mixing," *Combustion Science and Technology*, vol. 60, no. 4–6, pp. 391–421, 1988.

[93] Kerstein, A. R., "Linear-eddy modeling of turbulent transport. ii: Application to shear layer mixing," *Combustion and Flame*, vol. 75, no. 3–4, pp. 397–413, 1989.

[94] Kerstein, A. R., "Linear-eddy modelling of turbulent transport. part 3. mixing and differential molecular diffusion in round jets," *Journal of Fluid Mechanics*, vol. 216, pp. 411–435, 1990.

[95] Kerstein, A. R., "Linear-eddy modeling of turbulent transport. part v: Geometry of scalar interfaces," *Physics of Fluids*, vol. 3, pp. 1110–1114, 1991.

[96] Kerstein, A. R., "Linear-eddy modelling of turbulent transport. part 6. microstructure of diffusive scalar mixing fields," *Journal of Fluid Mechanics*, vol. 231, pp. 361–394, 1991.

[97] Kerstein, A. R., "Linear-eddy modeling of turbulent transport. part 4. structure of diffusion flames," *Combustion Science and Technology*, vol. 1–3, pp. 75–96, 1992.

[98] Kerstein, A. R., "Linear-eddy modelling of turbulent transport. part 7. finite-rate chemistry and multi-stream mixing," *Journal of Fluid Mechanics*, vol. 240, pp. 289–313, 1992.

[99] Khosla, S. and Crocker, D. S., "CFD modeling of the atomization of plain liquid jets in cross flow for gas turbine applications," in *Proceedings of ASME Turbo Expo*, (Vienna, Austria), June 2004. GT2004-54269.

[100] Khosla, S., Leach, T. T., and Smith, C. E., "Flame stabilization and role of von karman vortex shedding behind bluff body flameholders," *43rd AIAA/ASME/SAE/ASEE Joint Propulsion Conference, Cincinnati, Ohio*, 2007. AIAA Paper 2007-5653.

[101] Kiel, B., Garwick, K., Gord, J. R., Miller, J., Lynch, A., Hill, R., and Phillips, S., "A detailed investigation of bluff body stabilized flames," *45th AIAA Aerospace Sciences Meeting*, 2007. AIAA Paper 2007-168.

[102] Kiel, B., Garwick, K., Lynch, A., Gord, J. R., and Meyer, T., "Non-reacting and combusting flow investigation of bluff bodies in cross flow," *42nd AIAA/ASME/SAE/ASEE Joint Propulsion Conference, Scramento, California*, 2006. AIAA Paper 2006-5234.

[103] Kim, D. and Kwon, J. H., "A high-order accurate hybrid scheme using a central flux scheme and a WENO scheme for compressible flowfield analysis," *Journal of Computational Physics*, vol. 210, pp. 554–583, 2005.

[104] Kim, S. and Menon, S., "Large-eddy simulation of a high-pressure, single-element lean direct-injected gas-turbine combustor," in *52nd Aerospace Sciences Meeting*, (National Harbor, Maryland), January 2014. AIAA Paper 2014-131.

[105] Kim, W.-W. and Menon, S., "An unsteady incompressible Navier-Stokes solver for large eddy simulation of turbulent flows," *International Journal for Numerical Methods in Fluids*, vol. 31, pp. 983–1017, 1999.

[106] Kim, W. and Mungal, M. G., "The role of local base cavities in an augmentor bluffbody flameholder," *49th AIAA Aerospace Sciences Meeting, Orlando, Florida*, 2011. AIAA Paper 2011-63.

[107] Kitware, I., "Cmake; an extensible, open-source, compiler-independent build system management software." https://cmake.org, 2015. Version 3.3.2.

[108] Klein, M., "An attempt to assess the quality of Large Eddy Simulations in the context of implicit filtering," *Flow Turbulence and Combustion*, vol. 75, pp. 131–147, 2005.

[109] Klöckner, A., Warburton, T., Bridge, J., and Hesthaven, J., "Nodal discontinuous galerkin methods on graphics processors," *Journal of Computational Physics*, vol. 228, no. 21, pp. 7863–7882, 2009.

[110] Klusmeyer, A., Cross, C., Lubarsky, E., Bibik, O., Shcherbik, D., and Zinn, B. T., "Prediction of blow-offs of bluff body stabilized flames utilizing close-coupled injection of liquid fuels," *Journal of Engineering for Gas Turbines and Power*, vol. 135, January 2013. 011504.

[111] Kolaitis, D. I. and Founti, M. A., "A comparative study of numerical models for eulerian-lagrangian simulations of turbulent evaporating sprays," *International Journal of Heat and Fluid Flow*, vol. 27, pp. 424–435, 2006.

[112] Layton, W. J. and Rebholz, L., "Approximate deconvolution operators and models," in *Approximate Deconvolution Models of Turbulence*, vol. 2042 of *Lecture Notes in Mathematics*, pp. 61–88, Springer Berlin / Heidelberg, 2012. 10.1007/978-3-642-24409-4_3.

[113] Lele, S. K., "Compact finite difference schemes with spectral-like resolution," *Journal of Computational Physics*, vol. 103, pp. 16–42, 1992.

[114] Liu, A. B., Mather, D., and Reitz, R. D., "Modeling the effects of drop drag and breakup on fuel sprays," *SAE Technical Paper Series*, 1993. 930072.

[115] Liu, X.-D., Osher, S., and Chan, T., "Weighted essentially non-oscillatory schemes," *Journal of Computational Physics*, vol. 115, pp. 200–212, 1994.

[116] Lo, S.-C., Blaisdell, G. A., and Lyrintzis, A. S., "High-order shock capturing schemes for turbulence calculations," *International Journal for Numerical Methods in Fluids*, vol. 62, no. 5, pp. 473–498, 2010.

[117] Lodato, G., Domingo, P., and Vervisch, L., "Three-dimensional boundary conditions for direct and large-eddy simulation of compressible viscous flows," *Journal of Computational Physics*, vol. 227, no. 10, pp. 5105–5143, 2008.

[118] Lovett, J. A., Brogan, T. P., Philippona, D. S., Keil, B. V., and Thompson, T. V., "Development needs for advanced afterburner designs," in *40th AIAA/ASME/SAE/ASEE Joint Propulsion Conference and Exhibit*, (Fort Lauderdale, Florida), 2004. AIAA Paper 2004-4192.

[119] Lovett, J. A., Ahmed, K. A., Klusmeyer, A., Smith, A. G., Lubarsky, E., Menon, S., and Zinn, B. T., "On the influence of fuel distribution on the flame structure of bluff-body stabilized flames," *Journal of Engineering for Gas Turbines and Power*, vol. 136, April 2014.

[120] Lovett, J. A., Cross, C., Lubarsky, E., and Zinn, B. T., "A review of mechanisms controlling bluff-body stabilized flames with closely-coupled fuel injection," in *ASME Turbo Expo*, (Vancouver, British Columbia, Canada), June 2011. GT2011-46676.

[121] Lu, T., "Reduced mechanisms download (CHEMKIN-II versions)," 2015. [Online; accessed 1 January 2015].

[122] Lubarsky, E., Cutright, J. T., and Zinn, B. T., "Spray characterization at jet engine thrust augmentor flow conditions," in *46th AIAA Aerospace Sciences Meeting*, (Reno, Nevada), 2008. AIAA 2008-1041.

[123] Lubarsky, E., Cutright, J. T., Zinn, B. T., and McAmis, R., "Spray characterization at jet engine thrust augmentor flow conditions," in *Proceedings of ASME Turbo Expo 2008*, (Berlin, Germany), June 2008. GT2008-50867.

[124] Lubarsky, E., Reichel, J. R., Zinn, B. T., and McAmis, R., "Spray in crossflow: Dependence on weber number," *Journal of Engineering for Gas Turbines and Power*, vol. 132, no. 2, 2010. 021501-1.

[125] Luche, J., *Elaboration of reduced kinetic models of combustion. Application to a kerosene mechanism.* PhD thesis, LCSR Orléans, 2003.

[126] Lv, Y. and Ihme, M., "Discontinuous Galerkin method for multicomponent chemically reacting flows and combustion," *Journal of Computational Physics*, vol. 270, pp. 105–137, 2014.

[127] MacCormack, R. W., "The effect of viscosity in hypervelocity impact cratering," in *AIAA Hypervelocity Impact Conference*, (Cincinnati, Ohio), May 1969. AIAA Paper No. 69-354.

[128] Madabhushi, R. K., "A model for numerical simulation of breakup of a liquid jet in crossflow," *Atomization and Sprays*, vol. 13, pp. 413–424, 2003.

[129] Madabhushi, R. K., Leong, M. Y., and Hautman, D. J., "Simulation of the break-up of a liquid jet in crossflow at atmospheric conditions," in *Proceedings of ASME Turbo Expo*, (Vienna, Austria), June 2004. GT2004-54093.

[130] Marchioli, C., Armenio, V., and Soldati, A., "Simple and accurate scheme for fluid velocity interpolation for eulerianlagrangian computation of dispersed flows in 3d curvilinear grids," *Computers & Fluids*, vol. 36, pp. 1187–1198, 2007.

[131] Masquelet, M., *Large-Eddy Simulation Solver for O_2/H_2 Liquid Rocket Engine Applications.* PhD thesis, Georgia Institute of Technology, 2013.

[132] McMurty, P. A., Menon, S., and Kerstein, A. R., "A linear eddy subgrid model for turbulent reacting flows: applications to hydrogen-air combustion," *Proceedings of the Combustion Institute*, vol. 24, pp. 271–278, 1992.

[133] Mehta, P. and Soteriou, M., "Combustion heat release effects on the dynamics of bluff body stabilized premixed reacting flows," *41st AIAA Aerospace Sciences Meeting and Exhibit*, 2003. AIAA Paper 2003-835.

[134] Meijerink, J. A. W. and Jacobs, G. B., "A WENO-Z based eulerian-lagrangian code for simulation of shocked flows laden with evaporating droplets," in *48th AIAA Aerospace Sciences Meeting*, (Orlando, Florida), January 2010. AIAA Paper 2010-1553.

[135] Menon, S. and Patel, N., "Subgrid modeling for simulation of spray combustion in large-scale combustors," *AIAA Journal*, vol. 44, no. 4, pp. 709–723, 2006.

[136] Miller, R. S. and Bellan, J., "Direct numerical simulation of a confined three-dimensional gas mixing layer with one evaporating hydrocarbon-droplet-laden stream," *Journal of Fluid Mechanics*, vol. 384, pp. 293–338, 1999.

[137] Motamed, M., Macdonald, C. B., and Ruuth, S. J., "One the linear stability of the fifth-order WENO discretization," *Journal of Scientific Computing*, vol. 47, pp. 127–149, 2011.

[138] Nair, S., *Acoustic characterization of flame blowout phenomenon*. PhD thesis, Georgia Institute of Technology, 2006.

[139] Nair, S. and Lieuwen, T., "Near-blowoff dynamics of a bluff-body stabilized flame," *Journal of Propulsion and Power*, vol. 23, no. 2, pp. 421–427, 2007.

[140] Nonomura, T., Iizuka, N., and Fujii, K., "Freestream and vortex preservation properties of high-order WENO and WCNS on curvilinear grids," *Computers & Fluids*, vol. 39, no. 2, pp. 197–214, 2010.

[141] Nori, V. N. and Seitzman, J. M., "Chemiluminescence measurements and modeling in syngas, methane and jet-a fueled combustors," in *45th AIAA Aerospace Sciences Meeting and Exhibit*, (Reno, Nevada), 2007. AIAA Paper 2007-466.

[142] Nori, V. N. and Seitzman, J. M., "Ch * chemiluminescence modeling for combustion diagnostics," *Proceedings of the Combustion Institute*, vol. 32, pp. 895–903, 2009.

[143] Oefelein, J. C., "Large eddy simulaiton of turbulent combustion processes in propulsion and power systems," *Progress in Aerospace Sciences*, vol. 42, pp. 2–37, 2002.

[144] Ovsyannikov, A., *Further development of Level Set method: modified level set equation and its numerical assessment*. PhD thesis, Ecole Centrale de Lyon, 2013.

[145] P., A. F., Deniau, H., Lamarque, N., and Poinsot, T., "Comparison of outflow boundary conditions for subsonic aeroacoustic simulations," *International Journal for Numerical Methods in Fluids*, vol. 68, no. 10, pp. 1207–1233, 2012.

[146] P., A. F., Deniau, H., Sicot, F., and Sagaut, P., "Curvilinear finite-volume schemes using high-order compact interpolation," *Journal of Computational Physics*, vol. 229, pp. 5090–5122, 2010.

[147] Pandolfi, M. and D'Ambrosio, D., "Numerical instabilities in upwind methods: Analysis and cures for the Carbuncle phenomenon," *Journal of Computational Physics*, vol. 166, no. 2, pp. 271–301, 2001.

[148] Patel, N., Kirtas, M., Sankaran, V., and Menon, S., "Simulation of spray combustion in a lean-direct injection combustor," *Proceedings of the Combustion Institute*, vol. 31, pp. 2327–2334, 2007.

[149] Patel, N. and Menon, S., "Simulation of spray turbulence flame interactions in a lean direct injection combustor," *Combustion and Flame*, vol. 153, pp. 228–257, 2008.

[150] Pirozzoli, S., "Conservative hybrid compact-WENO schemes for shock-turbulence interaction," *Journal of Computational Physics*, vol. 178, pp. 81–117, 2002.

[151] Pitsch, H., Desjardins, O., Balarac, G., and Ihme, M., "Large-eddy simulation of turbulent reacting flows," *Progress in Aerospace Sciences*, vol. 44, pp. 466–478, August 2008.

[152] Pitsch, H. and Steiner, H., "Large-eddy simulation of a turbulent piloted methane/air diffusion flame," *Physics of Fluids*, vol. 12, pp. 2541–2554, October 2000.

[153] Poinsot, T. and Veynante, D., *Theoretical and Numerical Combustion*. Edwards, 2001.

[154] Poinsot, T. J. and Lele, S. K., "Boundary conditions for direct simulations of compressible viscous flows," *Journal of Computational Physics*, vol. 101, pp. 104–129, 1992.

[155] Pope, S. B., "Ten questions concerning the large-eddy simulation of turbulent flows," *New Journal of Physics*, vol. 6, no. 35, pp. 1–24, 2004.

[156] Porumbel, I. and Menon, S., "Large eddy simulation of bluff body stabilized premixed flame," in *44th AIAA Aerospace Sciences Meeting and Exhibit*, 2006. AIAA Paper 2006-152.

[157] Porumbel, I., *Large Eddy Simulation of bluff body stabilized premixed and partially premixed combustion*. PhD thesis, Georgia Institute of Technology, 2006.

[158] Pouangué, A. F., Denaiu, H., and Lamarque, N., "A sixth-order compact finite-volume scheme for aeroacoustics: application to a large eddy simulation of a jet," *European Conference on Computational Fluid Dynamics, ECCOMAS CFD 2010*, June 2010.

[159] Qian, C., Bing, W., Huiqiang, Z., Yunlong, Z., and Wei, G., "Numerical investigation of h_2/air combustion instability driven by large scale vortex in supersonic mixing layers," *International Journal of Hydrogen Energy*, vol. 41, pp. 3171–3184, 2016.

[160] Qiu, J. and Shu, C.-W., "On the construction, comparison, and local characteristic decomposition for high-order central WENO schemes," *Journal of Computational Physics*, vol. 183, pp. 187–209, 2002.

[161] Quéméré, P., Sagaut, P., and Couailler, V., "A new multi-domain/multi-resolution method for large-eddy simulation," *International Journal for Numerical Methods in Fluids*, vol. 36, no. 4, pp. 391–416, 2001.

[162] Quimby, D. and Jacobs, G. B., "Large eddy simulation of a supersonic underexpanded jet with a high-order hybrid WENO-Z/central scheme," in *54th AIAA Aerospace Sciences Meeting*, (San Diego, California, USA), January 2016. AIAA Paper 2016-497.

[163] Rachner, M., Becker, J., Hassa, C., and Doerr, T., "Modelling of the atomization of a plain liquid fuel jet in crossflow at gas turbine conditions," *Aerospace Science and Technology*, vol. 6, pp. 495–506, 2002.

[164] Rana, S. and Herrmann, M., "Primary atomization of a liquid jet in crossflow," *Physics of Fluids*, vol. 23, 2011. 091109.

[165] Rango, S. D. and Zingg, D. W., "Aerodynamic computations using a higher-order algorithm," in *37th Aerospace Sciences Meeting*, 1999. AIAA 1999-0167.

[166] Rango, S. D. and Zingg, D. W., "Higher-order spatial discretization for turbulent aerodynamic computations," *AIAA Journal*, vol. 39, no. 7, pp. 1296–1304, 2001.

[167] Reitz, R. D., "Modeling atomization processes in high-pressure vaporizing sprays," *Atomisation and Spray Technology*, vol. 3, pp. 309–337, 1987.

[168] Ren, Y.-X., Liu, M., and Zhang, H., "A characteristic-wise hybrid compact-WENO scheme for solving hyperbolic conservation laws," *Journal of Computational Physics*, vol. 192, pp. 365–386, 2003.

[169] Ren, Z.-X. and Wang, B., "A LES study on passive mixing in supersonic shear layer flows considering effects of baffle configuration," *Advances in Mechanical Engineering*, vol. 6, pp. 1–9, 2014.

[170] Ren, Z.-X. and Wang, B., "Response of dispersed droplets to shock waves in supersonic mixing layers," *Advances in Mechanical Engineering*, vol. 7, pp. 1–10, 2015.

[171] Renka, R. J., "Multivariate interpolation of large sets of scattered data," *ACM Transactions on Mathematical Software*, vol. 14, pp. 139–148, June 1988.

[172] Roach, P. J., "Quantification of uncertainty in computational fluid dynamics," *Annual Review of Fluid Mechanics*, vol. 29, pp. 123–160, 1997.

[173] Rohde, A., "Eigenvalues and eigenvectors of the Euler equations in general geometries," in *15th AIAA Computational Fluid Dynamics Conference*, 2001. AIAA 2001-2609.

[174] Rudy, D. H. and Strikwerda, J. C., "A nonreflecting outflow boundary condition for subsonic Navier-Stokes calculations," *Journal of Computational Physics*, vol. 36, pp. 55–70, 1980.

[175] Rudy, D. H. and Strikwerda, J. C., "Boundary conditions for subsonic compressible Navier-Stokes calculations," *Computers & Fluids*, vol. 9, pp. 327–338, 1981.

[176] Ruuth, S. J., "Global optimization of explicit Strong-Stability-Preserving Runge-Kutta methods," *Mathematics of Computation*, vol. 75, no. 253, pp. 183–207, 2005.

[177] Sagaut, P., *Large eddy simulation for incompressible flows*. Springer Berlin Heidelberg New York, third ed., 1998.

[178] Salewski, M., Duwig, C., Milosavljevic, V., and Fuchs, L., "Large eddy simulation of spray combustion in a swirl-stabilized gas turbine burner," in *43rd AIAA/ASME/SAE/ASEE Joint Propulsion Conference & Exhibit*, (Cincinnati, OH), July 2007. AIAA Paper 2007-5634.

[179] Sallam, K. A., Aalburg, C., and Faeth, G. M., "Breakup of round nonturbulent liquid jets in gaseous crossflow," 2003. AIAA Paper 2003-1326.

[180] Sanders, R., Morano, E., and Druguet, M.-C., "Multidimensional dissipation for upwind schemes: Stability and applications to gas dynamics," *Journal of Computational Physics*, vol. 145, no. 2, pp. 511–537, 1998.

[181] Sankaran, R., Hawkes, E., Chen, J., Lu, T., and Law, C., "Direct numerical simulation of stationary lean premixed methane-air flames under intense turbulence," in *5th US Combustion Meeting*, (San Diego, CA), March 2007.

[182] Sankaran, R., Hawkes, E. R., Chen, J. H., Lu, T., and Law, C. K., "Structure of a spatially developing turbulent lean methane-air bunsen flame," *Proceedings of the Combustion Institute*, vol. 31, no. 1, pp. 1291 – 1298, 2007.

[183] Sankaran, R., Hawkes, E. R., Chen, J. H., Lu, T., and Law, C. K., "Study of turbulent premixed flame thickness using direct numerical simulation in a slot burner configuration," in *44th AIAA Aerospace Sciences Meeting and Exhibit*, (Reno, Nevada), January 2009. AIAA Paper 2006-165.

[184] Sankaran, R., Hawkes, E. R., Yoo, C. S., and Chen, J. H., "Direct numerical simulation of turbulent premixed flames and the response of flame speeds to intense turbulence," in *6th US Combustion Meeting*, (Ann Arbor, CA), May 2009.

[185] Sankaran, R., Hawkes, E. R., Yoo, C. S., and Chen, J. H., "Response of flame thickness and propagation speed under intense turbulence in spatially developing lean premixed methaneair jet flames," *Combustion and Flame*, vol. 162, no. 9, pp. 3294–3306, 2015.

[186] Sankaran, V., *Sub-grid Combustion Modeling for Compressible Two-Phase Reacting Flows*. PhD thesis, Georgia Institute of Technology, 2003.

[187] Sankaran, V. and Menon, S., "Les of spray combustion in swirling flows," *Journal of Turbulence*, vol. 3, no. 11, 2002.

[188] Sankaran, V. and Merkle, C. L., "Fundamental physics and model assumptions in turbulent combustion models for aerospace propulsion," in *50th AIAA/ASME/SAE/ASEE Joint Propulsion Conference*, 2014. AIAA 2014-3941.

[189] Schulz, J. C., *A study of magnetoplasmadynamic effects in turbulent supersonic flows with application to detonation and explosion*. PhD thesis, Georgia Institute of Technology, 2015.

[190] Shanbhogue, S., Husain, S., and Lieuwen, T., "Lean blowoff of bluff body stabilized flames: Scaling and dynamics," *Progress in Energy and Combustion Science*, vol. 35, pp. 98–120, 2009.

[191] Shen, Y., Wang, B., and Zha, G., "Implicit WENO scheme and high order viscous formulas for compressible flows," in *25th AIAA Applied Aerodynamics Conference*, (Miami, FL), June 2007. AIAA 2007-4431.

[192] Shen, Y. and Zha, G., "Large eddy simulation using a new set of sixth order schemes for compressible viscous terms," *Journal of Computational Physics*, vol. 229, no. 22, pp. 8296–8312, 2010.

[193] Shen, Y., Zha, G., and Chen, X., "High order conservative differencing for viscous terms and the application to vortex-induced vibration flows," *Journal of Computational Physics*, vol. 228, no. 22, pp. 8283–8300, 2009.

[194] Shepard, D., "A two-dimensional interpolation function for irregularly-spaced data," in *Proceedings of the 1968 23rd ACM national conference*, ACM '68, (New York, NY, USA), pp. 517–524, ACM, 1968.

[195] Shu, C.-W., "High order weighted essentially nonoscillatory schemes for convection dominated problems," *SIAM Review*, vol. 51, no. 1, pp. 82–126, 2009.

[196] Shu, C.-W. and Osher, S., "Efficient implementation of essentially non-oscillatory shock-capturing schemes," *Journal of Computational Physics*, vol. 77, pp. 439–471, 1988.

[197] Shu, C.-W. and Osher, S., "Efficient implementation of essentially non-oscillatory shock-capturing schemes, ii," *Journal of Computational Physics*, vol. 83, pp. 32–78, 1989.

[198] Smirnov, A., Shi, S., and Celik, I., "Random flow generation technique for large eddy simulations and particle-dynamics modeling," *Journal of Fluids Engineering*, vol. 123, pp. 359–371, June 2001.

[199] Smith, A. G., Menon, S., Lovett, J. A., and Sen, B. A., "Large eddy simulation of a bluff body stabilized flame with close-coupled liquid fuel injection," *Journal of Engineering for Gas Turbines and Power*, vol. 136, March 2014.

[200] Smith, C. E., Nickolaus, D., Leach, T., Kiel, B., and Garwick, K., "LES blowout analysis of premixed flow past v-gutter flameholder," *45th AIAA Aerospace Sciences Meeting, Reno, Nevada*, 2007. AIAA Paper 2007-170.

[201] Smooke, M. and Giovangigli, V., "Formulation of the premixed and and nonpremixed test problems," in *Reduced Kinetic Mechanisms and Asymptotic Approximations for Methane-Air Flames* (Smooke, M., ed.), vol. 384 of *Lecture Notes in Physics*, pp. 1–28, Berlin: Springer Berlin / Heidelberg, 1991.

[202] Srinivasan, S., Ranjan, R., and Menon, S., "Flame dynamics during combustion instability in a high-pressure, shear-coaxial injector combustor," *Flow Turbulence and Combustion*, vol. 94, pp. 237–262, 2015.

[203] Srinivasan, S., Smith, A. G., and Menon, S., "Accuracy, reliability and performance of spray combustion models in large-eddy simulations," in *Quality and Reliability of Large-Eddy Simulations II* (Salvetti, M. V., Geurts, B., Meyers, J., and Sagaut, P., eds.), vol. 16 of *ERCOFTAC Series*, pp. 211–220, Springer Netherlands, 2011.

[204] Stolz, S., Adams, N. A., and Kleiser, L., "The approximate deconvolution model for large-eddy simulations of compressible flows and its application to shock-turbulent-boundary-layer interaction," *Physics of Fluids*, vol. 13, no. 10, pp. 2985–3001, 2001.

[205] Strakey, P. A. and Eggenspieler, G., "Development and validation of a thickened flame modeling approach for large eddy simulation of premixed combustion," *Journal of Engineering for Gas Turbines and Power*, vol. 132, July 2010. 071501.

[206] Sun, Z.-S., Luo, L., xin Ren, Y., and ying Zhang, S., "A sixth order hybrid finite difference scheme based on the minimized dispersion and controllable dissipation technique," *Journal of Computational Physics*, vol. 270, pp. 238–254, 2014.

[207] Sun, Z.-S., Ren, Y.-X., Zhang, S.-Y., and Yang, Y.-C., "High-resolution finite difference schemes using curvilinear coordinate grids for DNS of compressible turbulent flow over wavy walls," *Computers & Fluids*, vol. 45, no. 1, pp. 84–91, 2011. 22nd International Conference on Parallel Computational Fluid Dynamics (ParCFD 2010) ParCFD.

[208] Sun, Z. and Ren, Y.-X., "A characteristic-wise hybrid compact-WENO scheme for solving the Navier-Stokes equations on curvilinear coordinates," in *Computational Fluid Dynamics 2008* (Choi, H., Choi, H., and Yoo, J., eds.), pp. 437–442, Springer Berlin Heidelberg, 2009.

[209] Sutherland, J. C. and Kennedy, C. A., "Improved boundary conditions for viscous, reacting compressible flows," *Journal of Computational Physics*, vol. 191, pp. 502–524, 2003.

[210] Tannehill, J. C., Anderson, D. A., and Pletcher, R. H., *Computational fluid mechanics and heat transfer*. Taylor & Francis, second ed., 1997.

[211] Thompson, K. W., "Time dependent boundary conditions for hyperbolic systems, ii," *Journal of Computational Physics*, vol. 89, pp. 439–461, 1990.

[212] Thornber, B., Bilger, R., Masri, A., and Hawkes, E., "An algorithm for LES of premixed compressible flows using the Conditional Moment Closure model," *Journal of Computational Physics*, vol. 230, pp. 7687–7705, 2011.

[213] Thornber, B., Drikakis, D., Youngs, D., and Williams, R., "Growth of a Richtmyer-Meshkov turbulent layer after reshock," *Physics of Fluids*, vol. 23, no. 095107, pp. 1–14, 2011.

[214] Toro, E., Spruce, M., and Speares, W., "Restoration of the contact surface in the hll-riemann solver," *Shock Waves*, vol. 4, no. 1, pp. 25–34, 1994.

[215] Torvalds, L. and Hamano, J., "git: distributed version control system." https://git-scm.com, 2015. Version 2.6.

[216] Tovar, J. M., "Advances in turbulent combustion dynamics simulations in bluff-body stabilized flames," Master's thesis, University of California, Los Angeles, Los Angeles, California, 2015.

[217] Tuttle, S. G., Chaudhuri, S., Jr., S. K., Kopp-Vaughn, K. M., Jenson, T., Cetegen, B. M., and Renfro, M. W., "Time-resolved blowoff transition measurements for two-dimensional bluff body-stabilized flames in vitiated flow," *Combustion and Flame*, 2011.

[218] Tuttle, S. G., Chaudhuri, S., Kopp-Vaughan, K. M., Jenson, T., Cetegen, B. M., Renfro, M. W., and Cohen, J. M., "Blowoff dynamics of asymmetrically-fueled bluffbody flames," *49th AIAA Aerospace Sciences Meeting, Orlando, Florida*, 2011. AIAA Paper 2011-235.

[219] Undapalli, S., Srinivasan, S., and Menon, S., "LES of premixed and non-premixed combustion in a stagnation point reverse flow combustor," *Proceedings of the Combustion Institute*, vol. 32, pp. 1537–1544, 2009.

[220] van der Walt, S., Colbert, S. C., and Varoquaux, G., "The NumPy array: A structure for efficient numerical computation," *Computing in Science and Engineering*, vol. 13, no. 2, pp. 22–30, 2011.

[221] van Leer, B., "Towards the ultimate conservative difference scheme V. A second order sequel to Godunov's method," *Journal of Computational Physics*, vol. 32, no. 1, 1979.

[222] Vanella, M., Piomelli, U., and Balaras, E., "Effect of grid discontinuities on large-eddy simulation statistics and flow fields," *Journal of Turbulence*, vol. 9, no. 32, pp. 1–23, 2008.

[223] Vinokur, M., "An analysis of finite-difference and finite-volume formulations of conservation laws," *Journal of Computational Physics*, vol. 81, pp. 1–52, 1989.

[224] Visbal, M. R. and Gaitonde, D. V., "Shock capturing using compact-differencing-based methods," in *43rd AIAA Aerospance Sciences Meeting and Exhibit*, (Reno, Nevada), January 2005. AIAA Paper 2005-1265.

[225] Visbal, M. R. and Rizzetta, D. P., "Large-eddy simulation on curvilinear grids using compact differencing and filtering schemes," *Journal of Fluids Engineering*, vol. 124, pp. 836–847, 2002.

[226] Visbal, M. R. and Gaitonde, D. V., "High-order-accurate methods for complex unsteady subsonic flows," *AIAA Journal*, vol. 37, pp. 1231–1239, October 1999.

[227] Visbal, M. R. and Gaitonde, D. V., "On the use of higher-order finite-difference schemes on curvilinear and deforming meshes," *Journal of Computational Physics*, vol. 181, pp. 155–185, 2002.

[228] Vreman, A. W., van Oijen, J. A., de Goey, L. P. H., and Bastiaans, R. J. M., "Subgrid scale modeling in large-eddy simulation of turbulent combustion using premixed flamelet chemistry," *Flow Turbulence and Combustion*, vol. 82, pp. 511–535, 2009.

[229] Wang, J., Wang, L. P., Xiao, Z., Shi, Y., and Chen, S., "A hybrid numerical simulation of isotropic compressible turbulence," *Journal of Computational Physics*, vol. 229, pp. 5257–5279, July 2010.

[230] Wang, R. and Spiteri, R. J., "Linear instability of the fifth-order WENO method," *SIAM Journal on Numerical Analysis*, vol. 45, no. 5, pp. 1871–1901, 2007.

[231] Wang, Z. J., Fidkowski, K., Abgrall, R., Bassi, F., Caraeni, D., Cary, A., Deconinck, H., Hartmann, R., Hillewaert, K., Huynh, H. T., Kroll, N., May, G., Persson, P.-O., van Leer, B., and Visbal, M., "High-order CFD methods: current status and perspective," *International Journal for Numerical Methods in Fluids*, 2013.

[232] Weller, H. G., Tabor, G., Jasak, H., and Fureby, C., "A tensorial approach to computational continuum mechanics," *Computers in Physics*, vol. 12, no. 6, pp. 31–43, 1998.

[233] Wilke, C. R., "A viscosity equation for gas mixtures," *Journal of Chemical Physics*, vol. 18, no. 4, pp. 517–519, 1950.

[234] Williamson, J. H., "Low-storage Runge–Kutta schemes," *Journal of Computational Physics*, vol. 35, no. 1, pp. 48–56, 1980.

[235] Witherden, F., Vermeire, B., and Vincent, P., "Heterogeneous computing on mixed unstructured grids with PyFR," *Computers & Fluids*, vol. 120, pp. 173–186, 2015.

[236] Wong, S.-C. and Lin, A.-C., "Internal temperature distributions of droplets vaporizing in high-temperature convective flows," *Journal of Fluid Mechanics*, vol. 237, pp. 671–687, April 1992.

[237] Woodward, P. and Colella, P., "The numerical simulation of two-dimensional fluid flow with strong shocks," *Journal of Computational Physics*, vol. 54, no. 1, pp. 115–173, 1984.

[238] Xiao, F., Dianat, M., and McGuirk, J., "LES of turbulent liquid jet primary breakup in turbulent coaxial air flow," *International Journal of Multiphase Flow*, vol. 60, pp. 103–118, 2014.

[239] Yamaleev, N. K. and Carpenter, M. H., "Third-order energy stable WENO scheme," *Journal of Computational Physics*, vol. 228, pp. 3025–3047, 2009.

[240] Yee, H., Sandham, N., and Djomehri, M., "Low-dissipative high-order shock-capturing methods using characteristic-based filters," *Journal of Computational Physics*, vol. 150, no. 1, pp. 199 – 238, 1999.

[241] Yoo, C. S., Wang, Y., Trouvé, A., and Im, H. G., "Characteristic boundary conditions for direct simulations of turbulent counterflow flames," *Combustion Theory and Modelling*, vol. 9, pp. 617–646, November 2005.

[242] Yoo, C. and Im, H., "Characteristic boundary conditions for simulations of compressible reacting flows with multi-dimensional, viscous and reaction effects," *Combustion Theory and Modelling*, vol. 11, no. 2, pp. 259–286, 2007.

[243] Yuen, M. C. and Chen, L. W., "On drag of evaporating liquid drops," *Combustion Science and Technology*, vol. 14, pp. 147–154, 1976.

[244] Zhang, R., Zhang, M., and Shu, C.-W., "On the order of accuracy and numerical performance of two classes of finite volume WENO schemes," *Communications in Computational Physics*, vol. 9, pp. 807–827, March 2011.

[245] Zhao, S., Lardjane, N., and Fedioun, I., "Comparison of improved finite-difference WENO schemes for the implicit large eddy simulation of turbulent non-reacting and reacting high-speed shear flows," *Computers & Fluids*, vol. 95, pp. 74–87, 2014.

[246] Ziegler, J. L., Deiterding, R., Shepard, J. E., and Pullin, D., "An adaptive high-order hybrid scheme for compressive, viscous flows with detailed chemistry," *Journal of Computational Physics*, vol. 230, pp. 7598–7630, 2011.

[247] Zingg, D., Rango, S. D., Nemec, M., and Pulliam, T., "Comparison of several spatial discretizations for the Navier-Stokes equations," in *14th Computational Fluid Dynamics Conference*, 1999. AIAA Paper 1999-3260.

[248] Zingg, D., Rango, S. D., Nemec, M., and Pulliam, T., "Comparison of several spatial discretizations for the Navier-Stokes equations," *Journal of Computational Physics*, vol. 160, no. 2, pp. 683–704, 2000.